

1987

Characterization, kinetics and mechanisms of electron transfer reactions of superoxochromium (III) ion and a cobalt (II) macrocyclic complex with various substrates

Mark Erick Brynildson
Iowa State University

Follow this and additional works at: <https://lib.dr.iastate.edu/rtd>

 Part of the [Inorganic Chemistry Commons](#)

Recommended Citation

Brynildson, Mark Erick, "Characterization, kinetics and mechanisms of electron transfer reactions of superoxochromium (III) ion and a cobalt (II) macrocyclic complex with various substrates " (1987). *Retrospective Theses and Dissertations*. 8619.
<https://lib.dr.iastate.edu/rtd/8619>

This Dissertation is brought to you for free and open access by the Iowa State University Capstones, Theses and Dissertations at Iowa State University Digital Repository. It has been accepted for inclusion in Retrospective Theses and Dissertations by an authorized administrator of Iowa State University Digital Repository. For more information, please contact digirep@iastate.edu.

INFORMATION TO USERS

The most advanced technology has been used to photograph and reproduce this manuscript from the microfilm master. UMI films the original text directly from the copy submitted. Thus, some dissertation copies are in typewriter face, while others may be from a computer printer.

In the unlikely event that the author did not send UMI a complete manuscript and there are missing pages, these will be noted. Also, if unauthorized copyrighted material had to be removed, a note will indicate the deletion.

Oversize materials (e.g., maps, drawings, charts) are reproduced by sectioning the original, beginning at the upper left-hand corner and continuing from left to right in equal sections with small overlaps. Each oversize page is available as one exposure on a standard 35 mm slide or as a 17" × 23" black and white photographic print for an additional charge.

Photographs included in the original manuscript have been reproduced xerographically in this copy. 35 mm slides or 6" × 9" black and white photographic prints are available for any photographs or illustrations appearing in this copy for an additional charge. Contact UMI directly to order.



300 North Zeeb Road, Ann Arbor, MI 48106-1346 USA



Order Number 8805049

**Characterization, kinetics and mechanisms of electron transfer
reactions of superoxochromium(III) ion and a cobalt(II)
macrocyclic complex with various substrates**

Brynildson, Mark Erick, Ph.D.

Iowa State University, 1987

U·M·I

300 N. Zeeb Rd.
Ann Arbor, MI 48106



PLEASE NOTE:

In all cases this material has been filmed in the best possible way from the available copy. Problems encountered with this document have been identified here with a check mark .

1. Glossy photographs or pages _____
2. Colored illustrations, paper or print _____
3. Photographs with dark background _____
4. Illustrations are poor copy _____
5. Pages with black marks, not original copy _____
6. Print shows through as there is text on both sides of page _____
7. Indistinct, broken or small print on several pages
8. Print exceeds margin requirements _____
9. Tightly bound copy with print lost in spine _____
10. Computer printout pages with indistinct print _____
11. Page(s) _____ lacking when material received, and not available from school or author.
12. Page(s) _____ seem to be missing in numbering only as text follows.
13. Two pages numbered _____. Text follows.
14. Curling and wrinkled pages _____
15. Dissertation contains pages with print at a slant, filmed as received
16. Other _____

U·M·I



Characterization, kinetics and mechanisms of electron transfer
reactions of superoxochromium(III) ion and a cobalt(II)
macrocyclic complex with various substrates

by

Mark Erick Brynildson

A Dissertation Submitted to the
Graduate Faculty in Partial Fulfillment of the
Requirements for the Degree of
DOCTOR OF PHILOSOPHY

Department: Chemistry

Major: Inorganic Chemistry

Approved:

Signature was redacted for privacy.

In Charge of Major Work

Signature was redacted for privacy.

~~For the Major Department~~

Signature was redacted for privacy.

For the Graduate College

Iowa State University
Ames, Iowa

1987

TABLE OF CONTENTS

DEDICATION	xxi
GENERAL INTRODUCTION	1
CHAPTER I. EVIDENCE FOR A BOND HOMOLYSIS PATHWAY FOR O ₂ RELEASE IN THE DECOMPOSITION OF THE SUPEROXOCHROMIUM(III) ION CrO ₂ ²⁺	2
INTRODUCTION	3
Properties of molecular oxygen and dioxygen complexes	4
Reactivity of η ¹ and η ² dioxygen transition metal complexes	5
Dioxygen chromium chemistry	8
STATEMENT OF PROBLEM	11
EXPERIMENTAL SECTION	12
Solvents and reagents	12
Ultraviolet-visible spectroscopy	13
Kinetic simulation	13
Preparation of CrO ₂ ²⁺	13
Spectrum of CrO ₂ ²⁺	14
Cr ²⁺ trapping experiment	15
Kinetics	16
RESULTS	18
Stoichiometry	18
Product analysis	19
The kinetics of the decomposition of CrO ₂ ²⁺	25
Observed rate law	26
Activation parameters	33
Numerical modeling of kinetic data	39
DISCUSSION	46
Proposed structure of CrO ₂ ²⁺	46

Proposed mechanism-CrO ₂ ²⁺ decomposition	50
Activation parameters and bond strengths	61
Heterolytic dissociation of CrO ₂ ²⁺	63
SUMMARY	67
BIBLIOGRAPHY	68
CHAPTER II. REACTIONS OF THE SUPEROXOCHROMIUM(III) ION WITH TRANSITION METAL COMPLEXES	71
INTRODUCTION	72
STATEMENT OF PROBLEM	74
EXPERIMENTAL SECTION	75
Materials	75
Instrumentation	76
RESULTS	77
Outer-sphere electron transfer reactions	77
Inner-sphere electron transfer reactions	83
DISCUSSION	98
Outer-sphere reactions	98
Inner-sphere reactions	103
SUMMARY	105
BIBLIOGRAPHY	106
CHAPTER III. CHARACTERIZATION OF THE STRUCTURE, PROPERTIES, AND REACTIVITY OF A COBALT(II) MACROCYCLIC COMPLEX	108
INTRODUCTION	109
STATEMENT OF PROBLEM	114
EXPERIMENTAL SECTION	115
Solvents and reagents	115

X-ray crystallography	116
Magnetic susceptibility	117
Electron paramagnetic resonance spectroscopy	118
Cyclic voltammetry	118
Ultraviolet-visible spectroscopy	119
Kinetics using the stopped-flow technique	119
RESULTS	120
X-ray crystal structure	120
EPR spectroscopy of (B)(B')Co(dm _g BF ₂) ₂	127
Electrochemical measurements of (H ₂ O) ₂ Co(dm _g BF ₂) ₂	131
Reversible oxidation of (H ₂ O) ₂ Co(dm _g BF ₂) ₂	135
Equilibrium constant determination	136
Rate constant determination	137
The effect of chloride on the observed rate	141
Forward rate constant by the stopped-flow method	141
DISCUSSION	152
Structure	152
EPR spectroscopic analysis	156
Chemical characterization of cobalt(III)/cobalt(II)	157
Kinetics and mechanism	159
Analysis of the rate parameters	164
SUMMARY	167
BIBLIOGRAPHY	168
APPENDIX. CHARACTERIZATION, KINETICS, AND REACTION MECHANISMS FOR THE REACTION OF (H ₂ O) ₂ Co(dm _g BF ₂) ₂ WITH VARIOUS OXIDANTS	170
INTRODUCTION	171
STATEMENT OF PROBLEM	174
EXPERIMENTAL SECTION	175
Materials and measurements	175

RESULTS	177
Reaction between $(\text{H}_2\text{O})_2\text{Co}(\text{dmgBF}_2)_2$ and H_2O_2	177
NMR product analysis	180
Reaction between $(\text{H}_2\text{O})_2\text{Co}(\text{dmgBF}_2)_2$ and t-BuOOH	192
DISCUSSION	202
SUMMARY	206
BIBLIOGRAPHY	207
GENERAL SUMMARY	208
ACKNOWLEDGMENTS	209

LIST OF FIGURES

- Figure I-1.** UV-VIS spectrum of CrO_2^{2+} in 0.100 M HClO_4 17
- Figure I-2.** The UV-VIS spectra for the stoichiometric titration experiment between CrO_2^{2+} and Cr^{2+} (A). The loss in absorbance for CrO_2^{2+} corresponds to the consumption of CrO_2^{2+} by repeated injections of Cr^{2+} . The initial spectrum is of an air-free aqueous solution of CrO_2^{2+} ($[\text{CrO}_2^{2+}] = 4.8 \times 10^{-5}$ M, $\text{HClO}_4 = 0.100$ M, 5.00 cm cell, 15.5 mL cell volume) 21
- Figure I-3.** The spectrophotometric titration plot at 290 nm (B). The endpoint corresponds to a reactant ratio 1 CrO_2^{2+} : 3.2 Cr^{2+} (equation 17) 22
- Figure I-4.** A comparison between the observed and calculated yields of HCrO_4^- . The calculated yield is based on the proportion of the reaction proceeding by the kinetic term $k[\text{CrO}_2^{2+}]^2$, in which the best fit values of the four rate constants in equation 33 were used for numerical simulation in the program KINSIM 28

Figure I-5. Normalized CrO_2^{2+} absorbance-time decomposition traces showing the kinetic inhibition by increased O_2 concentrations, $\text{HClO}_4 = 0.100 \text{ M}$, $\mu = 0.10 \text{ M}$. The concentration of dissolved dioxygen in these four experiments is: (A) $[\text{O}_2] = 0 \text{ M}$, (B) $[\text{O}_2] = 5.25 \times 10^{-5} \text{ M}$, (C) $[\text{O}_2] = 1.05 \times 10^{-4} \text{ M}$, and (D) $[\text{O}_2] = 2.10 \times 10^{-4} \text{ M}$. The solid circles represent the observed data and the curves drawn through the experimental data are the final best fits (calculated with the numerical integration program KINSIM) using the full rate law, equation 33, and the best values of all four rate constants

29

Figure I-6. Normalized CrO_2^{2+} absorbance-time decomposition traces showing the kinetic inhibition by increased O_2 concentrations, $\text{HClO}_4 = 0.100 \text{ M}$, $\mu = 0.10 \text{ M}$. The concentration of dissolved dioxygen in these four experiments is: (E) $[\text{O}_2] = 3.15 \times 10^{-4} \text{ M}$, (F) $[\text{O}_2] = 6.83 \times 10^{-4} \text{ M}$, (G) $[\text{O}_2] = 1.05 \times 10^{-3} \text{ M}$, and (H) $[\text{O}_2] = 3.70 \times 10^{-3} \text{ M}$. The solid circles represent the observed data and the curves drawn through the experimental data are the final best fit (calculated with the numerical integration program KINSIM) using the full rate law, equation 33, and the best values of all four rate constants

30

- Figure I-7.** The plot of k' vs. $[\text{CrO}_2^{2+}]_0$. The Y-intercept yields the value for k' , and the slope yields the value for k'' according to equation 24 35
- Figure I-8.** The temperature dependences of k' (upper) and k'' according to activated complex theory, as $\ln(k/T)$ vs. $1/T$ 38
- Figure I-9.** A comparison of experimental (solid points) and numerically simulated (dashed lines) absorbance-time curves for the decomposition of CrO_2^{2+} at $[\text{O}_2] = 0 \text{ M}$. Parameter sets I and II give the same fit shown as the dashed lines 43
- Figure I-10.** A comparison of experimental (solid points) and numerically simulated (dashed lines) absorbance-time curves for the decomposition of CrO_2^{2+} at $[\text{O}_2] = 1.05 \times 10^{-4} \text{ M}$. The longer dashed lines correspond to parameter set I and the shorter dashed lines correspond to the parameter set II 44
- Figure I-11.** A comparison of experimental (solid points) and numerically simulated (dashed lines) absorbance-time curves for the decomposition of CrO_2^{2+} at $[\text{O}_2] = 3.7 \times 10^{-3} \text{ M}$. The longer dashed lines correspond to parameter set I and the shorter dashed lines correspond to parameter set II 45

Figure II-1. Dependence of k_{obs} on $[R]_{\text{ave}}$, ($\text{HClO}_4 = 0.100 \text{ M}$, $\mu = 0.10 \text{ M}$, $T = 25.0 \text{ }^\circ\text{C}$), $R = \text{Ru}(\text{NH}_3)_6^{2+}$ (circles), $\text{Co}(\text{sep})^{2+}$ (squares), $\text{V}(\text{OH}_2)_6^{2+}$ (triangles) 79

Figure II-2. The reaction between CrO_2^{2+} and Fe^{2+} was followed by recording a family of absorbance-time profiles. The first fifty data points of the upper figure (290 nm) were collected in 0.2 seconds and the second fifty collected in 2.8 seconds. The first fifty data points of the lower figure (240 nm) were collected in 1 second and the second fifty collected in 119 seconds. The family of traces results from stopped-flow experiments performed on the same solution at various times over a 2 hr period ($t = 0 \text{ hr}$ (A), $t = 2 \text{ hr}$ (B)) 84

Figure II-3. The reaction between CrO_2^{2+} and Fe^{2+} was followed by recording the absorbance-wavelength profiles. The absorbance at 320 nm decreases with a first-order rate constant (0.12 s^{-1}) similar to the rate constant of the increase in absorbance at 240 nm (0.11 s^{-1}). This family of spectra represent a total collection time of 430 seconds ($[\text{H}_3\text{O}^+] = 0.100 \text{ M}$, $\mu = 0.10 \text{ M}$, $T = 25.0 \text{ }^\circ\text{C}$, $[\text{CrO}_2^{2+}]_0 = 3.2 \times 10^{-5} \text{ M}$, and $[\text{Fe}^{2+}]_0 = 2.5 \times 10^{-4} \text{ M}$) 87

- Figure II-4.** The dependence of k_{obs} on $[\text{Fe}^{2+}]_{\text{ave}}$ (first stage, circles), the dependence of k_{obs} on $[\text{Fe}^{2+}]_{\text{ave}}$ (second stage, squares), and the dependence of k_{obs} on $[\text{Co}([\text{15}]\text{aneN}_4)^{2+}]_{\text{ave}}$ (triangles), ($[\text{H}_3\text{O}^+] = 0.100 \text{ M}$, $\mu = 0.10 \text{ M}$, $T = 25.0 \text{ }^\circ\text{C}$) 88
- Figure II-5.** The UV-vis reaction profile for the reaction between CrO_2^{2+} and $\text{Co}([\text{14}]\text{aneN}_4)(\text{OH}_2)_2^{2+}$, $[\text{Co}([\text{14}]\text{aneN}_4)(\text{OH}_2)_2^{2+}]_0 = 1.0 \times 10^{-4} \text{ M}$, $[\text{CrO}_2^{2+}]_0 = 2.0 \times 10^{-5} \text{ M}$, $\text{HClO}_4 = 0.100 \text{ M}$, and $\mu = 0.10 \text{ M}$, the spectra were collected in 1 second 95
- Figure II-6.** The UV-vis reaction profiles for the reaction between CrO_2^{2+} and $\text{Co}([\text{15}]\text{aneN}_4)(\text{OH}_2)_2^{2+}$, $[\text{Co}([\text{15}]\text{aneN}_4)(\text{OH}_2)_2^{2+}]_0 = 1.5 \times 10^{-4} \text{ M}$, $[\text{CrO}_2^{2+}]_0 = 2.0 \times 10^{-5} \text{ M}$, $\text{HClO}_4 = 0.100 \text{ M}$, and $\mu = 0.10 \text{ M}$. The upper figure illustrates 16 spectra collected in 1 second. The lower figure illustrates 16 spectra collected in 10 seconds 96
- Figure II-7.** The UV-vis reaction profile for the reaction between CrO_2^{2+} and $\text{Co}(\text{meso-Me}_6[\text{14}]\text{aneN}_4)(\text{OH}_2)_2^{2+}$, $[\text{Co}(\text{meso-Me}_6[\text{14}]\text{aneN}_4)(\text{OH}_2)_2^{2+}]_0 = 1.8 \times 10^{-4} \text{ M}$, $[\text{CrO}_2^{2+}]_0 = 2.0 \times 10^{-5} \text{ M}$, $\text{HClO}_4 = 0.100 \text{ M}$, and $\mu = 0.10 \text{ M}$. The upper figure illustrates 16 spectra collected in 0.35 seconds. The lower figure illustrates 16 spectra collected in 60 seconds 97

- Figure III-1.** Two Members of the Cobaloxime Family 110
- Figure III-2.** Full ORTEP drawing of the molecular structure of $(\text{CH}_3\text{OH})_2\text{Co}(\text{dmgBF}_2)_2$. The hydrogen atoms are not included in the ORTEP drawing for clarity. The thermal ellipsoids are drawn at the 50% probability 121
- Figure III-3.** EPR spectrum of $(\text{CH}_3\text{CN})_2\text{Co}(\text{dmgBF}_2)_2$ (top figure), EPR spectrum of $(\text{CH}_3\text{OH})_2\text{Co}(\text{dmgBF}_2)_2$ (bottom figure) 129
- Figure III-4.** EPR spectrum of $((\text{CH}_3)_2\text{CO})_2\text{Co}(\text{dmgBF}_2)_2$ (top figure), EPR spectrum of $((\text{CH}_3)_2\text{CO})\text{Co}(\text{dmgBF}_2)_2(\text{O}_2)$, (bottom figure) 130
- Figure III-5.** Cyclic voltammogram of $(\text{H}_2\text{O})_2\text{Co}(\text{dmgBF}_2)_2$, (top figure, redox couples = cobalt(III)/(II), cobalt(II)/(I), glassy carbon electrode, $\text{LiClO}_4 = 0.10 \text{ M}$, $\nu = 10 \text{ mV s}^{-1}$, potentials vs. Ag/AgCl reference electrode). Cyclic voltammogram of $(\text{H}_2\text{O})_2\text{Co}(\text{dmgBF}_2)_2$, (bottom figure, redox couples = cobalt(II)/(I), glassy carbon electrode,

$\text{LiClO}_4 = 0.10 \text{ M}$, $\nu = 10 \text{ mV s}^{-1}$, potentials vs.

Ag/AgCl reference electrode)

134

Figure III-6. Three UV-VIS spectral scans, recorded as a function of time, of the air-free oxidation of $(\text{H}_2\text{O})_2\text{Co}(\text{dmgBF}_2)_2$ ($8.0 \times 10^{-5} \text{ M}$) to $(\text{H}_2\text{O})_2\text{Co}(\text{dmgBF}_2)_2^+$ by Fe^{3+} ($1 \times 10^{-4} \text{ M}$, left figure). The right figure displays the UV-VIS spectral scan recorded immediately following the oxidation of $(\text{H}_2\text{O})_2\text{Co}(\text{dmgBF}_2)_2$ overlaid with the UV-VIS spectral scan recorded immediately following the reduction of the cobalt(III)⁺ by a slight excess of Cr^{2+} ($1.1 \times 10^{-4} \text{ M}$)

138

Figure III-7. The plot of $(\Delta\epsilon/\Delta D)[\text{Co(II)}]_0$ vs. $[\text{Fe}^{2+}]_{\text{ave}}/[\text{Fe}^{3+}]_{\text{ave}}$ for the reaction of $(\text{H}_2\text{O})_2\text{Co}(\text{dmgBF}_2)_2$ to determine the equilibrium constant. The concentrations of Fe^{3+} and Fe^{2+} were present in large excess ($[\text{Fe}^{3+}] = 0.9 - 3.0 \times 10^{-4} \text{ M}$, $[\text{Fe}^{2+}] = 3.0 - 5.0 \times 10^{-3} \text{ M}$, $\text{HClO}_4 = 0.400 \text{ M}$, $\mu = 0.500 \text{ M}$, $T = 25.0 \text{ }^\circ\text{C}$)

139

Figure III-8. The plot of $k_{\text{obs}}/[\text{Fe}^{2+}]_{\text{ave}}$ vs. $[\text{Fe}^{3+}]_{\text{ave}}/[\text{Fe}^{2+}]_{\text{ave}}$ for the reaction of $(\text{H}_2\text{O})_2\text{Co}(\text{dmgBF}_2)_2$ with pseudo-first-order concentrations of Fe^{3+} and Fe^{2+} ($[\text{Fe}^{3+}] = 0.9 - 3.0 \times 10^{-4} \text{ M}$, $[\text{Fe}^{2+}] = 3.0 - 5.0 \times 10^{-3} \text{ M}$, $\text{HClO}_4 = 0.400 \text{ M}$, $\mu = 0.500 \text{ M}$, $T = 25.0 \text{ }^\circ\text{C}$)

142

Figure III-9. The plot of k_{obs} vs. $([\text{Fe}^{3+}]_{\text{ave}} + [\text{Fe}^{2+}]_{\text{ave}}/K_{\text{eq}})$ for the reaction of $(\text{H}_2\text{O})_2\text{Co}(\text{dmgBF}_2)_2$ with pseudo-first-order concentrations of Fe^{3+} and Fe^{2+} ($[\text{Fe}^{3+}] = 0.9 - 3.0 \times 10^{-4}$ M, $[\text{Fe}^{2+}] = 3.0 - 5.0 \times 10^{-3}$ M, $\text{HClO}_4 = 0.400$ M, $\mu = 0.500$ M, $T = 25.0$ °C) 143

Figure III-10. The plot of k_{obs} vs. $([\text{Fe}^{2+}]_{\text{ave}} + K_{\text{eq}}[\text{Fe}^{3+}]_{\text{ave}})$ for the reaction of $(\text{H}_2\text{O})_2\text{Co}(\text{dmgBF}_2)_2$ with pseudo-first-order concentrations of Fe^{3+} and Fe^{2+} ($[\text{Fe}^{3+}] = 0.9 - 3.0 \times 10^{-4}$ M, $[\text{Fe}^{2+}] = 3.0 - 5.0 \times 10^{-3}$ M, $\text{HClO}_4 = 0.400$ M, $\mu = 0.500$ M, $T = 25.0$ °C) 144

Figure III-11. The plot of $\text{Log}(k_{\text{obs}}/[\text{Fe}^{3+}])$ vs. $\text{Log}([\text{H}^+])$ for the reaction of $(\text{H}_2\text{O})_2\text{Co}(\text{dmgBF}_2)_2$ with pseudo-first-order concentrations of Fe^{3+} ($[\text{Fe}^{3+}] = 2.0 - 30 \times 10^{-4}$ M, $\mu = 0.500$ M, $T = 25.0$ °C); only the forward reaction was observed in the stopped-flow experiments. The best fit line for each of the two rate law forms ($A + B/[\text{H}^+]$, solid line) and ($C/D + [\text{H}^+]$, broken line) are included 147

Figure III-12. The plot of k_f^{app} vs. $1/[\text{H}^+]$ for the reaction of $(\text{H}_2\text{O})_2\text{Co}(\text{dmgBF}_2)_2$ with pseudo-first-order concentrations of Fe^{3+} ($k_f^{\text{app}} = k_{\text{obs}}/[\text{Fe}^{3+}]_{\text{ave}}$, $[\text{Fe}^{3+}] = 2.0 - 30 \times 10^{-4}$ M, $\mu = 0.500$ M, $T = 25.0$ °C); only the forward reaction was observed in the stopped-flow experiments 148

- Figure III-13.** The plot of $1/k_f^{\text{app}}$ vs. $[\text{H}^+]$ for the reaction of $(\text{H}_2\text{O})_2\text{Co}(\text{dmgBF}_2)_2$ with pseudo-first-order concentrations of Fe^{3+} ($k_f^{\text{app}} = k_{\text{obs}}/[\text{Fe}^{3+}]_{\text{ave}}$, $[\text{Fe}^{3+}] = 2.0 - 30 \times 10^{-4} \text{ M}$, $\mu = 0.500 \text{ M}$, $T = 25.0 \text{ }^\circ\text{C}$); only the forward reaction was observed in the stopped-flow experiments 149
- Figure III-14.** The plot of $[\text{H}^+]k_f^{\text{app}}$ vs. $[\text{H}^+]$ for the reaction of $(\text{H}_2\text{O})_2\text{Co}(\text{dmgBF}_2)_2$ with pseudo-first-order concentrations of Fe^{3+} ($k_f^{\text{app}} = k_{\text{obs}}/[\text{Fe}^{3+}]_{\text{ave}}$, $[\text{Fe}^{3+}] = 2.0 - 30 \times 10^{-4} \text{ M}$, $\mu = 0.500 \text{ M}$, $T = 25.0 \text{ }^\circ\text{C}$); only the forward reaction was observed in the stopped-flow experiments 150
- Figure III-15.** The plots of percent deviation vs. $[\text{H}^+]$ for the reaction of $(\text{H}_2\text{O})_2\text{Co}(\text{dmgBF}_2)_2$ with pseudo-first-order concentrations of Fe^{3+} ($k_f^{\text{app}} = k_{\text{obs}}/[\text{Fe}^{3+}]_{\text{ave}}$, $[\text{Fe}^{3+}] = 2.0 - 30 \times 10^{-4} \text{ M}$, $\mu = 0.500 \text{ M}$, $T = 25.0 \text{ }^\circ\text{C}$); only the forward reaction was observed in the stopped-flow experiments. The top figure is the parallel path percent deviation and the bottom figure is the consecutive path percent deviation 151

- Figure A-1.** Proposed attack of H_2O_2 on $(\text{H}_2\text{O})_2\text{Co}(\text{dmgH})_2$ 173
- Figure A-2.** Dependence of k_{obs} on $[\text{ROOH}]$, $\text{HClO}_4 = 0.100 \text{ M}$, $\mu = 0.100 \text{ M}$, $\text{ROOH} = \text{HOOH}$ (circles), and $\text{ROOH} = \text{t-BuOOH}$ (squares) 179
- Figure A-3.** NMR spectrum of the products of the reaction between $(\text{H}_2\text{O})_2\text{Co}(\text{dmgBF}_2)_2$ and a slight excess of H_2O_2 , $(\text{H}_2\text{O})_2\text{Co}(\text{dmgBF}_2)_2 \sim 5 \times 10^{-4}$, and $\text{H}_2\text{O}_2 \sim 6 \times 10^{-4} \text{ M}$ 182
- Figure A-4.** NMR spectrum of the products of the reaction between $(\text{H}_2\text{O})_2\text{Co}(\text{dmgBF}_2)_2$ and a moderate excess of H_2O_2 , $(\text{H}_2\text{O})_2\text{Co}(\text{dmgBF}_2)_2 \sim 5 \times 10^{-4}$, and $\text{H}_2\text{O}_2 \sim 5 \times 10^{-3} \text{ M}$ 183
- Figure A-5.** NMR spectrum of the products obtained by bulk electrolysis of $(\text{H}_2\text{O})_2\text{Co}(\text{dmgBF}_2)_2$ in $\text{LiClO}_4 = 0.10 \text{ M}$ 184
- Figure A-6.** NMR spectrum of the products obtained by bulk electrolysis of $(\text{H}_2\text{O})_2\text{Co}(\text{dmgBF}_2)_2$ in $\text{LiClO}_4 = 0.10 \text{ M}$. HClO_4 was added before the spectrum was recorded, $\text{HClO}_4 \sim 0.05 \text{ M}$ 186
- Figure A-7.** NMR spectrum of the products of the reaction between $(\text{H}_2\text{O})_2\text{Co}(\text{dmgBF}_2)_2$ and t-BuOOH , $(\text{H}_2\text{O})_2\text{Co}(\text{dmgBF}_2)_2 \sim 5 \times 10^{-4} \text{ M}$ and $\text{t-BuOOH} \sim 1 \times 10^{-3} \text{ M}$ 187

- Figure A-8.** NMR spectrum of the products of the reaction between $(\text{H}_2\text{O})_2\text{Co}(\text{dmgBF}_2)_2$ and $\text{Na}_2\text{S}_2\text{O}_8$, $(\text{H}_2\text{O})_2\text{Co}(\text{dmgBF}_2)_2 \sim 5 \times 10^{-4}$ M, and $\text{Na}_2\text{S}_2\text{O}_8 \sim 1 \times 10^{-3}$ M 188
- Figure A-9.** NMR spectrum of the products of the reaction between $(\text{H}_2\text{O})_2\text{Co}(\text{dmgBF}_2)_2$ and $\text{Fe}(\text{ClO}_4)_3$, $(\text{H}_2\text{O})_2\text{Co}(\text{dmgBF}_2)_2 \sim 5 \times 10^{-4}$ M, and $\text{Fe}(\text{ClO}_4)_3 \sim 1 \times 10^{-3}$ M 189
- Figure A-10.** NMR spectrum of the products of the reaction between $(\text{H}_2\text{O})_2\text{Co}(\text{dmgBF}_2)_2$ and $\text{Fe}(\text{ClO}_4)_3$, $(\text{H}_2\text{O})_2\text{Co}(\text{dmgBF}_2)_2 \sim 5 \times 10^{-4}$, $\text{Fe}(\text{ClO}_4)_3 \sim 1 \times 10^{-3}$ M and $\text{HClO}_4 \sim 0.05$ M 193
- Figure A-11.** NMR spectrum of the products of the reaction between $(\text{H}_2\text{O})_2\text{Co}(\text{dmgBF}_2)_2$ and FeCl_3 , $(\text{H}_2\text{O})_2\text{Co}(\text{dmgBF}_2)_2 \sim 5 \times 10^{-4}$ M, and $\text{FeCl}_3 \sim 1 \times 10^{-3}$ M 194
- Figure A-12.** NMR spectrum of the products of the reaction between $(\text{H}_2\text{O})_2\text{Co}(\text{dmgBF}_2)_2$ and FeCl_3 , $(\text{H}_2\text{O})_2\text{Co}(\text{dmgBF}_2)_2 \sim 5 \times 10^{-4}$ M, $\text{FeCl}_3 = 1 \times 10^{-3}$ M, and $\text{HClO}_4 = 0.10$ M 195
- Figure A-13.** NMR spectrum of the same sample used in Figure A-12; however, this spectrum was taken 1 hour after the spectrum in Figure A-12 was recorded 196

Figure A-14. NMR spectrum of the same sample used in Figure A-12; however, this spectrum was taken 20 hours after the spectrum in Figure A-12 was recorded 197

Figure A-15. NMR spectrum of the products of the reaction between $((\text{CH}_3)_2\text{CO})_2\text{Co}(\text{dmgBF}_2)_2$ and $\text{Fe}(\text{OH})^{2+}$ in d_6 -acetone, $((\text{CH}_3)_2\text{CO})_2\text{Co}(\text{dmgBF}_2)_2 \sim 5 \times 10^{-3} \text{ M}$ and $\text{Fe}(\text{OH})^{2+} \sim 5 \times 10^{-3} \text{ M}$ 198

Figure A-16. The reaction between $(\text{H}_2\text{O})_2\text{Co}(\text{dmgBF}_2)_2$ and H_2O_2 (A) shows a 1:1 reaction stoichiometry $((\text{H}_2\text{O})_2\text{Co}(\text{dmgBF}_2)_2:\text{H}_2\text{O}_2)$, $([(\text{H}_2\text{O})_2\text{Co}(\text{dmgBF}_2)_2] = 2.24 \times 10^{-4} \text{ M}, [\text{H}_2\text{O}_2] = 8.80 \times 10^{-5} \text{ M}, 2 \text{ cm cell})$. The reaction between $(\text{H}_2\text{O})_2\text{Co}(\text{dmgBF}_2)_2$ and $t\text{-BuOOH}$ (B) shows a 2:1 reaction stoichiometry $((\text{H}_2\text{O})_2\text{Co}(\text{dmgBF}_2)_2:\text{H}_2\text{O}_2)$, $([(\text{H}_2\text{O})_2\text{Co}(\text{dmgBF}_2)_2] = 2.24 \times 10^{-4} \text{ M}, [t\text{-BuOOH}] = 8.80 \times 10^{-5} \text{ M}, 2 \text{ cm cell})$ 199

LIST OF TABLES

Table I-1.	Structural Classification of Dioxygen Complexes	5
Table I-2.	Stoichiometric Titration Data	20
Table I-3.	Observed Data for the Decomposition of CrO_2^{2+}	27
Table I-4.	The Percent of Reaction by the Bimolecular Path	34
Table I-5.	The Variation of $k'/2$ with Temperature	37
Table I-6.	The Variation of $k''/2$ with Temperature	37
Table I-7.	Numerical Modeling Test Parameters	42
Table II-1.	Summary of the Acid Dependence for the Outer-Sphere Reactions	81
Table II-2.	Kinetic Parameters for the Outer-Sphere Reactions	82
Table II-3.	Summary of Kinetic Data for Reductions of CrO_2^{2+} and $\text{Co}([\text{14}] \text{aneN}_4)(\text{OH}_2)\text{O}_2^{2+}$	101
Table II-4.	Summary of Kinetic Data for Various Outer-Sphere Reactions	102

Table III-1.	Crystallographic Data for $(\text{CH}_3\text{OH})_2\text{Co}(\text{dmgBF}_2)_2$	122
Table III-2.	Calculated Bond Distances for $(\text{CH}_3\text{OH})_2\text{Co}(\text{dmgBF}_2)_2$	123
Table III-3.	Selected Bond Angles in $(\text{CH}_3\text{OH})_2\text{Co}(\text{dmgBF}_2)_2$	124
Table III-4.	Atomic Positional and Average Isotropic Thermal Parameters for $(\text{CH}_3\text{OH})_2\text{Co}(\text{dmgBF}_2)_2$	125
Table III-5.	Temperature Factors [$\text{\AA} \times 10^3$] for $(\text{CH}_3\text{OH})_2\text{Co}(\text{dmgBF}_2)_2$	126
Table III-6.	EPR Parameters for $(\text{B})(\text{B}')\text{Co}(\text{dmgBF}_2)_2$	128
Table III-7.	Cyclic Voltammetry Results for $(\text{H}_2\text{O})_2\text{Co}(\text{dmgBF}_2)_2$	133
Table III-8.	Bond Lengths and Magnetic Susceptibilities of Some Cobalt(II) Macrocyclic Complexes	153
Table III-9.	Summary of the Equilibrium and Rate Constants	166

LIST OF SCHEMES

Scheme I-1. Proposed Decomposition Mechanism for CrO_2^{2+}	59
Scheme II-1. Simple Outer-Sphere Mechanism	78
Scheme II-2. Complete Outer-Sphere Mechanism	80
Scheme II-3. CrO_2^{2+} and Fe^{2+} Reaction Mechanism	89
Scheme II-4. CrO_2^{2+} and $(\text{H}_2\text{O})_2\text{Co}([\text{n}] \text{aneN}_4)^{2+}$ Reaction Mechanism	91
Scheme III-1. Parallel Path-Complete Mechanism	160
Scheme III-2. Consecutive Path-Complete Mechanism	161
Scheme A-1. Reaction Mechanism for $(\text{H}_2\text{O})_2\text{Co}(\text{dmgH})_2$ and ROOH	171
Scheme A-2. Reaction Mechanism for $(\text{H}_2\text{O})_2\text{Co}(\text{dmgBF}_2)_2$ and H_2O_2	180
Scheme A-3. Reaction Mechanism for $(\text{H}_2\text{O})_2\text{Co}(\text{dmgBF}_2)_2$ and $t\text{-BuOOH}$	200

DEDICATION

To Angela, my loving wife, and Shawn, my delightful son, thank you for all your love and support during my effort to explore a little bit of God's world through chemistry. I love you both dearly.

GENERAL INTRODUCTION

Chapter I describes the kinetics and mechanism of the decomposition of CrO_2^{2+} . Two decomposition pathways are proposed. The first consists of a bond homolysis, $\text{CrO}_2^{2+} \rightarrow \text{Cr}^{2+} + \text{O}_2$, and the second pathway a bimolecular reaction between two CrO_2^{2+} ions to form HCrO_4^- .

Chapter II describes the oxidation-reduction reactions of CrO_2^{2+} with various outer- and inner-sphere reductants.

Chapter III describes the characterization of $(\text{H}_2\text{O})_2\text{Co}(\text{dmgBF}_2)_2$ by various instrumental and chemical techniques. The kinetics and mechanism for the reaction of $(\text{H}_2\text{O})_2\text{Co}(\text{dmgBF}_2)_2$ with $(\text{H}_2\text{O})_5\text{Fe}(\text{OH})^{2+}$ are also discussed.

The Appendix describes the characterization, kinetics, and mechanisms of the reactions of $(\text{H}_2\text{O})_2\text{Co}(\text{dmgBF}_2)_2$ with H_2O_2 and $t\text{-BuOOH}$.

CHAPTER I. EVIDENCE FOR A BOND HOMOLYSIS PATHWAY FOR O₂ RELEASE IN THE
DECOMPOSITION OF THE SUPEROXOCHROMIUM(III) ION CrO₂²⁺

INTRODUCTION

The investigation of transition metal dioxygen complexes (the structural definition of these complexes requires only the continued existence of O-O bonding in the complex molecule) is generally accepted to have begun in 1852 with Fremy's report of the oxygenated ammoniacal salts of cobalt.¹ A satisfactory explanation of his results, however, first came when a general theory of coordination compounds was developed by Werner in the early twentieth century. Among the many complexes studied by Werner during his pioneering work with inorganic coordination complexes were the dioxygen bridged complexes of Co(III).² Twenty years later, work on the mechanism of the auto-oxidation of metal ions was reported and the first synthetic oxygen carriers discovered. The early research focused on three essentially different areas:

- (1) Complexes of cobalt with Schiff bases and nitrogen containing ligands.
- (2) Complexes of group VIII B in low oxidation states.
- (3) Complexes of biological interest such as dioxygen carriers and related model systems.

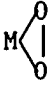

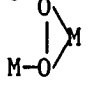
Although these three areas represent the majority of the investigated systems, interest outside these areas coupled with a greater understanding of the electronic and reaction properties of molecular oxygen has led to the investigation of other transition metal dioxygen complexes. These investigations have provided a better understanding of the reaction chemistry of transition metal dioxygen complexes.

Properties of molecular oxygen and dioxygen complexes

The molecular orbital description for dioxygen shows a vacancy for the addition of a single electron in both of the antibonding $2p\pi_g^*$ orbitals. Therefore, it has an electronic structure in the ground state of $^3\Sigma_g^-$.³ This triplet ground state provides a considerable kinetic barrier to the auto-oxidation of normally diamagnetic organic molecules. This barrier is associated with generally very slow reactions involving a change of spin or unstable triplet state products. This problem can be avoided by the reaction of dioxygen with a heavy transition metal where greater spin-orbit coupling considerably reduces the kinetic barrier to a change of spin. In addition, the formation of a metal dioxygen complex may provide sufficient energy to pair the spins, also reducing this kinetic barrier.⁴

The manner by which dioxygen is bound in metal complexes is a controversial problem because the ligation of molecular oxygen to a metal complex can involve metal to ligand electron transfer unlike the ligation of simple neutral or anionic species, e.g., NH_3 , Cl^- . When molecular oxygen reacts with transition metals, various structural arrangements can occur. The addition of one or two electrons to a neutral dioxygen complex results in the formation of superoxide (O_2^-) and peroxide (O_2^{2-}) anions, respectively. Examples of the known structural arrangements for transition metal dioxygen complexes are shown in Table I-1. These structural classifications were suggested by Vaska⁵ to aid in the discussion of the properties of dioxygen complexes. The structural arrangements appear to be controlled principally by the electronic structure of the dioxygen complex. Hoffmann, Chen and Thorn⁶ have developed a generalized Walsh diagram to predict the geometry of the dioxygen ligand, given a specific transition metal electronic configuration.

Table I-1. Structural Classification of Dioxygen Complexes

Type	Designation	Vaska Class	Example
M-O-O	η^1 dioxygen	Ia(superoxo)	$[\text{Co}(\text{CN})_5\text{O}_2]^{3-}$
	η^2 dioxygen	IIa(peroxo)	$(\text{Ph}_3\text{P})_2\text{PtO}_2$
M-O-O-M	$\eta^1:\eta^1$ dioxygen	Ib(superoxo)	$[(\text{H}_3\text{N})_5\text{CoO}_2\text{Co}(\text{H}_3\text{N})_5]^{5+}$
M-O-O-M	$\eta^1:\eta^1$ dioxygen	IIb(peroxo)	$[(\text{H}_3\text{N})_5\text{CoO}_2\text{Co}(\text{NH}_3)_5]^{4+}$
	$\eta^2:\eta^2$ dioxygen	-	$[(\text{UO}_2\text{Cl}_3)_2\text{O}_2]^{4-}$
	$\eta^1:\eta^2$ dioxygen	-	$[(\text{Ph}_3\text{P})_2\text{ClRh}]_2\text{O}_2$

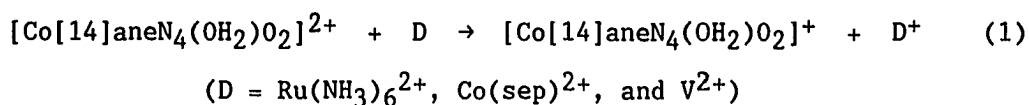
Reactivity of η^1 and η^2 dioxygen transition metal complexes

The importance of the spatial and electronic structure is seen in the reactivity of these complexes. Although there is considerable variation in the reactivity between and even within different structural types, one general feature of reactivity is seen. The binding of dioxygen to a transition metal is accompanied by 1) a reduction of the number of unpaired electrons on the oxygen (to one or zero) and 2) the transfer of charge density to the dioxygen. The first effect results in the elimination of the kinetic barrier to spin changes in the reaction of the dioxygen and the second effect causes the dioxygen ligand to acquire basic or nucleophilic character.

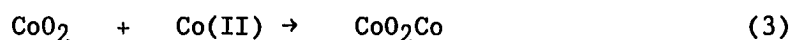
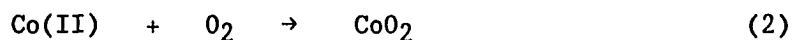
Within the category of η^1 transition metal dioxygen complexes, most of the published work is concerned with cobalt complexes, with a small amount

of literature dedicated to iron and rhodium complexes. Electron transfer reactions are an important feature of η^1 dioxygen transition metal reactivity. The reactions of η^1 dioxygen complexes can be grouped into three general types: 1) inner-sphere reactions, 2) outer-sphere reactions, and 3) H-atom abstraction reactions.

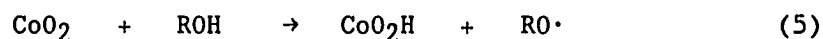
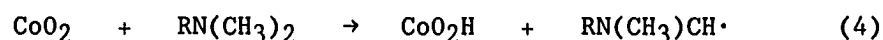
Outer-sphere mechanisms are proposed by Endicott and Kumar⁷ for the reaction of $[\text{Co}[\text{14}] \text{aneN}_4(\text{OH}_2)\text{O}_2]^{2+}$ with various reducing agents, equation 1.



Inner-sphere reduction of η^1 cobalt complexes by a second cobalt(II) is also a commonly accepted mechanism of transition metal dioxygen chemistry,⁸ equations 2 and 3.

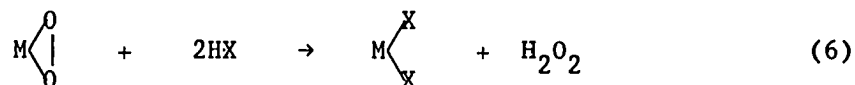


H-atom abstraction electron transfer reactions have recently been suggested for η^1 cobalt dioxygen complexes. Since these η^1 complexes are radicals, they can abstract hydrogen from $\text{N,N}'$ -tetramethyl-p-phenylenediamine and phenols,⁹ equations 4 and 5.



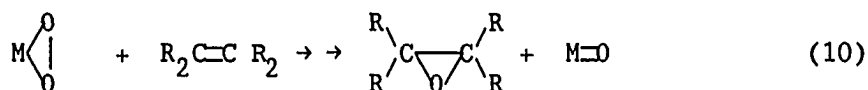
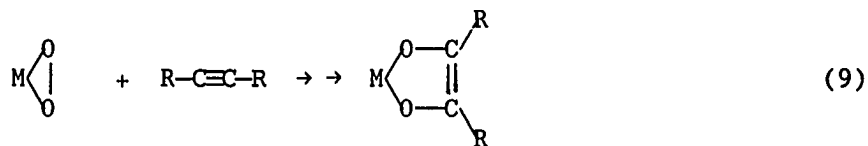
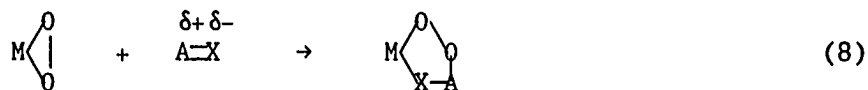
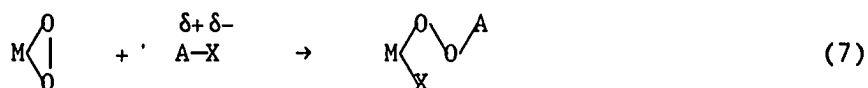
The reactions of η^2 complexes can be grouped into three general types: (1) protonation reactions, (2) reactions with nucleophilic attack on polar bonds, and (3) carbon-carbon multiple bond reactions.

Protonation reactions can be represented by equation 6.



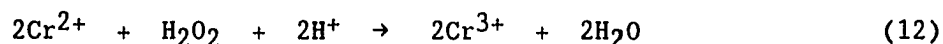
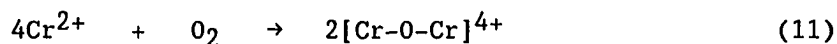
These reactions have been known for many years and can even occur for fairly weak acids.¹⁰ This scheme can be useful in the preparation of the cis-disubstituted products.

Nucleophilic attack on polar bonds is represented by equations 7 and 8. Examples of these reaction types are primarily restricted to group VIIIIB (i.e., Pt, Ni and Ir). Reactions with carbon-carbon multiple bonds can be represented by equations 9 and 10. Several examples of equation 8 have been seen for group VIIIIB metals (i.e., Pt and Pd)¹¹ and examples of equation 9 and 10 have been seen for groups VIB and IVB.¹²

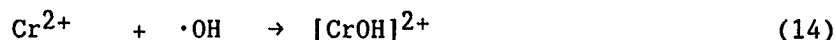
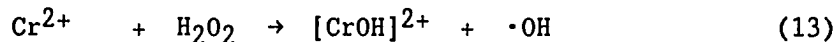


Dioxygen chromium chemistry

Chromium dioxygen complexes are among the many dioxygen transition metal complexes studied. Picard¹³ reported an early study of the reaction of chromium(II) in acidic aqueous solution with molecular oxygen. He reported the formation of two intermediates that are capable of oxidizing aqueous arsenious solutions to arsenate, a reaction not observed for molecular oxygen. Further investigations of the reaction of Cr(II) and molecular oxygen were reported many years later. A study by Ardon and Stein¹⁴ focused on the identification of the intermediates and products of the reaction. They observed that the oxidation of Cr(II) solutions by molecular oxygen and hydrogen peroxide produced different species (Cr(II) was in excess with respect to the oxidant). The reactions were postulated to proceed by the net reactions, equations 11 and 12.

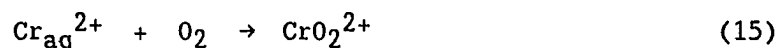


The mechanism for equation 11, suggested by Ardon and Stein, involves the formation of an η^1 chromium dioxygen intermediate, $[\text{Cr-O-O}]^{2+}$, followed rapidly by the formation of a labile metal-peroxy intermediate ($[\text{Cr-O-O-Cr}]^{4+}$) which would also react with the excess Cr(II) to form the polynuclear product $[\text{Cr-O-Cr}]^{4+}$ or $[\text{Cr}(\text{OH}_2)_4\text{OH}]_2^{4+}$. The mechanism suggested for the reaction of Cr(II) with H_2O_2 would be a Fenton-type mechanism, equations 13 and 14.



Several years later, Kolaczowski and Plane¹⁵ reported the oxidation of Cr(II) with molecular oxygen having a natural isotopic ratio in ¹⁸O labeled H₂O. They found the product to be [(H₂O)₄Cr(μ-OH)₂Cr(OH₂)₄]⁴⁺, with the unlabeled oxygen exclusively in the hydroxide bridges. They explained this result in terms of a mechanism which involves a peroxide-bridged intermediate since there was no indication that Cr(IV) was involved in the reaction mechanism. Other investigators, however, have suggested the involvement of Cr(IV).¹⁶

Ilan, Czapski and Ardon have investigated the reaction of Cr²⁺ and O₂ by the use of pulse radiolysis.¹⁶ This study measured the rate of the reaction of Cr(II) with molecular oxygen, $k = 1.6 \times 10^8 \text{ M}^{-1}\text{s}^{-1}$. It also confirmed that the dioxygen complex formed using the pulse radiolysis method had the same UV-VIS spectrum as the dioxygen complex formed by mixing Cr(II) with excess dissolved molecular oxygen. The reaction is thus written as shown in equation 15.



These results showed a slow decay of CrO₂²⁺ with concurrent formation of HCrO₄⁻, a product probably observed but not identified in Picard's study. Sellers and Simic¹⁷ have also reported a pulse radiolysis study of this reaction. They have reported the same rate constant for the reaction of Cr²⁺ and O₂ ($k = 1.6 \times 10^8 \text{ M}^{-1}\text{s}^{-1}$).

Another closely related chromium dioxygen complex is $[(\text{H}_3\text{N})_5\text{CrO}_2\text{Cr}(\text{NH}_3)_5]^{4+}$.¹⁸ Joyner and Wilmarth postulate this complex to be a chromium-peroxy species which at low Cr(II) concentrations is thought to result in a transient Cr(IV) species, $[(\text{H}_3\text{N})_5\text{Cr}(\text{OH})]^{3+}$.

It is also of interest to note two other chromium species. $\text{Cr}(\text{TPP})(\text{py})\text{O}_2$, in nonaqueous solvents, is an η^1 chromium dioxygen complex for which dimerization is prevented due to steric hindrance,¹⁹ and anhydrous Cr(II) bound in a zeolite matrix was observed to reversibly bind molecular oxygen.²⁰

The complexation of molecular oxygen is not only a relevant topic in biological systems, but it is also a promising research area due to the possibility that the proper use of transition metals might be a key to the efficient catalysis of auto-oxidation reactions. In view of the versatility and importance of molecular oxygen as an oxidant, a greater understanding of transition metal dioxygen chemistry, specifically chromium dioxygen chemistry, is of considerable interest.

STATEMENT OF PROBLEM

Within the initial reported investigation of the reaction between Cr(II) and molecular oxygen, a chromium dioxygen complex, CrO_2^{2+} , was postulated.¹³ This complex was thought to be the key intermediate in the first step of the activation of molecular oxygen as an oxidant. Subsequent investigations have shed light on the nature of CrO_2^{2+} , but much is left to be determined concerning its properties, reactions, and decomposition mechanism. A decomposition mechanism has been outlined in several reports; however, a detailed kinetic evaluation of the decomposition of CrO_2^{2+} has not been reported. By determining the decomposition process for CrO_2^{2+} , a greater understanding of the process by which transition metals activate molecular oxygen can be achieved. This understanding would certainly be an important stride towards the ultimate goal: to take advantage of the high oxidizing power of dioxygen in a controlled and selective manner.

In summary, the major objectives of this research are to: 1) gain a better understanding of the reaction of Cr(II) with molecular oxygen, 2) investigate the chemistry of the proposed intermediate complex, CrO_2^{2+} and 3) propose a decomposition mechanism for CrO_2^{2+} .

EXPERIMENTAL SECTION

Solvents and reagents

All water used throughout this investigation was first distilled, then passed through an Oilex filter and finally purified by passage through in-house anion and cation exchange columns. Additional purification for some experiments was obtained by passage of the purified water through a Millipore-Q purification system.

The chromium(III) perchlorate was prepared by the reduction of CrO_3 in an aqueous perchloric acid medium using H_2O_2 . The crude $\text{Cr}(\text{ClO}_4)_3$ was recrystallized three times from water and the purity checked by UV-VIS spectroscopy. The concentration of the $\text{Cr}(\text{ClO}_4)_3$ was determined by UV-VIS spectroscopic methods ($\lambda_{\text{max}} = 406 \text{ nm}$, $\epsilon = 15.85 \text{ M}^{-1}\text{cm}^{-1}$; $\lambda = 574 \text{ nm}$, $\epsilon = 13.3 \text{ M}^{-1}\text{cm}^{-1}$; $\lambda = 260 \text{ nm}$, $\epsilon = 5.0 \text{ M}^{-1}\text{cm}^{-1}$). The Cr(II) perchlorate was prepared by reducing acidic Cr(III) perchlorate solutions on Zn amalgam. A complete reduction of Cr(III) to Cr(II) was assumed, therefore, the concentration of the $\text{Cr}(\text{ClO}_4)_2$ solutions was equal to the concentration of the initial $\text{Cr}(\text{ClO}_4)_3$ solutions. The lithium perchlorate used for ionic strength control was prepared from the carbonate and recrystallized twice. $\text{Co}(\text{NH}_3)_5\text{F}(\text{ClO}_4)_2$ and $\text{Co}(\text{NH}_3)_5\text{Br}(\text{ClO}_4)_2$ were prepared from their halide salts.²¹ These compounds were recrystallized twice from perchloric acid. $\text{Co}(\text{NH}_3)_5\text{Br}_3$ was synthesized by a modification of the literature method in which CoBr_2 was used instead of CoCO_3 . The products were characterized by UV-visible spectroscopy. The perchloric acid (Fisher), cerium(IV) perchlorate (G. Frederick Smith), potassium chromate (Baker), molecular oxygen (99.5% pure, Air Products Corp.) and argon (99.99% pure, Air Products Corp.) were used as purchased.

Ultraviolet-visible spectroscopy

UV-VIS spectra and single wavelength absorbance vs. time data were acquired using a Cary model 219 recording spectrophotometer, a Perkin Elmer Lambda Array 3840 rapid scan diode array UV-VIS spectrophotometer, or a Cary model 14 recording spectrophotometer interfaced with an OLIS 3820 data system. Temperature control of ± 0.1 °C was maintained by circulating water from a constant-temperature bath through the jacket of a water-filled cell holder within the spectrophotometer. The fitting of the data to linear and nonlinear equations was accomplished using an APPLE II+ computer with the appropriate software for the analysis of kinetic data.

Kinetic simulation

The kinetic simulation was performed using the "Chemical Kinetic Simulation System, 'KINSIM', version 3.2" Barshop et al.²² The program was obtained from Dr. B. A. Barshop and Professor C. J. Frieden, Department of Biological Chemistry, Washington University, St. Louis, Missouri. This program performs chemical simulations using powerful numerical integration techniques. It is written in FORTRAN 77 and implemented on a Digital Equipment Corporation VAX 11/780 computer system at the Ames Laboratory, Iowa State University.

Preparation of CrO_2^{2+}

The reaction between Cr^{2+} and O_2 results in a metastable CrO_2^{2+} adduct.^{13,16,17} Under optimum conditions, the preparation yields only $\leq 1 \times 10^{-4}$ M CrO_2^{2+} . CrO_2^{2+} was prepared by a rapid injection of a dilute Cr^{2+} solution (0.010 L, $[\text{Cr}^{2+}] = 2 - 10 \times 10^{-4}$ M, $\text{HClO}_4 = 0.100$ M) into an

oxygen-saturated perchloric acid solution (0.030 L, $\text{HClO}_4 = 0.100 \text{ M}$). Sufficient lithium perchlorate was added to obtain the 1.00 M ionic strength used throughout this investigation. A fresh solution was prepared for nearly every experiment. In each case the UV spectrum was recorded, and samples containing appreciable concentrations of HCrO_4^- were discarded.

The experimental conditions for the preparation of CrO_2^{2+} were varied in an effort to optimize the yield and increase the concentration of CrO_2^{2+} . CrO_2^{2+} was observed to be semi-stable in acidic media ($\text{pH} < 2$). When the acid concentration was lowered below 0.010 M HClO_4 by the addition of aqueous NaOH, the CrO_2^{2+} rapidly decomposed to yield a species identified by its UV-VIS spectrum as CrO_4^{2-} . High acid concentrations ($[\text{HClO}_4] > 3 \text{ M}$) suppressed, but did not prevent, the formation of HCrO_4^- . When CrO_2^{2+} was prepared with higher concentrations of dilute Cr^{2+} , the solution rapidly turned the pale yellow color of HCrO_4^- immediately upon injection (about 3-4 seconds). The HCrO_4^- was identified by its characteristic UV-VIS spectrum. Attempts to increase the concentration and overall yield of CrO_2^{2+} by reacting Cr^{2+} in an acidic solution with higher dissolved oxygen concentrations ($[\text{O}_2] = 0.05 \text{ M}$, 50 atm of O_2 in a pressure bomb) also showed excessive HCrO_4^- formation.

Spectrum of CrO_2^{2+}

The UV-VIS spectrum of CrO_2^{2+} has been reported in the literature in association with two pulse radiolysis studies on CrO_2^{2+} . Sellers and Simic¹⁷ have determined the molar absorptivities to be $\epsilon_{290} = 3200 \text{ M}^{-1}\text{cm}^{-1}$ and $\epsilon_{245} = 7800 \text{ M}^{-1}\text{cm}^{-1}$ while Ilan, Czapski, and Ardon¹⁶ report $\epsilon_{290} =$

3000 $M^{-1}cm^{-1}$ and $\epsilon_{248} = 6900 M^{-1}cm^{-1}$. Although this minor discrepancy was not addressed in this study, the UV-VIS spectra of the CrO_2^{2+} solutions prepared by the method previously described were in good agreement with the reported spectrum of CrO_2^{2+} . The molar absorptivities used in this study were $\epsilon_{290} = 3000 M^{-1}cm^{-1}$ and $\epsilon_{245} = 6900 M^{-1}cm^{-1}$. The spectrum of CrO_2^{2+} is shown in Figure I-1.

Cr²⁺ trapping experiment

The concentration of Cr^{2+} formed by the homolysis of CrO_2^{2+} was determined by trapping Cr^{2+} with the oxidant $Co(NH_3)_5Br^{2+}$. This reaction is known to yield $CrBr^{2+}$, NH_4^+ and Co^{2+} in acidic aqueous solution. The concentration of the Co^{2+} , which is equal to the concentration of trapped Cr^{2+} , can be quantified by spectrophotometrically determining the Co^{2+} concentration as the thiocyanate complex in acetone/water.

The procedure for the Cr^{2+} trapping experiment is as follows. A 20 mL aliquot of a freshly prepared air-free CrO_2^{2+} solution was allowed to decompose at 25 °C in the presence of $Co(NH_3)_5Br^{2+}$, 0.05 M, for a total reaction time was 250 minutes ($HClO_4 = 0.100 M$). An experimental blank was simultaneously run as a part of this procedure, with a perchloric acid solution substituted for the CrO_2^{2+} solution. After the reaction was complete, 8 mL of the reacted solution was added to a solution of 12.5 mL of acetone, 0.5 mL of concentrated $HClO_4$, and 2 mL of saturated NH_4SCN . The visible absorbance of this solution with respect to the blank at $\lambda = 623$ nm, indicated Co^{2+} was formed in the decomposition of CrO_2^{2+} . The presence of Co^{2+} indicates Cr^{2+} was trapped by $Co(NH_3)_4Br^{2+}$ in the experiment.

Kinetics

The decomposition reactions of CrO_2^{2+} were monitored spectrophotometrically, usually at the 290 absorption maximum. The concentration range of dissolved dioxygen was $0 - 3.7 \times 10^{-3}$ M. The concentration of O_2 was obtained in solution by bubbling a vigorous stream of a calibrated $\text{O}_2 - \text{Ar}$ gas mixture through the CrO_2^{2+} solution in a flask equipped with a gas dispersion tube. To maintain constant the O_2 concentration in a kinetic run, the gas mixture was passed continuously through the reaction cell. To obtain an O_2 concentration of 3.7×10^{-3} M, an O_2 pressure of 3.5 atm was applied to a specially designed quartz spectrophotometer cell during the kinetic experiment.

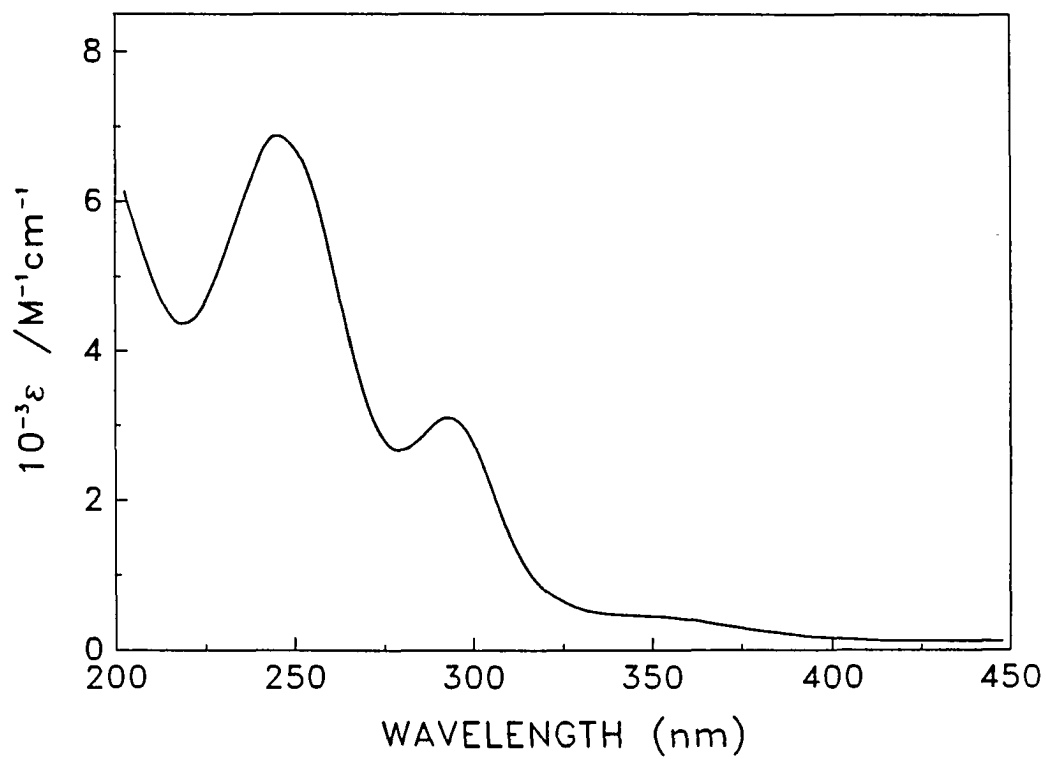
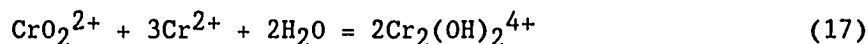
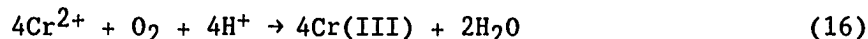


Figure I-1. UV-VIS spectrum of CrO_2^{2+} in 0.100 M HClO_4

RESULTS

Stoichiometry

The stoichiometry of the reaction of Cr^{2+} with O_2 has been reported to be $4\text{Cr}^{2+}:\text{O}_2$ in experiments where Cr^{2+} was in excess, equation 16.¹⁵ The species CrO_2^{2+} persists in solution only in the absence of excess Cr^{2+} . Attempts to determine the rate constant for the reaction of Cr^{2+} and CrO_2^{2+} were thwarted, however, because the reaction occurs too rapidly for the stopped-flow technique.



Assuming a multi-step reaction scheme, the stoichiometry of the reaction of CrO_2^{2+} with Cr^{2+} would be expected as $1\text{CrO}_2^{2+}:3\text{Cr}^{2+}$ consistent with equation 17. This stoichiometry was confirmed by monitoring the loss of absorbance of the CrO_2^{2+} complex (200 - 450 nm) following repeated microliter injections of Cr^{2+} . The reaction between Cr^{2+} and CrO_2^{2+} is complete in the mixing time suggesting a very rapid reaction. This experiment is illustrated in Figure I-2. Table I-2 contains the data used for the determination of the reaction stoichiometry. The stoichiometry was determined by constructing the titration plot, $[\text{CrO}_2^{2+}]$ vs. $[\text{Cr}^{2+}]/[\text{CrO}_2^{2+}]_0$, shown in Figure I-3. The slope of the line determined by the first eight titration points is -1.48 ± 0.03 M; the Y-intercept is 4.73 ± 0.04 M and the X-intercept is 3.2. This represents a reaction stoichiometry of $1\text{CrO}_2^{2+}:3.2\text{Cr}^{2+}$. Thus, CrO_2^{2+} has three oxidizing

equivalents with respect to the one electron reductant Cr^{2+} .

The products of this experiment had a nearly featureless UV-VIS spectrum, $[\text{Cr}]_{\text{T}} \sim 10^{-4}$, similar to that of Cr^{3+} . Figure I-2 also indicates that the low concentration of HCrO_4^- present in this experiment was consumed, since the initial HCrO_4^- absorbance, $\lambda \sim 345 \text{ nm}$, decreased as Cr^{2+} was introduced.

Product analysis

The kinetic trapping of reactive intermediates was attempted using various detection reagents. The analysis was based on a scheme in which CrO_2^{2+} decomposes via a homolytic cleavage, equation 18, followed by a step in which a second molecule of CrO_2^{2+} is consumed by Cr^{2+} , equation 19. To confirm this scheme, one needs chemical trapping agent for Cr^{2+} that is able to compete with this second reaction, thereby preventing the consumption of a second molecule of CrO_2^{2+} . If successful, the decomposition rate of CrO_2^{2+} would be reduced by a factor of two. Several Cr^{2+} traps were tried (Ce(IV) , K_2CrO_4 ,²³ $(\text{NH}_3)_5\text{CoF}^{2+}$, and $(\text{NH}_3)_5\text{CoBr}^{2+}$); however, only the $(\text{NH}_3)_5\text{CoBr}^{2+}$ trap experiment gave conclusive evidence for Cr^{2+} as an intermediate. Excessive UV absorption, low solubility or low reaction rates were experimental problems associated with the use of these kinetic trapping agents.

Evidence for Cr^{2+} as an intermediate comes from an experiment which trapped the Cr^{2+} by reacting high concentrations of $(\text{NH}_3)_5\text{CoBr}^{2+}$, under air-free conditions, with low concentrations of decomposing CrO_2^{2+} . These reaction conditions favored the detection of Cr^{2+} as much as possible; however, only 4.1×10^{-7} moles of Cr^{2+} was detected in a solution which initially contained 9.7×10^{-7} moles of CrO_2^{2+} . To calculate the expected

Table I-2. Stoichiometric Titration Data

$[\text{CrO}_2^{2+}]$	Volume of Cr^{2+} added ^a (μL)	$[\text{Cr}^{2+}]_{\text{T}}$
4.8×10^{-5}	0	0.0×10^{-5}
4.4×10^{-5}	2	1.2×10^{-5}
3.9×10^{-5}	2	2.4×10^{-5}
3.2×10^{-5}	4	4.8×10^{-5}
2.9×10^{-5}	3	5.9×10^{-5}
2.3×10^{-5}	3	7.7×10^{-5}
1.8×10^{-5}	3	9.5×10^{-5}
1.4×10^{-5}	3	1.1×10^{-4}
8.8×10^{-6}	3	1.3×10^{-4}
4.1×10^{-6}	3	1.5×10^{-4}
1.2×10^{-6}	3	1.7×10^{-4}
0	3	1.8×10^{-4}
0	3	2.0×10^{-4}

^a $[\text{Cr}^{2+}] = 0.095 \text{ M}$, $\text{HClO}_4 = 0.100 \text{ M}$, 5.00 cm cell, 15.5 mL cell volume. The concentration of CrO_2^{2+} is based on absorbance measurements taken at $\lambda = 290 \text{ nm}$.

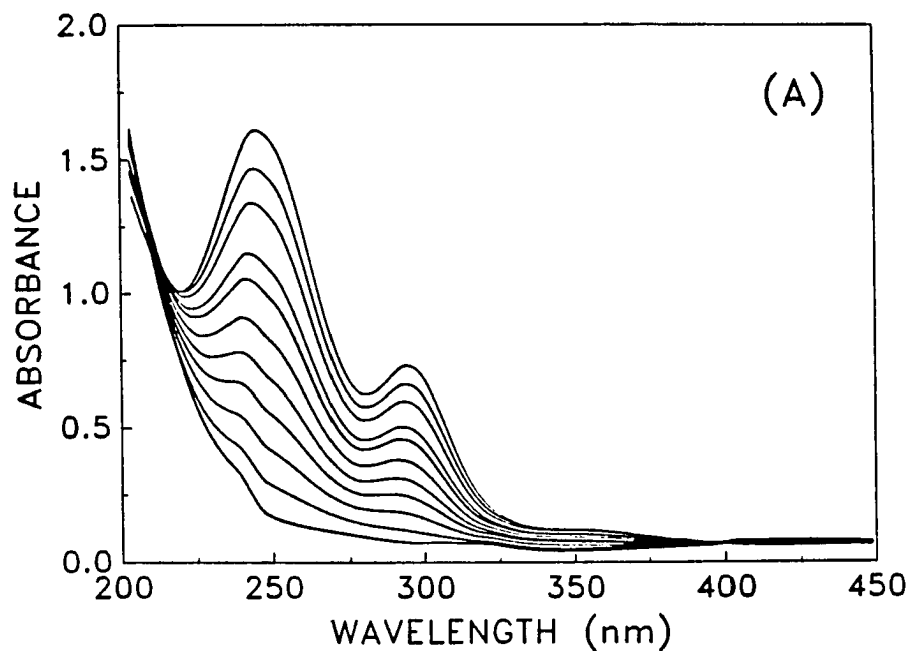


Figure I-2. The UV-VIS spectra for the stoichiometric titration experiment between CrO_2^{2+} and Cr^{2+} (A). The loss in absorbance for CrO_2^{2+} corresponds to the consumption of CrO_2^{2+} by repeated injections of Cr^{2+} . The initial spectrum is of an air-free aqueous solution of CrO_2^{2+} ($[\text{CrO}_2^{2+}] = 4.8 \times 10^{-5} \text{ M}$, $\text{HClO}_4 = 0.100 \text{ M}$, 5.00 cm cell, 15.5 mL cell volume)

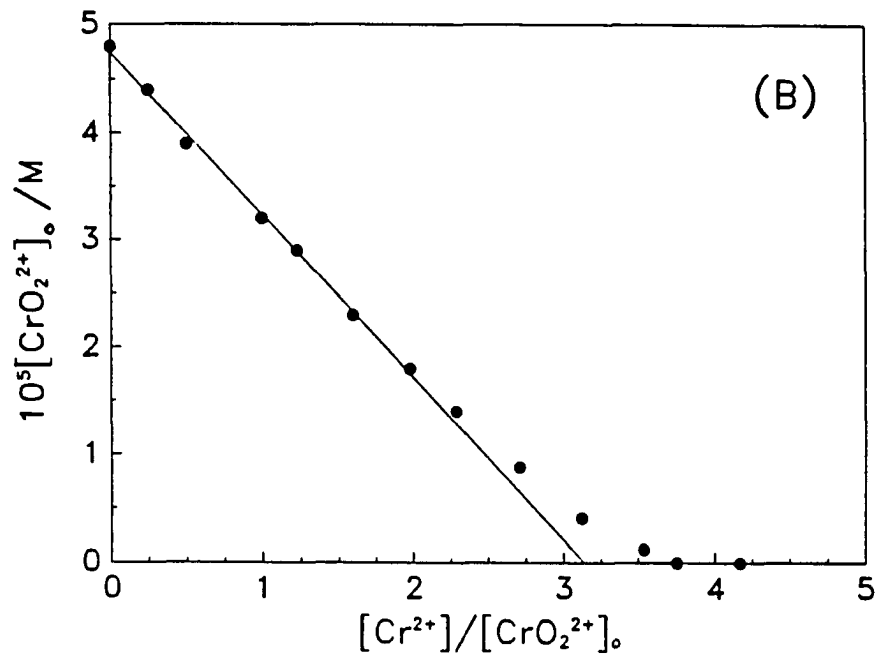
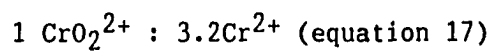
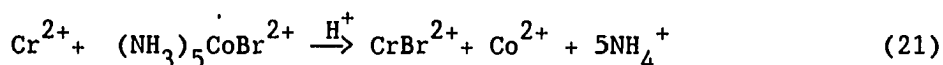
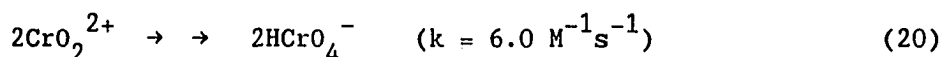
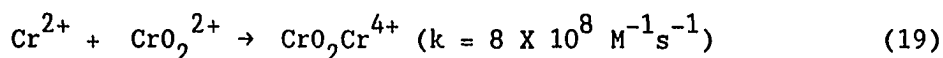
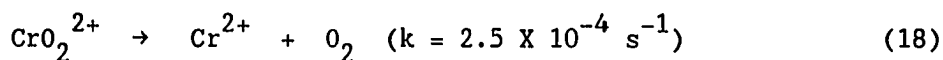


Figure I-3. The spectrophotometric titration plot at 290 nm (B).

The endpoint corresponds to a reactant ratio



trapping yield for Cr^{2+} , the trapping experiment was simulated using the computer program KINSIM. The reaction equations and rate constants used in the simulation are shown in equations 18 - 21. These equations illustrate the competition between CrO_2^{2+} and $\text{Co}(\text{NH}_3)_5\text{Br}^{2+}$ for Cr^{2+} . The bimolecular reaction between two CrO_2^{2+} molecules also plays a part in reducing the CrO_2^{2+} available to homolyze and needs to be accounted for in the Cr^{2+} trapping experiment. The computer simulation indicates out of the 9.7×10^{-7} moles of chromium in the experiment, 4.1×10^{-7} moles should have been trapped by $\text{Co}(\text{NH}_3)_5\text{Br}^{2+}$. The number of moles of Co^{2+} (or Cr^{2+} trapped) observed at the end of the trapping experiment was 4.1×10^{-7} mol which represents a trapping yield of ~ 100%.



$$(k_{21} \sim 2 \times 10^6 \text{ M}^{-1}\text{s}^{-1}, T = 25 \text{ }^\circ\text{C}, \mu = 0.25 \text{ M})$$

$(\text{NH}_3)_5\text{CoBr}^{2+}$ can compete with CrO_2^{2+} for Cr^{2+} , but only when CrO_2^{2+} concentrations are low and $(\text{NH}_3)_5\text{CoBr}^{2+}$ concentrations are as high as the solubility limit will allow, ~ 0.05 M in acidic aqueous solution.^{24,25} Since the Cr^{2+} trapping percent yield is based in part on data obtained by the simulation, errors in the estimated rate constants would result in a different percent yield.

A series of experiments was also designed to identify the products of the decomposition of CrO_2^{2+} . Two distinct features of the UV-VIS spectrum of decayed CrO_2^{2+} were the slow growth of a peak at 320 nm observed over a time period of days and also a sharp peak (actually twin peaks separated by 2 nm) observed at 240 nm. The peak at 240 nm was usually present in solutions of higher CrO_2^{2+} concentration, before CrO_2^{2+} had time to decay, and it did not appear to grow during or after the CrO_2^{2+} decomposition. The 320 nm peak was not seen until after the CrO_2^{2+} decayed. Although the species responsible for this peak has not been identified, since it occurs after the CrO_2^{2+} decomposition, it is incidental to it.

Cyclopentane was introduced into solutions of decomposing CrO_2^{2+} in an effort to detect the presence of H-atom abstracting radical species. In air-free solutions of decomposing CrO_2^{2+} and cyclopentane (0.02 M), the 240 nm peak grew for hours after CrO_2^{2+} had decayed. The 320 nm peak also initially appeared as the CrO_2^{2+} decayed, but it was observed to decay on the time scale of the decomposing CrO_2^{2+} . Following the decomposition of the CrO_2^{2+} in this experiment, the 320 nm peak grew slowly for several hours, but with a rate much faster than in solutions which contained no cyclopentane. Injections of Cr^{2+} arrested the absorbance change. The 240 and 320 nm peaks appear to be due to different species; however, a literature search for the identification of these species did not reveal any useful information. From the experimental evidence cited, the species are probably Cr(III) products with unknown structures.

In the section of this report dealing with the preparation of CrO_2^{2+} , HCrO_4^- was mentioned as a product of the preparation and decomposition of CrO_2^{2+} . The product HCrO_4^- has also been reported by Ilan, Czapski, and

Ardon;¹⁶ however, the details of the experimental conditions which promote the formation of HCrO_4^- have not been described.

HCrO_4^- is the only identified product of the decomposition of CrO_2^{2+} (the other observed products are presumably Cr(III) products). In the CrO_2^{2+} decomposition experiments where the initial CrO_2^{2+} concentration is low and $[\text{O}_2] = 0 \text{ M}$, very little HCrO_4^- is observed. In the decomposition experiments with higher CrO_2^{2+} concentrations and $[\text{O}_2] = 0 \text{ M}$, more HCrO_4^- is detected at the end of the experiment. As the dioxygen concentration is increased, increasing yields of HCrO_4^- are observed, Table I-3.

Other than the identification of HCrO_4^- , no product identification was possible in decomposed CrO_2^{2+} solutions. This was primarily due to the extremely low concentrations of the chromium species in the acidic aqueous solutions ($[\text{Cr}]_{\text{total}} = 2 \times 10^{-4} \text{ M}$) and the relatively featureless UV-VIS spectra obtained after CrO_2^{2+} solutions decay.

The kinetics of the decomposition of CrO_2^{2+}

The decomposition of CrO_2^{2+} was studied in 0.100 M HClO_4 with the ionic strength being controlled at 1.00 M by LiClO_4 . The decomposition was monitored spectrophotometrically ($\lambda = 290 \text{ nm}$) with the decomposition rate clearly dependent on the concentration of dissolved dioxygen. CrO_2^{2+} was observed to decay in a first-order manner in air-free solutions and the final solutions were essentially nonabsorbing in the UV. The lack of a strong UV absorption suggests that only Cr(III) species are formed by this pathway. In particular, HCrO_4^- is not formed in appreciable concentrations.

In experiments with increasing dioxygen concentrations, the

decomposition rate slowed and took on a mixed first-order and second-order character. Appreciable concentrations of HCrO_4^- were observed in the final solutions.

In the experiment with the highest dioxygen concentration, the decay became second-order and the highest concentration of HCrO_4^- was observed. This implies a limiting effect of increasing dissolved oxygen concentrations, Table I-3 and Figure I-4. The decay traces in Figures I-5 and I-6 represent the observed absorbance-time profiles accompanying the decomposition of CrO_2^{2+} . These traces have to be normalized to an absorbance change of unity ($\Delta D = 1$) to aid in the comparison between different experimental data with the simulated curves.

Observed rate law

In the limiting case where $[\text{O}_2] = 0 \text{ M}$, the observed traces for the decomposition of CrO_2^{2+} fit first-order kinetics, consistent with equation 22. This is a limiting form of the more complete rate law in equation 30.

$$\frac{-d[\text{CrO}_2^{2+}]}{dt} = k_{\text{app}}[\text{CrO}_2^{2+}] \quad (22)$$

The calculated values for the rate constant, k' , exhibited a slight dependence on $[\text{CrO}_2^{2+}]_0$, with the apparent first-order rate constants increasing with increasing initial CrO_2^{2+} concentrations. The dependence of the calculated first-order rate constant, k_{app} , on the initial CrO_2^{2+} concentration is consistent with equation 23, where higher initial CrO_2^{2+} concentrations result in an increasingly important parallel kinetic term k'' with a second-order dependence on $[\text{CrO}_2^{2+}]$. The slight deviation from

Table I-3. Observed Data for the Decomposition of CrO_2^{2+} ^a

$10^5[\text{CrO}_2^{2+}]_0$	$10^5[\text{O}_2]$	1 st Half-Time (min)	$[\text{HCrO}_4^-]_{\text{obs}}$	$[\text{HCrO}_4^-]_{\text{cal}}$
2.07	0.0	17	4.2×10^{-6}	3.9×10^{-6}
1.96	5.25	29	6.1×10^{-6}	6.2×10^{-6}
2.19	10.5	32	8.0×10^{-6}	9.0×10^{-6}
2.20	21.0	41	9.1×10^{-6}	$11. \times 10^{-6}$
2.24	31.5	42	$10. \times 10^{-6}$	$13. \times 10^{-6}$
2.40	68.3	43	$13. \times 10^{-6}$	$16. \times 10^{-6}$
2.15	105.	49	$13. \times 10^{-6}$	$15. \times 10^{-6}$
1.74	370.	81	$13. \times 10^{-6}$	$13. \times 10^{-6}$

^aT = 25.0 °C, μ = 1.00 M, and HClO_4 = 0.100 M. The $[\text{HCrO}_4^-]_{\text{obs}}$ was determined spectrophotometrically (λ = 345 nm). The $[\text{HCrO}_4^-]_{\text{cal}}$ was determined using computer simulations.

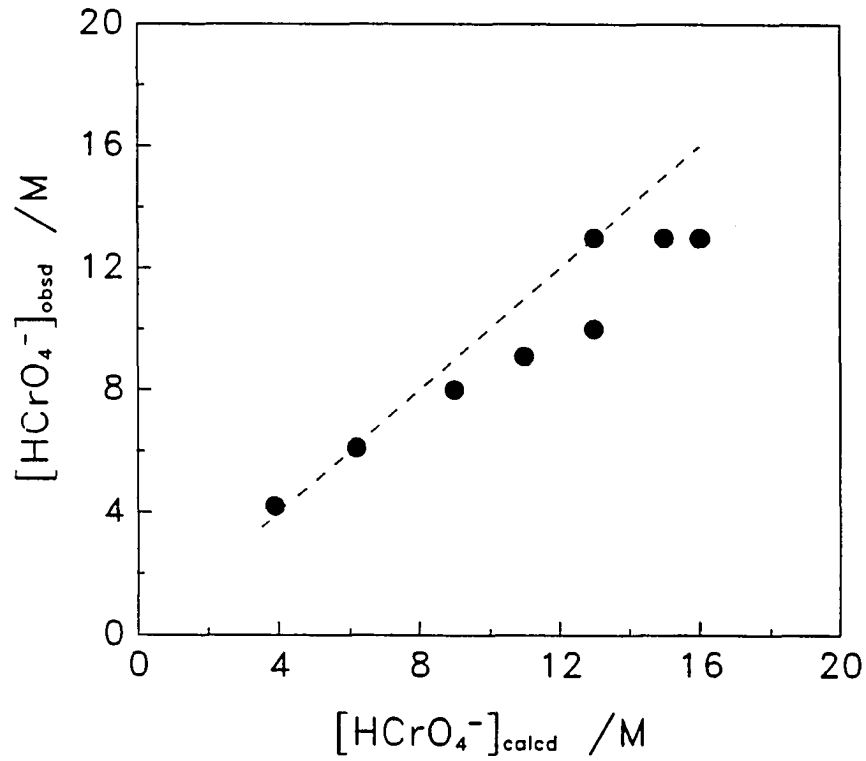


Figure I-4. A comparison between the observed and calculated yields of HCrO_4^- . The calculated yield is based on the proportion of the reaction proceeding by the kinetic term $k[\text{CrO}_2^{2+}]^2$, in which the best fit values of the four rate constants in equation 33 were used for numerical simulation in the program KINSIM

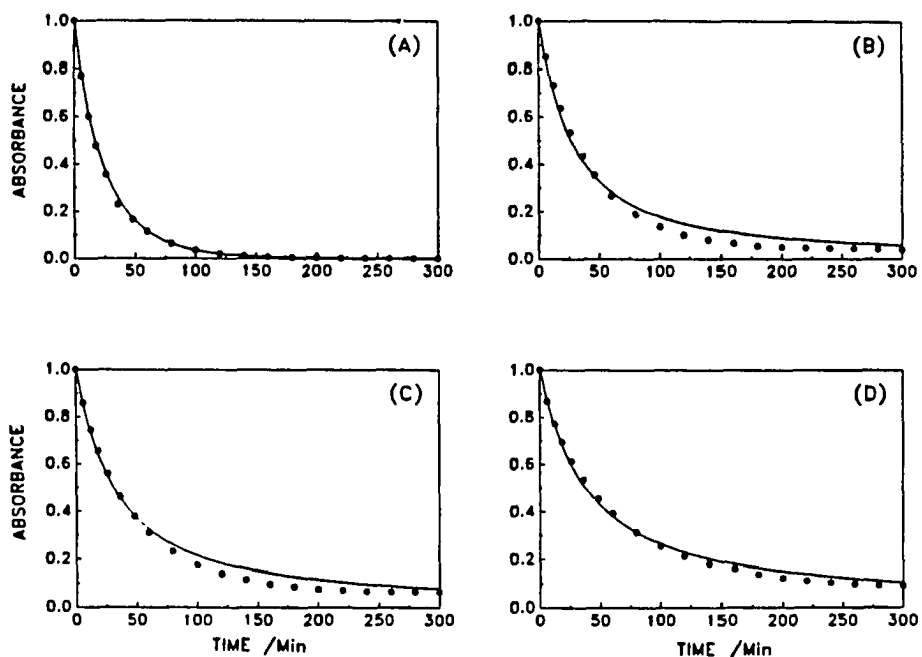


Figure I-5. Normalized CrO_2^{2+} absorbance-time decomposition traces showing the kinetic inhibition by increased O_2 concentrations, $\text{HClO}_4 = 0.100 \text{ M}$, $\mu = 1.00 \text{ M}$. The concentration of dissolved dioxygen in these four experiments is: (A) $[\text{O}_2] = 0 \text{ M}$, (B) $[\text{O}_2] = 5.25 \times 10^{-5} \text{ M}$, (C) $[\text{O}_2] = 1.05 \times 10^{-4} \text{ M}$, and (D) $[\text{O}_2] = 2.10 \times 10^{-4} \text{ M}$. The solid circles represent the observed data and the curves drawn through the experimental data are the final best fits (calculated with the numerical integration program KINSIM) using the full rate law, equation 33, and the best values of all four rate constants

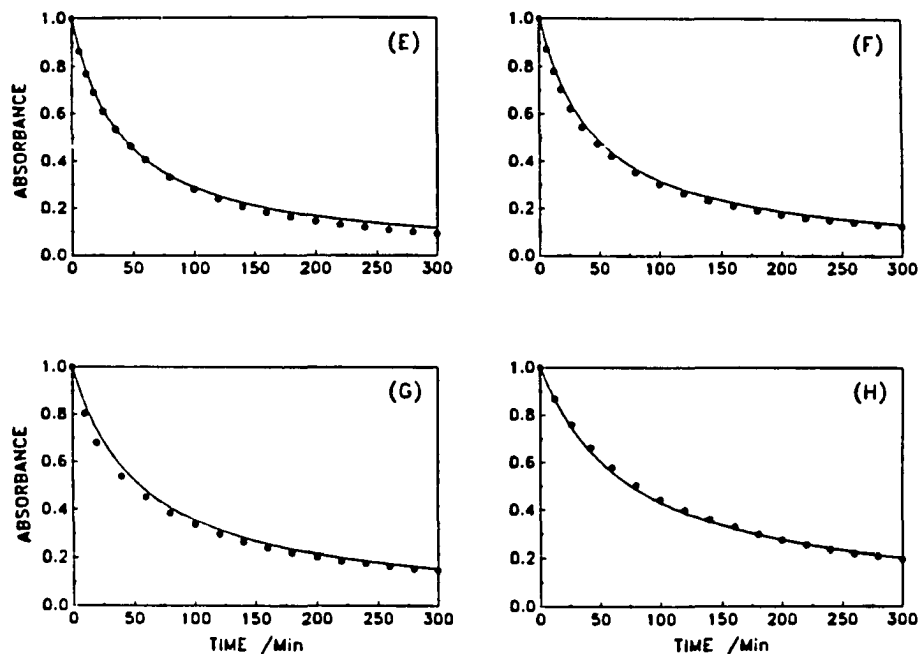


Figure I-6. Normalized CrO_2^{2+} absorbance-time decomposition traces showing the kinetic inhibition by increased O_2 concentrations, $\text{HClO}_4 = 0.100 \text{ M}$, $\mu = 1.00 \text{ M}$. The concentration of dissolved dioxygen in these four experiments is: (E) $[\text{O}_2] = 3.15 \times 10^{-4} \text{ M}$, (F) $[\text{O}_2] = 6.83 \times 10^{-4} \text{ M}$, (G) $[\text{O}_2] = 1.05 \times 10^{-3} \text{ M}$, and (H) $[\text{O}_2] = 3.70 \times 10^{-3} \text{ M}$. The solid circles represent the observed data and the curves drawn through the experimental data are the final best fit (calculated with the numerical integration program KINSIM) using the full rate law, equation 33, and the best values of all four rate constants

a first-order fit observed in the oxygen-free CrO_2^{2+} decomposition traces suggest the contribution from the k'' term is small compared to the k' under anerobic conditions. Equation 23 suggests that a plot of k_{app} vs. $[\text{CrO}_2^{2+}]_0$ will yield an estimate of k' as the Y-intercept and an estimate of k'' as the slope of the line, equation 24. This graph is shown in Figure I-7, $k' = (5.0 \pm 0.1) \times 10^{-4} \text{ s}^{-1}$ and $k'' = (12 \pm 4) \text{ M}^{-1}\text{s}^{-1}$.

The estimate for the second-order rate constant, k'' , can be improved by numerically fitting the air-free CrO_2^{2+} decomposition traces to the integrated form of the rate law in equation 23. The integrated equation adapted to analyze the data is shown in equation 25.

$$\frac{-d[\text{CrO}_2^{2+}]}{dt} = k' [\text{CrO}_2^{2+}] + k'' [\text{CrO}_2^{2+}]^2 \quad (23)$$

$$k_{\text{app}} = k' + k'' [\text{CrO}_2^{2+}]_0 \quad (24)$$

$$[\text{CrO}_2^{2+}]_t = \frac{k' [\text{CrO}_2^{2+}]_0}{e^{k' t} \{k' + k'' [\text{CrO}_2^{2+}]_0\} - k'' [\text{CrO}_2^{2+}]_0} \quad (25)$$

In the data analysis, the rate constant k' was fixed at the previously determined value of $5.0 \times 10^{-4} \text{ s}^{-1}$. The rest of the parameters were floated in the fitting routine to determine the best fit. In all cases the calculated absorbance infinity and calculated initial CrO_2^{2+} concentration agreed well with the experimentally observed data. The thirteen experiments used in this analysis are listed in Table I-4. The

average value for k'' based on these thirteen experiments is 11.7 ± 3.4 $M^{-1}s^{-1}$. In experiments which have higher initial concentrations of CrO_2^{2+} , but the same dioxygen concentration, the bimolecular decomposition path (k'') contributes more to the overall decomposition than the unimolecular decomposition path. As a consequence of this, the experiments with higher initial CrO_2^{2+} concentrations will reflect a more accurate value for k'' . A weighted average for the data in proportion to the extent to which it contributes to the whole is based on the percent of the reaction by the bimolecular path. This results in a greater emphasis of the higher CrO_2^{2+} concentration decomposition experiments and an improved value for k'' . The formula used for the weighted average is shown in equation 26.

$$\bar{k}'' = \frac{(\%)_1 k_1'' + (\%)_2 k_2'' + \dots + (\%)_{13} k_{13}''}{(\%)_1 + (\%)_2 + \dots + (\%)_{13}} \quad (26)$$

(%) = the percent of reaction by the bimolecular path

The value of the weighted bimolecular path rate constant is $\bar{k}'' = 12.0 \pm 1.7 M^{-1}s^{-1}$.

In the intermediate dissolved oxygen concentration experiments, the decay traces display mixed first- and second-order character. Three different but interrelated phenomena occurred when oxygen was added. (a) The reaction slowed substantially owing to an inverse dependence of the first term of equation 33 on the O_2 concentration; (b) the second-order dependence on $[CrO_2^{2+}]$ became more prominent; and (c) increasing proportions of $HCrO_4^-$ were observed in the UV spectra of the product solutions. These runs illustrate both the rate-inhibiting effect of

increased O_2 concentrations and a reaction order with respect to $[CrO_2^{2+}]$ that increases above unity at higher O_2 concentrations. These decay CrO_2^{2+} traces were not analyzed by a nonlinear least-squares analysis owing to the complexity of the integrated form of the rate law.

In the other limiting case, where $[O_2] = 3.7 \times 10^{-3} M$, the decay trace fit second-order kinetics, consistent with equation 27. A second-order analysis of this CrO_2^{2+} decomposition trace yielded a value for the second-order rate constant, $k'' = 11.9 \pm 0.1 M^{-1}s^{-1}$ ($[CrO_2^{2+}] = 1.74 \times 10^{-5} M$, $T = 25^\circ C$).

$$\frac{-d[CrO_2^{2+}]}{dt} = k'' [CrO_2^{2+}]^2 \quad (27)$$

Activation parameters

The observed rate law under the two limiting conditions indicates that the decomposition of CrO_2^{2+} can be attributed to a parallel reaction sequence, one first-order in $[CrO_2^{2+}]$ and the other second-order in $[CrO_2^{2+}]$. The activation parameters for the first-order path corresponding to the homolysis of CrO_2^{2+} were determined under reaction conditions which favored this reaction (air-free, low concentrations of $[CrO_2^{2+}]$, $\mu = 1.00 M$, $HClO_4 = 0.100 M$). The variation of the observed first-order rate constants due to the variation of the temperature was evaluated in a manner suggested by activated complex theory. Rearranging and taking the logarithm of the Eyring equation gives equation 28. This equation suggests that a plot of $\ln(k/T)$ vs. $1/T$ will be linear with ΔH^\ddagger determined by the slope and ΔS^\ddagger by the Y-intercept of Figure I-8.

Table I-4. The Percent of Reaction by the Bimolecular Path

$[\text{CrO}_2^{2+}]_0$	$k'' \text{ M}^{-1}\text{S}^{-1}$	% by bimolecular path ^a
1.46×10^{-5}	8.0	15.1
1.55×10^{-5}	10.8	15.9
1.71×10^{-5}	12.8	17.2
1.80×10^{-5}	13.0	17.8
1.89×10^{-5}	10.6	18.5
1.95×10^{-5}	6.5	19.0
2.03×10^{-5}	16.9	19.6
2.07×10^{-5}	12.9	19.9
2.32×10^{-5}	6.7	21.6
2.33×10^{-5}	16.1	21.7
2.41×10^{-5}	14.4	22.2
2.76×10^{-5}	8.6	24.5
3.71×10^{-5}	15.4	29.8

^aCalculated by computer simulation techniques; average $\bar{k}'' = 11.7 \pm 3.4$, weighted average (see text), $\bar{k}'' = 12.0 \pm 1.7$.

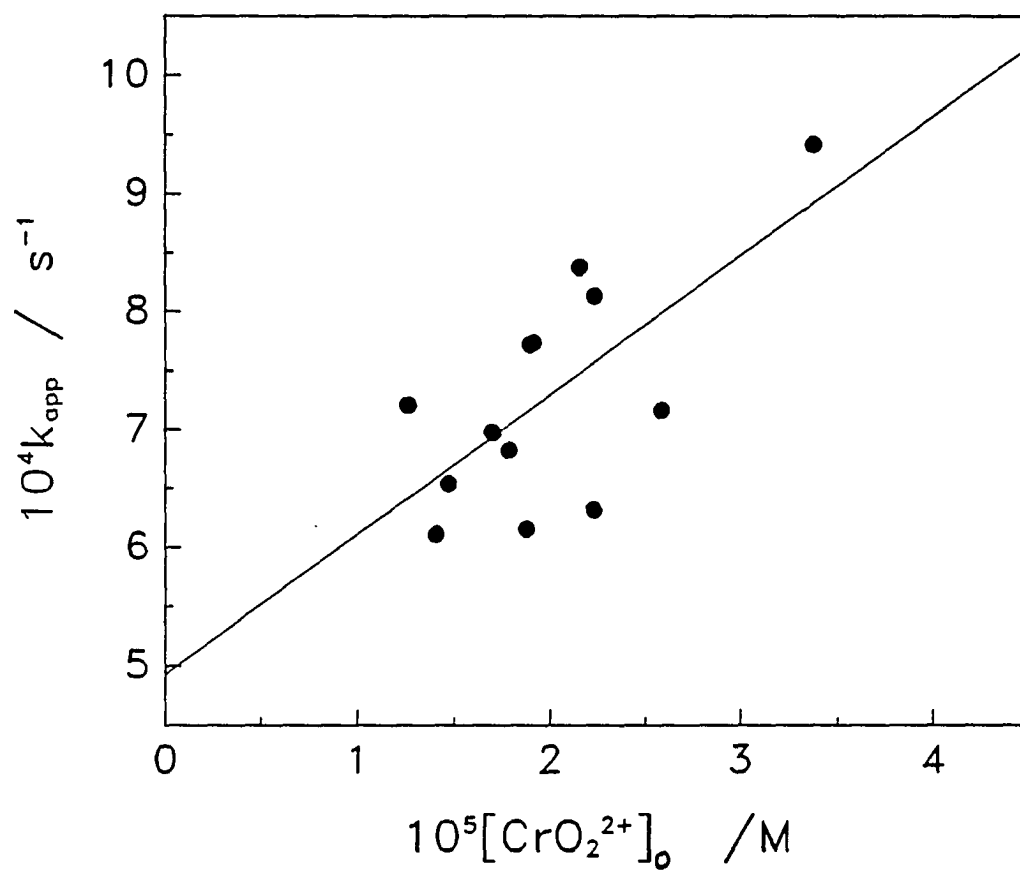


Figure I-7. The plot of k' vs. $[\text{CrO}_2^{2+}]_0$. The Y-intercept yields the value for k' , and the slope yields the value for k'' according to equation 24

$$\ln\left(\frac{k}{T}\right) = \frac{-\Delta H^\ddagger}{RT} + \ln\left(\frac{\kappa}{h}\right) + \frac{\Delta S^\ddagger}{R} \quad (28)$$

k = reaction rate constant R = gas constant
 T = absolute temperature κ = Boltzmann's constant
 ΔH^\ddagger = enthalpy of activation h = Planck's constant
 ΔS^\ddagger = entropy of activation

The activation parameters for the first-order path are $\Delta H^\ddagger = 25.1 \pm 1.1$ kcal mol⁻¹ and $\Delta S^\ddagger = 9.7 \pm 3.6$ cal mol⁻¹ K⁻¹. The data are listed in Table II-5.

The activation parameters of the second-order path were determined under reaction conditions which favored this path (that is, the same experimental conditions as above were used, except high concentrations of CrO₂²⁺ and of O₂ were used). The observed rate constants corresponding to this path were determined by computer-fitting the decomposition trace data to equation 23 which separated the contributions of the two paths. The first-order path rate constant was fixed in the nonlinear least-squares computer fitting routine using the rate constants determined in the activation parameter analysis for the first-order path. The activation parameters for the second-order path were then determined by plotting the observed second-order rate constants vs. the temperature again in the manner suggested by activated complex theory ($\ln(k/T)$ vs. $1/T$), Figure I-8. The activation parameters are $\Delta H^\ddagger = 12.0 \pm 1.7$ kcal mol⁻¹ and $\Delta S^\ddagger = -14.4 \pm 5.8$ cal mol⁻¹ K⁻¹. The data are listed in Table I-6.

Table I-5. The Variation of $k'/2$ with Temperature

Temperature ($^{\circ}\text{C}$)	$k'/2$ (s^{-1})
2.3	1.05×10^{-5}
14.8	6.08×10^{-5}
25.0	3.36×10^{-4}
34.9	1.45×10^{-3}

Table I-6. The Variation of $k''/2$ with Temperature

Temperature ($^{\circ}\text{C}$)	$k''/2$ ($\text{M}^{-1}\text{s}^{-1}$)
2.3	1.1
5.5	1.7
15.3	4.9
25.0	5.4
34.7	15.

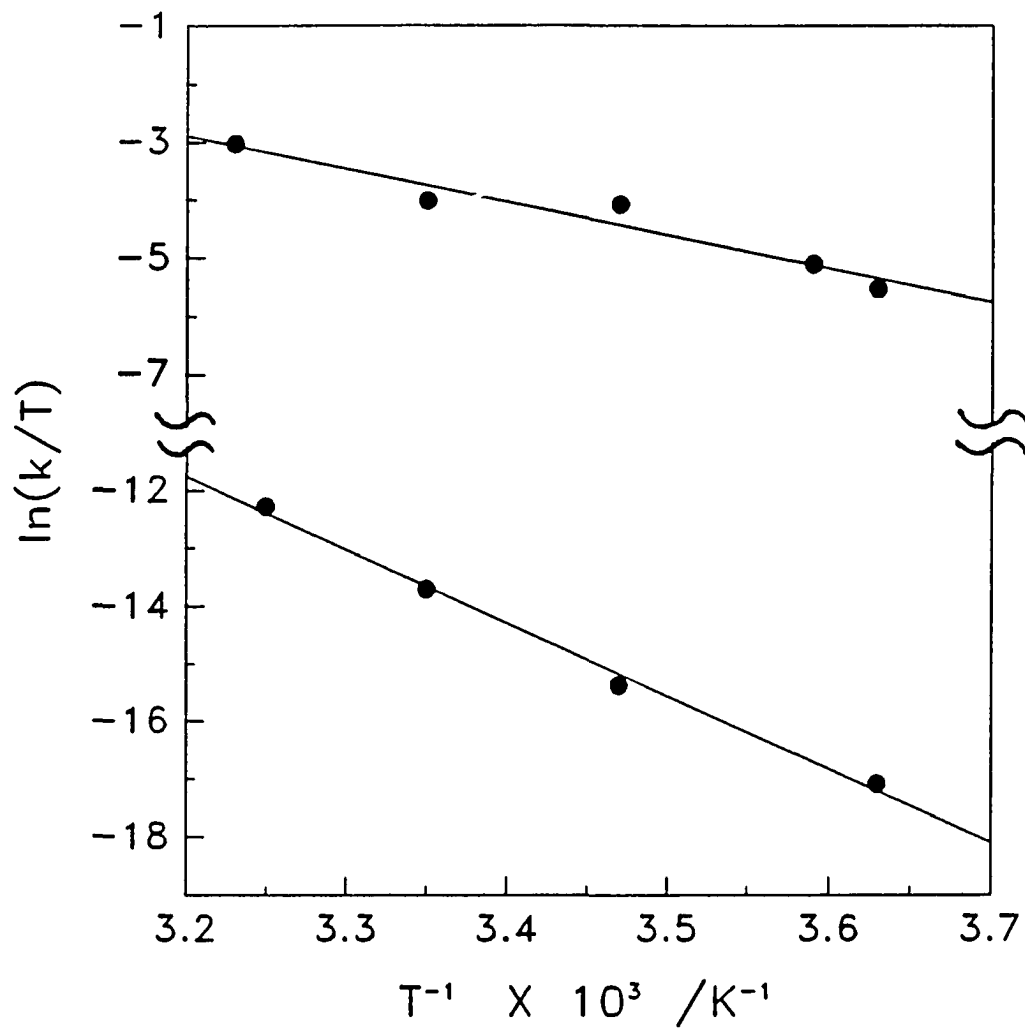
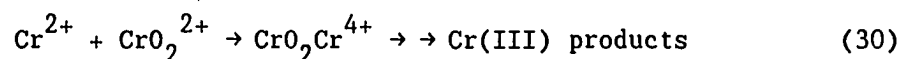


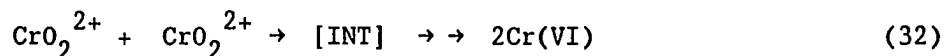
Figure I-8. The temperature dependences of k' (upper) and k'' according to activated complex theory, as $\ln(k/T)$ vs. $1/T$

Numerical modeling of kinetic data

The decomposition data for CrO_2^{2+} suggest a kinetic scheme consisting of a parallel set of reactions, one path with a unimolecular rate limiting step and the other with a bimolecular rate limiting step. Two variations of the following scheme were tested to see if they adequately reproduced the experimental absorbance vs. time profiles depicted in Figures I-5 and I-6. Equations 29 - 31 are referred to as the "simplified model", and equations 29 - 33 as the "full model".



$$\frac{-d[\text{CrO}_2^{2+}]}{dt} = \frac{2k_{29}[\text{CrO}_2^{2+}]}{1 + \{k_{-29}[\text{O}_2]/k_{30}[\text{CrO}_2^{2+}]\}} \quad (31)$$



$$\frac{-d[\text{CrO}_2^{2+}]}{dt} = \frac{2k_{29}[\text{CrO}_2^{2+}]}{1 + \{k_{-29}[\text{O}_2]/k_{30}[\text{CrO}_2^{2+}]\}} + 2k_{32}[\text{CrO}_2^{2+}]^2 \quad (33)$$

The data analysis based on the closed-form solution of the differential rate equations was not feasible; therefore, a program for their numerical solution, KINSIM, was applied to the proposed reaction schemes.

The first reaction scheme is derived from the supposition that the

observed rate data can simply be explained by equations 29 and 30. The rate law derived from these equations is shown in equation 31 and is consistent with observed oxygen dependent rate and reaction order (the second-order dependence on $[\text{CrO}_2^{2+}]$ arises from one limit of the term in equation 31, which applies when $k_{-29}[\text{O}_2] \gg k_{30}[\text{CrO}_2^{2+}]$). A test of this supposition includes the use of computer simulation techniques to determine whether a single set of rate constants can be found that are consistent with the observed CrO_2^{2+} decomposition data.

Three sets of observed CrO_2^{2+} decomposition data were used to test this simplified kinetic scheme. Two of these data sets represent the experimental limits of the oxygen concentration, $[\text{O}_2] = 0 \text{ M}$ and $[\text{O}_2] = 3.7 \times 10^{-3} \text{ M}$. An intermediate oxygen concentration experiment was also chosen $[\text{O}_2] = 1.05 \times 10^{-4} \text{ M}$. The value for k_{29} used in these test simulations can be determined by adjusting the k_{29} rate constant in the computer simulation to best fit the observed data at $[\text{O}_2] = 0 \text{ M}$. The best fit value for k_{29} is $3.17 \times 10^{-4} \text{ M}^{-1}\text{s}^{-1}$. The fit is illustrated in Figure I-9 and the parameters for the test simulations are shown in Table I-7. To estimate the value for k_{30} , the parameter described in the rate law as k_{-29}/k_{30} can be adjusted to fit the data for the decomposition of CrO_2^{2+} at $[\text{O}_2] = 1.05 \times 10^{-4} \text{ M}$. The best fit is illustrated in Figure I-9, with $k_{-29}/k_{30} = 0.0107$. Using the literature value for k_{-29} ($1.6 \times 10^8 \text{ M}^{-1}\text{s}^{-1}$),^{16,17} the value for $k_{30} = 1.5 \times 10^9 \text{ M}^{-1}\text{s}^{-1}$. This set of rate constants was applied to the data for the decomposition of CrO_2^{2+} at $[\text{O}_2] = 3.7 \times 10^{-3} \text{ M}$, and the results are illustrated in Figure I-11. The fit between the simulated and observed data is very poor, with the simulated data having a much lower reaction rate than the observed data.

A different set of rate constants can be estimated from the $[\text{O}_2] = 3.7$

$\times 10^{-3}$ M CrO_2^{2+} decomposition data. The best fit is illustrated in Figure I-10. The value for k_{30} is $1.5 \times 10^{10} \text{ M}^{-1}\text{s}^{-1}$. When this set of rate constants is applied to the $[\text{O}_2] = 1.05 \times 10^{-4}$ M CrO_2^{2+} decomposition rate data, a very poor fit results as shown in Figure I-10.

It should be noted that the poor fit between the simulated and observed data for the simplified model cannot arise from an incorrect value for the rate constant k_{29} . Regardless of the value of k_{29} , the ratio of k_{29}/k_{30} actually represents only one adjustable parameter. A single value for this parameter can not be found such that the observed data and these simulated for the simplified model agree. In view of that, the simplified mechanistic scheme can be discarded.

If equation 32 is included in the mechanistic scheme, the rate law consistent with this scheme is shown in equation 33. To conduct the simulations on this mechanism, the literature value^{16,17} for $k_{30} = 1.6 \times 10^8 \text{ M}^{-1}\text{s}^{-1}$ was used. The values for $k_{29} = 2.5 \times 10^{-4} \text{ s}^{-1}$ and $k_{32} = 6.0 \text{ M}^{-1}\text{s}^{-1}$ ($k''/2$) were set at values reported herein. The only unknown rate constant was k_{30} . That equation 30 represents a very fast reaction is suggested by the failure of direct attempts to measure the rate. The reaction is complete in the mixing time when Cr^{2+} is injected in an air-free CrO_2^{2+} solution and the ranges of oxygen concentration over which the rate-inhibitory effect of increasing $[\text{O}_2]$ is observed suggest a very fast reaction. The value of k_{30} used in the simulation was, therefore, determined by adjusting the value until the absorbance vs. time profiles for all runs matched satisfactorily, as shown in Figures I-5 and I-6. This method gives $k_{30} = 8 \times 10^8 \text{ M}^{-1}\text{s}^{-1}$. The precision of this value of k_{30} is judged to be no better than about $\pm 50\%$ based on the variations of this parameter made without the deviations becoming large.

Table I-7. Numerical Modeling Test Parameters

Parameter Set ^a	$10^{-9}k_{30}$	$M^{-1}s^{-1}$	$10^3[O_2]$	Quality of Fit	Figure #
I	1.5		0	GOOD	I-9
II	15.		0	GOOD	I-9
I	1.5		0.105	GOOD	I-10
II	15.		0.105	VERY POOR	I-10
I	1.5		3.7	VERY POOR	I-11
II	15.		3.7	GOOD	I-11

^aParameter set I: $k_{29} = 3.17 \times 10^{-4} s^{-1}$, $k_{-29} = 1.6 \times 10^8 M^{-1}s^{-1}$, and $k_{30} = 1.5 \times 10^9 M^{-1}s^{-1}$. Parameter set II: $k_{29} = 3.17 \times 10^{-4} s^{-1}$, $k_{-29} = 1.6 \times 10^8 M^{-1}s^{-1}$, and $k_{30} = 1.5 \times 10^{10} M^{-1}s^{-1}$

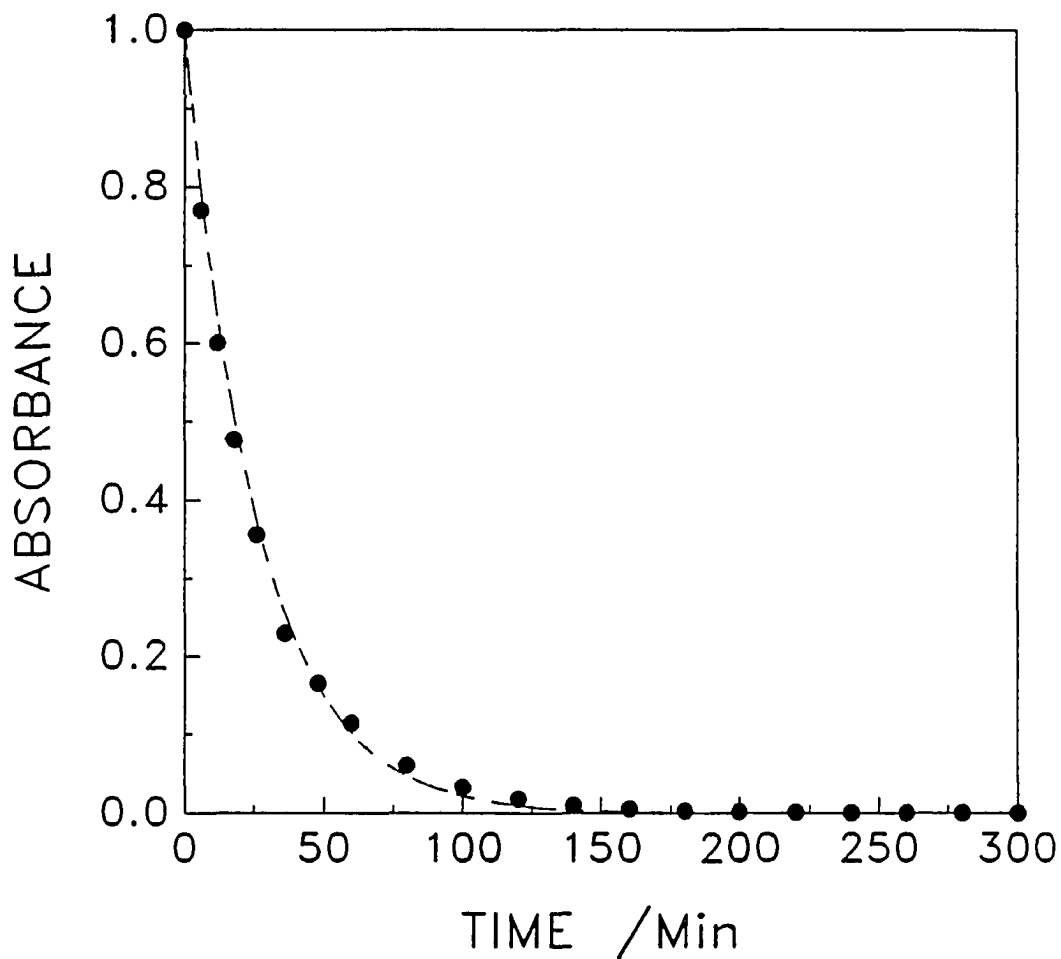


Figure I-9. A comparison of experimental (solid points) and numerically simulated (dashed lines) absorbance-time curves for the decomposition of CrO_2^{2+} at $[\text{O}_2] = 0 \text{ M}$. Parameter sets I and II give the same fit shown as the dashed lines

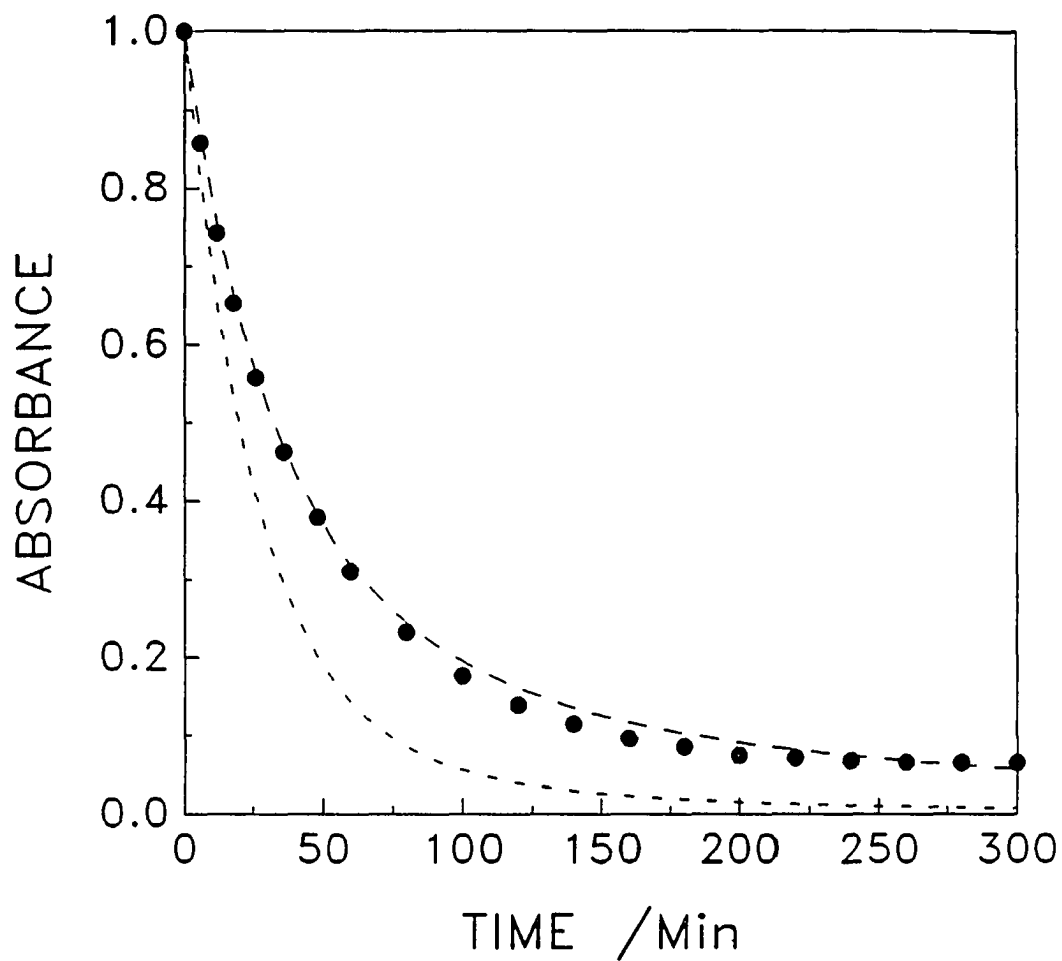


Figure I-10. A comparison of experimental (solid points) and numerically simulated (dashed lines) absorbance-time curves for the decomposition of CrO_2^{2+} at $[\text{O}_2] = 1.05 \times 10^{-4} \text{ M}$. The longer dashed lines correspond to parameter set I and the shorter dashed lines correspond to parameter set II

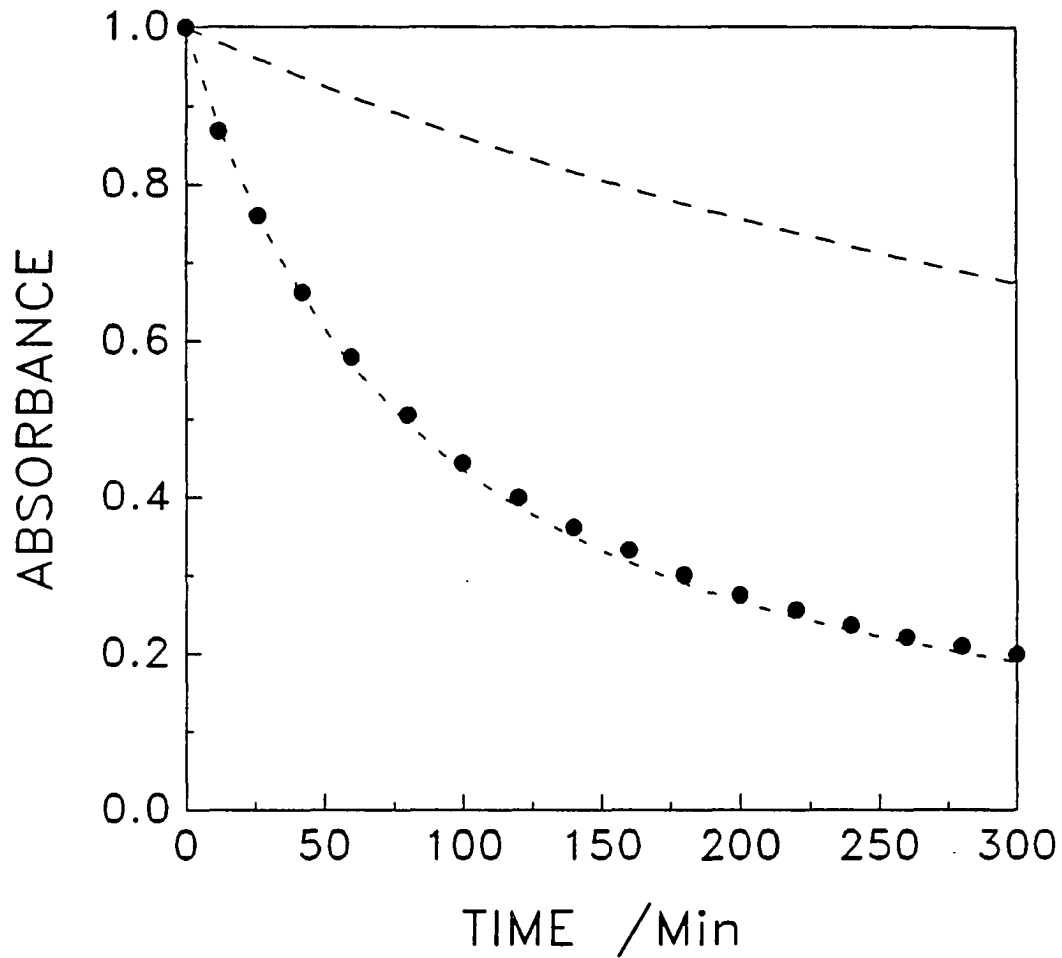
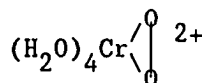
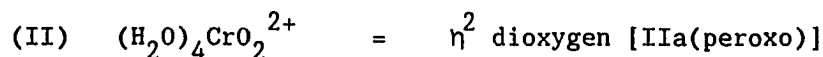
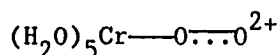
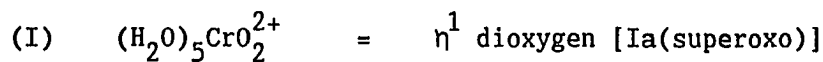


Figure I-11. A comparison of experimental (solid points) and numerically simulated (dashed lines) absorbance-time curves for the decomposition of CrO_2^{2+} at $[\text{O}_2] = 3.7 \times 10^{-3} \text{ M}$. The longer dashed lines correspond to parameter set I and the shorter dashed lines correspond to parameter set II

DISCUSSION

Proposed structure of CrO_2^{2+}

Two structures for the 1:1 $\text{Cr}^{2+}:\text{O}_2$ adduct, CrO_2^{2+} , in aqueous solution can be proposed:



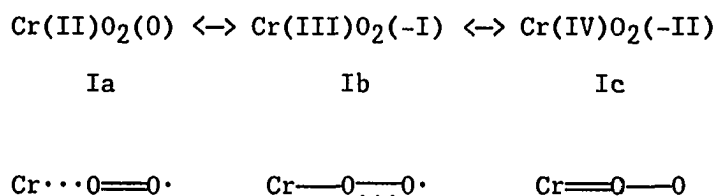
Presently there is no direct structural evidence to support either the η^1 or η^2 structural assignment since CrO_2^{2+} has not been isolated for characterization. Indirect evidence, however, implies the importance of various resonance structures.

Structure (I) formally assigns the oxidation state of the chromium as Cr(III), and the dioxygen ligand as $\text{O}_2(-1)$, the superoxo oxidation state of dioxygen. The assignment of formal oxidation states is based on literature precedents for η^1 -dioxygen complexes.²⁶ An alternative view of the oxidation state assignment involves a resonance structure scheme. The debate involving the degree of electron-transfer from the M^{n+} to the dioxygen ligand has been a subject discussed for several years and continues to be controversial.^{27,4,26}

Since the two proposed structures, I and II, imply specific formal oxidation states which cannot be supported by direct experimental evidence

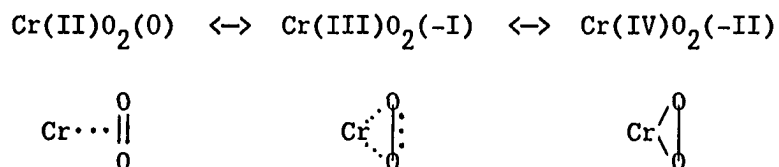
for the CrO_2^{2+} case, the formalism of oxidation states can be avoided by discussing the possible resonance structures which contribute to the overall chemical nature of the complex.

CrO_2^{2+} in an η^1 bonding arrangement has the following primary resonance forms.



Resonance structures which describe electron-transfer from the dioxygen ligand to the chromium are not included here since thermodynamic properties of these species strongly disfavor molecular oxygen acting as a reductant towards Cr(II). These resonance forms include chromium in oxidation states less than (II). The resonance contributions from $\text{Cr(V)O}_2(-\text{III})$ and $\text{Cr(VI)O}_2(-\text{IV})$, the other extreme resonance structures, should be very small since the Cr(V) and Cr(VI) oxidation states would be thermodynamically unstable as pseudo-octahedral 2+ cations. The dioxygen ligand in this case would also be thermodynamically unstable since the $\text{O}_2(-\text{III})$ formalism would leave half a bond between the oxygen atoms and the $\text{O}_2(-\text{IV})$ formalism would leave no bond between the oxygen atoms.

CrO_2^{2+} in an η^2 bonding arrangement has these primary resonance forms:



The resonance contribution from formal oxidation states other than those represented by these three structures are very unlikely in the η^2 structural arrangement for reasons similar to those given in the η^1 case. In the more positive chromium oxidation states, Cr(V) and Cr(VI), the O-O bond is broken in favor of Cr=O bonds. The Cr(VI)O₂(-IV) might at first appear to be a favored resonance form since HCrO₄⁻ has similar Cr=O bonds. However, an η^2 -Cr(VI)O₂(-IV) resonance structure would have a pseudo-octahedral arrangement with a 2+ overall charge making it thermodynamically unfavorable.

From the discussion of the primary resonance structures, it follows that some predictions can be made as to what the actual structure of CrO₂²⁺ is in aqueous solution. Discussion in the literature concerning these two structures (η^1 and η^2) has settled on the notion that the primary resonance structure for an η^1 -MO₂ complex corresponds to the superoxo formulation and in the case of CrO₂²⁺, this is represented by the Cr(III)O₂(-I)²⁺ resonance structure. An η^2 -MO₂ complex is formulated as a peroxo-complex and thus Cr(IV)O₂(-II)²⁺ is the primary resonance structure. Therefore, if experimental evidence for either primary resonance structure can be given, an important prediction concerning the structure of CrO₂²⁺ can be offered.

Evidence which supports structure (I) (η^1 -CrO₂²⁺) as an important resonance form comes from the following sources. Thermodynamic arguments clearly favor Cr(III) as the most stable chromium oxidation state. As a direct consequence of this, Cr(II) is considered a one-electron reductant towards oxidants consistent with the η^1 -Cr(III)O₂(-I) assignment as a predominant resonance structure.

Hoffmann, Chen, and Thorn⁶ have studied M-L complexes of various

electronic and structural formulations. They have developed an electronic notation that ignores electron transfer and merely counts the metal d and ligand π^* and σ^* electrons. According to this notation, CrO_2^{2+} would be $\{\text{CrO}_2^{2+}\}^6$, (Cr(II) is d^4 and O_2 has two electrons in π^* and σ^* valence orbitals for a total of 6 electrons). Hoffmann, Chen, and Thorn's theoretical molecular orbital calculations have indicated that, regardless of the formal oxidation state of the transition metal or dioxygen ligand, the most stable electronic structure for CrO_2^{2+} is an η^1 structure with a linear Cr-O-O geometry.

The chromium complex $\text{Cr}(\text{TPP})(\text{py})\text{O}_2$, prepared from $\text{Cr}(\text{II})(\text{TPP})(\text{py})$ and O_2 , has been assigned an η^1 structure on the basis of an IR study of the O-O stretching frequency of the dioxygen ligand.¹⁹ The study assigns the stretching frequency due to a superoxide-like electronic structure, $\text{Cr}(\text{III})(\text{TPP})(\text{py})(\text{O}_2^-)$. Since the equatorial TPP structure blocks adjacent coordination sites for the dioxygen ligand, an η^1 -superoxo structure is expected.

The chemical evidence is also consistent with the η^1 structure, particularly: a) the rapid reaction ($k_{30} \sim 8 \times 10^8 \text{ M}^{-1}\text{s}^{-1}$) between CrO_2^{2+} and Cr^{2+} is consistent with it, but not for an η^2 -peroxo or η^1 -peroxo structure;⁴ the reaction between Cr^{2+} and H_2O_2 has a second-order rate constant of $7 \times 10^4 \text{ M}^{-1}\text{s}^{-1}$ at 25 °C;²⁸ b) the initial step in the decomposition reaction of CrO_2^{2+} (k_{30}) is not assisted by H^+ , contrary to the expectation for the unimolecular dissociation of a peroxo complex; c) the amine analogue, $[(\text{NH}_3)_5\text{CrO}_2^{2+}]$, reacts with $\text{Cr}(\text{NH}_3)_6^{2+}$ to yield $[(\text{NH}_3)_5\text{CrO}_2\text{Cr}(\text{NH}_3)_5]^{4+18}$; d) the UV spectrum of CrO_2^{2+} has features qualitatively similar to HO_2/O_2^- in both the magnitude of the molar absorptivity and the wavelength of the maxima²⁹ and quite unlike that of

H_2O_2 or V^{3+} , the metal ion isoelectronic with $\text{Cr}(\text{IV})$. H_2O_2 has a wavelength maximum in the UV similar to HO_2/O_2^- and CrO_2^{2+} ; however, the molar absorptivity of H_2O_2 is two orders of magnitude smaller.

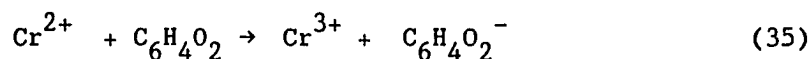
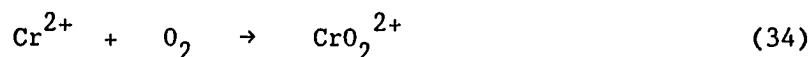
Additional evidence for the importance of the resonance structure with the η^1 -superoxo structural/electronic designation comes from the investigation of $\text{M}(\text{II})$ -dioxygen, specifically $\text{Co}(\text{II})$ -dioxygen complexes. The chemistry of $\text{Co}(\text{III})/\text{Co}(\text{II})$ is known to be similar to the chemistry of $\text{Cr}(\text{III})/\text{Cr}(\text{II})$. Numerous studies of $\text{Co}-\text{O}_2$ complexes have indicated the normal structure to be η^1 , with the $\text{Co}(\text{III})$ -superoxo electronic configuration being the primary resonance form. The η^2 - $\text{Co}(\text{IV})$ peroxo configuration is not seen for these complexes.

Thus, considering the indirect experimental evidence in support of the η^1 structural assignment, it seems reasonable to suggest that an η^1 - CrO_2^{2+} electronic/structural configuration is the proper formulation of CrO_2^{2+} .

Proposed mechanism- CrO_2^{2+} decomposition

A mechanistic pathway for the decomposition of CrO_2^{2+} formed by the reduction of molecular oxygen by Cr^{2+} has been suggested by several researchers^{13,15,17}. The first step of the mechanism is thought to involve the formation of the CrO_2^{2+} adduct by the reaction of Cr^{2+} and O_2 . This reaction has been studied in two independent pulse radiolysis studies. In these studies, Cr^{2+} was formed by the very fast reaction of Cr^{3+} with e^-_{aq} . Since the solutions contained dissolved molecular oxygen, the reaction of Cr^{2+} with O_2 proceeded to form CrO_2^{2+} . Sellers and Simic report that no change in the conductivity of the solution was observed, indicating that the reaction of Cr^{2+} and O_2 is not accompanied by the loss or uptake of protons in the pH region of their study (pH = 2.6 - 4.3).

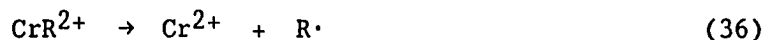
They report no evidence for the reversibility of equation 34 and indicate from their competition experiments with benzoquinone that if an equilibrium did exist, it would lie well to the right, $K_{34} > 2 \times 10^5 \text{ M}^{-1}$.



$$(k_{35} = 3.2 \times 10^8 \text{ M}^{-1}\text{s}^{-1})$$

The reversibility of equation 34, albeit in a much slower time scale, is perhaps the most important topic addressed in the present investigation. Three lines of evidence have been obtained to support the suggested bond-homolysis step. First, the form of the rate law indicates two successive kinetic steps with activated complexes $[\text{CrO}_2^{2+}]^\ddagger$ and $[\text{Cr}_2\text{O}_2^{4+}]^\ddagger$. The inverse dependence of the rate on $[\text{O}_2]$ implies that O_2 is released in the first step, as in equation 29. Depending on $[\text{O}_2]/[\text{CrO}_2^{2+}]$ (relative to $k_{29}/30$) one or the other of the two steps is rate-limiting in a given experiment.

Second, the large value of ΔH_{29}^\ddagger and especially the substantial and positive value of ΔS_{29}^\ddagger are consistent with unimolecular homolysis. The related dissociations of organochromium(2+) ions have been well-characterized as bond-homolysis reactions, equation 36.^{30,31}



Their activation parameters are similar to those found for k_{29} , although ΔS^\ddagger is less positive (10 as compared to ~ 27 cal mol⁻¹ K⁻¹). This is consistent with the nature of the released radical: O₂ should disrupt the solvent structure of water less than an aliphatic radical does.

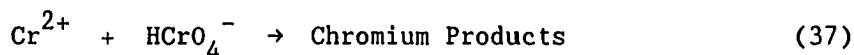
Third, a reducing intermediate was detected. This is presumed to be Cr²⁺, because it converts (NH₃)₅CoBr²⁺ to Co_{aq}²⁺.

The first clear evidence which supports the reversible binding of molecular oxygen by a chromium(II) ion was reported in a study which ion-exchanged divalent chromium on zeolite A.²⁰ Each chromium(II) ion contained in the zeolite A matrix reversibly binds one molecule of oxygen.

Evidence for reversible binding of molecular oxygen in the present study first became apparent when the decomposition rates of freshly prepared solutions of CrO₂²⁺ appeared to be very erratic. This erratic decomposition behavior was also apparent in the observed order of the decomposition traces (the decay order varied from first- to mixed first- and second-order), and in the variation in the amount of HCrO₄⁻ produced detected in the UV-VIS spectra of the decomposed CrO₂²⁺ solutions. Systematic variation of the dissolved oxygen concentration at a fixed acid concentration (HClO₄ = 0.10 M, μ = 1.00 M) clearly indicated that the erratic behavior of the decomposition of CrO₂²⁺ was due to the varying concentrations of dissolved molecular oxygen in these experiments. Thus, the primary kinetic evidence which supports the importance of the homolytic cleavage of the Cr-O bond is from the reversibility of equation 29. This is supported by the dependence of the decomposition rate, the reaction order and the observed products on the varying dissolved molecular oxygen concentration.

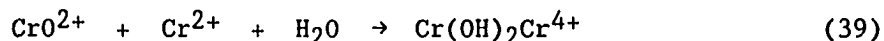
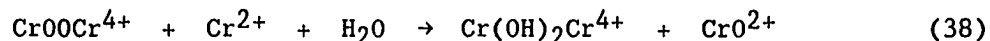
The second step in the proposed decomposition mechanism of CrO_2^{2+} involves the Cr^{2+} formed in the homolysis of CrO_2^{2+} . Since Cr^{2+} is a one-electron reductant, it can react with the three observed oxidants present in solution- O_2 , CrO_2^{2+} , and HCrO_4^- . Since these three oxidants are essentially in competition for the Cr^{2+} , the predominant pathway will be indicated by the magnitude of the rate constants and the relative concentrations of the species. The rate constants are estimated to be of a similar magnitude; therefore, the relative concentrations of these oxidants define the major pathways by which CrO_2^{2+} decomposes.

The first oxidant, O_2 , has already been discussed but this reaction clearly does not represent a net decomposition pathway for CrO_2^{2+} since the reaction of Cr^{2+} and O_2 forms CrO_2^{2+} . The reaction of Cr^{2+} with HCrO_4^- can be considered to be a minor pathway. This is especially true when the dissolved oxygen concentrations are low, since the concentrations of HCrO_4^- produced in these experiments are very small. The decomposition of CrO_2^{2+} in higher dissolved oxygen concentrations produces more HCrO_4^- , but these concentrations are also small and only approach the CrO_2^{2+} concentration after most of the CrO_2^{2+} has decomposed (Cr^{2+} trapping experiments with added HCrO_4^- indicate the rate constant for the reaction between Cr^{2+} and HCrO_4^- is less than k_{30} by at least an order of magnitude $k_{37} < k_{30}$). Thus, the major pathway for the consumption of Cr^{2+} formed



from the homolysis of CrO_2^{2+} is by the reaction of Cr^{2+} with another molecule of CrO_2^{2+} , equation 30. The initial step of this reaction is shown in equation 30. The 3:1 stoichiometry for this reaction, expected

from the stoichiometry of the overall O_2 - Cr^{2+} reaction, was directly confirmed by spectrophotometric titration of CrO_2^{2+} with Cr^{2+} , as cited above. In combination with the kinetic scheme, with a 1:1 reaction between CrO_2^{2+} and Cr^{2+} , equation 30, the overall 3:1 reaction requires additional step(s). Following equation 30, equations 38 and 39 can be proposed to occur.

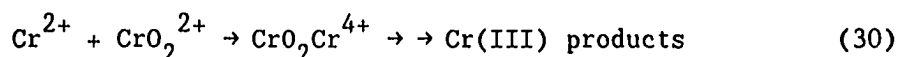


These reactions, although proposed without direct evidence obtained in the course of this work, appear reasonable. The first, equation 38, finds analogy in the reactions of other metal ions with oxygen.^{32,33,34} Moreover, it can be viewed as the attack of chromium on the O-O bond of the dinuclear chromium peroxide complex. As such, it is analogous to the attack of Cr^{2+} on the O-O bond of hydrogen peroxide and alkyl hydroperoxides.^{35,36}

The analogy between the chromium(IV) species, the chromyl ion CrO^{2+} , and hydroxyl (and alkoxy) radicals can be recognized; note their similarity to the ferryl ion FeO^{2+} .³⁷ The second, equation 39, is simply the reaction of this chromium(IV) species and chromium(II). These reactions are formulated to yield directly the observed product, the dinuclear complex containing two bridging OH groups.¹⁵ The distinction between this and the authentic μ -oxo species $Cr-O-Cr^{4+}$ is now recognized.³⁸ Although experiments were not done to explore these points further, we

also note that further slow changes in UV spectra were seen in many of the kinetic runs, after CrO_2^{2+} had completely reacted. These could be arrested by addition of Cr^{2+} , which is consistent with the chemistry suggested.

The decomposition mechanism proposed thus far includes the homolysis of CrO_2^{2+} , equation 29, and the capture of the homolytically produced Cr^{2+} by an additional molecule of CrO_2^{2+} , equation 30. The rate law derived from this scheme is shown in equation 31.



$$\frac{-d[\text{CrO}_2^{2+}]}{dt} = \frac{2k_{29}[\text{CrO}_2^{2+}]}{1 + \{k_{-29}[\text{O}_2]/k_{30}[\text{CrO}_2^{2+}]\}} \quad (31)$$

$$\frac{-d[\text{CrO}_2^{2+}]}{dt} \sim 2k_{29}[\text{CrO}_2^{2+}] \quad (\text{limit at } \text{O}_2 = 0 \text{ M}) \quad (40)$$

In the limit where $[\text{O}_2] = 0 \text{ M}$, the expression reduces to equation 40. This result allows the assignment of the observed first-order rate constant k_{obs} equal to $2k_{29}$. Equation 31 qualitatively describes the mixed first- and second-order character for the intermediate molecular oxygen concentrations and predicts a CrO_2^{2+} decomposition second-order in $[\text{CrO}_2^{2+}]$ at high concentrations of dissolved molecular oxygen. Equation 41 represents the other limiting case of high dissolved molecular oxygen concentrations. The following calculations are based on the experiment

where $[O_2] = 3.52 \times 10^{-3} \text{ M}$ and $[CrO_2^{2+}]_0 = 1.74 \times 10^{-5} \text{ M}$ ($k_{obs} \sim 12 \text{ M}^{-1}\text{s}^{-1}$). Since k_{-29} is known and $2k_{29}$ can be assigned to k_{obs} when $[O_2] = 0 \text{ M}$, the value for k_{30} can be estimated, equation 41.

$$k_{obs} = \frac{2k_{29}}{1 + \{k_{-29}[O_2]/k_{30}[CrO_2^{2+}]\}} \quad (41)$$

$$12 \text{ M}^{-1}\text{s}^{-1} = \frac{2(2.5 \times 10^{-4} \text{ s}^{-1})}{1 + \{(1.6 \times 10^8 \text{ M}^{-1}\text{s}^{-1})(3.70 \times 10^{-3} \text{ M})/k_{30}[CrO_2^{2+}]\}}$$

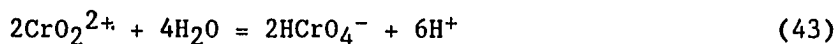
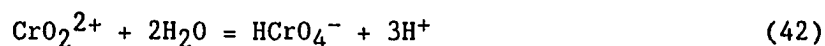
$$k_{30} \sim 2 \times 10^{10} \text{ M}^{-1}\text{s}^{-1}$$

Intuitively, the reaction of Cr^{2+} and CrO_2^{2+} (k_{30}) will be a very fast reaction; however, $k_{30} \sim 2 \times 10^{10} \text{ M}^{-1}\text{s}^{-1}$ is presumably too high an estimate for several reasons. The rate of the substitution of H_2O on Cr^{2+} is only $\sim 7 \times 10^9 \text{ M}^{-1}\text{s}^{-1}$, preventing any faster substitution at Cr^{2+} .³⁹ The rate of the substitution of CrO_2^{2+} on Cr^{2+} should also be slower than the aquo substitution rate due to the 2^+ charge of both cations. This estimate for k_{30} should also be viewed in light of the rate constant for the analogous reaction of Cr^{2+} and O_2 ($k = 1.6 \times 10^8 \text{ M}^{-1}\text{s}^{-1}$). It seems unlikely that the rate constant for the reaction of CrO_2^{2+} and Cr^{2+} would be two orders of magnitude greater than the rate constant for the reaction of O_2 and Cr^{2+} .

This mechanism was tested with computer modeling by a kinetic simulation program using various values of k_{30} . The computer simulation clearly indicated that the value of k_{30} had to be unreasonably large ($k_{30} \sim 1.5 \times 10^{10} \text{ M}^{-1}\text{s}^{-1}$) before the observed kinetic results ($[O_2] = 3.7 \times$

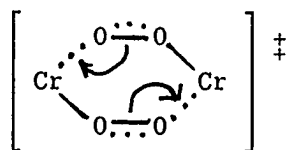
10^{-3} M) resembled the simulation. An additional problem with this mechanism is that it does not predict the formation of HCrO_4^- , a readily observed product when the dissolved oxygen concentrations are moderate or high.

An important modification of the mechanism includes an additional path for the decomposition of CrO_2^{2+} . The observed data indicate that this path is bimolecular and is only a dominant pathway for the decomposition of CrO_2^{2+} when the CrO_2^{2+} concentrations are high or when the dissolved oxygen concentration is moderate to high. This step is responsible for the formation of HCrO_4^- , and so proceeds by a mechanism quite different from the Cr(III)-forming reactions along the path that begins with bond homolysis. In a formal sense CrO_2^{2+} and HCrO_4^- are equivalent, in that these species are related not by oxidation-reduction, but by simple hydrolysis:



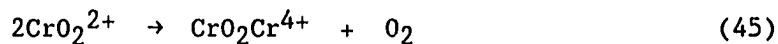
The structures of the two are quite different, however, and one would anticipate that a mechanism considerably more intricate than hydrolysis would be needed for their interconversion. That contention is supported by the second-order kinetics for the rate of the net transformation, as in equation 43. This reaction step proceeds with a substantially lower enthalpy of activation (compensation of bond-making and bond breaking) and by the negative enthalpy of activation (consistent with the additional organizational entropy of a bimolecular reaction).

A plausible transition state for this reaction step is one in which the pair of CrO_2^{2+} ions interact to create a new Cr-O bond from the O-O bond of the other partner:



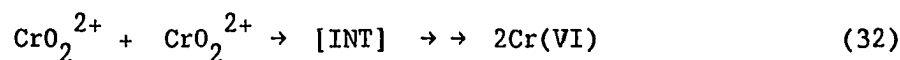
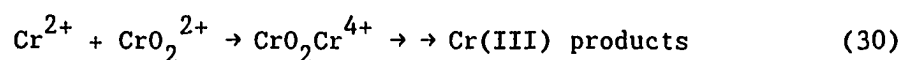
If this is a reasonable representation of the transition state, then its dissociation as shown will lead to a dioxo species, $(\text{H}_2\text{O})_n\text{Cr}(\text{O})_2^{2+}$. Loss of protons from the dioxochromium(VI) ion, now much more acidic in the higher oxidation state, will (according to the process depicted) occur spontaneously, preceded or followed by dissociation of coordinated water, ultimately yielding HCrO_4^- . It has been reported that early transition metals, including chromium, show the tendency to break O-O single bonds and undergo intramolecular electron-transfer in order to make $\text{M}=\text{O}$ double bonds.⁴ This is a reaction unknown for $\eta^1:\eta^1$ dioxygen complexes of cobalt, but it has been proposed for $\eta^1:\eta^1$ dioxygen complexes of iron.^{40,41,42}

Alternatively, bimolecular decomposition of CrO_2^{2+} might proceed analogously to the disproportionation of HO_2 ; for example:



Here the intermediate product is a μ -peroxo dichromium complex. The same dimetallic species, however, is believed to be formed in the reaction between CrO_2^{2+} and Cr^{2+} , equation 30, along the other pathway for CrO_2^{2+} decomposition. There it does not lead to HCrO_4^- . Clearly, the same species cannot react in different ways in similar circumstances, and thus the path shown in equation 45 seems unlikely.

Scheme I-1. Proposed Decomposition Mechanism for CrO_2^{2+}



$$\frac{-d[\text{CrO}_2^{2+}]}{dt} = \frac{2k_{29}[\text{CrO}_2^{2+}]}{1 + \{k_{-29}[\text{O}_2]/k_{30}[\text{CrO}_2^{2+}]\}} + 2k_{32}[\text{CrO}_2^{2+}]^2 \quad (33)$$

The following calculations are based on the experiment where $[\text{O}_2] = 3.52 \times 10^{-3} \text{ M}$ and $[\text{CrO}_2^{2+}]_0 = 1.74 \times 10^{-5} \text{ M}$. The observed CrO_2^{2+} decomposition absorbance vs. time profile was second-order with a $k_{\text{obs}} \sim 12 \text{ M}^{-1}\text{s}^{-1}$. The rate constant k_{29} can be estimated from the kinetic data according to equation 35.

$$k_{\text{obs}} = \frac{2k_{29}}{1 + \{k_{-29}[O_2]/k_{30}[CrO_2^{2+}]\}} + 2k_{32} \quad (46)$$

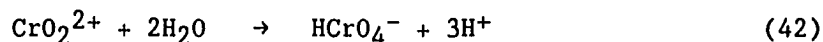
$$12 \text{ M}^{-1}\text{s}^{-1} = \frac{2(2.5 \times 10^{-4} \text{ s}^{-1})}{1 + \{(1.6 \times 10^8 \text{ M}^{-1}\text{s}^{-1})(3.70 \times 10^{-3} \text{ M})/k_{30}[CrO_2^{2+}]\}} + 2k_{32} \quad (47)$$

$$k_{32} \sim 8 \text{ M}^{-1}\text{s}^{-1}$$

The value for k_{30} was estimated for this calculation to be $8 \times 10^8 \text{ M}^{-1}\text{s}^{-1}$. This estimate for k_{30} appears to be reasonable based on the known substitution properties of Cr^{2+} . This rate constant is not empirically determined, but represents an estimated rate constant consistent with the chemistry of Cr^{2+} and provides good agreement between observed and simulated data. The term $k_{30}[CrO_2^{2+}]$ in the denominator of equation 46 is small with respect to $k_{-29}[O_2]$, simplifying the calculation.

This proposed mechanism, shown in Scheme I-1, was tested with computer modeling by the kinetic simulation program and good agreement between the observed and simulated data was obtained at all the various dissolved oxygen concentrations.

It has been suggested that $HCrO_4^-$ is formed in the decomposition of CrO_2^{2+} by the following net reaction, equation 42.16



This pathway would include intramolecular electron transfer to formally oxidize the chromium to Cr(VI) and reduce the dioxygen to the

oxidation state of water, O(-II). Additional rearrangement is required such as the loss of two H₂O ligands (CrO₂²⁺ is thought to be six-coordinate (H₂O)₅CrO₂²⁺) and the deprotonation of the two remaining aquo ligands. Any mechanistic scheme which would accommodate this net reaction would not be a pathway second-order in [CrO₂²⁺] as indicated by the observed kinetic data. Thus, the observed kinetics do not support the scheme represented by equation 42.

Activation parameters and bond strengths

The activation parameters for the two rate determining steps in the CrO₂²⁺ decomposition scheme were determined to additionally characterize the system. Owing to the complicated nature of the parallel path decomposition scheme, the activation parameters had to be extracted by a detailed computer analysis of the absorbance vs. time traces at various temperatures and various CrO₂²⁺ concentrations. The activation parameters assigned to the homolysis of the Cr-O bond are shown below (M, s, thermochemical data):

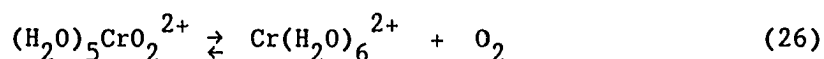
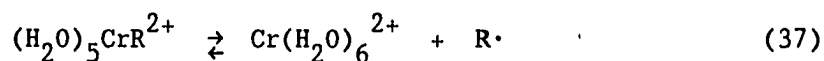
<u>Kinetic Parameters:</u>	k(298 K)	ΔG^\ddagger_{298}	ΔH^\ddagger	ΔS^\ddagger
Forward (k ₂₉):	2.5 X 10 ⁻⁴	22.3(5)	25.1	9.7
Reverse (k ₋₂₉):	1.6 X 10 ⁸	6.2(6)	2±2(est)	-15±6
 <u>Equilibrium Parameters:</u>	 K ₂₉ (298 K)	 ΔG°_{298}	 ΔH°	 ΔS°
	1.6 X 10 ⁻¹²	16.1	23±2	25±10

The enthalpy of activation is not very indicative of a specific mechanism; however, in a dissociative scheme the ΔH^\ddagger is an indication of the bond strength of the Cr-O bond. The ΔS^\ddagger determined for this system is indicative of a dissociative mechanism and clearly supports the proposed homolytic-capture scheme.

The forward and reverse rate constants have been determined for the homolytic dissociation/recombination reaction represented by equation 29. The quotient of these rate constants is the equilibrium constant. Ochiai estimates that irreversible oxygenation reactions will have an uptake or release ΔG° that is more negative than $-13 \text{ kcal mol}^{-1}$.⁴³ This estimate in terms of M-O₂ homolytic reactions, the reverse of the oxygenation reaction, would classify reactions in which the ΔG° is more positive than 13 kcal mol^{-1} as irreversible. Technically Ochiai's conclusion is invalid since the equilibrium, while strongly shifted toward oxygenation, still allows the formation of very low concentrations of dissolved species.⁴⁴ It is interesting to note that Ochiai would characterize the oxygenation of Cr²⁺ as an irreversible reaction. Clearly Ochiai's estimate is somewhat arbitrary and can only be used as a guideline for the assignment of the reversible/irreversible character of an oxygenation reaction.

The homolytic dissociation of organochromium complexes has been studied in detail and provides a suitable set of reactions analogous to the homolytic dissociation of CrO₂²⁺.³⁰ The ΔH^\ddagger 's for the homolysis of organochromium complexes fall in the range 21-33 kcal mol⁻¹. The ΔH^\ddagger for the homolysis of CrO₂²⁺ (25.1 kcal mol⁻¹) is well within this range. The ΔS^\ddagger for the homolysis of CrO₂²⁺ (9.7 cal mol⁻¹ K⁻¹), however, is smaller than the ΔS^\ddagger for the organochromium complexes (20-37 cal mol⁻¹

K⁻¹). The difference in the entropy of activation for the two reactions, equation 47 and 29, is apparently due to larger solvation requirements for organic radicals as compared to molecular oxygen in aqueous solution.

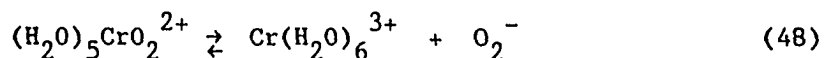


The activation parameters assigned to the second rate determining step, equation 29, ($\Delta H_{29}^\ddagger = 12.0 \pm 1.7$ kcal mol⁻¹ and $\Delta S_{29}^\ddagger = -14.4 \pm 5.8$ cal mol⁻¹ K⁻¹) are consistent with this type of reaction. The ΔH^\ddagger in this case is also not very indicative of the mechanism but it is consistent with a bimolecular reaction of two CrO_2^{2+} molecules to form an intermediate. The entropy of activation is negative, indicative of an associative mechanism. A more negative value for the entropy of activation might be expected considering the ordered nature of the proposed cyclic intermediate. However, the dissociation of the two H_2O molecules required by this scheme might account for the relatively positive ΔS^\ddagger value.

Heterolytic dissociation of CrO_2^{2+}

From the kinetically derived value of K_{29} and the standard reduction potentials for the $\text{Cr}^{3+}/\text{Cr}^{2+}$ and $\text{O}_2(\text{aq})/\text{O}_2^-$ couples (-0.41 and -0.16 V, respectively), the value of K_{48} is calculated to be 3×10^8 M, which is about $10^{4.2}$ times more favorable than K_{29} . Both the homolysis and heterolysis reactions require energy to occur, with ΔG° values of 15.9 and

10.3 kcal mol⁻¹, respectively. Therefore, if either reaction is the initial step in a kinetic sequence, subsequent reactions which release sufficient energy would be required to drive the overall dissociation process. Even though homolysis is less favorable thermodynamically, the kinetic data suggest it is the better initial step. It would then follow that a severe disadvantage for heterolytic dissociation exists forcing the reaction to proceed by a homolytic process.



If k_{-48} is given a typical value for ligand substitution of $\text{Cr}(\text{H}_2\text{O})_6^{3+}$, $\sim 10^{-6} \text{ M}^{-1}\text{s}^{-1}$, then $k_{48} \sim 10^{-14} \text{ s}^{-1}$. A better estimate for k_{-48} does not need to be made since any reasonable value makes k_{48} negligibly small. The very slow ligand substitution rates of $\text{Cr}(\text{H}_2\text{O})_6^{3+}$ suggest k_{-48} is limited by ligand substitution resulting in a substantial kinetic barrier for k_{48} .

The following data (formation constants, M^{-1}) allow comparison of the bond strengths of a $\text{Cr}(\text{III})\text{-O}_2^-$ species and a $\text{Cr}(\text{III})\text{-OH}^-$ species with those of analogous $\text{Co}(\text{III})$ species. A comparison of the formation constants for Cr^{3+} and O_2^- versus Cr^{3+} and $\text{X}^- = \text{OH}^-$ is presented since OH^- is usually one of the most strongly bound X^- ions.

	O_2^-	OH^-
$\text{Cr}(\text{H}_2\text{O})_6^{3+}$	$10^{7.5}$	10^{10}
$\text{Co}([\text{14}]\text{aneN}_4)(\text{H}_2\text{O})_2^{3+}$	$10^{13.7}$	10^{11}

The enhanced stability of the cobalt-superoxide species was proposed by Taube⁴⁵ in a treatment of O_2^- coordination for cobalt macrocycles.⁴⁶ This analysis indicates the presence of a charge-transfer interaction, as in $Co(IV)-O_2^{2-}$. The reversal in ordering between the chromium and cobalt systems implies that a metal(IV)-peroxide state is much less important for chromium.

Now compare the Lewis acidity of $Cr(H_2O)_6^{3+}$ toward O_2^- versus its acidity toward acetate ions.^{47,48} These anions are comparable bases toward the hydrated proton as both HO_2 and $HOAc$ have pK_a 's of 4.8 ± 0.1 . CrO_2^{2+} forms with a higher stability constant than $CrOAc^{2+}$, with the log k 's being 7.5 and < 4.7 , respectively. Even though aqueous superoxide anion is very strongly hydrogen-bonded, comparable to fluoride ions,⁴⁹ the larger value for the CrO_2^{2+} may signal a charge-transfer interaction in the superoxo complex.

In fact, the binding of fluoride and other simple anions can be considered in the same context as the superoxide interaction. $(H_2O)_5CrX^{2+}$ and $(NH_3)_5CoX^{2+}$ complexes are similar and can be easily compared because stability constant data are available for both series.^{50,51} The close analogy between pentaamine cobalt complexes and saturated tetraamine cobalt macrocycles (to return to the Taube⁴⁶-Endicott⁴⁷ example), and the electronic nature of the ground state⁵² which appears to be $M(III) \cdot X^-$ for the simple anions, except for possibly the superoxide, aids in the comparison. The values of the K_{Cr}/K_{Co} ratio are as follows:

X^- :	OH^-	F^-	Cl^-	Br^-	NCS^-
K_{Cr}/K_{Co} :	65	850	0.088	0.006	0.39

The F^- ion shows a strong preference toward $Cr(H_2O)_6^{3+}$, even with the very hard base OH^- showing a smaller enhancement. Fluoride ions in the aquochromium complex may partially retain the hydrogen-bonding interactions characteristic of the free anion, utilizing cis water molecules in the coordination sphere. If this is correct, the relative stability of the aminocobalt bonding of fluoride ions would be correspondingly lower. This would explain the large stability constant of CrO_2^{2+} compared to those for other CrX^{2+} ions ($10^{7.5}$ vs. $10^{4.3}$ for fluoride). This large stability constant is thought to arise because the coordination of aqueous (i.e., hydrated) superoxide ions to the aquo complex does not completely eliminate the hydrogen-bonded interactions of the anion.

To relate this point to electronic structures, consider the values of K_{Cr}/K_{Co} for $X^- = OH^-$ (13) vs. O_2^- ($10^{-6.2}$), now using K_{Co} for $(H_2O)_2Co([14]aneN_4)^{3+}$.⁵³ It was pointed out that K_{Cr} for O_2^- is exceptionally large (relative to values for CrX^{2+}); however, this very small value of K_{Cr}/K_{Co} for superoxide ions emphasizes the unusual stability between O_2^- and $(H_2O)_2Co([14]aneN_4)^{3+}$. This further strengthens Taube's case⁴⁶ for charge-transfer stabilization of that complex. However, this analysis does not provide sufficient evidence to support the formulation of $(H_2O)_5Cr^{2+}$ as other than a superoxo chromium(III) complex.⁵⁴

SUMMARY

The cation $(\text{H}_2\text{O})_5\text{CrO}_2^{2+}$ has a considerable lifetime in aqueous solution in the absence of Cr^{2+} . One pathway for decomposition consists of bond homolysis, $\text{CrO}_2^{2+} \longrightarrow \text{Cr}^{2+} + \text{O}_2$. The resulting Cr^{2+} then reacts very rapidly with CrO_2^{2+} . A second pathway, which yields HCrO_4^- , proceeds by a bimolecular reaction between two CrO_2^{2+} ions. The data do not require a description of CrO_2^{2+} as other than a superoxochromium(III) ion.

BIBLIOGRAPHY

1. Fremy, E. Ann. Chim. Phys., 1852, 35, 257.
2. Werner, A. Ann. Chem. Liebigs, 1910, 375, 1.
3. (a) Arnold, S. J.; Browne, R. J.; Ogryzio, E. A. Photochem. Photobiol., 1965, 4, 963.; (b) Hoytink, G. H. Acc. Chem. Res., 1969, 2, 114.
4. Gubelmann, M. H.; Williams, A. F. Structure and Bonding, 1983, 55, 1.
5. Vaska, L. Acc. Chem. Res., 1976, 9, 175.
6. Hoffmann, R.; Chen, M. M-L.; Thorn, D. L. Inorg. Chem., 1977, 16, 503.
7. Endicott, J. F.; Kumar, K. ACS Symp. Series, 1982, 198, 425.
8. Wilkins, R. G. Adv. Chem. Ser., 1971, 100, 111.
9. Abel, E. W.; Pratt, J. M.; Whelan, R.; Wilkinson, R. J. J. Am. Chem. Soc., 1974, 96, 7119.
10. Briant, C. E.; Hughes, G. R.; Minshall, P. C.; Mingoos, D. M. P. J. Organomet. Chem., 1980, 202, C18.
11. Mimoun, H. Angew. Chem. Int. Ed., 1982, 21, 734.
12. Tatsuno, Y.; Otsuka, S. J. J. Am. Chem. Soc., 1981, 103, 5832.
13. Picard, J. Ber. 1913, 46, 2477.
14. Ardon, M.; Stein, G. J. Chem. Soc., 1956, 2095.
15. Kolaczowski, R. W.; Plane, R. A. Inorg. Chem., 1964, 3, 322.
16. Ilan, Y. A.; Czapski, G.; Ardon, M. Isr. J. Chem., 1975, 13, 15.
17. Sellers, R. M.; Simic, M. G. J. Am. Chem. Soc., 1976, 98, 6145.
18. Joyner, T. B.; Wilmarth, W. K. J. Am. Chem. Soc., 1961, 83, 516.
19. Cheung, S. K.; Grimes, C. J.; Wong, J.; Reed, C. A. J. Am. Chem. Soc., 1976, 98, 5028.
20. Kellerman, R.; Hutta, P. J.; Klier, K. J. Am. Chem. Soc., 1974, 96, 5946.
21. a) Hynes, W. A.; Yanowski, L. K.; Shiller, M. J. Am. Chem. Soc., 1938, 60, 3053; b) Parker, O. J.; Espenson, J. H. J. Am. Chem. Soc., 1969, 91, 1968.

22. Barshop, B. A.; Wrenn, R. F.; Frieden, C. J. Anal. Biochem., 1983, 130, 134.
23. CrO_2^{2+} , 5×10^{-5} M, was allowed to decompose in the presence of $[\text{HCrO}_4^-] \leq 10^{-4}$ M. No CrO_2^{2+} decomposition rate reduction was observed, therefore, HCrO_4^- was not effective in competition with CrO_2^{2+} for Cr^{2+} at these concentrations.
24. Candlin, J. C.; Halpern, J. Inorg. Chem., 1965, 4, 766.
25. The value $k_{\text{Co}} = 2.0 \times 10^6 \text{ M}^{-1}\text{s}^{-1}$ was used in the experimental simulation. This estimate was required since the ionic strength was 0.250 M.
26. Jones, R. D.; Summerville, D. A.; Basolo, F. Chem. Rev., 1979, 79, 139.
27. Reed, C. A.; Cheung, S. K.; Proc. Natl. Acad. Sci. U.S.A., 1977, 74, 1780.
28. Bakac, A.; Espenson, J. H. Inorg. Chem., 1983, 22, 779.
29. Bielski, B. H. J. Photochem. Photobiol., 1978, 28, 645.
30. Kirker, G. W.; Bakac, A.; Espenson, J. H. J. Am. Chem. Soc., 1982, 104, 1249.
31. Espenson, J. H. Prog. Inorg. Chem., 1983, 30, 189.
32. Ochiai, E. J. Inorg. Nucl. Chem., 1973, 35, 3375.
33. Rush, J. D.; Bielski, B. H. J. Inorg. Chem., 1985, 24, 4282.
34. Hills, E. F.; Norman, P. R.; Ramasami, T.; Richens, D. T.; Sykes, A. G. J. Chem. Soc., Dalton Trans., 1986, 157.
35. (a) Kochi, J. K.; Davies, D. D. J. Am. Chem. Soc., 1964, 86, 5264;
(b) Kochi, J. K.; Mocadlo, P. E. J. Org. Chem., 1965, 30, 1133.
36. (a) Hyde, M. R.; Espenson, J. H. J. Am. Chem. Soc., 1976, 98, 4463;
(b) Bakac, A.; Espenson, J. H. Inorg. Chem., 1983, 22, 779.
37. Koppenol, W. H.; Liebman, J. F. J. Phys. Chem., 1984, 88, 99.
38. Johnston, R. F.; Holwerda, R. A. Inorg. Chem., 1983, 22, 2942.
39. Basolo, F.; Pearson, R. G. "Mechanisms of Inorganic Reactions"; John Wiley and Sons: New York, N.Y., 1967.
40. Chin, D. H.; La Mar, G. N.; Balch, A. L.; J. Am. Chem. Soc., 1980, 102, 4344.

41. Chin, D. H.; La Mar, G. N.; Balch, A. L.; J. Am. Chem. Soc., 1977, 99, 5486.
42. Latos-Grazynski, L.; Cheng, R.-J., La Mar, G. N.; Balch, A. L. J. Am. Chem. Soc., 1982, 104, 5992.
43. Ochiai, E. J. Inorg. Nucl. Chem., 1973, 35, 3375.
44. Niederhoffer, E. C.; Timmions, J. H.; Martell, A. E. Chem. Rev., 1984, 84, 153.
45. Taube, H. Prog. Inorg. Chem., 1986, 34, 607.
46. Wong, C. J.; Switzer, J. A.; Balakrishnan, P. K.; Endicott, J. F. J. Am. Chem. Soc., 1980, 102, 5511.
47. Deutsch, E.; Taube, H. Inorg. Chem., 1968, 7, 1532.
48. Thermodynamic data do not appear to be available for $(\text{H}_2\text{O})_5\text{CrOAc}^{2+}$, however, although the kinetics of its (heterolytic) dissociation have been studied.⁴⁷ Since aquation proceeded to completion at 0.04 M H^+ , a conservative estimate affords a stability constant for $\text{Cr}^{3+} + \text{OAc}^- = \text{CrOAc}^{2+}$ of $K < 5 \times 10^4 \text{ M}^{-1}$.
49. (a) Sawyer, D. T.; Valentine, J. S. Acc. Chem. Res., 1981, 14, 393; (b) Yamdagni, R.; Payzant, J. D.; Kebarle, P. Can. J. Chem., 1973, 51, 2507.
50. Swaddle, T. W.; King, E. L. Inorg. Chem., 1965, 4, 532. Stability constants for $(\text{H}_2\text{O})_5\text{CrX}^{2+}$ complexes have been summarized by Swaddle, T. W.; Guastalla, G. Inorg. Chem., 1968, 7, 1915.
51. Stability constants for $(\text{H}_2\text{O})_5\text{CrX}^{2+}$ complexes have been summarized by Basolo, F.; Pearson, R. G. "Mechanisms of Inorganic reactions", Second Edition; Wiley, New York, 1968; p 165.
52. An analysis of the energetics of electron transfer in $(\text{NH}_3)_5\text{CoX}^{2+}$ complexes has been given: (a) Taube, H.; Gould, E. S. Acc. Chem. Res., 1969, 321; (b) Taube, H. "Electron Transfer Reactions of Complex Ions in Solution"; Academic Press, New York, 1970.
53. The available data for the latter are based on the [14]ane N_4 macrocycle, and so this comparison entails use of the same complex for O_2^- and OH^- . Little is sacrificed, however, since, where known, stability constants towards a given X^- are comparable for $\text{Co}(\text{NH}_3)_5\text{OH}_2^{3+}$ and $(\text{H}_2\text{O})_2\text{Co}[\text{14}]\text{aneN}_4^{3+}$.
54. An interesting possibility not addressed here, is whether the ground state of this ion might be formulated as the hydroxo-hydroperoxo tautomer $(\text{H}_2\text{O})_4\text{Cr}(\text{OH})(\text{OOH})^{2+}$.

**CHAPTER II. REACTIONS OF THE SUPEROXOCHROMIUM(III)
ION WITH TRANSITION METAL COMPLEXES**

INTRODUCTION

Oxidations that depend on dioxygen are of fundamental importance to many chemical and biological processes.¹ Although dioxygen is an integral part of many redox systems, it is known to be sluggish in many of its reactions, often utilizing a transition metal complex to activate it in redox processes. The triplet ground state of dioxygen provides a considerable kinetic barrier to the auto-oxidation of normally diamagnetic organic molecules. This barrier is associated with generally very slow reactions involving a change of spin or unstable triplet state products. This problem can be avoided in reactions of dioxygen with a transition metal where greater spin-orbit coupling considerably reduces the kinetic barrier to a change of spin. In addition, the formation of a metal dioxygen complex may provide sufficient energy to pair the spins.^{1b} The coordination of dioxygen to reduced transition metals often yields potent and efficient oxidants.

Little is known about the reactivity patterns of transition metal-dioxygen adducts in aqueous solution since the lifetimes of these adducts vary from moderately long to extremely short. One dioxygen adduct that has been studied in some detail is $\text{Co}([\text{14}] \text{aneN}_4)(\text{OH}_2)\text{O}_2^{2+}$.² The report of the reactivity of this species represents much of what is known about the chemistry of transition metal-dioxygen adducts.

The complex, which readily decomposes in aqueous solutions, is a moderately strong oxidant (estimated $E^\circ \sim 0.3 \pm 0.1 \text{ V}$).^{2b} The oxidations of several transition metal complexes with the in situ generated $\text{Co}([\text{14}] \text{aneN}_4)(\text{OH}_2)\text{O}_2^{2+}$ proceed with high rate constants and utilize all

three oxidizing equivalents provided by the coordinated superoxide.

Another transition metal dioxygen adduct, $(\text{H}_2\text{O})_5\text{CrO}_2^{2+}$, has been known for over 75 years.³ The kinetics and mechanism of its decomposition under aerobic and anaerobic conditions, however, were reported only recently.⁴ CrO_2^{2+} is a semi-stable species with a half-life of ~15 minutes under anaerobic conditions ($\text{HClO}_4 = 0.10 \text{ M}$, $T = 25.0 \text{ }^\circ\text{C}$). Only very dilute solutions of CrO_2^{2+} can be prepared, $[\text{CrO}_2^{2+}] \leq 5 \times 10^{-5} \text{ M}$, before HCrO_4^- , a product of the decomposition of CrO_2^{2+} , becomes a significant interference. Even with these limitations, the preparation and handling of CrO_2^{2+} solutions is easier than the complex techniques required for $(\text{H}_2\text{O})\text{Co}([\text{14}] \text{aneN}_4)\text{O}_2^{2+}$ solutions.

Owing to its relative stability towards one reductant (Cr^{2+}), it appeared to be an interesting candidate for a kinetic and mechanistic study of its reactions with a series of reducing complexes.

STATEMENT OF PROBLEM

The reactions of $(\text{H}_2\text{O})\text{Co}([\text{14}] \text{aneN}_4)\text{O}_2^{2+}$ with transition metal complexes have been reported in the literature;² however little else is known about the reactivity patterns of transition metal-dioxygen adducts in aqueous solution since these adducts exist with reactivity characteristics ranging from semi-stable species to highly reactive transients.

The cation $(\text{H}_2\text{O})_5\text{CrO}_2^{2+}$, a dioxygen adduct similar to $(\text{H}_2\text{O})\text{Co}([\text{14}] \text{aneN}_4)\text{O}_2^{2+}$, has been recently characterized making possible a further investigation into the chemistry of transition-metal dioxygen adducts.

In the present study we report on the reaction chemistry of CrO_2^{2+} with various transition metal complexes in an effort to further the understanding of the process by which transition metals activate molecular oxygen. This understanding would certainly be an important stride towards the ultimate goal: to take advantage of the high oxidizing power of dioxygen in a controlled and selective manner.

In summary, the major objective of this research is to gain a better understanding of the chemistry of CrO_2^{2+} with various reductants to further the understanding of transition metal-dioxygen adducts.

EXPERIMENTAL SECTION

Materials

Dilute solutions of CrO_2^{2+} were prepared according to the literature procedure.⁴ The ligands, [14]aneN₄, [15]aneN₄, and meso-Me₆[14]aneN₄ were obtained from Strem Chemical Co. Samples of Co(meso-Me₆[14]aneN₄)(OH₂)₂(ClO₄)₂ and Co(tmc)(OH₂)(ClO₄)₂ were donated by S. Lee,⁵ the Co(sep)Cl₃ was a gift from A. M. Sargeson, and a standardized Fe(ClO₄)₃ solution was prepared by D. G. Kelley. The Ru(NH₃)₆Cl₃ was obtained from Aldrich Chemical Co.

Solutions of Co([14]aneN₄)(OH₂)₂²⁺ were prepared by mixing a 10% stoichiometric excess of the ligand with deaerated solutions of Co(ClO₄)₂. Sufficient HClO₄ was added after the reaction was complete to make the solution 0.10 M in acid. The concentration of the stock solution of Co([14]aneN₄)(OH₂)₂²⁺ was determined from the absorbance at 465 nm ($\epsilon = 22 \text{ M}^{-1}\text{cm}^{-1}$).⁶

Solutions of Co([15]aneN₄)(OH₂)₂²⁺ were prepared similarly and used at the natural pH since the cobalt(II) complex is demetallated by H₃O⁺. The concentration of the stock solution of Co([15]aneN₄)(OH₂)₂²⁺ was determined from the absorbance at 497 nm ($\epsilon = 13.9 \text{ M}^{-1}\text{cm}^{-1}$).⁷

The concentrations of the stock solutions of Co(meso-Me₆[14]aneN₄)(OH₂)₂²⁺ and Co(tmc)(OH₂)₂²⁺ were determined by the mass of the cobalt complexes dissolved in a given volume of H₂O.

Solutions of Co(sep)²⁺, Ru(NH₃)₆²⁺, and Fe²⁺ were prepared by a zinc-amalgam reduction of Co(sep)(ClO₄)₃, Ru(NH₃)₆Cl₃, and Fe(ClO₄)₃ respectively, in H₂O. The concentration of the reduced species was considered to be equal to that of the parent species. The concentration

of the $\text{Co}(\text{sep})^{3+}$ solution was determined from the measurement of the visible spectrum of the $\text{Co}(\text{sep})^{3+}$ stock solution at 470 nm ($\epsilon = 110 \text{ M}^{-1}\text{cm}^{-1}$).⁸

The stock solution of vanadium(IV) perchlorate was prepared by ion exchange (Dowex 50W - X8) of the sulfate. Vanadium(IV) was eluted with 1 M perchloric acid and standardized spectrophotometrically ($\lambda = 760 \text{ nm}$, $\epsilon = 17.2 \text{ M}^{-1}\text{cm}^{-1}$).⁹ The $\text{V}(\text{H}_2\text{O})_6^{2+}$ used in the experiments was prepared by a zinc-amalgam reduction of $\text{VO}(\text{ClO}_4)_2$ in 0.10 M HClO_4 .

Instrumentation

Routine UV-visible spectra were recorded on a Perkin-Elmer Lambda Array 3840 UV/VIS spectrophotometer. The kinetic measurements were made on a Durrum stopped-flow spectrophotometer interfaced with an OLIS 3820 Data System. Multiwavelength stopped-flow experiments used a George W. Gates Co. GID-25 rapid-scan monochromator which served as the light source when interfaced to the Durrum stopped-flow spectrophotometer. Unless stated otherwise, all the stopped-flow experiments were done under anaerobic conditions at 25 °C and with a cell path length of 2 cm. The single-wavelength kinetic measurements for the outer-sphere electron transfer reactions were monitored spectrophotometrically at the two maxima of CrO_2^{2+} , 247 nm ($\epsilon = 7400 \text{ M}^{-1}\text{cm}^{-1}$) and 290 nm ($\epsilon = 3100 \text{ M}^{-1}\text{cm}^{-1}$).¹⁰ The concentrations of the outer-sphere reductants were in pseudo-first-order excess relative to those of the CrO_2^{2+} . The observed rate constants for the reactions agree with each other; therefore, the calculated second-order rate constants are based on data collected at both wavelengths. Analysis of the kinetic traces was done using standard first-order, second-order, and biexponential routines on the OLIS computer system.

RESULTS

Outer-sphere electron transfer reactions

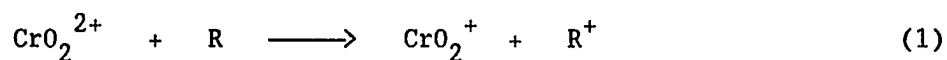
The reactions are first-order in $[\text{CrO}_2^{2+}]$ and $[\text{R}]$, ($[\text{R}] = \text{Ru}(\text{NH}_3)_6^{2+}$, $\text{Co}(\text{sep})^{2+}$, and $\text{V}(\text{H}_2\text{O})_6^{2+}$). They exhibit a modest rate acceleration with increasing acid concentrations and a slight rate decrease due to increasing ionic strength, Table II-1. There is no effect on the observed rate constant due to chloride in the concentration range $3 \times 10^{-4} \text{ M} - 0.05 \text{ M}$ for the reaction of CrO_2^{2+} with $\text{Ru}(\text{NH}_3)_6^{2+}$; therefore, the chloride dependence for the reaction of CrO_2^{2+} with $\text{Co}(\text{sep})^{2+}$ or V^{2+} was not studied. No spectroscopic evidence for an intermediate was obtained in any of the reactions.

The absorbances at 290 and 247 nm decrease during the reaction of CrO_2^{2+} with $\text{Ru}(\text{NH}_3)_6^{2+}$ and V^{2+} ; whereas they decrease at 290 nm but increase at 247 nm during the reaction of CrO_2^{2+} with $\text{Co}(\text{sep})^{2+}$. The decreasing absorbance-time traces represent the direct observation of the consumption of CrO_2^{2+} during the reaction since the other species in solution absorb very little light relative to the CrO_2^{2+} at 247 and 290 nm. At 247 nm, $\text{Co}(\text{sep})^{3+}$ is a strongly absorbing species ($\epsilon \sim 14000 \text{ M}^{-1} \text{ cm}^{-1}$) resulting in an increasing absorbance as the reaction of CrO_2^{2+} with $\text{Co}(\text{sep})^{2+}$ produces $\text{Co}(\text{sep})^{3+}$. The change in absorbance at 247 nm suggests a 1:1 stoichiometry for the reaction of CrO_2^{2+} with $\text{Co}(\text{sep})^{2+}$. The UV spectrum of the products of the reaction is consistent with the formation of $\text{Co}(\text{sep})^{3+}$.

Kinetic data was obtained at $\mu = [\text{H}_3\text{O}^+] = 0.100 \text{ M}$ and $T = 25.0 \text{ }^\circ\text{C}$. The results are consistent with an outer-sphere reaction mechanism as outlined in Scheme II-1. Figure II-1 illustrates the three plots of k_{obs}

vs. $[R]_{\text{ave}}$ suggested by equation 3. A least-squares analysis yielded second-order rate constants for the three reagents $\text{Ru}(\text{NH}_3)_6^{2+}$, $\text{Co}(\text{sep})^{2+}$ and V^{2+} as $(9.5 \pm 0.2) \times 10^5 \text{ M}^{-1}\text{s}^{-1}$, $(8.5 \pm 0.2) \times 10^5 \text{ M}^{-1}\text{s}^{-1}$ and $(2.28 \pm 0.05) \times 10^5 \text{ M}^{-1}\text{s}^{-1}$ respectively.

Scheme II-1. Simple Outer-Sphere Mechanism



$$\frac{-d[\text{CrO}_2^{2+}]}{dt} = k_1[\text{CrO}_2^{2+}][\text{R}]_{\text{ave}} \quad (2)$$

$$k_{\text{obs}} = k_1[\text{R}]_{\text{ave}} \quad (3)$$

A more complex reaction mechanism is suggested by the acid dependence, Table II-1, features CrO_2^{2+} and $\text{CrO}_2\text{H}^{3+}$ reacting in parallel reaction pathways, Scheme II-2. The concentration of CrO_2^{2+} and $\text{CrO}_2\text{H}^{3+}$ is controlled by the acid dependent equilibrium, equation 4. A least-squares analysis of the data suggested by equation 9 yields an estimate for k_5 and k_6 for each reaction, Table II-2, and an estimate for K_a ($K_a \sim 0.54 \text{ M}$).

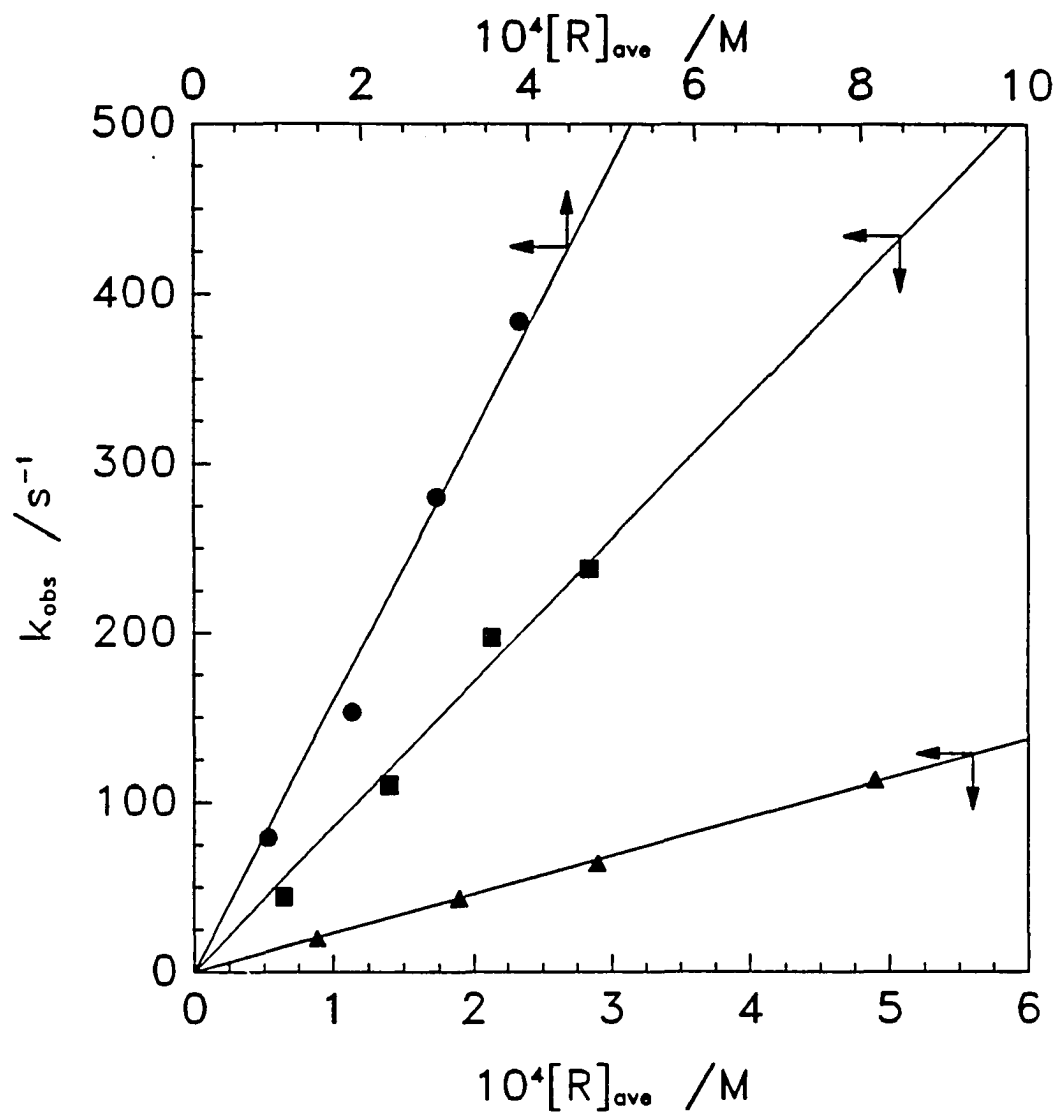
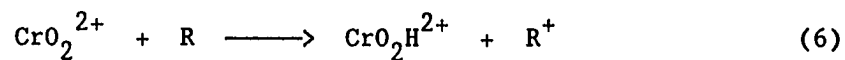
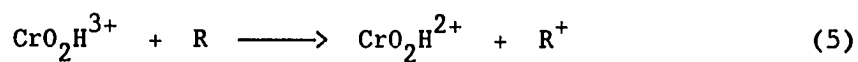
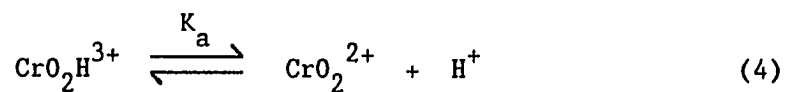


Figure II-1. Dependence of k_{obs} on $[R]_{\text{ave}}$, ($\text{HClO}_4 = 0.100 \text{ M}$, $\mu = 0.10$, $T = 25.0 \text{ }^\circ\text{C}$). $R = \text{Ru}(\text{NH}_3)_6^{2+}$ (circles), $\text{Co}(\text{sep})^{2+}$ (squares), $\text{V}(\text{OH}_2)_6^{2+}$ (triangles)

Scheme II-2. Complete Outer-Sphere Mechanism



$$\frac{-d[\text{R}]}{dt} = \left(\frac{k_6 K_a + k_5 [\text{H}^+]}{K_a + [\text{H}^+]} \right) [\text{R}]_{\text{ave}} [\text{Cr}]_{\text{T}} \quad (7)$$

$$k_{\text{obs}} = \left(\frac{k_6 K_a + k_5 [\text{H}^+]}{K_a + [\text{H}^+]} \right) [\text{R}]_{\text{ave}} \quad (8)$$

$$k_{\text{app}} = \frac{k_{\text{obs}}}{[\text{R}]_{\text{ave}}} = \left(\frac{k_6 K_a + k_5 [\text{H}^+]}{K_a + [\text{H}^+]} \right) \quad (9)$$

Table II-1. Summary of the Acid Dependence for the Outer-Sphere Reactions

[H ₃ O ⁺] ^b	Reductant k _{app} (M ⁻¹ s ⁻¹) ^a		
	Ru(NH ₃) ₆ ²⁺	Co(sep) ²⁺	V(H ₂ O) ₆ ²⁺
0.10	1.9 X 10 ⁵	4.3 X 10 ⁵	2.0 X 10 ⁵
0.23	3.0 X 10 ⁵	-	-
0.35	-	6.9 X 10 ⁵	2.5 X 10 ⁵
0.55	-	8.9 X 10 ⁵	-
1.00	5.7 X 10 ⁵	-	2.9 X 10 ⁵
0.10 ^c	(9.5 ± 0.2) X 10 ⁵	(8.5 ± 0.2) X 10 ⁵	(2.28 ± 0.05) X 10 ⁵

^ak_{app} = k_{obs}/[R].

^bμ = 1.00 M.

^cμ = 0.10 M, T = 25.0 °C; data covered a range of [R] as shown in Figure II-1.

Table II-2. Kinetic Parameters for the Outer-Sphere Reactions^a

Reductant	$k_5 / \text{M}^{-1}\text{s}^{-1}$	$k_6 / \text{M}^{-1}\text{s}^{-1}$	K_a / M
$\text{Ru}(\text{NH}_3)_6^{2+}$	8.4×10^5	6.9×10^4	0.54
$\text{Co}(\text{sep})^{2+}$	1.5×10^6	2.2×10^6	0.54^b
	-	-	- ^c
$\text{V}(\text{H}_2\text{O})_6^{2+}$	3.6×10^5	1.7×10^5	0.54^b
	3.3×10^5	1.6×10^5	0.30

^a $\mu = 1.00 \text{ M}$; $T = 25.0 \text{ }^\circ\text{C}$; all parameters were floated in the calculation unless otherwise noted.

^bA fixed parameter in the calculation.

^cConvergence was not possible when the K_a parameter was floated.

Inner-sphere electron transfer reactions

Reaction between CrO_2^{2+} and $\text{Fe}(\text{OH}_2)_6^{2+}$ A biexponential reaction is observed with a rapid consumption of CrO_2^{2+} signaled by the absorbance changes. Once the effect of HCrO_4^- is allowed for (see next paragraph), it became evident that the reaction of interest gives rise to a decrease in the absorbance at 290 nm (first stage) and a slower increase in the absorbance at 240 nm (second stage). The consumption of CrO_2^{2+} was monitored at 290 nm, and the formation of Fe^{3+} at 240 nm, Figure II-2. The experiments were done with Fe^{2+} in pseudo-first-order excess ($\mu = 0.100 \text{ M}$, $\text{HClO}_4 = 0.100 \text{ M}$, $T = 25.0 \text{ }^\circ\text{C}$) under aerobic or anaerobic conditions. All of the initial experiments were done anaerobically; however, since the concentration of dissolved dioxygen did not affect the reaction (Fe^{2+} does not react rapidly with dioxygen), control of the oxygen concentration was not attempted in later experiments.

In the anaerobic experiments the CrO_2^{2+} solution was about five minutes. This time is sufficient a build up of the HCrO_4^- concentration to $\leq 5 \times 10^{-6} \text{ M}$.⁴ The amount of HCrO_4^- in solution at a given time depends on the age of the CrO_2^{2+} solution and initial concentrations of dioxygen and CrO_2^{2+} .⁴ The presence of HCrO_4^- , formed as a minor but significant byproduct during the decomposition of CrO_2^{2+} , can account for the second of two reaction stages observed at 290 nm and the first of two reaction stages observed at 240 nm. This assignment is based on a previous study of the $\text{HCrO}_4^-/\text{Fe}(\text{II})$ system,¹¹ confirmed by blank experiments with genuine HCrO_4^- .

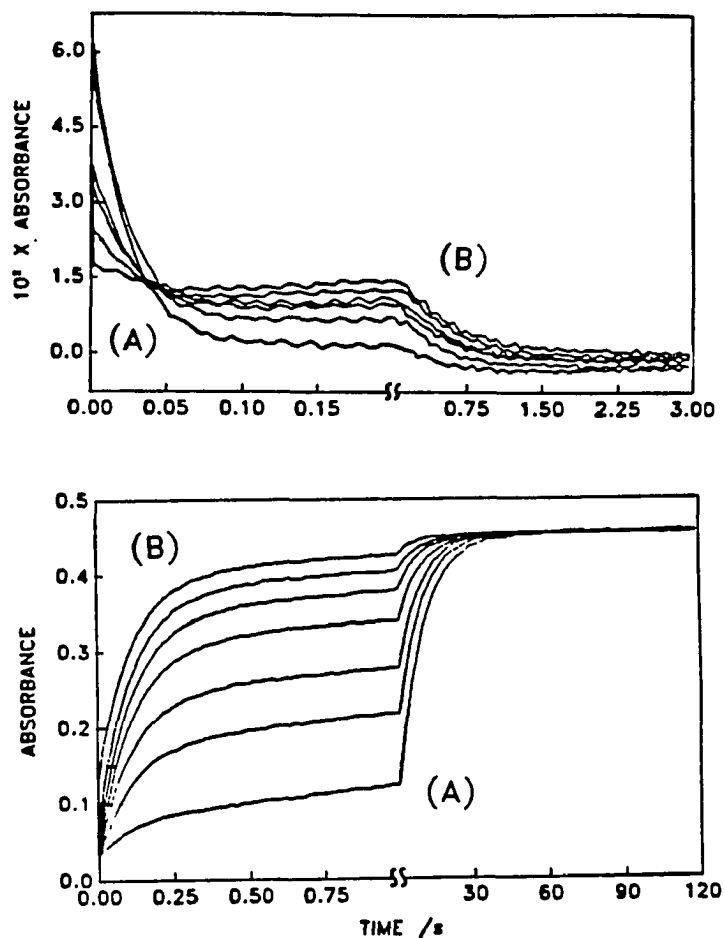


Figure II-2. The reaction between CrO_2^{2+} and Fe^{2+} was followed by recording a family of absorbance-time profiles. The first fifty data points of the upper figure (290 nm) were collected in 0.2 seconds and the second fifty collected in 2.8 seconds. The first fifty data points of the lower figure (240 nm) were collected in 1 second and the second fifty collected in 119 seconds. The family of traces results from stopped-flow experiments performed on the same solution at various times over a 2 hr period ($t = 0$ hr (A), $t = 2$ hr (B))

The first stage at 290 nm and the second stage at 240 nm can be assigned to the reaction system of interest, $\text{CrO}_2^{2+}/\text{Fe(II)}$. The overall absorbance change observed at 240 nm suggests that one molecule of CrO_2^{2+} oxidizes three molecules of Fe^{2+} to Fe^{3+} . The data also suggest that an intermediate is formed which has a molar absorptivity on the order of 6000 - 7000 $\text{M}^{-1}\text{cm}^{-1}$ at 240 nm. This estimate is based on absorbance-wavelength profiles which indicate upon completion of the first stage observed at 290 nm, the absorbance change at 240 nm is zero. Assuming the reaction of CrO_2^{2+} and Fe^{2+} accounts for the first stage at 290 nm and the change in absorbance is due to the consumption of CrO_2^{2+} , a negligible absorbance change at 240 nm indicates that a product of this reaction absorbs light to the same extent as the reactant CrO_2^{2+} ($\sim 6800 \text{ M}^{-1}\text{cm}^{-1}$) masking the detection of the first stage assigned to the reaction of CrO_2^{2+} and Fe^{2+} at 240 nm.

The formation of an intermediate in the reaction of CrO_2^{2+} and Fe^{2+} can be confirmed by the observation of a transient species which exhibits an absorption peak at 320 nm, Figure II-3. The $\text{CrO}_2\text{Fe}^{4+}$ is proposed to decompose as in equation 11, owing to the substitutional lability of Fe(III) . Thus, the intermediate observed at 320 nm is assigned to CrO_2^+ . The molar absorptivity of this species is estimated to be 1300 $\text{M}^{-1}\text{cm}^{-1}$ assuming it is formed in a 1:1 stoichiometric reaction of CrO_2^{2+} and Fe^{2+} . The formation of this species is clearly shown in Figure II-3. The absorbance at 320 nm decreases with a first-order rate constant equal to the first-order rate constant for the formation of the species observed at 240 nm. The lifetime of the species observed at 320 nm is greatly increased in the absence of Fe^{2+} and greatly decreased in the presence of

excess Fe^{2+} . The fact that the rate constant for the reaction of this intermediate with Fe^{2+} observed at 320 nm is equal within the experimental error to the rate constant for the formation of Fe^{3+} at 240 nm implies that the intermediate reacts with Fe^{2+} to form Fe^{3+} .

The reaction at 290 nm was independent of $[\text{H}_3\text{O}^+]$ in the concentration range, $[\text{H}_3\text{O}^+] = 0.010 - 0.10 \text{ M}$ and first-order in $[\text{Fe}^{2+}]$ and $[\text{CrO}_2^{2+}]$. The observed absorbance of HCrO_4^- -free solutions at 290 nm was about 50% of the calculated value, suggesting that an absorbing species was formed as a product of the reaction of CrO_2^{2+} and Fe^{2+} . The results are consistent with an inner-sphere reaction mechanism as outlined in Scheme II-3. Equation 10 is proposed for the first reaction stage of the $\text{CrO}_2^{2+}/\text{Fe}^{2+}$ system. It is a simple bimolecular inner-sphere reaction between CrO_2^{2+} and Fe^{2+} resulting in the formation of the binuclear intermediate $\text{CrO}_2\text{Fe}^{4+}$. Figure II-4 illustrates a plot of k_{obs} vs. $[\text{Fe}^{2+}]_{\text{ave}}$ for the reaction of CrO_2^{2+} and Fe^{2+} suggested by equation 13. A least-squares analysis yields a second-order rate constant, $k_{10} = (2.45 \pm 0.05) \times 10^4 \text{ M}^{-1}\text{s}^{-1}$ ($\mu = 0.100 \text{ M}$, $\text{HClO}_4 = 0.100 \text{ M}$, $T = 25.0 \text{ }^\circ\text{C}$).

The reaction observed at 240 nm assigned to the $\text{CrO}_2^{2+}/\text{Fe}^{2+}$ system was independent of $[\text{H}_3\text{O}^+]$ in the concentration range $[\text{H}_3\text{O}^+] = 0.010 - 0.10 \text{ M}$, and first-order in $[\text{Fe}^{2+}]$. The results for this reaction stage are consistent with equations 14 and 15. Figure II-4 illustrates a plot of k_{obs} vs. $[\text{Fe}^{2+}]_{\text{ave}}$ suggested by equation 18. A least-squares analysis yields a second-order rate constant for the reaction of the intermediate and Fe^{2+} , $k_{14} = 60 \pm 2 \text{ M}^{-1}\text{s}^{-1}$ ($\mu = 0.100 \text{ M}$, $\text{HClO}_4 = 0.100 \text{ M}$, $T = 25.0 \text{ }^\circ\text{C}$).

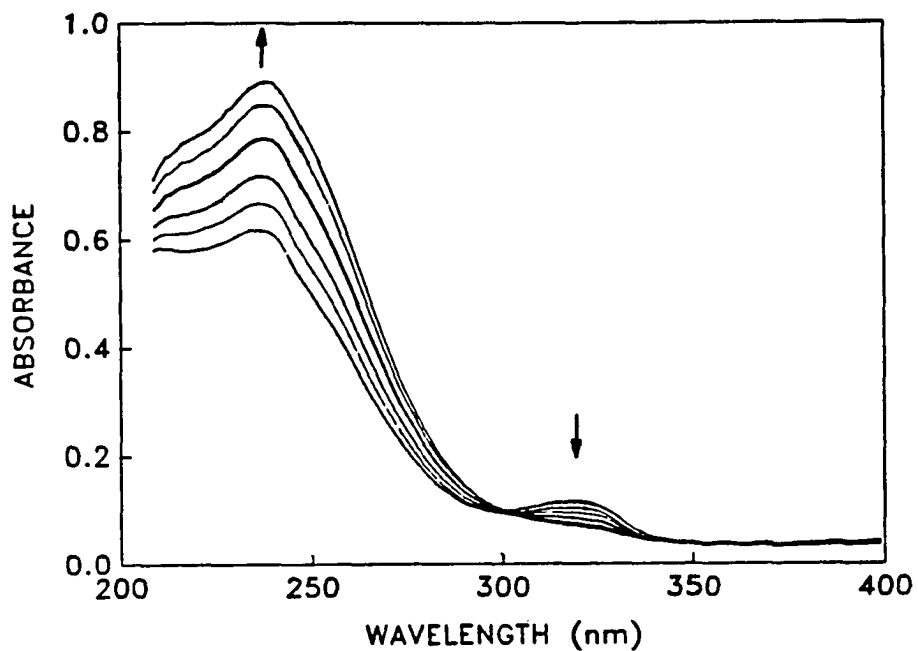


Figure II-3. The reaction between CrO_2^{2+} and Fe^{2+} was followed by recording the absorbance-wavelength profiles. The absorbance at 320 nm decreases with a first-order rate constant (0.012 s^{-1}) similar to the rate constant of the increase in absorbance at 240 nm (0.011 s^{-1}). This family of spectra represent a total collection time of 430 seconds ($[\text{H}_3\text{O}^+] = 0.100 \text{ M}$, $\mu = 0.10 \text{ M}$, $T = 25.0 \text{ }^\circ\text{C}$, $[\text{CrO}_2^{2+}]_0 = 3.2 \times 10^{-5} \text{ M}$, and $[\text{Fe}^{2+}]_0 = 2.5 \times 10^{-4} \text{ M}$)

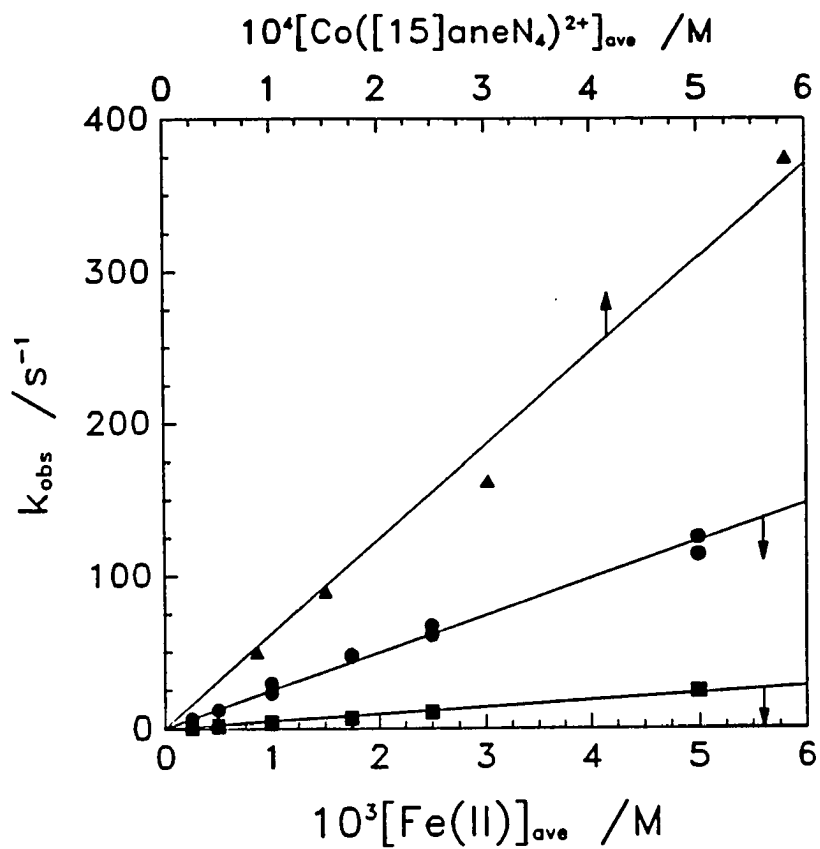
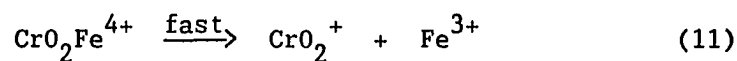
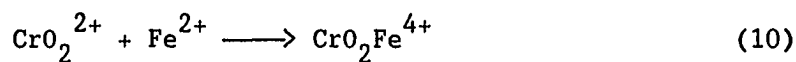


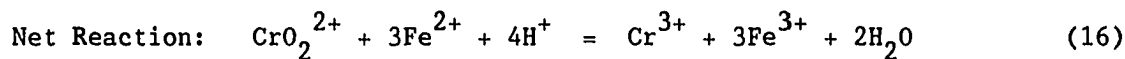
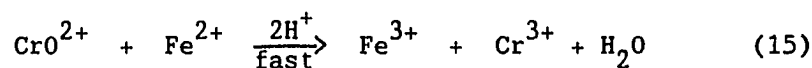
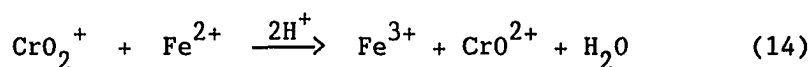
Figure II-4. The dependence of k_{obs} on $[\text{Fe}^{2+}]_{\text{ave}}$ (first stage, circles), the dependence of k_{obs} on $[\text{Fe}^{2+}]_{\text{ave}}$ (second stage, squares), and the dependence of k_{obs} on $[\text{Co}([15]\text{aneN}_4)^{2+}]_{\text{ave}}$ (triangles), ($[\text{H}_3\text{O}^+] = 0.100 \text{ M}$, $\mu = 0.10 \text{ M}$, $T = 25.0 \text{ }^\circ\text{C}$)

Scheme II-3. CrO_2^{2+} and Fe^{2+} Reaction Mechanism



$$\frac{-d[\text{CrO}_2^{2+}]}{dt} = k_{10}[\text{CrO}_2^{2+}][\text{Fe}^{2+}] \quad (12)$$

$$k_{\text{obs}} = k_{10}[\text{Fe}^{2+}]_{\text{ave}} \quad (13)$$



$$\frac{-d[\text{CrO}_2^+]}{dt} = k_{14}[\text{CrO}_2^+][\text{Fe}^{2+}] \quad (17)$$

$$k_{\text{obs}} = k_{14}[\text{Fe}^{2+}]_{\text{ave}} \quad (18)$$

Reactions of CrO_2^{2+} with $\text{Co}([\text{14}] \text{aneN}_4)(\text{OH}_2)_2^{2+}$ and $\text{Co}([\text{15}] \text{aneN}_4)(\text{OH}_2)_2^{2+}$ The UV-vis reaction profiles recorded in the multiwavelength stopped-flow experiments indicated multiphasic kinetics for both reactions. A rapid rise in the absorbance of the reaction mixture from 240 - 400 nm with a maximum centered around 250 nm is observed as the first stage in each system. The reaction profile for CrO_2^{2+} with $\text{Co}([\text{14}] \text{aneN}_4)(\text{OH}_2)_2^{2+}$ is shown in Figure II-5 and the reaction profiles for the reaction of CrO_2^{2+} with $\text{Co}([\text{15}] \text{aneN}_4)(\text{OH}_2)_2^{2+}$ are shown in Figure II-6. Additional reaction stages are observed which have decreasing absorbances from 260 - 400 nm with maxima centered around 320 nm.

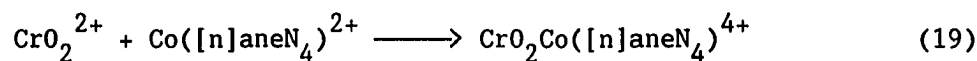
The reactions were monitored spectrophotometrically in single wavelength stopped-flow experiments at 320 nm. Since CrO_2^{2+} does not absorb light at 320 nm, the kinetic experiments follow a rising absorbance assigned to the formation of an intermediate (first stage). The subsequent decomposition of this intermediate to the final products (second and third stages) are also observed in much slower time scales.

The first reaction stage, equation 19 ($n = 14$), is very rapid for the reaction of CrO_2^{2+} with $\text{Co}([\text{14}] \text{aneN}_4)(\text{OH}_2)_2^{2+}$. Efforts to lower the observed rate by lowering the concentration of the excess reagent, $\text{Co}([\text{14}] \text{aneN}_4)(\text{OH}_2)_2^{2+}$ were not feasible due to the experimental uncertainty associated with the handling of the extremely oxygen sensitive $\text{Co}([\text{14}] \text{aneN}_4)(\text{OH}_2)_2^{2+}$ at the very low (10^{-5} M) concentration levels. A single kinetic measurement indicates that the rate constant for the reaction between $\text{Co}([\text{14}] \text{aneN}_4)(\text{OH}_2)_2^{2+}$ and CrO_2^{2+} is $k \sim 7 \times 10^6 \text{ M}^{-1}\text{s}^{-1}$ ($\mu = 0.100 \text{ M}$, $\text{HClO}_4 = 0.100 \text{ M}$, $T = 25.0 \text{ }^\circ\text{C}$).

The second and third reaction stages equation 22, are observed as decreasing first-order absorbance-time traces at 320 nm. The second stage has an observed rate constant of 2.5 s^{-1} and the third 0.064 s^{-1} ($\mu = 0.100 \text{ M}$, $\text{HClO}_4 = 0.100 \text{ M}$, $T = 25.0 \text{ }^\circ\text{C}$). Very little is known about these stages due to the limited number of experiments performed, and as such the other reaction in Scheme II-4 must be regarded only as an internally consistent and reasonable proposal.

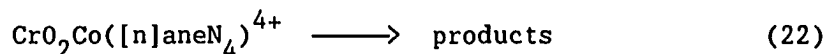
An inner-sphere reaction mechanism can be proposed for the first stage which is consistent with the data, Scheme II-4. This proposed mechanism is supported by the observation of an intermediate, and by the known, rapid, axial-ligand substitution properties of $\text{Co}([\text{14}] \text{aneN}_4)(\text{OH}_2)_2^{2+}$ and consistent with the known reaction chemistry of $\text{Co}([\text{14}] \text{aneN}_4)(\text{OH}_2)_2^{2+}$.²

Scheme II-4. CrO_2^{2+} and $\text{Co}([\text{n}] \text{aneN}_4)(\text{OH}_2)_2^{2+}$ Reaction Mechanism



$$\frac{-d[\text{CrO}_2^{2+}]}{dt} = k_{19}[\text{CrO}_2^{2+}][\text{Co}([\text{n}] \text{aneN}_4)^{2+}] \quad (20)$$

$$k_{\text{obs}} = k_{19}[\text{Co}([\text{n}] \text{aneN}_4)^{2+}]_{\text{ave}} \quad (21)$$



$$\frac{-d[\text{CrO}_2\text{Co}([\text{n}] \text{aneN}_4)^{4+}]}{dt} = k_{22}[\text{CrO}_2\text{Co}([\text{n}] \text{aneN}_4)^{4+}] \quad (23)$$

$$k_{\text{obs}} = k_{22} \quad (n = 14, 15) \quad (24)$$

The data for the reaction of CrO_2^{2+} with $\text{Co}([\text{15}] \text{aneN}_4)(\text{OH}_2)_2^{2+}$ are consistent with the inner-sphere reaction mechanism outlined in Scheme II-4. The observation of an intermediate coupled with the known, rapid, axial-ligand substitution properties of $\text{Co}([\text{15}] \text{aneN}_4)(\text{OH}_2)_2^{2+}$ provides support for the proposed mechanism.

The first reaction stage, equation 19 ($n = 15$), is first-order in $[\text{CrO}_2^{2+}]$ and $[\text{Co}([\text{15}] \text{aneN}_4)(\text{OH}_2)_2^{2+}]$. The reaction is also independent of $[\text{H}^+]$ in the range 0.08 - 0.50 M HClO_4 . Figure II-4 illustrates a plot of k_{obs} vs. $[\text{Co}([\text{15}] \text{aneN}_4)(\text{OH}_2)_2^{2+}]_{\text{ave}}$ suggested by equation 21. A least-squares analysis yields a rate constant for the reaction between CrO_2^{2+} and $\text{Co}([\text{15}] \text{aneN}_4)(\text{OH}_2)_2^{2+}$, $k = (6.2 \pm 0.3) \times 10^5 \text{ M}^{-1}\text{s}^{-1}$ ($\mu = 0.100 \text{ M}$, $\text{HClO}_4 = 0.100 \text{ M}$, $T = 25.0 \text{ }^\circ\text{C}$).

The second reaction stage is independent of $[\text{CrO}_2^{2+}]$, $[\text{Co}([\text{15}] \text{aneN}_4)(\text{OH}_2)_2^{2+}]$ and independent of $[\text{H}_3\text{O}^+]$ in the range 0.08 - 0.50 M HClO_4 . An average value for the first-order rate constants for the second stage, equation 22, is $k = 0.48 \pm 0.02 \text{ s}^{-1}$ ($\mu = 0.100 \text{ M}$, $\text{HClO}_4 = 0.100 \text{ M}$, $T = 25.0 \text{ }^\circ\text{C}$).

Other Reactions of CrO_2^{2+} Limited studies have been made of the reaction between CrO_2^{2+} and $\text{Co}(\text{tmc})^{2+}$. No reaction was detected apart from the known, rapid decomposition of $\text{Co}(\text{tmc})^{2+}$ in the acidic medium (0.10 M HClO_4).

The reaction of CrO_2^{2+} and $\text{Co}(\text{meso-Me}_6[\text{14}] \text{aneN}_4)^{2+}$ was also investigated. A UV-vis profile recorded in the multiwavelength stopped-flow experiments indicated a rapid increase in the absorbance in the wavelength range 240 - 320 nm, Figure II-7 (upper figure). A second reaction stage

is observed which has a decreasing absorbance from 290 - 400 nm and a maximum centered around 340 nm, Figure II-7 (lower figure). The multiwavelength stopped-flow experiments indicate 300 nm as an adequate wavelength for the observation of the first reaction stage and 340 nm as an ideal wavelength to observe both the first and second reaction stages. The observed rate constant for the first reaction stage observed at 300 nm and 340 nm is independent of the concentration of the excess reagent, $\text{Co(meso-Me}_6[14]\text{aneN}_4)(\text{OH}_2)_2^{2+}$, with average first-order rate constants of 13 s^{-1} at 300 nm and 21 s^{-1} at 340 nm ($\mu = 0.100 \text{ M}$, $\text{HClO}_4 = 0.100 \text{ M}$, $T = 25.0 \text{ }^\circ\text{C}$). The second reaction stage is also independent of the concentration of the $\text{Co(meso-Me}_6[14]\text{aneN}_4)(\text{OH}_2)_2^{2+}$. The observed average rate constant is 0.10 s^{-1} at 340 nm ($\mu = 0.100 \text{ M}$, $\text{HClO}_4 = 0.100 \text{ M}$, $T = 25.0 \text{ }^\circ\text{C}$). No variation of the acid concentration was attempted.

Several experiments were conducted to understand the unusual kinetic results. The concentration of the limiting reagent, CrO_2^{2+} , was lowered to 20% of the previous experimental value ($2.5 \times 10^{-5} \text{ M}$ to $0.5 \times 10^{-5} \text{ M}$). The change in the absorbance decreased as expected; however, the observed rate constant of the first reaction stage was still independent of the concentration of the $\text{Co(meso-Me}_6[14]\text{aneN}_4)(\text{OH}_2)_2^{2+}$, with an observed rate constant agreeing with the previous experiments.

The concentration of both reagents was lowered to a very low but equal concentration ratio, $[\text{Co(meso-Me}_6[14]\text{aneN}_4)(\text{OH}_2)_2^{2+}] \approx [\text{CrO}_2^{2+}] \approx 5 \times 10^{-6} \text{ M}$. The observed rate constant for the first stage was 104 s^{-1} at 250 nm and the second stage was not detected due to the very small absorbance change at 340 nm. When the concentration of the $\text{Co(meso-Me}_6[14]\text{aneN}_4)(\text{OH}_2)_2^{2+}$ was raised to 1×10^{-5} while the concentration of

CrO_2^{2+} was 5×10^{-6} M, the absorbance change doubled and the observed rate constant for the first stage decreased to 55 s^{-1} . The data suggest that as the concentration of the excess reagent, $\text{Co}(\text{meso-Me}_6[14]\text{aneN}_4)(\text{OH}_2)_2^{2+}$, is increased, the observed rate constant will decrease until it reaches a limiting value of $\sim 13 \text{ s}^{-1}$ ($\mu = 0.100 \text{ M}$, $\text{HClO}_4 = 0.100 \text{ M}$, $T = 25.0 \text{ }^\circ\text{C}$). At present no reasonable mechanism can be proposed.

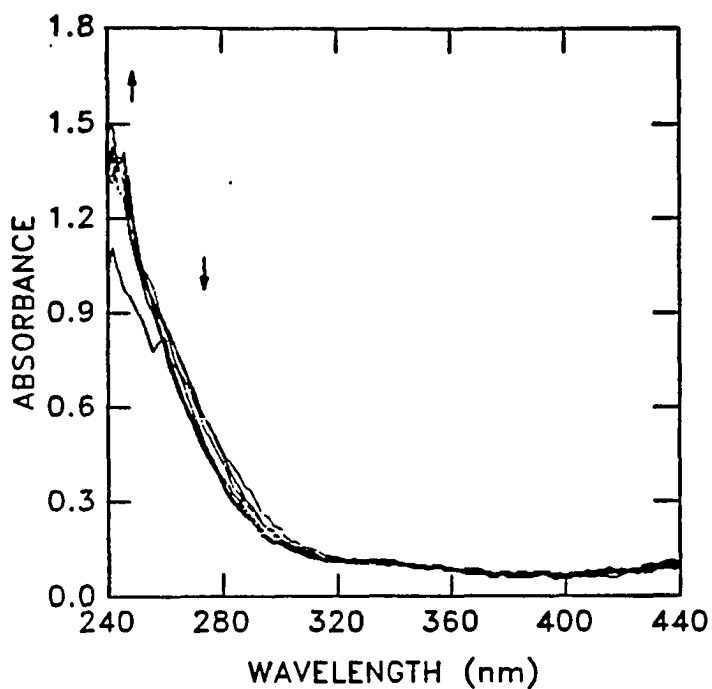


Figure II-5. The UV-vis reaction profile for the reaction between CrO_2^{2+} and $\text{Co}([\text{14}]\text{aneN}_4)(\text{OH}_2)_2^{2+}$, $[\text{Co}([\text{14}]\text{aneN}_4)(\text{OH}_2)_2^{2+}]_0 = 1.0 \times 10^{-4} \text{ M}$, $[\text{CrO}_2^{2+}] = 2.0 \times 10^{-5} \text{ M}$, $\text{HClO}_4 = 0.100 \text{ M}$, and $\mu = 0.10 \text{ M}$, the spectra were collected in 1 second

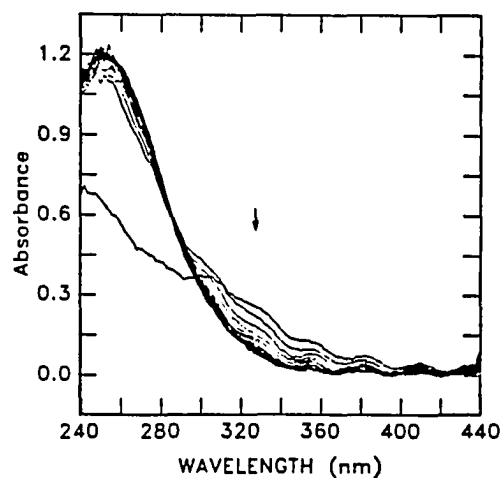
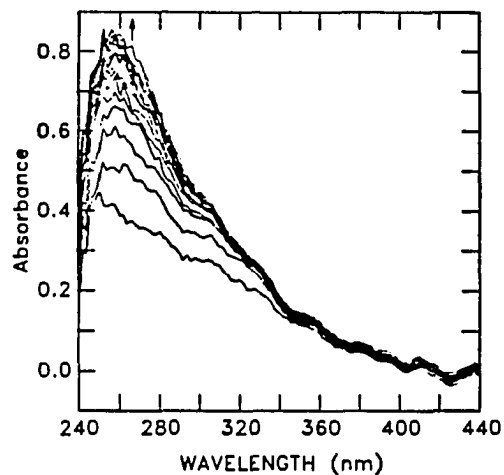


Figure II-6. The UV-vis reaction profiles for the reaction between CrO_2^{2+} and $\text{Co}([\text{15}] \text{aneN}_4)(\text{OH}_2)_2^{2+}$, $[\text{Co}([\text{15}] \text{aneN}_4)(\text{OH}_2)_2^{2+}]_0 = 1.5 \times 10^{-4} \text{ M}$, $[\text{CrO}_2^{2+}]_0 = 2.0 \times 10^{-5} \text{ M}$, $\text{HClO}_4 = 0.100 \text{ M}$, and $\mu = 0.10 \text{ M}$. The upper figure illustrates 16 spectra collected in 1 second. The lower figure illustrates 16 spectra collected in 10 seconds

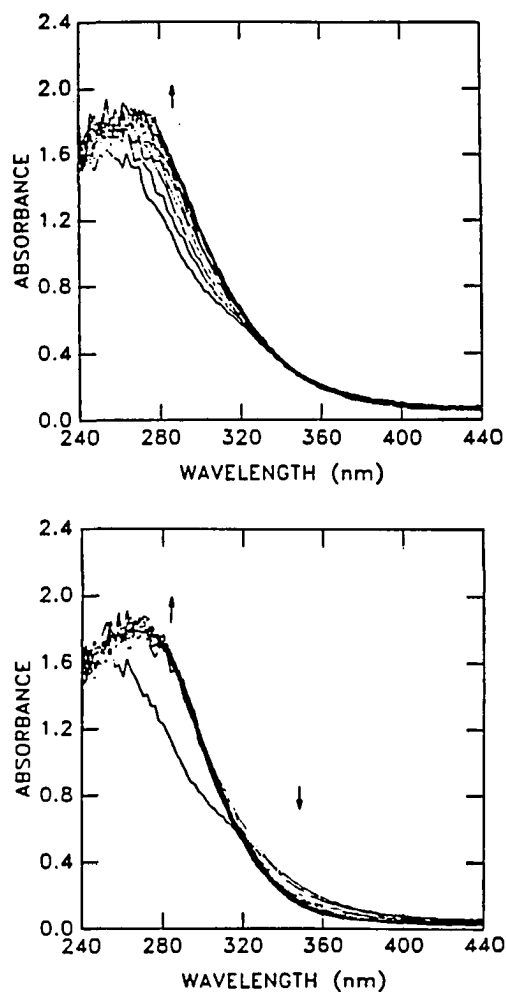


Figure II-7. The UV-vis reaction profile for the reaction between CrO_2^{2+} and $\text{Co}(\text{meso-Me}_6[14]\text{aneN}_4)(\text{OH}_2)_2^{2+}$, $[\text{Co}(\text{meso-Me}_6[14]\text{aneN}_4)(\text{OH}_2)_2^{2+}]_0 = 1.8 \times 10^{-4} \text{ M}$, $[\text{CrO}_2^{2+}]_0 = 2.0 \times 10^{-5} \text{ M}$, $\text{HClO}_4 = 0.100 \text{ M}$, and $\mu = 0.10 \text{ M}$. The upper figure illustrates 16 spectra collected in 0.35 seconds. The lower figure illustrates 16 spectra collected in 60 seconds

DISCUSSION

The simple electron transfer reactions of the dioxygen ligand in CrO_2^{2+} are considered to proceed by an outer-sphere reaction pathway when ligand substitution for the reducing agent is slow in comparison to the observed rates of electron transfer. Reducing agents which feature ligand substitution rates in excess of the observed electron transfer rates can react utilizing inner-sphere reaction pathways. If sufficient product stability exists for these inner-sphere reactions, adduct formation (μ - peroxy intermediates) usually dominates.^{2c}

Outer-sphere reactions

The general outer-sphere mechanism proposed for the reactions of CrO_2^{2+} with an outer-sphere reducing agent R, includes the protonation of CrO_2^{2+} equations 4 - 6. This acid dissociation equilibrium is included in mechanistic Scheme II-2 to explain the modest acid and ionic strength dependence observed for these reactions.

Equation 1 is analogous to the mechanism proposed to explain the modest acid dependence observed for the reaction of $\text{Co}([\text{14}] \text{aneN}_4)(\text{OH}_2)\text{O}_2^{2+}$ with the outer-sphere reductant $\text{Ru}(\text{NH}_3)_6^{2+}$.^{2c} This simple description of the reaction mechanism does not adequately explain the acid and ionic strength dependence observed for these reactions. Scheme II-2 includes an acid dissociation equilibrium, equation 4. The ionic strength and acid dependence of this equilibrium is such that with increasing ionic strength or acid concentrations, the equilibrium will shift to the left resulting in an increasing concentration of $\text{CrO}_2\text{H}^{3+}$ relative to CrO_2^{2+} . The net result is an increase in the observed rate of reaction because the

reaction pathway utilizing the more reactive $\text{CrO}_2\text{H}^{3+}$ begins to dominate. Since these outer-sphere reductions are only modestly dependent on the acid concentration, the pK_a for $\text{CrO}_2\text{H}^{3+}$ must be less than 1. A calculation of the K_a for $\text{CrO}_2\text{H}^{3+}$ based on the limited acid dependent data yields an estimate for the pK_a ($K_a \sim 0.54$, therefore, $\text{pK}_a \sim 0.27$). The existence and higher electron transfer reactivity of $\text{CrO}_2\text{H}^{3+}$ relative to CrO_2^{2+} has been proposed in the related reaction with hydrazine.¹²

The ionic strength dependence is puzzling and is not explained by either Scheme II-1 or II-2. The ionic strength dependence predicted for the reaction of two positively charged ions by the Bronsted-Debye-Huckel relation,^{13,14} equation 25, indicates the rate constant for the reaction should increase as the ionic strength increases. The magnitude of this increase, however, cannot be accurately predicted by this relation at the high ionic strengths used in this study.

$$\log(k) = \log(k^\circ) + 2Z_a Z_b \mu^{1/2} / (1 + \mu^{1/2}) \quad (25)$$

There is no evidence for the back electron-transfer reaction, which would be represented by the reverse reaction of the general equation 1, since the kinetics show clean pseudo-first-order absorbance-time traces and no appreciable intercepts are noted. Therefore, the reaction proceeds cleanly to completion in all cases, with the reduction potential of $\text{Ru}(\text{NH}_3)_6^{3+}/\text{Ru}(\text{NH}_3)_6^{2+}$ (0.06 V)¹⁵ defining a lower limit for the $\text{CrO}_2^{2+}/\text{CrO}_2^{1+}(\text{H}^+)$ reduction potential.

It was not possible to evaluate the data using a Marcus theory correlation since the self-exchange rate constant for CrO_2^{2+} and the reduction potential for the $\text{CrO}_2^{2+}/\text{CrO}_2^+$ couple are not known. The

assignment of an outer-sphere electron transfer mechanism for the reactions of CrO_2^{2+} with $\text{Co}(\text{sep})^{2+}$, V^{2+} and $\text{Ru}(\text{NH}_3)_6^{2+}$ is, however, supported by a correlation of rate constants for the reactions of various oxidants with these three outer-sphere reductants. Tables II-3 and II-4 contain a summary of the kinetic data for various outer-sphere reactions with $\text{Co}(\text{sep})^{2+}$, V^{2+} , and $\text{Ru}(\text{NH}_3)_6^{2+}$. These oxidants were selected because the rate constants with all three reductants have been reported in the literature. The overall trend observed is that the reactions of oxidants with $\text{Co}(\text{sep})^{2+}$, V^{2+} , and $\text{Ru}(\text{NH}_3)_6^{2+}$ occur at similar rates and are usually within an order of magnitude of each other. These rates are controlled by the equilibrium constant of the reaction and the reduction potential of the species. In most cases, the reaction of the oxidants with $\text{Co}(\text{sep})^{2+}$ occurs with the highest rate constant and the reaction of the oxidants with V^{2+} , the lowest rate constant. The data for the reactions of CrO_2^{2+} or $\text{Co}([\text{14}] \text{aneN}_4)(\text{OH}_2)^{2+}$ with outer-sphere oxidants, Table II-3, agrees with this observed trend, supporting the assignment of outer-sphere reaction mechanisms.

The rate constants for the reactions of CrO_2^{2+} are consistently equal to or higher than those for reactions of the various oxidants cited in Tables II-3 and II-4. The data for $\text{Co}([\text{14}] \text{aneN}_4)(\text{OH}_2)\text{O}_2^{2+}$ is of special importance since this oxidant is a dioxygen adduct and most closely resembles CrO_2^{2+} in structure and reactivity. The higher rate constants for the CrO_2^{2+} reactions imply that the intrinsic barrier to electron transfer processes is lower for the CrO_2^{2+} with respect to the other oxidants cited.

Table II-3. Summary of Kinetic Data for Reductions of CrO_2^{2+} and $\text{Co}([\text{14}] \text{aneN}_4)(\text{OH}_2)\text{O}_2^{2+}$

Reductant	E^f , V (vs. NHE)	Oxidant $k / \text{M}^{-1}\text{s}^{-1}$	
		$(\text{H}_2\text{O})_5\text{CrO}_2^{2+}$ ^a	$\text{Co}([\text{14}] \text{aneN}_4)(\text{OH}_2)\text{O}_2^{2+}$ ^{2b}
$\text{Ru}(\text{NH}_3)_6^{2+}$	0.06 ^{2b}	$(9.5 \pm 0.2) \times 10^5$	$(2.3 \pm 0.1) \times 10^5$ ^a
$\text{Co}(\text{sep})^{2+}$	-0.30 ¹⁶	$(8.5 \pm 0.3) \times 10^5$	$\sim 10^6$ ^b
$\text{V}(\text{OH}_2)_6^{2+}$	-0.226 ¹⁷	$(2.3 \pm 0.1) \times 10^5$	$(1.8 \pm 0.3) \times 10^5$ ^a
$\text{Co}([\text{14}] \text{aneN}_4)^{2+}$	0.421 ¹⁸	$\sim 7 \times 10^6$	$(4.9 \pm 0.4) \times 10^5$ ^a
$\text{Co}([\text{15}] \text{aneN}_4)_2^{2+}$	0.65 ¹⁹	$(6.2 \pm 0.3) \times 10^5$	$(3.7 \pm 0.4) \times 10^4$ ^b
$\text{Fe}(\text{OH}_2)_6^{2+}$	0.74 ¹⁹	$(4.5 \pm 0.2) \times 10^3$	$(1.1 \pm 0.1) \times 10^3$ ^c
$\text{Cr}(\text{OH}_2)_6^{2+}$	-0.41 ¹⁹	$\sim 8 \times 10^8$ ⁴	-

^a $\text{HClO}_4 = 0.10 \text{ M}$, $\mu = 0.10 \text{ M}$, $T = 25.0 \text{ }^\circ\text{C}$.

^b $(\text{HClO}_4 + \text{NaClO}_4) = 0.1 \text{ M}$.

^c $\text{HClO}_4 = 0.1 \text{ M}$ and $\text{NaClO}_4 = 0.2 \text{ M}$.

Table II-4. Summary of Kinetic Data for Various Outer-Sphere Reactions

Oxidants	Reductants $k / M^{-1}s^{-1}$ (ionic strength)					
	Co(sep) ²⁺		V(H ₂ O) ₆ ²⁺		Ru(NH ₃) ₆ ²⁺	
Co(NH ₃) ₆ ³⁺	1.5 X 10 ⁻¹	(0.2 M) ²⁰	3.7 X 10 ⁻²	(0.2 M) ²¹	1.1 X 10 ⁻²	(0.2 M) ²²
Co(NH ₃) ₅ Cl ²⁺	5.8 X 10 ¹	(0.2 M) ²⁰	~5 X 10 ⁰	(1.0 M) ²¹	2.6 X 10 ²	(0.2 M) ²⁰
Co(en) ₃ ³⁺	5.0 X 10 ⁻²	(0.2 M) ²⁰	~2 X 10 ⁻⁴	(1.0 M) ²¹	~2 X 10 ⁻³	(0.2 M) ²⁰
Co(phen) ₃ ³⁺	4.8 X 10 ³	(0.2 M) ²⁰	3.8 X 10 ³	(1.0 M) ²³	9.3 X 10 ³	(0.2 M) ²⁰
Co(bpy) ₃ ³⁺	1.0 X 10 ⁴	(0.2 M) ²⁴	1.1 X 10 ³	(2.0 M) ²⁵	1.1 X 10 ⁴	(0.1 M) ²⁶
Ru(NH ₃) ₆ ³⁺	3.5 X 10 ⁴	(0.5 M) ²⁴	1.3 X 10 ³	(0.1 M) ²⁷	3 X 10 ³	(0.1 M) ²⁸

Inner-sphere reactions

Due to the similarity of the reaction chemistry of CrO_2^{2+} and $\text{Co}([\text{14}] \text{aneN}_4)(\text{OH}_2)\text{O}_2^{2+}$, several conclusions from the cobalt/dioxygen system should apply to the chromium/dioxygen system. Very rapid reactions are observed for both CrO_2^{2+} and $\text{Co}([\text{14}] \text{aneN}_4)(\text{OH}_2)\text{O}_2^{2+}$ with the same mild reducing agents. Detailed product analysis studies for reactions of $\text{Co}([\text{14}] \text{aneN}_4)(\text{OH}_2)\text{O}_2^{2+}$ with several mild reducing agents has shown these reactions to form metastable μ -peroxo complexes. The formation of the μ -peroxo adducts for these cases has been shown to make a large contribution to the overall free energy change, making adduct formation (inner-sphere pathway) the preferred reaction pathway.²⁹ This is also expected to be true for the inner-sphere reactions of CrO_2^{2+} with mild reducing agents.

CrO_2^{2+} has been suggested to react with Fe^{2+} , $\text{Co}([\text{14}] \text{aneN}_4)(\text{OH}_2)\text{O}_2^{2+}$ and $\text{Co}([\text{15}] \text{aneN}_4)(\text{OH}_2)\text{O}_2^{2+}$ by an inner-sphere mechanism. All three reactions form observed intermediates which have absorbance maxima at 320 nm. A presumably related species with a 320 nm maximum has been observed but not characterized in a previous study of the reaction of CrO_2^{2+} with N_2H_5^+ .¹² It was presumed to be a feature of subsequent chromium chemistry in that study and not directly related to the reaction of interest. A similar peak begins to form when $\text{Cr}(\text{OH}_2)_6^{3+}$ and H_2O_2 are allowed to stand and, given the complexity of the species found in chromium-peroxide reactions,³⁰ it would not be surprising that all these species have related chromophores.

The intermediates formed by the reaction of CrO_2^{2+} with Fe^{2+} , $\text{Co}([\text{14}] \text{aneN}_4)(\text{OH}_2)\text{O}_2^{2+}$ and $\text{Co}([\text{15}] \text{aneN}_4)(\text{OH}_2)\text{O}_2^{2+}$ are suggested to be analogous μ -peroxo adducts; however, these intermediates decompose by

various pathways. The CrO_2^+ , formed from the $\text{CrO}_2\text{Fe}^{4+}$ adduct, decomposes in a $[\text{Fe}^{2+}]$ dependent pathway, but the $\text{CrO}_2\text{Co}([\text{15}]\text{aneN}_4)(\text{OH}_2)_2^{2+}$ adduct does not decompose with a $[\text{Co}([\text{15}]\text{aneN}_4)(\text{OH}_2)_2^{2+}]$ dependent pathway. This is evidence in support of the labile ligand substitution of Fe(III) on the stopped-flow time scale ($3 \times 10^3 \text{ s}^{-1}$).³¹ This is suggested in equation 11, with the formation of a peroxo-chromium species, CrO_2^+ . This resulting species is not sterically hindered toward normal inner-sphere peroxide reactions as $\text{CrO}_2\text{M}^{n+}$ species might be, thus further reaction with additional Fe^{2+} is facilitated. Co(III) metal centers are substitutionally inert on the stopped-flow reaction time scale, preventing the formation of CrO_2^+ . Thus, the decomposition reaction of $\text{CrO}_2\text{Co}^{4+}$ is suggested to be a unimolecular decomposition forming chromium and cobalt products. Due to the very dilute reagent concentrations, a detailed product analysis, which would have aided in the elucidation of the mechanism of the decomposition reactions of the intermediates, was not possible.

The coordinated superoxo ligand of CrO_2^{2+} is a mild oxidizing center which appears to have only a small barrier to electron transfer processes. This is suggested since very fast reactions are found with both strongly reducing outer-sphere and mildly reducing inner-sphere electron transfer reagents.

SUMMARY

The oxidation-reduction reactions of the superoxochromium(III) ion, CrO_2^{2+} , have been examined with several well-known one electron outer-sphere reducing agents, $\text{Ru}(\text{NH}_3)_6^{2+}$, $\text{Co}(\text{sep})^{2+}$, and $\text{V}(\text{OH}_2)_6^{2+}$. The results are consistent with outer-sphere type mechanisms. The rate constants for these reactions are ($\text{M}^{-1}\text{s}^{-1}$): $(9.5 \pm 0.2) \times 10^5$, $(8.5 \pm 0.3) \times 10^5$, and $(2.3 \pm 0.1) \times 10^5$ respectively ($\mu = 0.100 \text{ M}$, $\text{HClO}_4 = 0.100 \text{ M}$, $T = 25.0 \text{ }^\circ\text{C}$). Studies were also carried out with several mild reducing agents with labile coordination positions, $\text{Fe}(\text{OH}_2)_6^{2+}$, $\text{Co}([\text{14}]\text{aneN}_4)(\text{OH}_2)_2^{2+}$, and $\text{Co}([\text{15}]\text{aneN}_4)(\text{OH}_2)_2^{2+}$. The results are consistent with inner-sphere mechanisms characterized by the formation and subsequent decomposition of a binuclear intermediate. The rate constants for the former reactions are ($\text{M}^{-1}\text{s}^{-1}$): $(4.5 \pm 0.2) \times 10^3$ ($\text{Fe}(\text{OH}_2)_6^{2+}$), $\sim 7 \times 10^6$ ($\text{Co}([\text{14}]\text{aneN}_4)(\text{OH}_2)_2^{2+}$), and $(6.2 \pm 0.3) \times 10^5$ ($\text{Co}([\text{15}]\text{aneN}_4)(\text{OH}_2)_2^{2+}$), ($\mu = 0.100 \text{ M}$, $\text{HClO}_4 = 0.100 \text{ M}$, $T = 25.0 \text{ }^\circ\text{C}$).

BIBLIOGRAPHY

1. (a) Neiderhoffer, E. C.; Timmon, J. H.; Martell, A. E. Chem. Rev., **1984**, 84, 137.
 (b) Gubelmann, M. H.; Williams, A. F. Structure and Bonding, **1983**, 55, 1.
 (c) Spiro, T. G. (ed) "Metal Ion Activation of Dioxygen"; Wiley: New York, **1980**.
 (d) Hayaishi, O. (ed) "Molecular Mechanisms of Oxygen Activation"; Academic Press: New York, **1976**.
 (e) Schultz, J.; Cameron, B. f. (eds) "The Molecular Basis for Electron Transport"; Academic Press: New York, **1972**.
2. (a) Wong, C.-L.; Endicott, J. F. Inorg. Chem., **1981**, 20, 2233.
 (b) Kumar, K.; Endicott, J. F. Inorg. Chem., **1984**, 23, 2447.
 (c) Munakata, M.; Endicott, J. F. Inorg. Chem., **1984**, 23, 3693.
3. (a) Picard, J. Ber., **1913**, 46, 2477.
 (b) Ardon, M.; Stein, G. J. Chem. Soc., **1956**, 2095.
 (c) Kolaczowski, R. W.; Plane, R. A. Inorg. Chem., **1964**, 3, 322.
 (d) Ilan, Y. A.; Czapski, G.; Ardon, M. Isr. J. Chem., **1975**, 13, 15.
 (e) Sellers, R. M.; Simic, M. G. J. Am. Chem. Soc., **1976**, 98, 6145.
4. Brynildson, M. E.; Bakac, A.; Espenson, J. H. J. Am. Chem. Soc., **1987**, 109, 4579.
5. tmc = 1,4,8,11-tetramethyl-1,4,8,11-tetraaza-cyclotetradecane
 Rillema, D. P.; Endicott, J. F.; Papaconstantinou, E. Inorg. Chem., **1971**, 8, 1739.
6. Heckman, R. A.; Espenson, J. H. Inorg. Chem., **1978**, 18, 38.
7. Wong, C.; Switzer, J. A.; Balakrishnan, K. P.; Endicott, J. F. J. Am. Chem. Soc., **1980**, 102, 5511.
8. Creaser, I. I.; Harrowfield, J. MacB.; Herlt, A. J.; Sargeson, A. M.; Springborg, J.; Geue, R. J.; Snow, M. R. J. Am. Chem. Soc., **1977**, 99, 3181.
9. Sykes, A. G.; Green, M. J. Chem. Soc. (A), **1970**, 3221.
10. Sellers, R. M.; Simic, M. G. J. Am. Chem. Soc., **1976**, 98, 6145.
11. Espenson, J. H. J. Am. Chem. Soc., **1970**, 92, 1880.
12. Bruhn, S. L.; Bakac, A.; Espenson, J. H. Inorg. Chem., **1986**, 25, 535.
13. a) Pethybridge, A. D.; Prue, J. E. Prog. Inorg. Chem., **1972**, 17, 327-90.
 b) Permutter-Hayman, B. Prog. React. Kinet., **1972**, 6, 239-67.

14. $A = 0.509$ in H_2O , $T = 25.0\text{ }^\circ C$, $\mu =$ ionic strength, Z_a and Z_b are the ionic charges on the species in a given bimolecular elementary reaction characterized by a rate constant k .
15. Lim, H. S.; Barclay, D. J.; Anson, F. Inorg. Chem., 1972, 11, 1460.
16. Sargeson, A. M. Chem. Br., 1979, 15, 23.
17. Latimer, W. M. "Oxidation Potentials", 2nd ed.; Prentice-Hall, Englewood Cliffs, NJ, 1952.
18. Endicott, J. F.; Durham, B.; Glick, M. D.; Anderson, T. J.; Kuszaj, J. M.; Schmonsees, W. G.; Balakrishnan, K. P. J. Am. Chem. Soc., 1981, 103, 1431.
19. Yee, E. L.; Cave, R. J.; Guyer, K. L.; Tyma, P. D.; Weaver, M. J. J. Am. Chem. Soc., 1979, 101, 1131.
20. Ramasami, T.; Endicott, J. F. J. Am. Chem. Soc., 1985, 107, 389.
21. Candlin, J. P.; Halpern, J.; Trimm, D. L. J. Am. Chem. Soc., 1964, 86, 1019.
22. Endicott, J. F.; Taube, H. J. Am. Chem. Soc., 1968, 86, 1686.
23. Przystas, T. J.; Sutin, N.; J. Am. Chem. Soc., 1973, 95, 5545.
24. Endicott, J. F.; Brubaker, G. R.; Ramasami, T.; Kumar, K.; Dwarakanath, K.; Cassel, J.; Johnson, D. Inorg. Chem., 1983, 22, 3754.
25. Davies, R.; Green, M.; Sykes, A. G. J. Chem. Soc. Dalton, 1972, 1171.
26. Chou, M.; Creutz, C.; Sutin, N. J. Am. Chem. Soc., 1977, 99, 5615.
27. Jacks, C. A.; Bennett, L. E. Inorg. Chem., 1974, 13, 2035.
28. Marcus, R. A.; Sutin, N. Biochim. Biophys. Acta, 1985, 811, 265.
29. Endicott, J. F.; Kumar, K. ACS Symp. Ser., 1982, 425.
30. Adams, A. C.; Crook, J. R.; Bockhoff, F.; King, E. L. J. Am. Chem. Soc., 1968, 90, 5761.
31. Basolo, F.; Pearson, R. G. "Mechanisms of Inorganic Reactions"; John Wiley and Sons, New York, 1967.

**CHAPTER III. CHARACTERIZATION OF THE STRUCTURE, PROPERTIES, AND
REACTIVITY OF A COBALT(II) MACROCYCLIC COMPLEX**

INTRODUCTION

Cobalt- N_4 complexes have long been of interest in inorganic and organometallic chemical research. Indeed, they became a focus of intensive research immediately after the surprising discovery that a coenzyme of vitamin B_{12} contained a stable cobalt-carbon sigma bond.¹ The general research goal was to find suitable synthetic models for the naturally occurring organometallic vitamin B_{12} . In early vitamin B_{12} research, it was determined that the ligands needed to stabilize a cobalt-carbon bond depended on the nature of the equatorial ligand system. Thus, the thrust of the early vitamin B_{12} research focused on the premise that in order to understand the steric and/or electronic requirements of the coordination chemistry of vitamin B_{12} , it was necessary to synthesize a large number of model molecules exhibiting gradual changes in their physical and chemical properties.

A sufficiently strong, essentially planar tetradentate ligand coordinated to a cobalt ion was required. Many polydentate ligands satisfied this requirement. The model complexes most commonly investigated had essentially planar equatorial ligand systems and either a pseudo-octahedral or square-pyramidal coordination geometry. The axial ligands commonly included a Lewis base such as pyridine for the fifth coordination site and an alkyl or aryl group to complete the sixth coordination site.

One very successful family of model complexes shown to duplicate many of the reactions and reactivities of vitamin B_{12} is the family of so-called "cobaloximes", Figure III-1. These complexes have been the subject

of many investigations in the attempt to understand the complexities of transition metal macrocyclic chemistry.² The variation of the macrocyclic ligand has been shown to alter the reduction potential, the substitution properties, and the reactivity patterns of these complexes. Thus, by understanding the features of cobalt macrocyclic complexes in general, we can begin to understand vitamin B₁₂ chemistry.

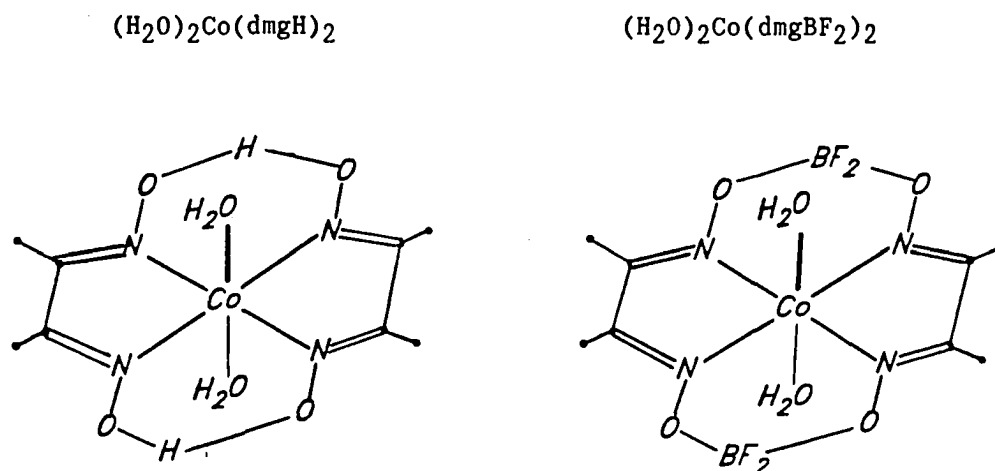


Figure III-1. Two Members of the Cobaloxime Family

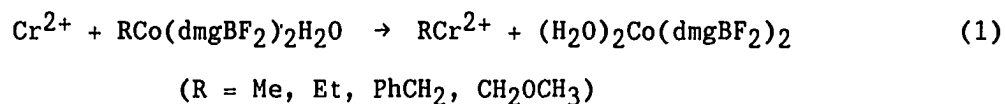
As a vital part of these investigations, a number of structural modifications were examined. Wong and coworkers³ have confirmed the assertion that the nature and the redox reactivity of the macrocyclic cobalt complexes can be altered by systematically modifying the equatorial ligand. One example of such equatorial ligand modification is achieved by capping the equatorial ligand of the cobaloxime with two BF_2^+ groups. This ligand modification was first reported by Schrauzer and Windgassen⁴ and subsequently a few minimally characterized BF_2^+ capped cobalt

macrocyclic complexes have been reported.⁵

Schrauzer and coworkers first used the BF_2^+ capped cobalt(III) organocobaloxime, $\text{RCo}(\text{dmgBF}_2)_2(\text{py})$, in their studies of the chemical, photochemical, and thermal cobalt-carbon bond cleavage of alkylcobaloximes and alkylcobalmins.^{6,7} They have also used the BF_2^+ capped cobalt(I) cobaloxime anion, $\text{Co}(\text{dmgBF}_2)_2^-$, in their studies of the nucleophilicity of alkylcobaloximes.⁸

A thorough physical and chemical characterization of the BF_2^+ capped cobalt(II) cobaloxime has not been reported. The complex was merely used as an additional member in a series of model organocobalt macrocyclic complexes.

Bakac and Espenson⁹ have reported the first extensive study of the reaction chemistry of $\text{RCo}(\text{dmgBF}_2)_2\text{H}_2\text{O}$ complexes. Their work focuses on the subject of homolytic metal-carbon bond cleavage. They have reported a complete kinetic and thermodynamic description of reversible alkyl transfer between Cr^{2+} and $\text{RCo}(\text{dmgBF}_2)_2\text{H}_2\text{O}$, equation 1.

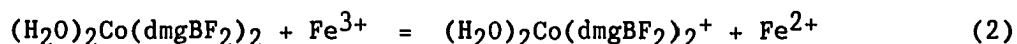


They have also reported on the unimolecular thermal homolysis of $\text{PhCH}_2\text{Co}(\text{dmgBF}_2)_2\text{H}_2\text{O}$. Two of their reasons for selecting $\text{RCo}(\text{dmgBF}_2)_2\text{H}_2\text{O}$ are: 1) the unusual acid (H_3O^+) stability of the BF_2^+ capped cobalt(II) macrocycle; and 2) the lack of observable molecular oxygen binding at 25.0 °C to $(\text{H}_2\text{O})_2\text{Co}(\text{dmgBF}_2)_2$ in acidic aqueous solution. In the acidic media required by the chromium species, pH 1-3, the parent cobalt(II) cobaloxime decomposes almost instantly to $\text{Co}(\text{aq})^{2+}$.¹⁰ This precluded any study of a

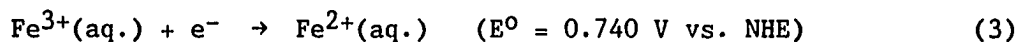
reversible alkyl transfer equilibrium. By using the acid stable BF_2^+ capped complex, a reversible alkyl transfer was observed and subsequently described in their study.

As has already been mentioned, the BF_2^+ capped cobaloxime offers the opportunity to study the reaction chemistry of a vitamin B_{12} model complex in an aqueous acidic solution. Cobalt(II)- N_4 complexes are attractively set up to react in an inner-sphere manner. Since the majority of the cobalt(II) macrocyclic complexes have a pseudo-octahedral low spin d^7 electron configuration, they exhibit a Jahn-Teller like distortion leading to highly labile axial ligands. In solution, many cobalt(II) macrocyclic complexes are either five coordinate, square pyramidal, or six coordinate, pseudo-octahedral. These structural and electronic features of cobalt(II) complexes enhance their ability to accept readily an incoming ligand in the axial coordination site.

The substitution lability has also proved exceptionally useful in our study of the redox reaction chemistry of $(\text{H}_2\text{O})_2\text{Co}(\text{dmgBF}_2)_2$, which was investigated by studying the reaction with iron(III) perchlorate, equation 2.



The mild oxidant iron(III) perchlorate was chosen as the mechanistic probe not only because it has been extensively studied and well characterized, but also because it has a suitable reduction potential of 0.740 V. vs. NHE, ($\mu = 0.50 \text{ M}$, $T = 25.0 \text{ }^\circ\text{C}$), in aqueous acid media, equation 3.¹¹



Oxidations by iron(III) are usually highly dependent on the hydrogen ion concentration.¹² The known acid ionization pre-equilibrium accounts for the highly reactive species $\text{Fe}(\text{OH})^{2+}$, ideally suited for inner-sphere electron transfer through the hydroxide ligand. Indeed, all the aspects of a predictable redox mechanism, including a reversible redox equilibrium, are present in this system and it becomes an attractive reaction for "calibrating" the inner-sphere reactivity of $(\text{H}_2\text{O})_2\text{Co}(\text{dmgBF}_2)_2$. Since the details of the characterization of this particularly interesting and versatile complex, $(\text{H}_2\text{O})_2\text{Co}(\text{dmgBF}_2)_2$, have not been reported, we decided to explore the nature of the BF_2^+ capped cobaloxime.

STATEMENT OF PROBLEM

Although a considerable amount of research effort has been devoted to the vitamin B₁₂ model complexes, only recently has research uncovered the potential of a previously overlooked family of cobalt macrocyclic complexes, the BF₂⁺ capped cobaloximes.

A recent kinetic and mechanistic study has shed light on the potential of the (H₂O)₂Co(dmgbF₂)₂ complex.⁹ Further research dealing with the structural characterization of (H₂O)₂Co(dmgbF₂)₂ by x-ray crystallographic and magnetic susceptibility methods, should yield interesting details regarding the similarities and differences among a series of related cobalt macrocyclic complexes.

Additional research in the areas of the chemical characterization and reactivity of (H₂O)₂Co(dmgbF₂)₂ should also prove vital in the understanding of the effect of the BF₂⁺ capped equatorial ligand on the Co(III)/(II) reduction potential and intramolecular electron transfer reactivity.

In summary, the major objectives of this research are: 1) to determine the structure of the BF₂⁺ capped cobaloxime, (H₂O)₂Co(dmgbF₂)₂; 2) to explore the chemical effects of the capping of the equatorial ligand (i.e., by measurement of the reduction potential and chemical reactivity); and 3) to determine the nature of the reactivity of (H₂O)₂Co(dmgbF₂)₂ toward inner-sphere oxidants (i.e., Fe³⁺).

EXPERIMENTAL SECTIONSolvents and reagents

Most solvents (acetone, methanol, acetonitrile, dichloromethane, toluene, and diethyl ether) were used as purchased. All the water used throughout this investigation was first distilled, then passed through an Oilex filter and finally purified by passage through inhouse anion and cation exchange columns. Additional purification for some experiments was obtained by passage of the purified water through a Millipore-Q purification system.

The $(\text{H}_2\text{O})_2\text{Co}(\text{dmgBF}_2)_2$ was prepared by the reported literature procedure.⁹ $\text{Co}(\text{OAc})_2 \cdot 4\text{H}_2\text{O}$, (2g), and dmgH_2 , (1.9g), were suspended in 150 mL of air-free diethyl ether. $\text{BF}_3 \cdot \text{Et}_2\text{O}$ was added, the mixture was stirred at room temperature for six hours and filtered. The brown solid, $(\text{H}_2\text{O})_2\text{Co}(\text{dmgBF}_2)_2$, was purified by several washings with ice-cold water followed by a recrystallization from methanol. The purity was checked by analytical and spectroscopic methods. Elemental analysis calculated for $(\text{H}_2\text{O})_2\text{Co}(\text{dmgBF}_2)_2$: Co, 14.0; C, 22.8; H, 3.80; N, 13.3. Found: Co, 14.0; C, 23.1; H, 3.78; N, 13.1. Spectrophotometric data: UV-VIS, $\lambda(\text{max})/\text{nm}$ ($\epsilon/\text{M}^{-1}\text{cm}^{-1}$), 456 (4.06×10^3), 328 (1.92×10^3), 260 (5.82×10^3), in H_2O .

The hydrated iron(III) perchlorate was donated by Dr. A. Bakac. It was prepared by fuming the chloride with perchloric acid. The iron(II) perchlorate was prepared in solution by reduction of $\text{Fe}(\text{ClO}_4)_3$ on a Zn-amalgam and standardized by a potentiometric titration using Ce(IV). The concentration of unreduced iron(III) in

the iron(II) solution was determined by the measurement of the concentration of the iron(III) thiocyanate complex ($\lambda_{\text{max}} = 460 \text{ nm}$) formed upon addition of KSCN to the iron(II) solution. This Fe^{3+} correction was very small, usually less than two percent of the total Fe^{3+} concentration in the experiments. The lithium perchlorate used for ionic strength control was prepared from the carbonate and recrystallized twice. The purity was checked by UV-VIS spectroscopy. Other reagents were used as purchased.

X-ray crystallography

The very limited solubility of $(\text{H}_2\text{O})_2\text{Co}(\text{dmgBF}_2)_2$ in water makes it difficult to grow single crystals of the diaquo complex. Thus single crystals of $(\text{CH}_3\text{OH})_2\text{Co}(\text{dmgBF}_2)_2$ suitable for X-ray diffraction were grown by the slow evaporation of a solution of $(\text{H}_2\text{O})_2\text{Co}(\text{dmgBF}_2)_2$ dissolved in methanol. These crystals lose solvent of crystallization readily, fracturing within minutes on contact with air. In order to prevent this, the crystal (approximate dimensions $0.25 \times 0.17 \times 0.14 \text{ mm}$), was mounted in a sealed 0.3 mm Lindeman glass capillary tube containing the mother liquor. The diffraction data were collected using a Syntex P2₁ four circle X-ray diffractometer. The crystal system and orientation matrix was obtained using an automatic indexing program.¹³ The resulting triclinic reduced cell and reduced cell scalars indicated no transformation to a higher symmetry. All data collected were unique and within a 2θ of 50° in the hkl , $h\bar{k}l$, $hk\bar{l}$, and $h\bar{k}\bar{l}$ octants. The intensity data were corrected for the Lorentz and polarization but not for the absorption effects. The space

group was determined as PT by a successful refinement. Direct methods and the automated map analysis approach built around MULTAN¹⁴ were used to obtain a trial structure. Full-matrix refinement was done by minimizing the function $\sum w(|F_o| - |F_c|)^2$, $w = \sigma_F^{-2}$, using anisotropic thermal parameters for all non-hydrogen atoms and fixed isotropic thermal parameters for the hydrogen atoms. The refinement converged to a residual index of $R = 4.5\%$ and a weighted residual index of $R_w = 4.6\%$. Additional crystallographic data are presented in Table III-1. The data collection was conducted by Mr. J. Benson and the structure refinement was completed with the help of S. Kim and L. Miller at Iowa State University.

Magnetic susceptibility

The magnetic susceptibility of $(H_2O)_2Co(dmgbF_2)_2$ was determined by the Gouy method.¹⁵ The reference cited very accurately describes the apparatus and technique employed in the determination. The two standards chosen were $HgCo(NCS)_4$ and $[Ni(en)_3]S_2O_3$. The calculated magnetic susceptibility was based on $[Ni(en)_3]S_2O_3$ as the standard, since some difficulty with the $HgCo(NCS)_4$ standard was observed (this standard was drawn to the magnet). No temperature dependent magnetic susceptibility measurements were attempted in this determination. The value of the magnetic susceptibility for $(H_2O)_2Co(dmgbF_2)_2$ was determined to be 1.92 ± 0.02 B.M. at ambient temperature. Therefore, $(H_2O)_2Co(dmgbF_2)_2$ is a low spin d^7 cobalt complex.

Electron paramagnetic resonance spectroscopy

Electron paramagnetic resonance spectra were collected on a Bruker/IBM ER 200D-SRC spectrometer equipped with a Systron-Donner frequency counter. Cooling was provided by cold nitrogen gas, producing a probe temperature of 100 - 110 K. The field was calibrated using DPPH, phenylpicryl-hydrazide ($g = 2.0037$), MnO powder diluted in MgO and a built-in NMR gaussmeter.

Samples of $\text{Co}(\text{dmgBF}_2)_2$ Lewis Base adducts were prepared by dissolving $(\text{CH}_3\text{OH})_2\text{Co}(\text{dmgBF}_2)_2$ in a degassed Lewis base-solvent mixture (the mixture is a 50/40/10 by volume mixture of toluene, dichloromethane, and Lewis base). Samples of $(\text{B})\text{Co}(\text{dmgBF}_2)_2(\text{O})_2$ were prepared by rapidly injecting an air-free solution of $(\text{B})_2\text{Co}(\text{dmgBF}_2)_2$ dissolved in the appropriate base into an oxygenated solution of toluene/dichloromethane at about -50°C . Following injection, the samples were then frozen in an EPR tube by liquid nitrogen. This solvent system was used because $(\text{CH}_3\text{OH})_2\text{Co}(\text{dmgBF}_2)_2$ is readily soluble in the mixture and upon freezing a good glass could be obtained with reproducible EPR spectra.

The EPR spectra are axial in appearance, therefore, the g and A values were calculated by the method described by Tovrog in his study of similar cobalt(II) macrocyclic complexes.¹⁶

Cyclic voltammetry

The cyclic voltammetry experiments were performed using a Bioanalytical Systems Inc. BAS-100 Electrochemical Analyzer. The glass sample compartment (solution volume ca. 10 mL) held the three electrodes needed for cyclic voltammetry in an air-free environment.

The working electrodes used were a commercial hanging mercury drop electrode, a glassy carbon disk electrode (electrode diameter 3.2 mm), and a platinum disk electrode (electrode diameter 1.6 mm). The auxiliary electrode was a platinum wire and the reference electrode was an Ag/AgCl reference electrode with a potential of 0.222 V vs. NHE. The solvent used in this study was distilled water and the electrolytes used in this study were LiClO_4 , HClO_4 , LiCl , and HCl .

Ultraviolet-visible spectroscopy

UV-VIS spectra and single wavelength absorbance vs. time data were acquired using a Cary model 219 recording spectrophotometer. Temperature control of ± 0.1 °C was maintained by circulating water from a constant-temperature bath through the jacket of a water-filled cell holder within the spectrophotometer. The fitting of the data to linear and nonlinear equations was accomplished using an APPLE II+ computer with the appropriate software for the analysis of first and second order kinetic data.

Kinetics using the stopped-flow technique

Reactions too rapid for the conventional kinetic methods were followed using a Canterbury model SF-3A stopped-flow spectrometer interfaced with a Nicolet model 206 digital storage oscilloscope. The data analysis was done using an APPLE II+ computer with the appropriate software for first order kinetic data analysis. The reaction of iron(III) perchlorate with $(\text{H}_2\text{O})_2\text{Co}(\text{dmgBF}_2)_2$ was monitored at $\lambda = 456$ nm, ($\mu = 0.50$ M, 25.0 ± 0.1 °C).

RESULTS

X-ray crystal structure

The refinement of the diffraction pattern resulted in the determination of the crystal and molecular structure of the complex, which is represented by the ORTEP drawing in Figure III-2. An objective of this portion of the investigation was to determine the structure of $(\text{H}_2\text{O})_2\text{Co}(\text{dmgBF}_2)_2$ thus confirming the substitution of the two BF_2^+ groups into the equatorial ligand system. This confirms the chemical composition of the ligand, and establishes that in the recrystallization procedure methanol replaced the two axial water molecules in the original complex.

The molecule is highly symmetric and has C_{2h} point group symmetry. Slight distortions in the macrocyclic ring were detected in the solid state structure by the X-ray data lowering the point group symmetry to C_i (pseudo- C_{2h}). Owing to the inversion center of symmetry, only half of the geometric parameters are independent. The calculated bond distances are reported in Table III-2 and the calculated bond angles in Table III-3. The positional and anisotropic thermal parameters, Table III-4, and the temperature factors, Table III-5, have also been included in the crystallographic data.

The ORTEP drawing of the structure of $(\text{CH}_3\text{OH})_2\text{Co}(\text{dmgBF}_2)_2$, Figure III-2, is labeled to identify specific atoms listed in the crystallographic tables.

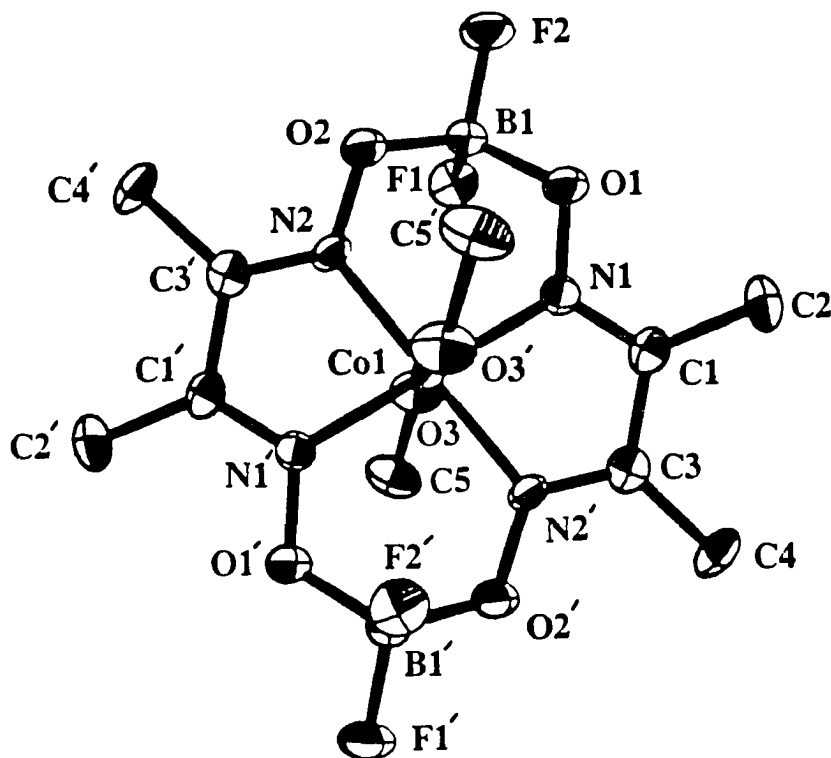


Figure III-2. Full ORTEP drawing of the molecular structure of $(\text{CH}_3\text{OH})_2\text{Co}(\text{dmgbF}_2)_2$. The hydrogen atoms are not included in the ORTEP drawing for clarity. The thermal ellipsoids are drawn at the 50% probability

Table III-1. Crystallographic Data for $(\text{CH}_3\text{OH})_2\text{Co}(\text{dmgBF}_2)_2$

formula	$\text{CoC}_{10}\text{H}_{20}\text{B}_2\text{F}_4\text{N}_4\text{O}_6$
fw	448.84
space group	PI
a, Å	7.955(6)
b, Å	8.180(6)
c, Å	7.918(6)
α , °	99.55(2)
β , °	118.13(2)
γ , °	66.52(2)
Z	1
V, Å ³	416.60
d_{calcd} , g/cm ³	1.51
crystal size, mm	0.25 X 0.17 X 0.14
crystal color	red
radiation	Mo K α ($\lambda = 0.70926$ Å)
μ , cm ⁻¹	11.43 (no correction applied)
temperature	Room Temperature
2 θ limits	2° - 50°
goodness of fit (GOF ^a)	1.34
data collected	1612
unique data	1595
data used in refinement	1027 ($ F_o \geq 3\sigma(F_o)$)
R ^b	0.045
R _w ^c	0.046

^aGOF = $\{\sum w(|F_o| - |F_c|)^2 / (\text{NO} - \text{NV})\}^{1/2}$, where NO = number of observations and NV = number of variables.

$${}^bR = \sum ||F_o| - |F_c|| / \sum |F_o|.$$

$${}^cR_w = \{\sum w(|F_o| - |F_c|)^2 / \sum w F_o^2\}^{1/2}.$$

Table III-2. Calculated Bond Distances for $(\text{CH}_3\text{OH})_2\text{Co}(\text{dmgBF}_2)_2$

<u>Atom Pair</u>	<u>Distance (Å)</u>	<u>Atom Pair</u>	<u>Distance (Å)</u>
Co1 - N1	1.882(4)	Co1 - N2	1.873(4)
Co1 - O3	2.264(4)	N1 - O1	1.354(5)
N1 - C1	1.266(6)	N2 - O2	1.361(5)
N2 - O2	1.361(5)	N2 - C3	1.273(7)
O1 - B1	1.483(7)	O2 - B1	1.493(7)
B1 - F1	1.395(7)	B1 - F2	1.357(7)
O3 - C5	1.407(7)	C1 - C2	1.492(8)
C1 - C3	1.473(7)	C3 - C4	1.484(8)
O3 - H3	0.739(62)	C2 - H21	0.936(71)
C2 - H22	0.809(72)	C2 - H23	0.913(72)
C4 - H41	0.826(68)	C4 - H42	0.758(74)
C4 - H43	0.946(70)	C5 - H51	0.966(67)
C5 - H52	0.844(74)	C5 - H53	1.029(69)

Table III-3. Selected Bond Angles in $(\text{CH}_3\text{OH})_2\text{Co}(\text{dmgBF}_2)_2$

<u>Atoms</u>	<u>Angle (°)</u>	<u>Atoms</u>	<u>Angle (°)</u>
N1 - Co1 - O3	91.17(16)	N2 - Co1 - O3	89.36(16)
Co1 - N1 - O1	123.65(29)	Co1 - N1 - C1	116.20(33)
Co1 - O3 - C5	128.04(37)	Co1 - N2 - O2	123.78(30)
N1 - O1 - B1	114.04(36)	N2 - O2 - B1	114.37(36)
O1 - N1 - C1	119.76(39)	O1 - C1 - C2	93.42(34)
C2 - C1 - C3	122.63(44)	N1 - C1 - C2	124.64(46)
N1 - C1 - C3	112.72(42)	O1 - B1 - O2	114.91(43)
O1 - B1 - F1	109.37(42)	O1 - B1 - F2	106.04(42)
O2 - B1 - F1	108.65(42)	O2 - B1 - F2	105.33(41)
F1 - B1 - F2	112.56(45)	C1 - C3 - C4	123.08(45)

Table III-4. Atomic Positional and Average Isotropic Thermal Parameters^a for $(\text{CH}_3\text{OH})_2\text{Co}(\text{dmgBF}_2)_2$

Atom	x	y	z	U(ave)
Co1	0	0	0	20(0)
N1	2627(6)	-1253(5)	1917(5)	25(1)
N2	-1347(6)	-1415(5)	30(5)	24(1)
O1	3134(5)	-2815(4)	2735(5)	31(1)
O2	-381(5)	-2949(4)	1099(5)	29(1)
O3	851(6)	-1806(5)	-2197(5)	38(2)
C1	4009(7)	-659(6)	2288(7)	23(2)
C2	6221(8)	-1544(8)	3628(8)	34(2)
C3	3210(7)	1012(6)	1221(7)	25(2)
C4	4451(10)	2109(8)	1605(9)	37(3)
C5	1616(11)	-3681(8)	-2198(11)	45(3)
B1	1444(9)	-2969(8)	2941(9)	28(2)
F1	811(5)	-1588(4)	4058(4)	37(1)
F2	2208(5)	-4603(4)	3758(4)	39(1)
H21	644(10)	-245(9)	437(9)	38
H22	686(11)	-212(9)	304(9)	38
H23	667(11)	-66(9)	429(9)	38
H3	-941(9)	-141(8)	-311(9)	38
H41	477(10)	250(8)	270(10)	38
H42	547(11)	158(9)	159(10)	38
H43	-362(10)	-309(9)	-73(9)	38
H51	-108(10)	-568(9)	178(10)	38
H52	-714(11)	-412(9)	-196(10)	38
H53	-91(11)	-563(9)	334(10)	38

^aAtomic coordinates [$\times 10^4$], temperature factors [$\text{\AA}^2 \times 10^3$]; U(ave) is the average of U_{11} , U_{22} , U_{33} .

Table III-5. Temperature Factors [$\text{\AA}^2 \times 10^3$] for $(\text{CH}_3\text{OH})_2\text{Co}(\text{dmgBF}_2)_2$

Atom	U ₁₁	U ₂₂	U ₃₃	U ₁₂	U ₁₃	U ₂₃
C01	15(1)	25(1)	20(1)	-6(0)	6(0)	4(0)
N1	19(2)	28(2)	22(2)	-4(2)	6(2)	7(2)
N2	24(2)	30(2)	19(2)	-11(2)	9(2)	1(2)
O3	52(3)	30(2)	35(2)	-6(2)	27(2)	0(2)
O1	25(2)	28(2)	36(2)	-3(2)	11(2)	12(2)
O2	27(2)	27(2)	32(2)	-7(2)	11(2)	9(2)
C1	22(3)	29(3)	20(3)	-8(2)	12(2)	-3(2)
C2	18(3)	46(3)	28(3)	-6(3)	6(3)	4(3)
C3	20(3)	31(3)	26(3)	-9(2)	15(2)	-7(2)
C4	33(4)	42(4)	41(4)	-19(3)	15(3)	-5(3)
B1	25(3)	26(3)	29(3)	-9(3)	9(3)	5(3)
F1	41(2)	37(2)	33(2)	-11(2)	20(2)	-2(1)
F2	38(2)	34(2)	40(2)	-6(2)	15(2)	17(1)
C5	59(5)	29(4)	58(4)	-15(3)	37(4)	-2(3)

EPR spectroscopy of (B)(B')Co(dm_gBF₂)₂

The EPR spectra of (B)₂Co(dm_gBF₂)₂ are in excellent agreement with the EPR spectra of (B)₂Co(dpgBF₂)₂, a very close analogue to (B)₂Co(dm_gBF₂)₂.¹⁶ The spectra are also very similar to other cobalt(II) macrocyclic complexes also studied by EPR techniques.^{5,17,18} The EPR parameters obtained from the analysis of the spectra are shown in Table III-6. The EPR spectrum of (CH₃CN)₂Co(dm_gBF₂)₂ is shown in Figure III-3, the EPR spectrum of (CH₃OH)₂Co(dm_gBF₂)₂ is shown in Figure III-3 and the EPR spectrum of ((CH₃)₂CO)₂Co(dm_gBF₂)₂ is shown in Figure III-4.

The characterization of the reversible binding of molecular oxygen by (B)₂Co(dm_gBF₂)₂ is also of interest since binding of molecular oxygen by several cobalt(II) macrocyclic complexes has been investigated.^{5,17,18} The reversible binding of molecular oxygen by (B)₂Co(dm_gBF₂)₂ was first observed when an oxygenated aqueous solution of (H₂O)₂Co(dm_gBF₂)₂ was cooled in a dry ice/acetone bath. As the solution cooled, the color of the solution changed from a golden yellow to a pink/red color. Upon warming, the golden color returned. The cycle was repeated a number of times implying reversible binding of molecular oxygen. An identical deoxygenated sample showed no color change during an identical cooling-freezing-warming cycle. Similar results were obtained in organic solvents such as methanol, acetonitrile, and acetone. The temperature dependent color changes in the organic solvents were more intense than in aqueous solutions. The observed temperature dependent color changes in the organic solvents were from a golden yellow to red/brown as the samples were cooled.

Oxygenation of the air-free samples was attempted by bubbling O₂ into the solution for 5-10 minutes at reduced temperatures (0 to -50 °C);

however, even though a color change was readily observed, the solutions were EPR silent. After numerous attempts to observe the Co-O₂ EPR spectrum, a rapid oxygenation procedure was devised. An air-free solution of (B)₂Co(dm_gBF₂)₂ in the appropriate Lewis base (CH₃OH, (CH₃)₂CO, or CH₃CN) was rapidly injected into an oxygenated toluene/dichloromethane solution cooled to about -50 °C. The appropriate color change was immediately observed and a sample rapidly frozen in an EPR tube by liquid nitrogen. Samples prepared this way gave weak EPR spectra for the Co-O₂ adducts. The three bases used in the experiment all gave similar results; however, the acetone adduct gave the best results and is shown in Figure III-4. The important parameters for this spectrum are found in Table III-6. The perpendicular region of the spectrum is clearly apparent; however, the parallel region is less resolved and the uncertainty greater.

Table III-6. EPR Parameters for (B)(B')Co(dm_gBF₂)₂^a

(B)	(B')	g_{\parallel}	$ A_{\parallel} ^b$	g_{\perp}	$ A_{\perp} ^b$
CH ₃ OH	CH ₃ OH	2.013	107	2.28	10
CH ₃ CN	CH ₃ CN	2.015	104	2.28	10
(CH ₃) ₂ CO	(CH ₃) ₂ CO	2.008	107	2.29	10
(CH ₃) ₂ CO	(CH ₃) ₂ CO	2.08	19	2.01	13

^aIn toluene/dichloromethane/Lewis base glass at 100 - 110 K.

^bX 10⁻⁴ cm⁻¹.

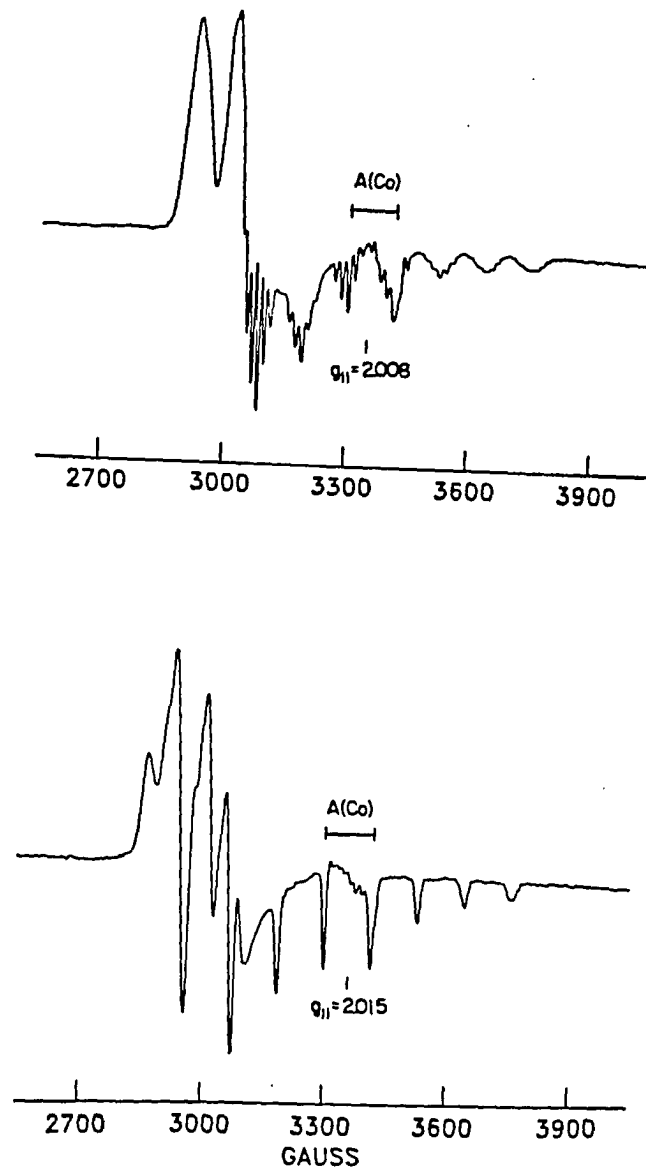


Figure III-3. EPR spectrum of $(\text{CH}_3\text{CN})_2\text{Co}(\text{dmgBF}_2)_2$ (top figure),
EPR spectrum of $(\text{CH}_3\text{OH})_2\text{Co}(\text{dmgBF}_2)_2$ (bottom figure)

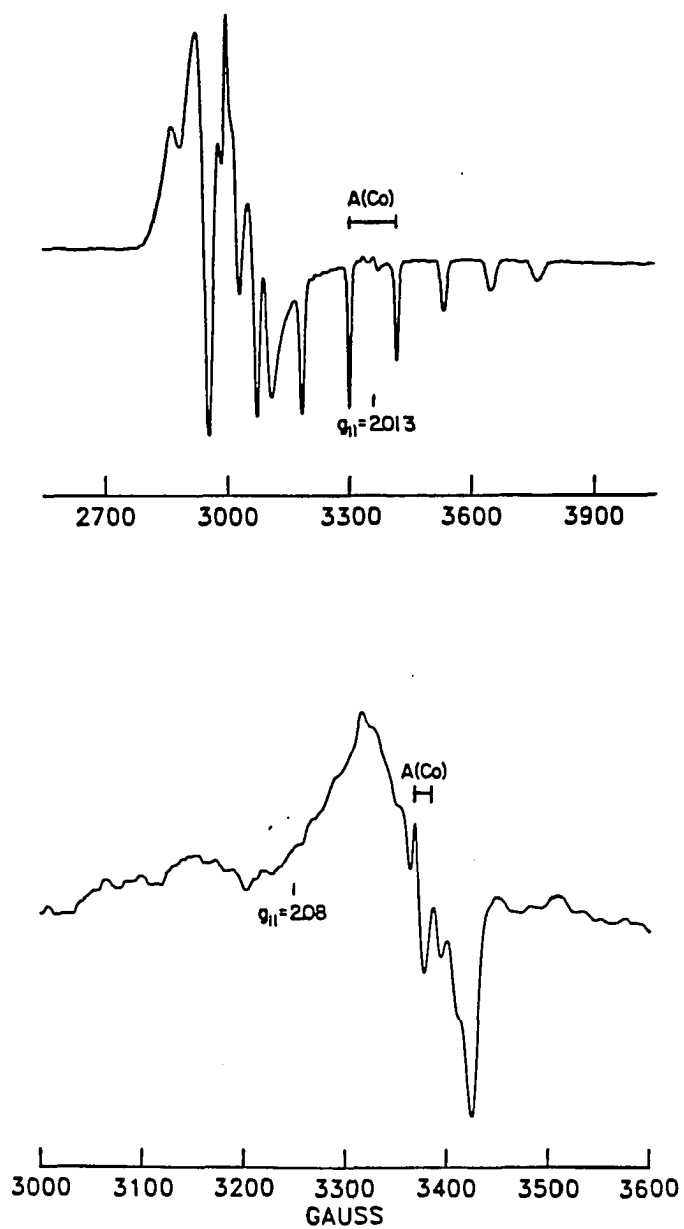
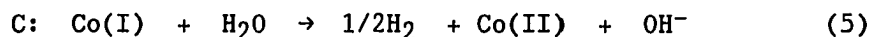
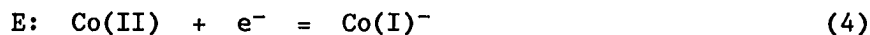


Figure III-4. EPR spectrum of $((\text{CH}_3)_2\text{CO})_2\text{Co}(\text{dmgBF}_2)_2$ (top figure), EPR spectrum of $((\text{CH}_3)_2\text{CO})\text{Co}(\text{dmgBF}_2)_2(\text{O}_2)$, (bottom figure)

Electrochemical measurements of $(\text{H}_2\text{O})_2\text{Co}(\text{dmgBF}_2)_2$

Cyclic voltammetry of $(\text{H}_2\text{O})_2\text{Co}(\text{dmgBF}_2)_2$ clearly shows the cobalt(II)/(I) redox couple to be nearly reversible. Plots of the peak currents vs. the square root of the scan velocity are linear except for the fastest scan rate, 1003 mV/s and the peak separations are 70-90 mV also except at the fastest scan rate. These results are indicative of sluggish electron transfer at the electrode surface. Plots of i_{pa}/i_{pc} vs. scan rate (v) also indicate the slight electrochemical irreversibility is due, at least in part, to a decomposition of the cobalt(I) species according to the EC mechanism:¹⁹



These results are consistent with the observed tendency for $(\text{H}_2\text{O})_2\text{Co}(\text{dmgBF}_2)_2^-$ to decompose in acidic or neutral aqueous solutions.

These cyclic voltammetry results depend on the type of electrode used. The cobalt(III)/(II) redox couple appears to be quasi-reversible at best, since the peak separation increases with increasing scan rates. The quasi-reversible character is probably due to sluggish electron transfer on the electrode surface. The sluggish electron transfer appears to affect the cobalt(III)/(II) redox couple more than the cobalt(II)/(I) couple. The HMDE produced the best cyclic voltammograms for the cobalt(II)/(I) redox couple; however, the HMDE could not be used for the determination of the cobalt(III)/(II) redox potential due to problems associated with the oxidation of the mercury drop at fairly positive

potentials. The platinum disk electrode and the glassy carbon disk electrode did show acceptable results under certain conditions. The use of the platinum electrode for the cobalt(II)/(I) redox couple produced poorly resolved cyclic voltammograms; however, this electrode gave acceptable results in acidic or chloride media for the cyclic voltammetry of the cobalt(III)/(II) redox couple. The glassy carbon electrode did not work well in acidic or chloride media, but gave the best results for the cobalt(III)/(II) redox couple in the solutions of LiClO_4 .

Chloride was added to the solutions in an attempt to eliminate the irreversible redox character displayed by the redox couples. The reversible character did improve slightly, but the E^0 for the redox for the redox couple also shifted implying a new species was formed in the solutions $(\text{Cl})(\text{H}_2\text{O})\text{Co}(\text{dmgBF}_2)_2^-$ or $(\text{Cl})_2\text{Co}(\text{dmgBF}_2)_2^{2-}$. Since the species of interest is the bis-aquo complex, the cyclic voltammetry results focused on the results in the noncomplexing perchlorate media.

Experiments using acetonitrile as the solvent, $(\text{CH}_3\text{CH}_2)_4\text{NPF}_6$ as the electrolyte and the glassy carbon electrode were similar to the experiments using the glassy carbon electrode in neutral aqueous solutions. The cobalt(II)/(I) redox couple was nearly reversible, but the cobalt(III)/(II) redox couple was quasi-reversible. Figure III-5 shows an example of the cyclic voltammetry for the cobalt(II)/(I) and cobalt(III)/(II) redox couples. A summary of the electrochemical data is shown in Table III-7.

Table III-7. Cyclic Voltammetry Results for $(\text{H}_2\text{O})_2\text{Co}(\text{dmgBF}_2)_2$

Electrode	Electrolyte	Couple	E_a (mV)	E_c (mV)	ΔmV	ν (mV/s)	E^0 (mV)
HMDE	0.10 M LiClO_4	II/I	-392	-462	70	10	-427
Carbon	0.10 M LiClO_4	II/I	-392	-477	85	10	-434
Carbon	0.10 M LiClO_4	III/II	835	531	304	10	683
Carbon	1.00 M LiClO_4	II/I	-389	-463	74	10	-426
Carbon	0.10 M LiCl	II/I	-395	-472	77	10	-433
Carbon	1.00 M LiCl	II/I	-365	-442	77	10	-404
Platinum	0.10 M LiCl	III/II	673	497	176	10	585
Platinum	1.00 M LiCl	III/II	628	444	184	10	536
Platinum	0.10 M HClO_4	III/II	766	542	224	10	654
Platinum	0.10 M HCl	III/II	643	535	108	10	589

"HMDE" = Hanging Mercury Drop Electrode; "Carbon" = Glassy Carbon Disk Electrode; "Platinum" = Platinum Disk Electrode; " E_a " = Anodic Peak Potential; " E_c " = Cathodic Peak Potential; " ΔmV " = Peak Separation; " ν " = Scan Rate; " E^0 " = $(E_a + E_c)/2$; The solvent used in these experiments was H_2O , the temperature was approximately 25 °C. All potentials reported vs. NHE.

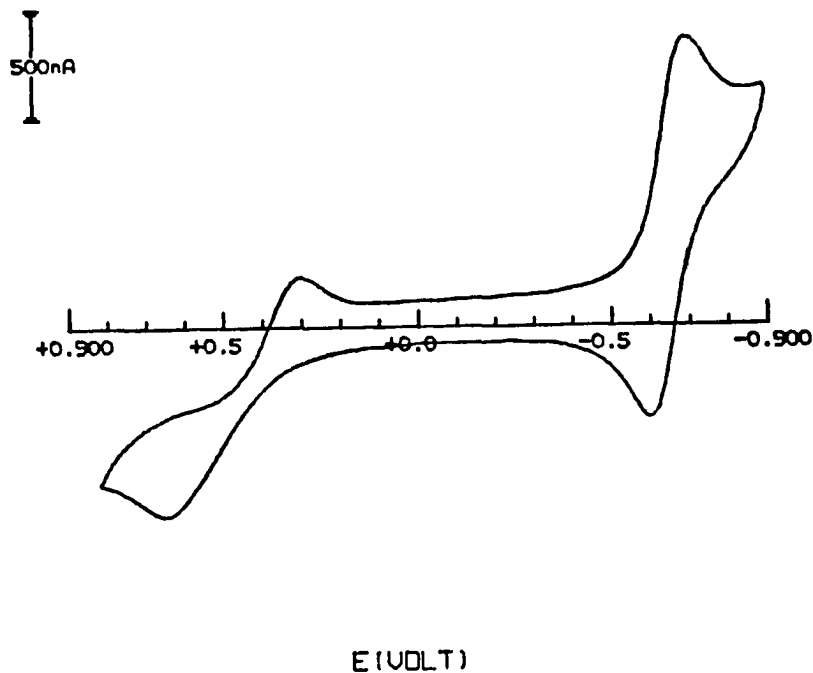
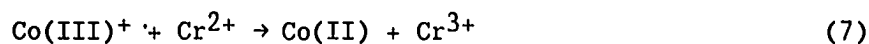
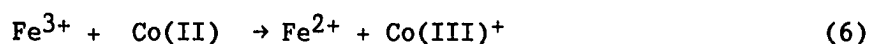


Figure III-5. Cyclic voltammogram of $(\text{H}_2\text{O})_2\text{Co}(\text{dmgbF}_2)_2$, (top figure, redox couples = cobalt(III)/(II), cobalt(II)/(I), glassy carbon electrode, $\text{LiClO}_4 = 0.10 \text{ M}$, $\nu = 10 \text{ mV s}^{-1}$, potentials vs. Ag/AgCl reference electrode). Cyclic voltammogram of $(\text{H}_2\text{O})_2\text{Co}(\text{dmgbF}_2)_2$, (bottom figure, redox couples = cobalt(II)/(I), glassy carbon electrode, $\text{LiClO}_4 = 0.10 \text{ M}$, $\nu = 10 \text{ mV s}^{-1}$, potentials vs. Ag/AgCl reference electrode)

Reversible oxidation of $(\text{H}_2\text{O})_2\text{Co}(\text{dmgBF}_2)_2$

The reversible redox nature of $(\text{H}_2\text{O})_2\text{Co}(\text{dmgBF}_2)_2$, designated cobalt(II), was observed by first oxidizing the Co(II) to $(\text{H}_2\text{O})_2\text{Co}(\text{dmgBF}_2)_2^+$, or cobalt(III)⁺, with a slight excess of Fe^{3+} in an air-free spectrophotometric cell, equation 6. The UV-VIS spectrum revealed a bleaching of the cobalt(II) absorbance at $\lambda = 456 \text{ nm}$, $\Delta\epsilon = 3590 \text{ M}^{-1}\text{cm}^{-1}$ where $\Delta\epsilon$ is the difference between the molar absorptivity of cobalt(II), $\epsilon = 4060 \text{ M}^{-1}\text{cm}^{-1}$, and cobalt(III)⁺, $\epsilon = 470 \text{ M}^{-1}\text{cm}^{-1}$ at this wavelength. A slight excess of Cr^{2+} was injected into the cell to reduce the cobalt(III)⁺ complex, equation 7, and the final UV-VIS spectrum was recorded as seen in Figure III-6. This final spectrum records the restoration of the cobalt(II) absorbance, indicating that greater than 95% of the cobalt(II) was reversibly oxidized and then reduced by this procedure.



Cobalt(II) is fairly unreactive toward acid; however, cobalt(III)⁺ is more reactive. At 0.0500 - 0.500 M HClO_4 , the rate constant for the reaction of cobalt(II) with acid is $k = 6.9 \times 10^{-4} \text{ M}^{-1}\text{s}^{-1}$, ($t_{1/2} = 335 \text{ min.}$, $\text{HClO}_4 = 0.0500 \text{ M}$, $T = 25.0 \text{ }^\circ\text{C}$). The decomposition of cobalt(III)⁺ in 0.0500 M HClO_4 has a half life of about 9 minutes at 25.0 $^\circ\text{C}$. The decomposition rate was estimated from a series of experiments which: 1) oxidized cobalt(II) to cobalt(III)⁺ with Fe^{3+} , 2) allowed the cobalt(III)⁺

to decompose for varying lengths of time in the acidic solution ($\text{HClO}_4 = 0.500 \text{ M}$), and 3) measured, by spectroscopic means, the degree of decomposition by determining the amount of cobalt(II) recovered after an injection of Cr^{2+} . Therefore, considering the increased acid sensitivity of cobalt(III)⁺, to insure a high reversible redox yield, the oxidation and reduction must be done as rapidly as possible.

The extent of the oxidation of cobalt(II) by Fe^{3+} , and thus the position of the equilibrium in the reaction described by equation 6, is also affected by the Fe^{3+} and Fe^{2+} concentrations. The extent of the oxidation increases with increasing Fe^{3+} concentration and decreasing Fe^{2+} concentration. This is an example of a reversible redox equilibrium situation and provides additional evidence for the reversible nature of this cobalt(III)/(II) couple.

Equilibrium constant determination

The equilibrium constant (K_{eq}) for the reaction described in equation 6 was determined by two methods.

$$K_{\text{eq}} = \frac{[\text{Fe}^{2+}][\text{Co(III)}^+]}{[\text{Fe}^{3+}][\text{Co(II)}]} \quad (8)$$

The first method was based on the spectrophotometric determination of the equilibrium concentrations of the species in solution. The initial concentrations of Fe^{3+} , Fe^{2+} , and cobalt(II) and their molar absorptivities at $\lambda = 456 \text{ nm}$ were known. From ΔD (ΔD is the difference between the initial and final absorbance values) it is possible to calculate the concentrations of all the species in the equilibrium expression, equation 8. In these experiments the initial concentrations

of Fe^{3+} and Fe^{2+} were in considerable excess over the cobalt species. Thus the changes in the concentrations of Fe^{3+} and Fe^{2+} from the initial to the equilibrium state were small. The expression for the equilibrium constant can be related, as in equation 9, to the concentrations and absorbance change in these experiments.

$$(\Delta\epsilon/\Delta D)[\text{Co(II)}]_0 = [\text{Fe}^{2+}]_{\text{eq}}/K_{\text{eq}}[\text{Fe}^{3+}]_{\text{eq}} + 1 \quad (9)$$

The equilibrium constant was evaluated at various acid concentrations in the range 0.1–0.5 M HClO_4 . No dependence of K_{eq} on $[\text{H}^+]$ was observed. The plot of $(\Delta\epsilon/\Delta D)[\text{Co(II)}]_0$ vs. $[\text{Fe}^{3+}]_{\text{eq}}/[\text{Fe}^{2+}]_{\text{eq}}$ which yields $1/K_{\text{eq}}$ as the slope is shown in Figure III-7. The equilibrium constant calculated using a least-squares analysis of the spectrophotometric data according to equation 9 is 34.7 ± 2.9 , ($\lambda = 456$ nm, $\mu = 0.50$ M, $T = 25.0^\circ\text{C}$).

A second method for the determination of the equilibrium constant utilized the kinetic data according to the expression: $K_{\text{eq}} = k_f/k_r$. The method for the determination of these forward and reverse rate constants is detailed in the next section titled "Rate Constant Determination". The equilibrium constant determined kinetically is $K_{\text{eq}} = k_f/k_r = 575 \text{ M}^{-1}\text{s}^{-1} / 18.3 \text{ M}^{-1}\text{s}^{-1} = 31.4 \pm 3.4$, ($\text{HClO}_4 = 0.40$ M, $\mu = 0.50$ M, $T = 25.0^\circ\text{C}$)

Rate constant determination

The absorbance readings, taken as a function of time from the experiments used to obtain the values of the overall absorbance change, ΔD , also yielded values for the forward and reverse rate constants, k_f and k_r . The concentrations of Fe^{3+} and Fe^{2+} were chosen high enough such that the approach to equilibrium can be represented as opposing pseudo-first-

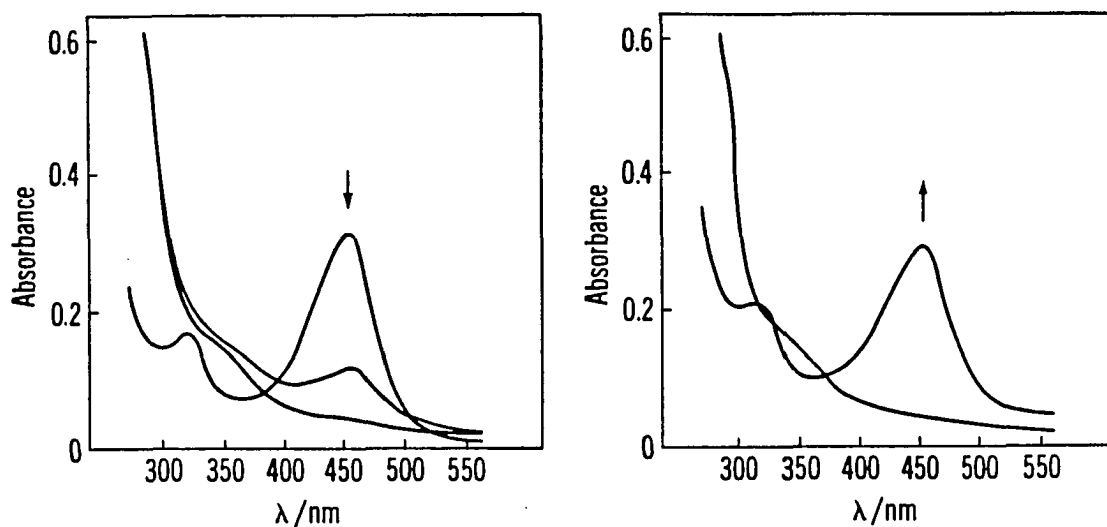


Figure III-6. Three UV-VIS spectral scans, recorded as a function of time, of the air-free oxidation of $(\text{H}_2\text{O})_2\text{Co}(\text{dmgBF}_2)_2$ ($8.0 \times 10^{-5} \text{ M}$) to $(\text{H}_2\text{O})_2\text{Co}(\text{dmgBF}_2)_2^+$ by Fe^{3+} ($1 \times 10^{-4} \text{ M}$, left figure). The right figure displays the UV-VIS spectral scan recorded immediately following the oxidation of $(\text{H}_2\text{O})_2\text{Co}(\text{dmgBF}_2)_2$ overlaid with the UV-VIS spectral scan recorded immediately following the reduction of the cobalt(III)⁺ by a slight excess of Cr^{2+} ($1.1 \times 10^{-4} \text{ M}$)

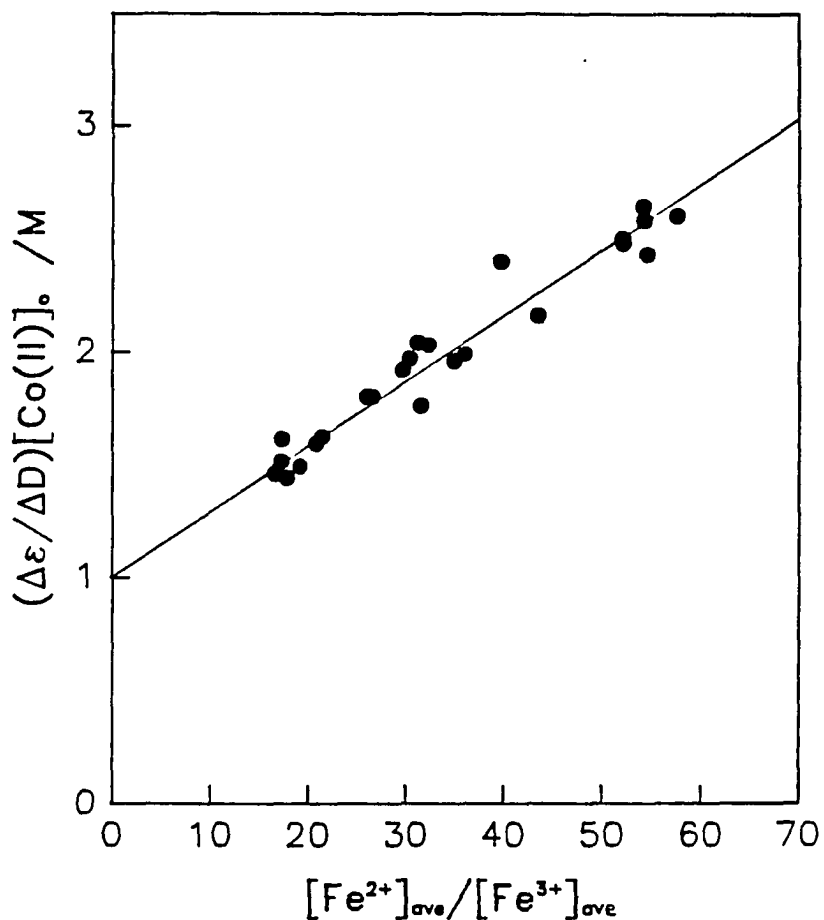


Figure III-7. The plot of $(\Delta\varepsilon/\Delta D)[\text{Co(II)}]_0$ vs. $[\text{Fe}^{2+}]_{\text{ave}}/[\text{Fe}^{3+}]_{\text{ave}}$ for the reaction of $(\text{H}_2\text{O})_2\text{Co}(\text{dmgBF}_2)_2$ to determine the equilibrium constant. The concentrations of Fe^{3+} and Fe^{2+} were present in large excess ($[\text{Fe}^{3+}] = 0.9 - 3.0 \times 10^{-4} \text{ M}$, $[\text{Fe}^{2+}] = 3.0 - 5.0 \times 10^{-3} \text{ M}$, $\text{HClO}_4 = 0.400 \text{ M}$, $\mu = 0.500 \text{ M}$, and $T = 25.0 \text{ }^\circ\text{C}$)

order reactions. Equations 10, 11, and 12 were used to evaluate the kinetic data.

$$d[\text{Co(III)}^+]/dt = k_f[\text{Fe}^{3+}][\text{Co(II)}] - k_r[\text{Fe}^{2+}][\text{Co(III)}^+] \quad (10)$$

$$k_{\text{obs}} = k_f[\text{Fe}^{3+}] + k_r[\text{Fe}^{2+}] \quad (11)$$

$$k_{\text{obs}}/[\text{Fe}^{2+}] = k_f[\text{Fe}^{3+}]/[\text{Fe}^{2+}] + k_r \quad (12)$$

The plot of $k_{\text{obs}}/[\text{Fe}^{2+}]_{\text{ave}}$ vs. $[\text{Fe}^{3+}]_{\text{ave}}/[\text{Fe}^{2+}]_{\text{ave}}$ is shown in Figure III-8. This plot yields k_f as the slope and k_r as the intercept. The least-squares values are $k_f = 575 \pm 45 \text{ M}^{-1}\text{s}^{-1}$, $k_r = 18.3 \pm 1.8 \text{ M}^{-1}\text{s}^{-1}$.

The value of the forward rate constant can also be calculated from the kinetic data using equation 13, which is obtained from equation 12 by substitution of $K_{\text{eq}} = k_f/k_r$.

$$k_{\text{obs}} = k_f([\text{Fe}^{3+}]_{\text{ave}} + [\text{Fe}^{2+}]_{\text{ave}}/K_{\text{eq}}) \quad (13)$$

If the value of the equilibrium constant is fixed at the spectrophotometric value of $K_{\text{eq}} = 34.7$, the refined value of the forward rate constant is $k_f = 599 \pm 10 \text{ M}^{-1}\text{s}^{-1}$. The plot of the kinetic data defined by equation 13, k_{obs} vs. $([\text{Fe}^{3+}]_{\text{ave}} + [\text{Fe}^{2+}]_{\text{ave}}/K_{\text{eq}})$, is shown in Figure III-9. The slope is drawn to correspond to the least-squares fit, $k_f = 599 \text{ M}^{-1}\text{s}^{-1}$.

The value of the reverse rate constant can likewise be calculated from the kinetic data by analogous methods. Equation 13 can be recast to yield the reverse rate constant as the slope of a plot suggested by equation 14.

$$k_{\text{obs}} = k_r([\text{Fe}^{2+}]_{\text{ave}} + K_{\text{eq}}[\text{Fe}^{3+}]_{\text{ave}}) \quad (14)$$

If the value of the equilibrium constant is fixed at the spectrophotometric value of $K_{\text{eq}} = 34.7$, the refined value of the reverse rate constant is $k_r = 17.3 \pm 0.3 \text{ M}^{-1}\text{s}^{-1}$. The plot of the kinetic data according to equation 14, k_{obs} vs $([\text{Fe}^{2+}]_{\text{ave}} + K_{\text{eq}}[\text{Fe}^{3+}]_{\text{ave}})$, is shown in Figure III-10. The slope is drawn to correspond to the least-squares fit, $k_r = 17.3 \text{ M}^{-1}\text{s}^{-1}$.

The effect of chloride on the observed rate

The effect of chloride ion on the observed rate for the reaction of $(\text{H}_2\text{O})_2\text{Co}(\text{dmgBF}_2)_2$ and Fe^{3+} was qualitatively measured by the introduction of NaCl (aq.) into a reaction mixture of Fe^{3+} and $(\text{H}_2\text{O})_2\text{Co}(\text{dmgBF}_2)_2$. Two different chloride concentrations were used, 0.11 and 0.23 M ($\text{HClO}_4 = 0.30 \text{ M}$). A significant rate enhancement was observed with increasing chloride concentrations, $k_{\text{obs}} = 0.0478 \text{ s}^{-1}$ ($[\text{Cl}^-] = 0 \text{ M}$), $k_{\text{obs}} = 0.252 \text{ s}^{-1}$ ($[\text{Cl}^-] = 0.11$), and $k_{\text{obs}} = 0.527$ ($[\text{Cl}^-] = 0.23 \text{ M}$), with the observed rate doubling as the chloride concentration was doubled.

Forward rate constant by the stopped-flow method

Kinetic data were also determined by stopped-flow experiments in which the concentrations of Fe^{3+} were chosen such that the reaction proceeds essentially to completion. These conditions were such that only the forward reaction contributed to the observed rate constant. The observed rate is decidedly dependent on the acid concentration with the observed rate increasing with decreasing acid concentrations. To complete the

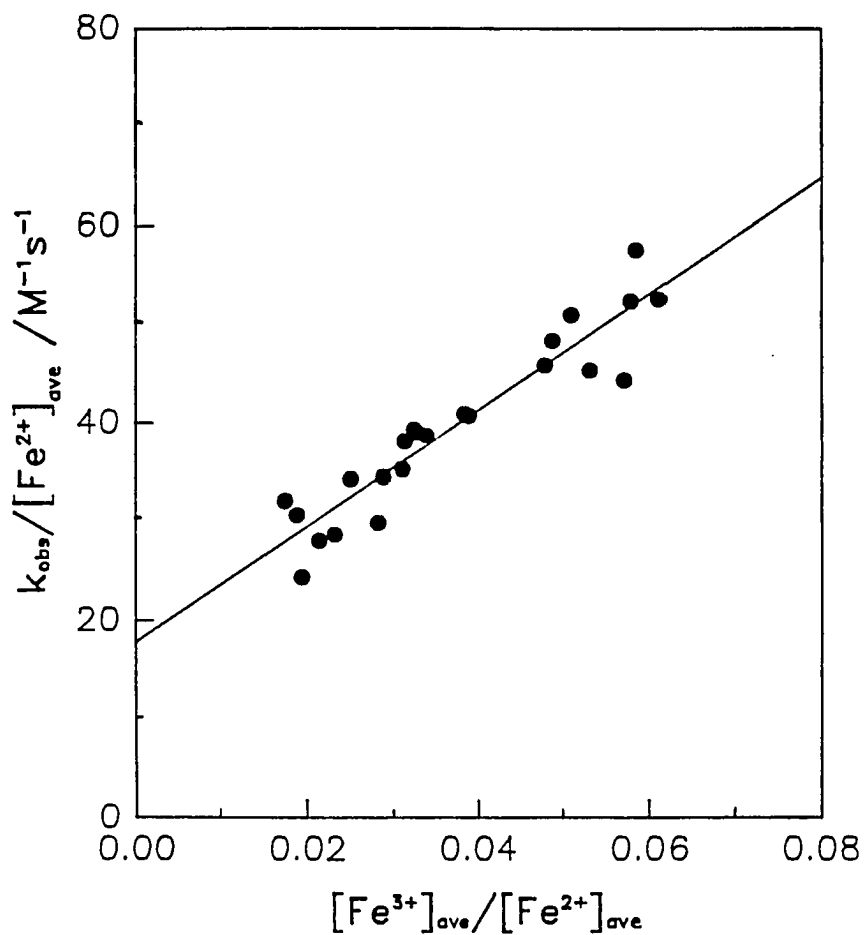


Figure III-8. The plot of $k_{\text{obs}}/[\text{Fe}^{2+}]_{\text{ave}}$ vs. $[\text{Fe}^{3+}]_{\text{ave}}/[\text{Fe}^{2+}]_{\text{ave}}$ for the reaction of $(\text{H}_2\text{O})_2\text{Co}(\text{dmgBF}_2)_2$ with pseudo-first-order concentrations of Fe^{3+} and Fe^{2+} ($[\text{Fe}^{3+}] = 0.9 - 3.0 \times 10^{-4} \text{ M}$, $[\text{Fe}^{2+}] = 3.0 - 5.0 \times 10^{-3} \text{ M}$, $\text{HClO}_4 = 0.400 \text{ M}$, $\mu = 0.500 \text{ M}$, and $T = 25.0 \text{ }^\circ\text{C}$)

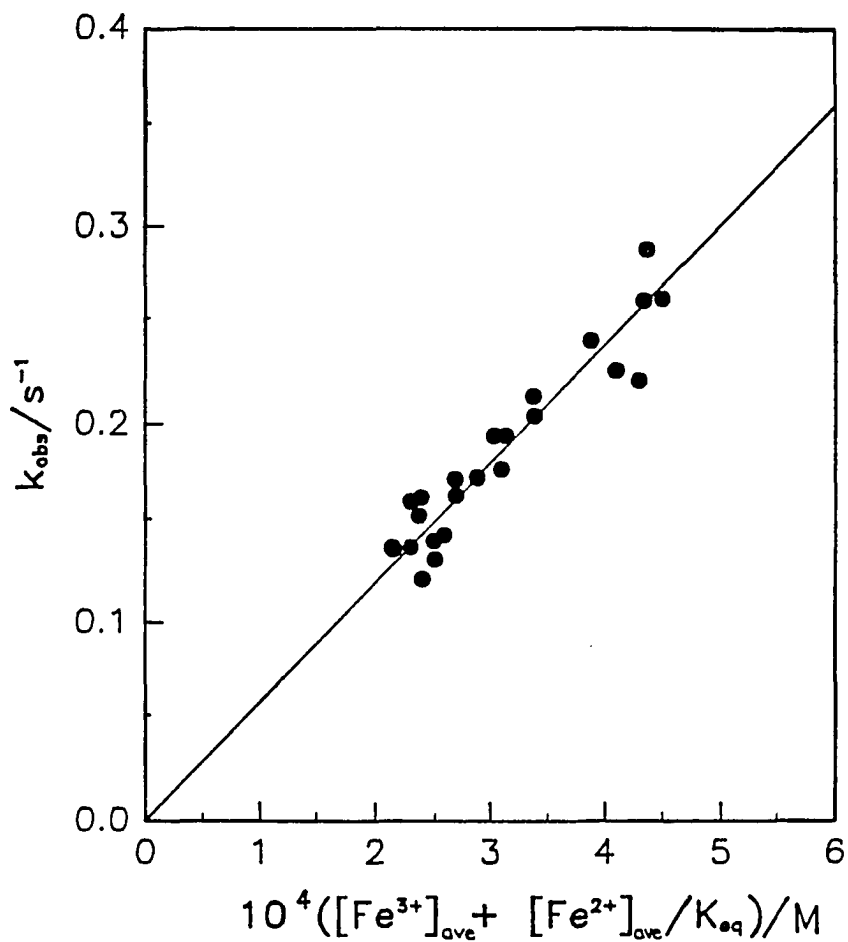


Figure III-9. The plot of k_{obs} vs. $([\text{Fe}^{3+}]_{\text{ave}} + [\text{Fe}^{2+}]_{\text{ave}}/K_{\text{eq}})$ for the reaction of $(\text{H}_2\text{O})_2\text{Co}(\text{dmgBF}_2)_2$ with pseudo-first-order concentrations of Fe^{3+} and Fe^{2+} ($[\text{Fe}^{3+}] = 0.9 - 3.0 \times 10^{-4} \text{ M}$, $[\text{Fe}^{2+}] = 3.0 - 5.0 \times 10^{-3} \text{ M}$, $\text{HClO}_4 = 0.400 \text{ M}$, $\mu = 0.500 \text{ M}$, and $T = 25.0 \text{ }^\circ\text{C}$)

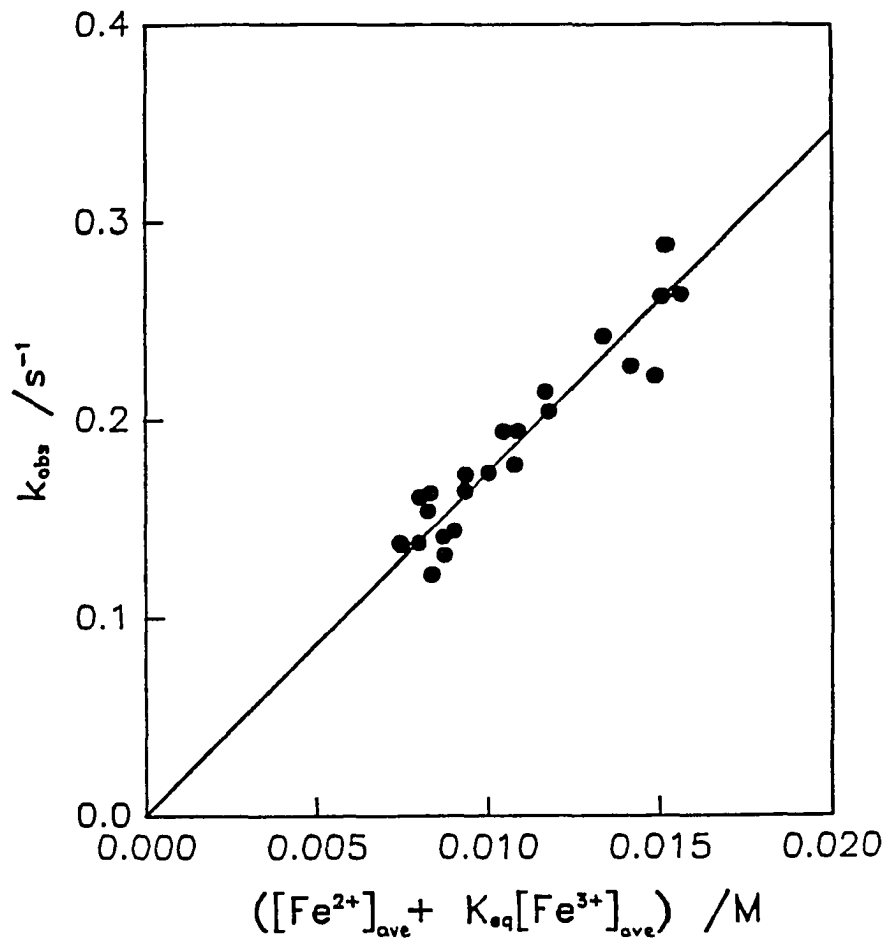


Figure III-10. The plot of k_{obs} vs. $([\text{Fe}^{2+}]_{\text{ave}} + K_{\text{eq}}[\text{Fe}^{3+}]_{\text{ave}})$ for the reaction of $(\text{H}_2\text{O})_2\text{Co}(\text{dmgBF}_2)_2$ with pseudo-first-order concentrations of Fe^{3+} and Fe^{2+} ($[\text{Fe}^{3+}] = 0.9 - 3.0 \times 10^{-4} \text{ M}$, $[\text{Fe}^{2+}] = 3.0 - 5.0 \times 10^{-3} \text{ M}$, $\text{HClO}_4 = 0.400 \text{ M}$, $\mu = 0.500 \text{ M}$, and $T = 25.0 \text{ }^\circ\text{C}$)

characterization of the reaction, a series of experiments with varying perchloric acid concentrations was conducted. The ionic strength was controlled throughout these experiments at $\mu = 0.50$ M with LiClO_4 . The perchloric acid concentration range used was 0.003-0.49 M.

Several algebraic functions showing an inverse acid dependence on the observed rate constant were examined to find the correct functional form. Guided by precedents in the literature, the two rate law functions most likely to fit the data are those in equations 15 and 16. The stopped-flow data was fit to the two forms of the rate laws arising from such mechanisms by a least-squares computer analysis.

$$k_{\text{obs}}/[\text{Fe}^{3+}] = k_f^{\text{app}} = A + B/[\text{H}^+] \quad (15)$$

$$k_{\text{obs}}/[\text{Fe}^{3+}] = k_f^{\text{app}} = C/(D + [\text{H}^+]) \quad (16)$$

This computer fit is illustrated in the plot of the logarithm of the apparent forward rate constant, $\text{Log}(k_{\text{obs}}/[\text{Fe}^{3+}])$ vs. the logarithm of the acid concentration, $\text{Log}([\text{H}^+])$, Figure III-11.

The two best fit lines are plotted along with the observed data. This graphical plot clearly indicates that the form in equation 15 is more consistent with the data than the form in equation 16. This is especially seen in the low and high acid regions of the graph. The values of the parameters obtained by the least-squares fit for the rate equation in equation 15 are $A = 289 \pm 11 \text{ M}^{-1}\text{s}^{-1}$, $B = 120 \pm 2 \text{ M}^{-1}\text{s}^{-1}$

Additional evaluation can be done by other plots. The form in equation 15 implies a linear plot of k_f^{app} vs. $1/[\text{H}^+]$ and a nonlinear plot

of $1/k_f^{\text{app}}$ vs. $[\text{H}^+]$. The situation is just the opposite for the rate law in equation 16 which rearranges to $1/k_f^{\text{app}} = D/C + [\text{H}^+]/C$, thereby implying a linear plot of $1/k_f^{\text{app}}$ vs. $[\text{H}^+]$ and a nonlinear plot of k_f^{app} vs. $1/[\text{H}^+]$. When the stopped-flow experimental data are plotted in these two fashions, Figures III-12 and III-13, some curvature is apparent in both plots. Within experimental error, however, the data are fit much more satisfactorily by the plot of k_f^{app} vs. $1/[\text{H}^+]$, thus supporting equation 15 as the best algebraic expression for the data in this graphical analysis.

The rate expression in equation 15 can also be linearized as in equation 17. The plot of $[\text{H}^+]k_f^{\text{app}}$ vs. $[\text{H}^+]$, as in Figure III-14, is fairly linear over the acid concentration examined.

$$[\text{H}^+]k_f^{\text{app}} = A[\text{H}^+] + B \quad (17)$$

As a further analysis of the data, the percent deviation from the computer fits of Figure III-10 can be plotted. The plots of the percent deviation vs. acid concentration are shown in Figure III-15. This plot helps to illustrate the random scatter of the deviations when the data is fitted to equation 15 and the systematic deviation associated when the data is fitted to equation 16. Therefore, based on the evidence presented in the graphical analyses, the algebraic expression which best fits the data is equation 15.

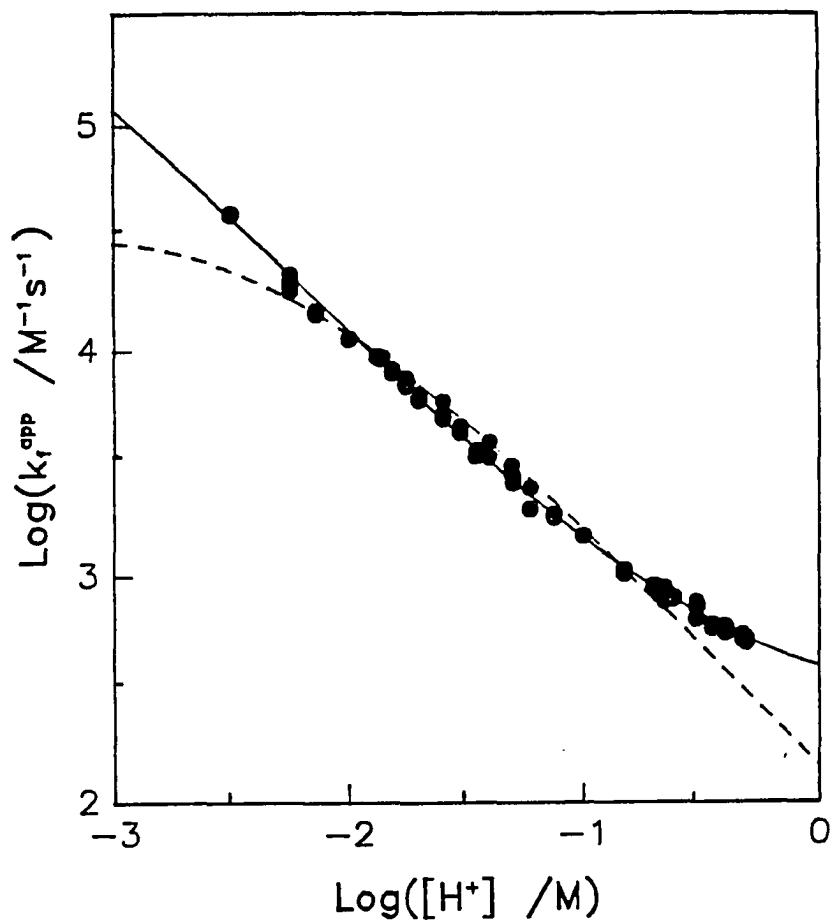


Figure III-11. The plot of $\text{Log}(k_{\text{obs}}/[\text{Fe}^{3+}])$ vs. $\text{Log}([\text{H}^+])$ for the reaction of $(\text{H}_2\text{O})_2\text{Co}(\text{dmgBF}_2)_2$ with pseudo-first-order concentrations of Fe^{3+} ($[\text{Fe}^{3+}] = 2.0 - 30 \times 10^{-4} \text{ M}$, $\mu = 0.500 \text{ M}$, $T = 25.0 \text{ }^\circ\text{C}$); only the forward reaction was observed in the stopped-flow experiments. The best fit line for each of the two rate law forms ($A + B/[\text{H}^+]$, solid line) and ($C/D + [\text{H}^+]$, broken line) are included

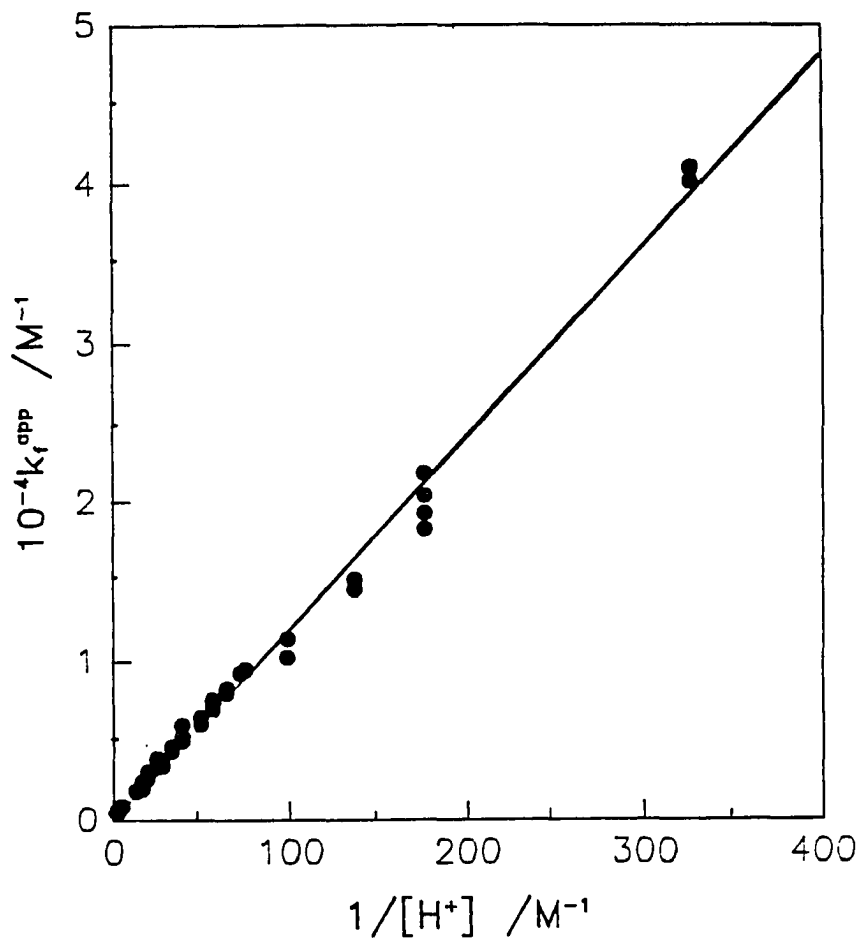


Figure III-12. The plot of k_f^{app} vs. $1/[H^+]$ for the reaction of $(H_2O)_2Co(dmgbF_2)_2$ with pseudo-first-order concentrations of Fe^{3+} ($k_f^{app} = k_{obs}/[Fe^{3+}]_{ave}$, $[Fe^{3+}] = 2.0 - 30 \times 10^{-4} M$, $\mu = 0.500 M$, $T = 25.0 \text{ } ^\circ C$); only the forward reaction was observed in the stopped-flow experiments

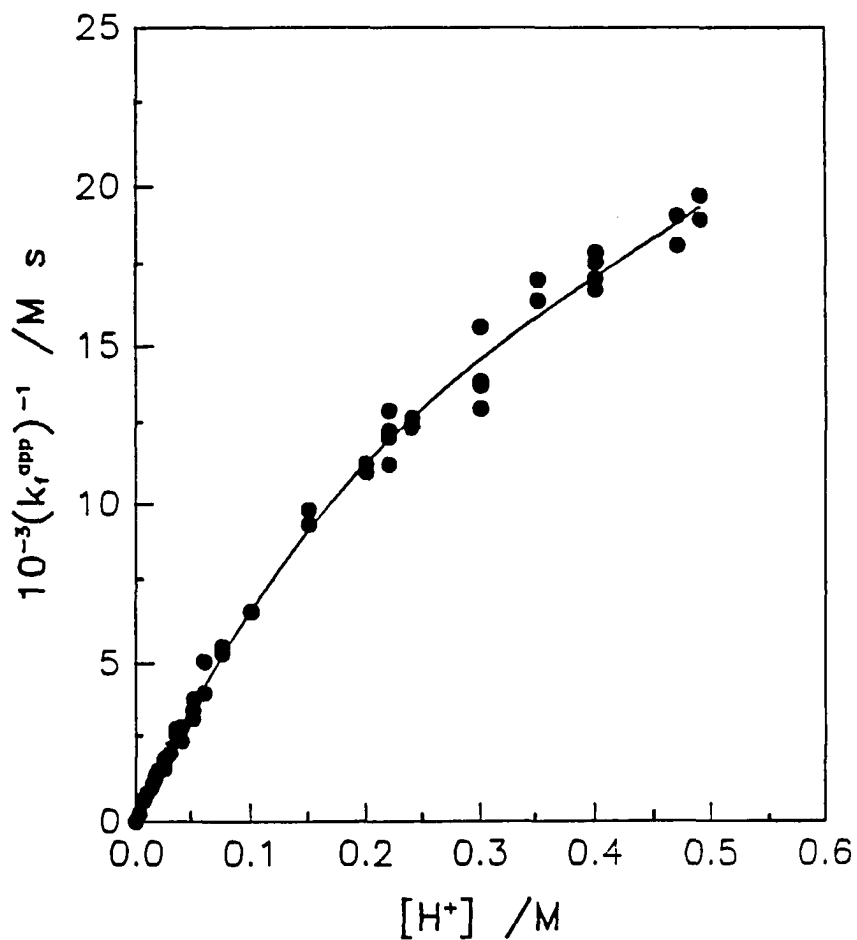


Figure III-13. The plot of $1/k_f^{\text{app}}$ vs. $[\text{H}^+]$ for the reaction of $(\text{H}_2\text{O})_2\text{Co}(\text{dmgBF}_2)_2$ with pseudo-first-order concentrations of Fe^{3+} ($k_f^{\text{app}} = k_{\text{obs}}/[\text{Fe}^{3+}]_{\text{ave}}$, $[\text{Fe}^{3+}] = 2.0 - 30 \times 10^{-4} \text{ M}$, $\mu = 0.500 \text{ M}$, $T = 25.0 \text{ }^\circ\text{C}$); only the forward reaction was observed in the stopped-flow experiments

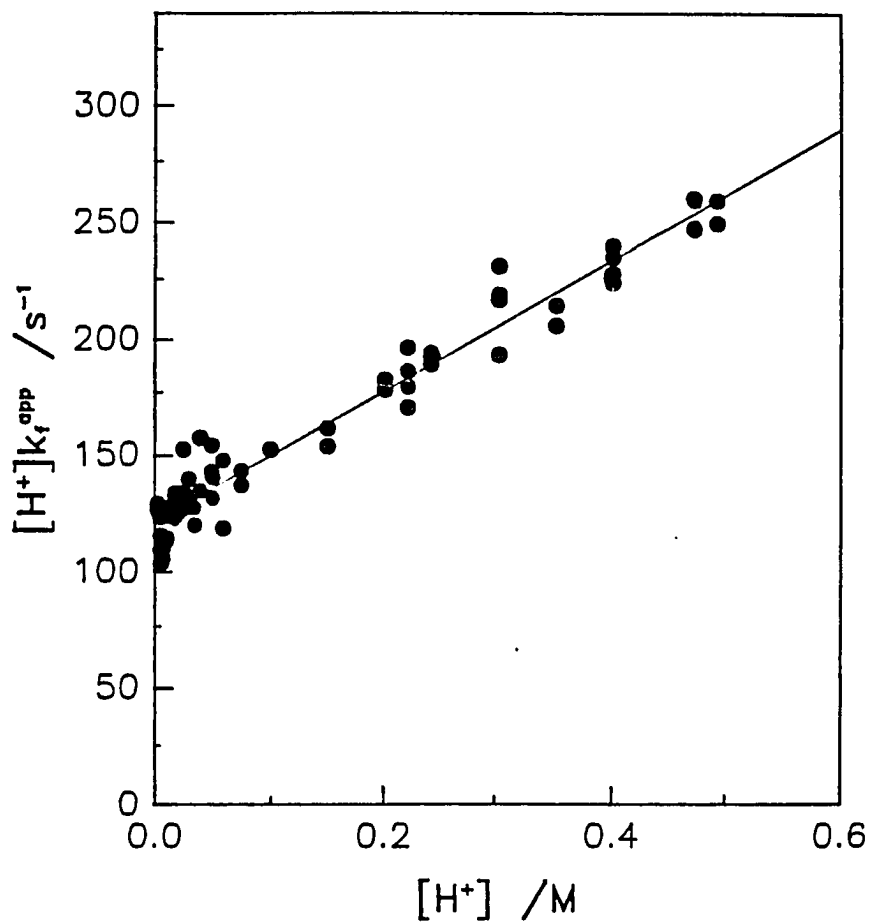


Figure III-14. The plot of $[H^+]k_f^{app}$ vs. $[H^+]$ for the reaction of $(H_2O)_2Co(dmgbF_2)_2$ with pseudo-first-order concentrations of Fe^{3+} ($k_f^{app} = k_{obs}/[Fe^{3+}]_{ave}$, $[Fe^{3+}] = 2.0 - 30 \times 10^{-4} M$, $\mu = 0.500 M$, $T = 25.0 \text{ }^\circ C$); only the forward reaction was observed in the stopped-flow experiments

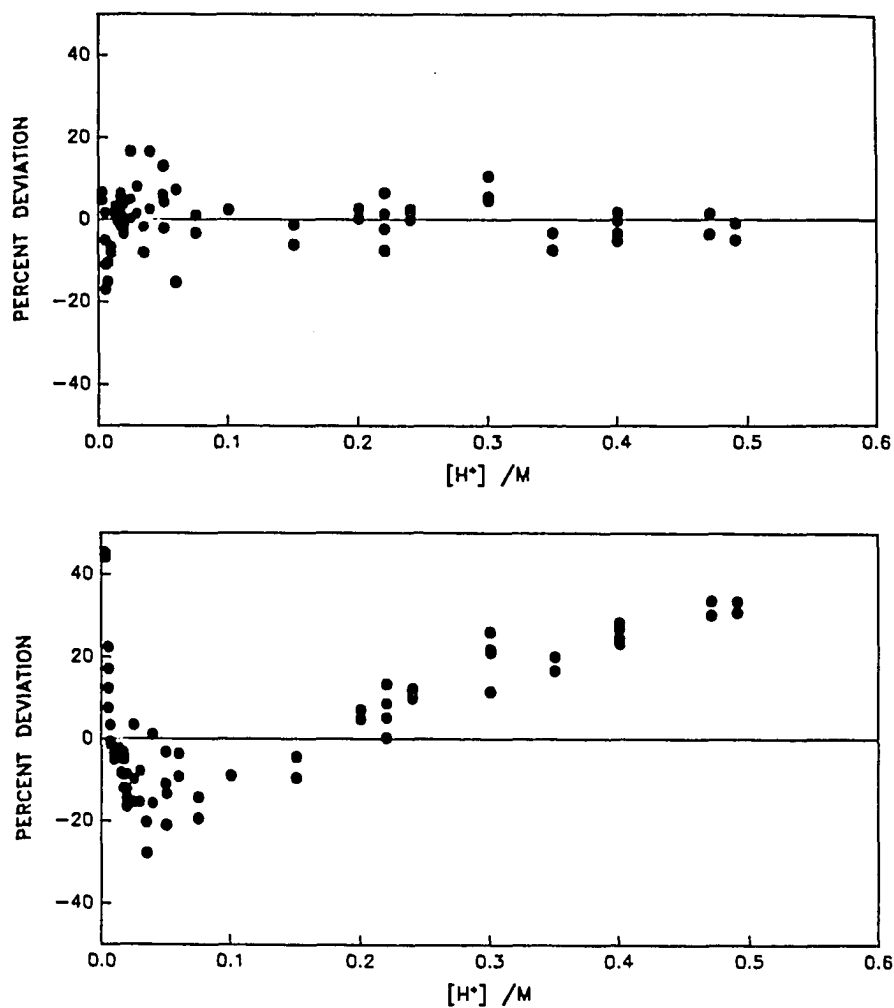


Figure III-15. The plots of percent deviation vs. $[H^+]$ for the reaction of $(H_2O)_2Co(dmgbF_2)_2$ with pseudo-first-order concentrations of Fe^{3+} ($k_f^{app} = k_{obs}/[Fe^{3+}]_{ave}$, $[Fe^{3+}] = 2.0 - 30 \times 10^{-4} M$, $\mu = 0.500 M$, $T = 25.0 \text{ }^\circ C$); only the forward reaction was observed in the stopped-flow experiments. The top figure is the parallel path percent deviation and the bottom figure is the consecutive path percent deviation

DISCUSSION

Structure

Most cobalt(II) complexes which contain nonmacrocylic tetradentate ligands with nitrogen and/or oxygen donors are high spin ($\mu_{\text{eff}} = 4.9 - 5.2$ B.M.), five- or six-coordinate species.²⁰ The axial coordination sites are generally occupied by solvent molecules or by anionic ligands. In order to stabilize cobalt(II) complexes in a low spin environment, various workers have used unsaturated tetradentate macrocyclic ligands with large field strengths. Endicott and coworkers²¹ have reported a list of the cobalt(II) fourteen-membered tetraaza macrocyclic complexes which contain cobalt-oxygen bonds in their axial positions, Table III-8. The complex $(\text{CH}_3\text{OH})_2\text{Co}(\text{dmgBF}_2)_2$ can be compared with these complexes and useful conclusions about the nature of this compound can be drawn.

The equatorial ligands in the complexes studied all have high ligand fields. The cobalt(II) complexes are therefore low-spin d^7 molecules. This electronic configuration is shown by the effective magnetic moments at room temperature, Table III-8.

As expected for low-spin d^7 complexes, the magnetic moment values are only slightly higher than the spin-only value for one unpaired electron, 1.73 B.M. The values are also much lower than the spin-only moment for the high-spin d^7 electronic configuration having three unpaired electrons and a magnetic moment value of 3.46 B.M. This electronic configuration leads to a Jahn-Teller like distortion, weak cobalt-oxygen axial bonds, and very labile axial ligands.

The metal ion in $(\text{CH}_3\text{OH})_2\text{Co}(\text{dmgBF}_2)_2$ and in several other complexes

**Table III-8. Bond Lengths and Magnetic Susceptibilities of
Some Cobalt(II) Macrocyclic Complexes**

Complex	Equatorial M-N		Axial	μ_{eff} (B.M.)	$E^{\circ a}$ (V.)
	amine	imine(Å)	M-O(Å)		
[Co(AL) ₂ (H ₂ O) ₂]		1.88 ^{b,c}	2.27 ^{b,c}	1.92 ^{b,d}	0.649 ^b
[Co(BL)(OH ₂)](ClO ₄) ₂		1.90 ²²	2.29 ²²	1.82 ^{22,e}	0.564 ²¹
[Co(CL)(OH ₂) ₂](ClO ₄) ₂	1.98 ²³	1.92 ²³	2.28, 2.39 ²³		0.600 ²¹
[Co(DL)(OH ₂) ₂](ClO ₄) ₂	1.98 ²⁴	1.92 ²⁴	2.48 ²⁴	1.86 ^{24,d}	0.564 ²¹
[Co(EL)(OH ₂)](PF ₆) ₂	1.99 ²⁰	1.92 ²⁰	2.28 ²⁰	2.05 ^{20,f}	
[Co(FL)(OH ₂) ₂](ClO ₄) ₂				2.03 ^{25,d}	0.567 ²¹
[Co(GL) ₂ (OH ₂) ₂]				1.92 ^{26,d}	0.36 ²⁷

"AL" = the monoanion of (difluoroboryl)2,3-butanedione dioxime = (dmgBF₂)⁻; "BL" = 2,3,9,10-tetramethyl-1,4,8,11-tetraazacyclotetradeca-1,3,8,10-tetraene; "CL" = 12,14-dimethyl-1,4,8,11-tetraazacyclotetradeca-1,11,diene-13-one; "DL" = 5,7,7,12,14,14-hexamethyl-1,4,8,11-tetraazacyclodeca-4,11-diene; "EL" = 2,4,-dimethyl-1,5,8,12-tetraazacyclo-tetradeca-1,4-diene; "FL" = 2,12-dimethyl-3,7,11,17-tetraazabicyclo[11.3.1]septadeca-1(17),2,11,13,15-pentaene; "GL" = the monoanion of 2,3-butanedione dioxime = (dmgH)⁻.

^aCobalt(III)/(II) reduction potential vs. NHE.

^bThis work.

^c[Co(AL)₂(CH₃OH)₂].

^dGouy method-solid state.

^eEvans Method (1.0 M NaCl).

^fFaraday Method.

listed in Table III-1 lie on crystallographic centers of inversion; thus, these complexes have crystallographic molecular symmetry (-1) with the metal(II) ion centered in the equatorial plane. This molecular symmetry is common in these types of macrocyclic complexes and confirms the planarity of the equatorial ligand.

A dramatic dependence of axial bond lengths on the equatorial ligand for cobalt(II) complexes has been reported.²³ The authors observed that the axial cobalt(II)-OH₂ bond is very susceptible to distortions induced by nonbonded repulsive (steric) or electronic interactions with substituents of the equatorial ligand. The axial bonding interactions also increase in strength with increased unsaturation in the equatorial ligand. The data collected in Table III-8 are consistent with these assertions. The equatorial Co-N (imine) and Co-N (amine) bond lengths are constant (1.92 ± 0.02 Å and 1.98 ± 0.01 Å, respectively) for complexes with 14-membered macrocyclic ligands. The Co-O axial bond lengths in Table III-8, vary within the range of 2.27 to 2.48 Å. This variation is a direct result of the Jahn-Teller like distortion seen for low-spin d⁷ cobalt(II) complexes. The degree of the axial elongation can be best determined when the elongated axial bond lengths are compared with a suitable standard. A number of standards can be chosen. The most suitable one appears to be a high-spin cobalt(II) complex (no axial distortion) containing a nonmacrocyclic tetradentate equatorial ligand system. One such complex is aquo-NN'-ethylenebis-(3-methoxysalicylideneiminato)-cobalt(II) with the cobalt(II)-oxygen axial bond distance of 2.12 Å.²⁸ This value is close to the reported six-coordinate cobalt(II)-oxygen bond distance of 2.13 Å for CoO,²⁹ 2.12 Å for CoCl₂·6H₂O,³⁰ and an accepted average cobalt(II)-oxygen

bond distance of $2.14 \pm .01 \text{ \AA}$.³¹ It is clear from Table III-8 that the Co-N equatorial and the Co-O axial bond lengths for $(\text{CH}_3\text{OH})_2\text{Co}(\text{dmgBF}_2)_2$ agree very well with other values characteristic of this collection of cobalt(II) macrocyclic complexes.

Several studies indicate that various macrocyclic cobalt(II) species are five-coordinate in aqueous solution²², but are tetragonally distorted six-coordinate diaquo species in the solid state.³¹ Since the isolated species in this crystallographic investigation is the six-coordinate bismethanol complex, we cannot confirm by direct structural analysis the coordination number of the aquo species. However, since water is a better Lewis base and thus more tightly bound than methanol, it is very probable that the solid state aquo species is a diaquo, six-coordinate complex. Additional evidence for the six-coordinate diaquo species in the solid state comes from the elemental analyses of $(\text{H}_2\text{O})_n\text{Co}(\text{dmgBF}_2)_2$. The observed and calculated cobalt, carbon, hydrogen, and nitrogen analyses consistently show a much better agreement when the molecular weight for the diaquo species is used in the calculations rather than the molecular weight of the five-coordinate monoquo species.⁹

Several conclusions have been drawn based on structural studies of several cobalt(II) macrocycles. These conclusions should also apply in the case of $(\text{CH}_3\text{OH})_2\text{Co}(\text{dmgBF}_2)_2$. These conclusions are: (1) Low spin d^7 systems are axially labile. (2) Axial lability in these systems is correlated with an elongation of axial bond lengths found in X-ray structural studies. (3) Low temperature EPR studies indicate that the unpaired electron in these systems is in an axial orbital of significant d_{z^2} character. (4) The range of axial bonding interactions, including an apparent axial trans influence, is at least qualitatively described by a

three-center, five-electron bonding model. (5) The inferred synergistic trans influence has significant implications for models of inner-sphere electron transfer reactions.²³

EPR spectroscopic analysis

The EPR spectra of toluene/dichloromethane/Lewis base solutions indicate a nearly axial symmetry about the cobalt(II) ion. This result is consistent with the known electronic structure of low spin cobalt(II) complexes which are d^7 and have one paired electron in the d_z^2 orbital.

The EPR analysis of the oxygen Lewis base adducts of $(B)_2Co(dmgBF_2)_2$ presents a problem because it is difficult to assign unambiguously the presence of two axial base ligands for the cobalt complex in solution at low temperature. Coordination of bases possessing nuclei with nonzero nuclear moments give rise to hyperfine interactions with these nuclei. Nitrogen donor 2:1 adducts are easily recognized by the characteristic five line hyperfine pattern from two equivalent nitrogens. This is not the case for oxygen Lewis bases. The ^{16}O nucleus does not have a nuclear spin, thus, EPR hyperfine splitting cannot be observed. This problem, although not addressed in this study, was overcome for the nearly identical complex $(B)_2Co(dpgBF_2)_2$.¹⁶ Tovrog showed the coordination of oxygen Lewis bases by first observing the five line hyperfine splitting by the two axially coordinated nitrogen bases in $(CH_3CN)_2Co(dpgBF_2)_2$. He then added a stoichiometric amount of an oxygen donor Lewis base, THF, which produced three line nitrogen hyperfine splitting indicating the complex formed in solution was $(CH_3CN)(THF)Co(dpgBF_2)_2$. Addition of excess THF resulted in complete loss of the nitrogen hyperfine splitting indicating $(THF)_2Co(dpgBF_2)_2$ was formed. Due to the similarity of the

molecular and electronic structure of $(B)_2Co(dpgBF_2)_2$ and $(B)_2Co(dmgbF_2)_2$ evidenced by the almost perfect match of the EPR spectra, a six-coordinate arrangement can be expected for $(CH_3OH)_2Co(dmgbF_2)_2$ and $((CH_3)_2CO)_2Co(dmgbF_2)_2$. Evidence for the six-coordinate nature of $(CH_3CN)_2Co(dmgbF_2)_2$ in solution comes from a more informative EPR spectrum. The five line nitrogen hyperfine splitting seen for this complex illustrates a six-coordinate macrocyclic molecule with two CH_3CN molecules bound through the nitrogens in equivalent axial positions.

Tovrog has indicated in the study of $(B)_2Co(dpgBF_2)_2$ and other cobalt(II) macrocyclic complexes, that a strong Lewis acidity is exhibited by $(B)_2Co(dpgBF_2)_2$ relative to $(B)_2Co(dpgH)_2$, four-coordinate Schiff bases and porphyrin complexes.¹⁶ The strong Lewis acidity is due to the inductive withdrawal of electron density by the oxime oxygens and BF_2^+ groups. This inductive effect is clearly seen in the example, $(B)_2Co(dpgBF_2)_2$ vs. $(B)_2Co(dpgH)_2$ and should be equally valid for the case $(B)_2Co(dmgbF_2)_2$ vs. $(B)_2Co(dmgbH)_2$. This enhanced Lewis acidity is also indicated by the more positive cobalt(III)/(II) reduction potential for $(H_2O)_2Co(dmgbF_2)_2$ vs. $(H_2O)_2Co(dmgbH)_2$ (0.649 V vs 0.36 V relative to NHE).²⁷

Chemical characterization of cobalt(III)/cobalt(II)

$(H_2O)_2Co(dmgbF_2)_2$ is stable as a solid in air for months and in water for hours. The stability of cobalt(II) decreases as the acid concentration increases while the cobalt(III)⁺ is also unstable in acidic solutions. At 0.01 - 0.50 M $HClO_4$ the decomposition of cobalt(III)⁺ formed from the stoichiometric oxidation of cobalt(II) with Fe^{3+} is essentially complete within an hour, as determined from the absorbance

versus time traces at $\lambda = 456$ nm.

The observation of the equilibrium, equation 6, led to the determination of the equilibrium constant by static and kinetic means. The less precise value of the equilibrium constant from the kinetics (31.4) agrees quite well with that of the static equilibrium constant, 34.7. The cobalt(III)/(II) reduction potential of 0.649 ± 0.003 V vs. NHE was determined by relating the static equilibrium constant to the reduction potential of Fe(III)/(II), equation 18.

$$E^{\circ}(\text{Fe(III)/(II)}) - E^{\circ}(\text{Co(III)/(II)}) = RT \ln(K_{\text{eq}}) / nF \quad (18)$$

$$E^{\circ}(\text{Fe(III)/(II)}) = 0.740 \text{ V} \quad (\text{ref. 11})$$

This value is similar to those of other unsaturated cobalt macrocycles listed in Table III-8. The reduction potential range listed, 0.36 - 0.649 V, places $(\text{H}_2\text{O})_2\text{Co}(\text{dmgBF}_2)_2$ at the more positive end of this range due to the electron withdrawing effect of the BF_2^+ substituents. The dramatic stabilization of the cobalt(II) oxidation state is clearly indicated by the more positive reduction potential for the BF_2^+ substituted cobaloxime, 0.649 V vs. 0.36 V for the cobaloxime.²⁷

The BF_2^+ substituents also structurally stabilize the equatorial ligand system relative to the parent cobaloxime. The BF_2^+ substituents are located in the bridging positions of the equatorial ligand system, thus forming an authentic macrocycle. This contrasts with the parent cobaloxime's pseudo-macrocylic ring where the hydrogen atoms are weakly bound in the bridging positions.

Kinetics and mechanism

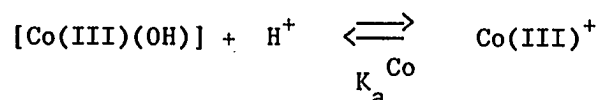
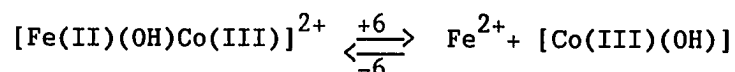
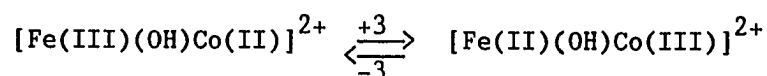
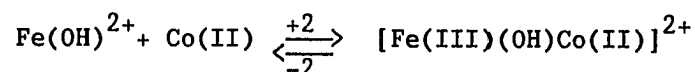
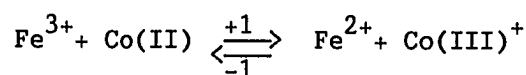
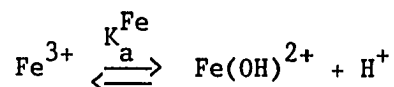
The forward rate constant for the reaction of cobalt(II) with Fe^{3+} , equation 6, determined by the opposing pseudo-first-order reactions method, is in good agreement with the forward rate constant determined independently by the stopped-flow method. At 0.400 M HClO_4 the values are: $k_f = 575 \pm 45 \text{ M}^{-1}\text{s}^{-1}$ - opposing pseudo-first-order reactions method vs. $589 \pm 16 \text{ M}^{-1}\text{s}^{-1}$ - stopped-flow method with high $[\text{Fe(III)}]$. The value for k_r ($18.3 \pm 1.8 \text{ M}^{-1}\text{s}^{-1}$ at 0.400 M HClO_4) has been determined only by the opposing pseudo-first-order reactions method, but it is believed to be an equally accurate value. The consistency of these results and of the chemical formulation is indicated by the agreement of the kinetic and thermodynamic data.

The mechanism of oxidation of the cobalt(II) was probed by the reaction of Fe^{3+} with cobalt(II) in acidic aqueous solution in an effort to understand the potential of cobalt(II) as an inner-sphere reactant. Since the observed reaction rate increased with a decrease in acid concentration, the two common algebraic functions which show this type of dependence are derived from the parallel and consecutive path mechanisms, Schemes III-1 and III-2.

Both of these mechanisms follow second-order rate expressions with respect to the metal ion concentrations and in each case the apparent rate constant increases as the acid concentration decreases.

The mechanistic interpretation of the two schemes is distinctly different. The parallel path mechanism is readily interpreted in terms of the known acid-ionization preequilibrium, equation 19.



Scheme III-1.Parallel Path-Complete MechanismMechanismRate Law - Forward Reaction

$$\frac{-d[\text{Co(II)}]}{dt} = \left(k_1 + \frac{k_2 k_3 K_a^{\text{Fe}}/k_{-2}}{[\text{H}^+]} \right) [\text{Co(II)}][\text{Fe}^{3+}]$$

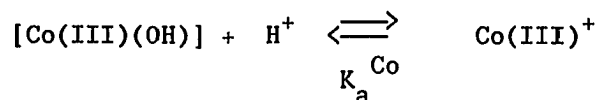
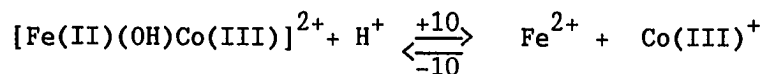
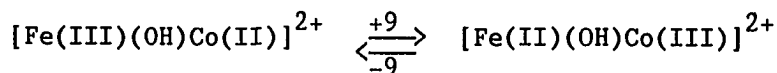
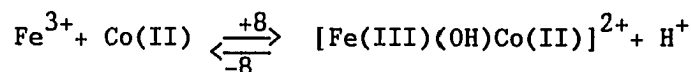
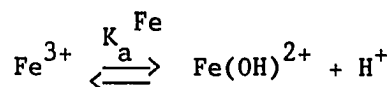
Rate Law - Reverse Reaction

$$\frac{-d[\text{Co(III)}]}{dt} = \left(k_{-1} + \frac{k_{-6} k_{-3} K_a^{\text{Co}}/k_6}{[\text{H}^+]} \right) [\text{Co(III)}][\text{Fe}^{2+}]$$

Algebraic Forms

$$k_f^{\text{app}} = \frac{k_f^{\text{obs}}}{[\text{Fe}^{3+}]} = \left(A + \frac{B}{[\text{H}^+]} \right); \quad k_r^{\text{app}} = \frac{k_r^{\text{obs}}}{[\text{Fe}^{2+}]} = \left(a + \frac{b}{[\text{H}^+]} \right)$$

$$A = k_1; \quad B = k_2 k_3 K_a^{\text{Fe}}/k_{-2}; \quad a = k_{-1}; \quad b = k_{-6} k_{-3} K_a^{\text{Co}}/k_6$$

Scheme III-2.Consecutive Path-Complete MechanismMechanismRate Law - Forward Reaction

$$\frac{-d[\text{Co}(\text{II})]}{dt} = \left(\frac{k_8 k_9 / k_{-8}}{k_9 / k_{-8} + [\text{H}^+]} \right) [\text{Co}(\text{II})][\text{Fe}^{3+}]$$

Rate Law - Reverse Reaction

$$\frac{-d[\text{Co}(\text{III})]}{dt} = \left(\frac{k_{-10} k_{-9} / k_{10}}{k_{-9} / k_{-8} + [\text{H}^+]} \right) [\text{Co}(\text{III})][\text{Fe}^{2+}]$$

Algebraic Forms

$$k_f^{\text{app}} = \frac{k_f^{\text{obs}}}{[\text{Fe}^{3+}]} = \left(\frac{C}{D + [\text{H}^+]} \right); \quad k_r^{\text{app}} = \frac{k_r^{\text{obs}}}{[\text{Fe}^{2+}]} = \left(\frac{c}{d + [\text{H}^+]} \right)$$

$$C = k_8 k_9 / k_{-8}; \quad D = k_9 / k_{-8}; \quad c = k_{-10} k_{-9} / k_{10}; \quad d = k_{-9} / k_{10}$$

The equilibrium constant is small ($K_a = 1.94 \times 10^{-3}$ M) compared to the range of the acid concentrations used (0.003 - 0.50 M HClO_4) such that the reaction rate is readily attributed to parallel reactions of the two Fe(III) species, Fe^{3+} and $\text{Fe}(\text{OH})^{2+}$. Conversely, the consecutive path mechanism incorporates only one reaction path.

Both of these mechanisms have kinetically equivalent variations. The essence of these variations has been explored in detail for the similar reaction of Cr^{2+} with V^{3+} .^{32,33}

It is clear from the kinetic data analysis, detailed in the results section, that the parallel path rate law offers a more consistent numerical fit of the data. On this basis, the consecutive path mechanism can be discarded. Two mechanistic interpretations consistent with the parallel path rate law can be proposed. These interpretations are kinetically equivalent and further distinction between them is not possible with the experimental data obtained. However, a detailed discussion of these variations is useful in understanding the proposed parallel path mechanisms.

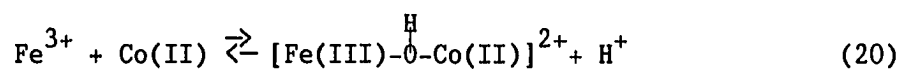
The first path in these mechanisms is acid independent and designated step 2 of Scheme III-1. This is the reversible reaction of Fe^{3+} with cobalt(II) and represents a minor path, especially at lower acid concentrations. There is no clear basis in which to determine the mechanism details of this pathway. It can be described as either an outer- or an inner-sphere, aquo-bridged, electron transfer reaction.

The second path of the parallel path mechanism is most commonly interpreted as the reaction of $\text{Fe}(\text{OH})^{2+}$ with cobalt(II). The concentration of $\text{Fe}(\text{OH})^{2+}$ is controlled by the acid concentration through the acid ionization equilibrium of Fe^{3+} , step 1 of Scheme III-1. This

species is ideally prepared to donate the hydroxide ligand as the electron transfer bridge. The reaction path begins by the dissociation of a proton to form $\text{Fe}(\text{OH})^{2+}$, followed by the association of the reactants to form the precursor complex, steps 1 and 3. Upon intramolecular electron transfer in the rate determining step, step 4, the successor complex dissociates, accompanied by protonation, in a rapid step to form the products. The precise timing of the protonation cannot be determined from the experiments since the successor complex cannot be directly observed. However, the protonation probably occurs after the dissociation of the successor complex.

The dissociation of the successor complex and the hydroxide bridge transfer to the cobalt(III) is supported by the substitution properties of the two metals in their various oxidation states. Iron(III) and cobalt(III) are substitutionally inert, while iron(II) and cobalt(II) are labile. This insures a bridging ligand on the iron(III) and an open coordination site on the cobalt(II) promoting the association. After the rate-determining electron transfer step, the substitution properties on the metal centers reverse. The iron-oxygen bond of the bridge breaks, leaving the hydroxide on the cobalt which is protonated in a fast step.

The kinetically equivalent variation of the inverse acid dependent path has the precursor complex formed directly in a reaction between Fe^{3+} and cobalt(II), equation 20.



The sequence of events for the identical precursor complex is the same from this point on assuming electron transfer is again the rate limiting

step. The timing of the loss of the proton in equation 20 is the only difference between this interpretation and the original variation described in the two preceding paragraphs and illustrated in Scheme III-1. In either case, since these variations are kinetically equivalent, it is not possible to distinguish between these by further analysis of the data.

Analysis of the rate parameters

The analysis of the rate parameters allows the calculation and/or estimation of the rate constants for the forward and reverse reactions, Table III-9. The principle of microscopic reversibility relates the forward rate parameters A and B to the reverse rate parameters a and b, equations 21 and 22. Equation 22 yields values for the reverse parameters ($a = 8.3 \pm 1.0 \text{ M}^{-1}\text{s}^{-1}$ and $b = 3.5 \pm 0.3 \text{ s}^{-1}$).

$$(A + B/[H^+]) = (a + b/[H^+])K_{\text{eq}} \quad (21)$$

$$K_{\text{eq}} = 34.7 = A/a = B/b \quad (22)$$

With these reverse parameters the composite reverse rate constant ($\text{HClO}_4 = 0.400 \text{ M}$) is calculated to be $k_r = 17.1 \text{ M}^{-1}\text{s}^{-1}$. This is consistent with the experimentally determined composite reverse rate constant ($k_r = 18.3 \pm 1.8 \text{ M}^{-1}\text{s}^{-1}$).

The value of K_a^{Fe} is $1.94 \times 10^{-3} \text{ M}$ ($\mu = 0.500 \text{ M}$).³⁴ The value of K_a^{Co} however, is not known but can be estimated. This estimate should reflect an enhanced acidic nature relative to the parent cobaloxime ($K_a = 7.2 \times 10^{-6} \text{ M}$),³⁵ due to the presence of the two BF_2^+ substituents. The value of $K_a^{\text{Co}} \sim 10^{-4} \text{ M}$ appears to be a reasonable estimate to $\pm 1 \text{ p}K_a$ units.

The bimolecular rate constants k_1 and k_{-1} come directly from the parameters A and a ($k_1 = 289 \text{ M}^{-1}\text{s}^{-1}$ and $k_{-1} = 8.3 \text{ M}^{-1}\text{s}^{-1}$). Using the values of K_a^{Fe} and K_a^{Co} , the composite rate constants associated with B and b can be evaluated ($k_2k_3/k_{-2} = 6.2 \times 10^4 \text{ M}^{-1}\text{s}^{-1}$, $k_{-4}k_{-3}/k_4 = 3.5 \times 10^4 \text{ M}^{-1}\text{s}^{-1}$). The bimolecular rate constants k_2 and k_{-4} have upper limits defined by diffusion control ($k_2, k_{-4} < 10^{10} \text{ M}^{-1}\text{s}^{-1}$). The unimolecular rate constants, k_{-2} and k_4 , can be estimated by the known rates of water exchange on cobalt(II) macrocycles²³ and Fe^{2+} ($k_{-2} \sim 10^9 \text{ s}^{-1}$ and $k_4 \sim 10^7 \text{ s}^{-1}$). Since k_3 is the rate determining step in the forward direction and k_{-3} the rate determining step in the reverse direction, a lower limit on these rate constants can be estimated, equations 23, 24 and 25.

$$\frac{k_2k_3}{k_{-2}} = 6.2 \times 10^4 \text{ M}^{-1}\text{s}^{-1} = \frac{(<10^{10} \text{ M}^{-1}\text{s}^{-1})k_3}{(10^9 \text{ s}^{-1})} < (10 \text{ M}^{-1})k_3 \quad (23)$$

$$\frac{k_{-4}k_{-3}}{k_4} = 3.5 \times 10^4 \text{ M}^{-1}\text{s}^{-1} = \frac{(<10^{10} \text{ M}^{-1}\text{s}^{-1})k_{-3}}{(10^7 \text{ s}^{-1})} < (10^3 \text{ M}^{-1})k_{-3} \quad (24)$$

$$k_3 > 6.2 \times 10^3 \text{ s}^{-1} \quad ; \quad k_{-3} > 35 \text{ s}^{-1} \quad (25)$$

Upper limits on k_3 and k_{-3} can be estimated since these reactions are rate determining and slower than competing reactions. The values of k_3 and k_{-3} are thus: $k_3 < 10^9 \text{ s}^{-1}$ and $k_{-3} < 10^7 \text{ s}^{-1}$.

The assumptions used in the analysis are consistent with reported rate constant and diffusion control limits. The rate parameters and constants, Table III-9, therefore represent a satisfactory and entirely consistent description of the parallel path mechanism for the reaction of $(\text{H}_2\text{O})_2\text{Co}(\text{dmgBF}_2)_2$ with iron(III).

Table III-9. Summary of the Equilibrium and Rate Constants

$$K_a^{\text{Fe}} = 1.94 \times 10^{-3} \text{ M}$$

$$K_a^{\text{Co}} \sim 1 \times 10^{-4} \text{ M}$$

$$k_1 = 289 \text{ M}^{-1}\text{s}^{-1}$$

$$k_{-1} = 8.3 \text{ M}^{-1}\text{s}^{-1}$$

$$k_2 < 10^{10} \text{ M}^{-1}\text{s}^{-1}$$

$$k_{-2} \sim 10^9 \text{ s}^{-1}$$

$$6 \times 10^3 \text{ s}^{-1} < k_3 < 10^9 \text{ s}^{-1}$$

$$35 < k_{-3} < 10^7 \text{ s}^{-1}$$

$$k_4 \sim 10^7 \text{ s}^{-1}$$

$$k_{-4} < 10^{10} \text{ M}^{-1}\text{s}^{-1}$$

SUMMARY

The structural aspects of $(\text{H}_2\text{O})_2\text{Co}(\text{dmgBF}_2)_2$ have been explored principally through the determination of the crystal structure of $(\text{CH}_3\text{OH})_2\text{Co}(\text{dmgBF}_2)_2$. Several important questions have been addressed in this study: 1) the geometric configuration of the axial and equatorial ligand system, 2) the coordination number of the complex in the solid state, and 3) the Jahn-Teller like axial distortion of the low spin d^7 complex.

The chemical characterization has also been investigated by various methods. $(\text{H}_2\text{O})_2\text{Co}(\text{dmgBF}_2)_2$ can be oxidized to the more acid-sensitive cobalt(III)⁺ form by various oxidants and quantitatively reduced by various reductants. This illustrates the reversible redox character of $(\text{H}_2\text{O})_2\text{Co}(\text{dmgBF}_2)_2$ which was confirmed by the observed chemical equilibrium, equation 2, which also yielded the value of the cobalt(III)/(II) reduction potential. The E^0 value clearly indicates a stabilization of the cobalt(II) oxidation state relative to the parent cobaloxime.

A correlation of the relevant structural and chemical features of cobalt(II) macrocyclic complexes has confirmed the similarity of $(\text{H}_2\text{O})_2\text{Co}(\text{dmgBF}_2)_2$ to other 14-membered cobalt(II) macrocyclic complexes.

The reactivity of $(\text{H}_2\text{O})_2\text{Co}(\text{dmgBF}_2)_2$ has been probed by studying the reaction with Fe^{3+} . Based on the various mathematical treatments and graphical analyses of the kinetic data, the reaction is proposed to take place by a parallel path mechanism, as do many other oxidations by Fe^{3+} . This analysis suggests $(\text{H}_2\text{O})_2\text{Co}(\text{dmgBF}_2)_2$ will be a useful acid-compatible reagent for probing the outer- and inner-sphere reactivity of other oxidizing reagents.

BIBLIOGRAPHY

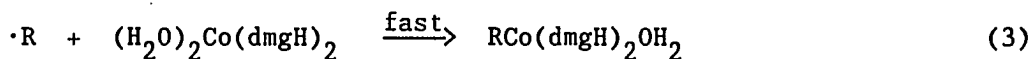
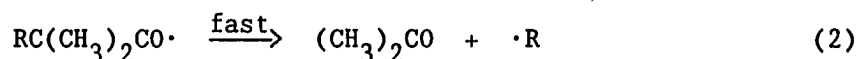
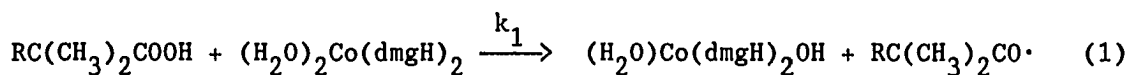
1. Lenhert, P. G.; Hodgkin, D. C. Nature, 1961, 192, 937.
2. Cobaloxime = $\text{Co}(\text{dmgH})_2$ (where dmgH^- represents the monoanion of dimethylglyoxime (2,3-butanedione dioxime), Schrauzer, G. N. Acc. Chem. Res., 1968, 4, 97.
3. Wong, Chung-Lai; Switzer, J. A.; Balakrishnan, K. P.; Endicott, J. F. J. Am. Chem. Soc., 1980, 102, 5511.
4. Schrauzer, G. N.; Windgassen, R. J. J. Am. Chem. Soc., 1966, 88, 3738.
5. Drago, R. S.; Tovrog, B. S.; Kitko, D. J. J. Am. Chem. Soc., 1976, 98, 5144.
6. Schrauzer, G. N.; Sibert, J. W.; Windgassen, R. J. J. Am. Chem. Soc., 1968, 90, 6681.
7. Schrauzer, G. N.; Weber, J. H.; Beckman, J. M. J. Am. Chem. Soc. 1970, 92, 7078.
8. Schrauzer, G. N.; Deutsch, E. J. Am. Chem. Soc., 1969, 91, 3341.
9. Bakac, A.; Espenson, J. H. J. Am. Chem. Soc., 1984, 106, 5197.
10. Gjerde, H. B.; Espenson, J. H. Organometallics, 1982, 1, 435.
11. Weaver, M. J.; Nettles, S. M. Inorg. Chem., 1980, 19, 1641.
12. Carlyle, D. W.; Espenson, J. H. J. Am. Chem. Soc., 1968, 90, 2272.
13. Jacobson, R. A. J. Appl. Crystallogr., 1976, 9, 115.
14. Main, P.; Woolfson, M. M.; Germain, G. "MULTAN, a Computer Program for the Automated Solution of Crystal Structures", University of York, Great Britain.
15. Angelici, R. J. "Synthesis and Technique in Inorganic Chemistry", 2nd edition, W. B. Saunders Company: Philadelphia, 1977; p 46.
16. Tovrog, B. S. Diss. Abstr. Int. B, 1976, 36(9), 4471.
17. Walker, F. A. J. Am. Chem. Soc., 1970, 92, 4235.
18. Hoffman, B. M.; Diemente, D. L.; Basolo, F. J. Am. Chem. Soc., 1970, 92, 61.

19. Nicholson, R. S.; Shane, I. Anal. Chem., 1964, 36, 706.
20. Roberts, G. W.; Cummings, S.C.; Cunningham, J. A. Inorg. Chem., 1976, 15, 2503.
21. Endicott, J. F.; Durham, B.; Glick, M. D.; Anderson, T. J.; Kuszaj, J. M.; Schmonsees, W. G.; Balakrishnan, K. P. J. Am. Chem. Soc., 1981, 103, 1431.
22. Tait, A. M.; Busch, D. H. Inorg. Chem., 1976, 15, 197.
23. Endicott, J. F.; Lilie, J.; Kuszaj, J. M.; Ramaswamy, B. S.; Schmonsees, W. G.; Simic, M. G.; Glick, M. D.; Rillema, J. A. J. Am. Chem. Soc., 1977, 99, 429.
24. Glick, M. D.; Schmonsees, W. G.; Endicott, J. F. J. Am. Chem. Soc., 1974, 96, 5661.
25. Long, K. M.; Busch, D. H. Inorg. Chem., 1970, 9, 505.
26. Sharpe, A. G.; Wakefield, D. B. J. Chem. Soc., 1957, 281.
27. Espenson, J. H.; Heckman, R. A. Inorg. Chem., 1979, 18, 38.
28. Calligaris, M.; Nardin, G.; Randaccio, L. J. Chem. Soc. Dalton, 1974, 1903.
29. MacGillavry, C. H.; Rieck, G. D. "International Tables for X-Ray Crystallography, Vol III Physical and Chemical Tables"; The Kynoch Press: Birmingham, Great Britain, 1962.
30. Wyckoff, R. W. G. "Crystal Structures, Vol. 3"; John Wiley and Sons: New York, 1965.
31. Endicott, J. F.; Glick, M. D.; Kuszaj, J. M. J. Am. Chem. Soc., 1973, 95, 5097.
32. Espenson, J. H. Inorg. Chem., 1966, 4, 1025.
33. Haim, A. Inorg. Chem., 1966, 5, 2081.
34. Milburn, R. M.; Vosburgh, W. C. J. Am. Chem. Soc., 1955, 77, 1352.
35. Costa, G. Pure and Applied Chem., 1972, 30, 344.

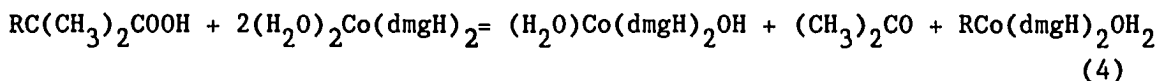
APPENDIX. CHARACTERIZATION, KINETICS, AND REACTION MECHANISMS FOR THE
REACTION OF $(\text{H}_2\text{O})_2\text{Co}(\text{dmgBF}_2)_2$ WITH VARIOUS OXIDANTS

INTRODUCTION

The reaction of $(\text{H}_2\text{O})_2\text{Co}(\text{dmgH})_2$ with various alkyl hydroperoxides, $\text{RC}(\text{CH}_3)_2\text{OOH}$, in aqueous or semiaqueous solution, has been previously investigated.¹ The general mechanism in Scheme A-1 has been proposed. The cobalt products of these reactions are the corresponding organocobalt complexes, $\text{RCo}(\text{dmgH})_2\text{OH}_2$. The net 2:1 stoichiometry ($(\text{H}_2\text{O})_2\text{Co}(\text{dmgH})_2:\text{ROOH}$) and the rate law are shown in equations 4 and 5 respectively.

Scheme A-1. Reaction Mechanism for $(\text{H}_2\text{O})_2\text{Co}(\text{dmgH})_2$ and ROOH

NET REACTION:



$$\frac{-d[(\text{H}_2\text{O})_2\text{Co}(\text{dmgH})_2]}{dt} = 2k_1[(\text{H}_2\text{O})_2\text{Co}(\text{dmgH})_2][\text{RC}(\text{CH}_3)_2\text{COOH}] \quad (5)$$

The reaction of $(\text{H}_2\text{O})_2\text{Co}(\text{dmgH})_2$ with hydrogen peroxide, a closely related system, has also been investigated.² The experimental observations indicate a more complex mechanism which is not well understood.

This reaction is reported to occur with a stoichiometry of 1:1 ($(\text{H}_2\text{O})_2\text{Co}(\text{dmgH})_2:\text{H}_2\text{O}_2$) in contrast to the 2:1 ($(\text{H}_2\text{O})_2\text{Co}(\text{dmgH})_2:\text{ROOH}$) stoichiometry reported for alkyl hydroperoxides with $(\text{H}_2\text{O})_2\text{Co}(\text{dmgH})_2$. The two major products of the reaction were $(\text{H}_2\text{O})_2\text{Co}(\text{dmgH})_2^+$, which was reported in a 40% yield and another cobalt species that could not be identified (no percent yield reported). Since no hydroxyl radical was identified, the reaction does not proceed via a Fenton-type mechanism which is a common mechanism for the oxidation of metal complexes by hydrogen peroxide.

The kinetic data were obtained under pseudo-first-order conditions using excess peroxide and were in accord with the rate law in equation 6.

$$\frac{-d[(\text{H}_2\text{O})_2\text{Co}(\text{dmgH})_2]}{dt} = k[(\text{H}_2\text{O})_2\text{Co}(\text{dmgH})_2][\text{H}_2\text{O}_2] \quad (6)$$

In the proposed mechanism, the attack of the peroxide on the ligand occurs simultaneously with the initial adduct formation step, or immediately following it. Either of the hydrogen atom abstraction possibilities, shown in Figure A-1, are considered likely.

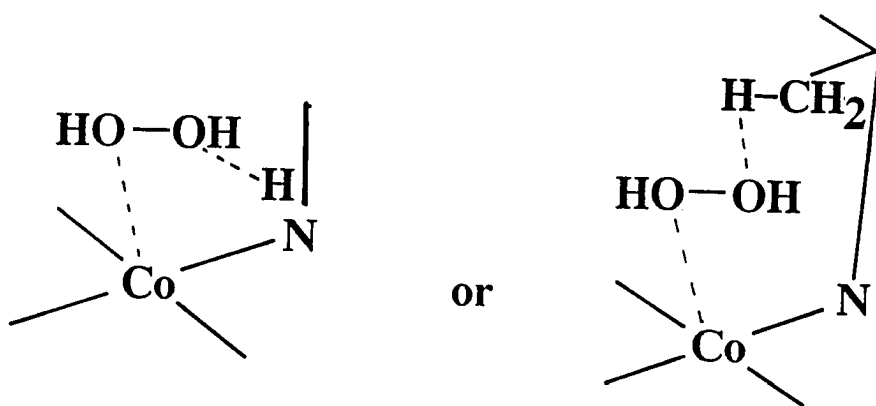


Figure A-1. Proposed attack of H₂O₂ on (H₂O)₂Co(dmgh)₂

STATEMENT OF PROBLEM

The reactions of $(\text{H}_2\text{O})_2\text{Co}(\text{dmgH})_2$ and related cobalt(II) macrocyclic complexes with peroxides such as hydrogen peroxide and various alkyl hydroperoxides have been previously investigated. The reactions with alkyl hydroperoxides appear to be well understood; however, the reactions with hydrogen peroxide are not understood. To better understand the mechanism of the reaction of unsaturated cobalt macrocyclic complexes with hydrogen peroxide and related hydroperoxides in aqueous solution, the reactions of the recently characterized "daughter" complex of $(\text{H}_2\text{O})_2\text{Co}(\text{dmgH})_2$, $(\text{H}_2\text{O})_2\text{Co}(\text{dmgBF}_2)_2$, with hydrogen peroxide and various hydroperoxides have been investigated. The understanding of this reaction chemistry could lead to the elucidation of the general reactivity of cobalt(II) macrocyclic complexes with hydrogen peroxide.

EXPERIMENTAL SECTION

Materials and measurements

The $(\text{H}_2\text{O})_2\text{Co}(\text{dmgBF}_2)_2$,³ was prepared according to the literature procedure. Other materials were reagent grade chemicals.

UV-vis spectra and kinetic measurements were recorded on a Cary 219 spectrophotometer and a Cary 14 spectrophotometer interfaced with an OLIS 3820 data system. Analysis of the kinetic data were performed using standard first-order and biexponential routines on an Apple II+ computer or the OLIS 3820 data system. Routine ^1H NMR spectra were collected on a Nicolet NT-300. The NMR experiments were all done in D_2O with H_2O as the reference at 4.63 ppm, pH = natural unless stated. This reference was verified by a small addition of acetone which had a chemical shift of 2.05 ppm, an accepted value.

The stoichiometry of the reaction of $(\text{H}_2\text{O})_2\text{Co}(\text{dmgBF}_2)_2$ with various oxidants was obtained by two methods. Method (A) determined the amount of ROOH consumed in the reaction between $(\text{H}_2\text{O})_2\text{Co}(\text{dmgBF}_2)_2$ and excess ROOH. These solutions were allowed to react airfree, pH ~ 3, for one to two hours depending on the rate constant and the ROOH concentration. The reaction in all cases was signaled by a color change, with the gold colored solutions of $(\text{H}_2\text{O})_2\text{Co}(\text{dmgBF}_2)_2$ turning pale yellow when oxidized. After the reaction was considered complete, the solution was passed through a Dowex 50W-8X cation-exchange column to separate the positively charged cobalt species from the ROOH. The ROOH solution was diluted, acidified with H_2SO_4 and degassed. KI was added and the ROOH concentration was determined volumetrically using thiosulfate.

Method (B) determined the amount of $(\text{H}_2\text{O})_2\text{Co}(\text{dmgBF}_2)_2$ consumed in the reaction of excess $(\text{H}_2\text{O})_2\text{Co}(\text{dmgBF}_2)_2$ with ROOH. The reaction was monitored spectrophotometrically ($\lambda = 456 \text{ nm}$, $(\text{H}_2\text{O})_2\text{Co}(\text{dmgBF}_2)_2 \epsilon = 4.06 \times 10^3 \text{ M}^{-1}\text{cm}^{-1}$, $(\text{H}_2\text{O})\text{Co}(\text{dmgBF}_2)_2^+ \epsilon \sim 650 \text{ M}^{-1}\text{cm}^{-1}$). The absorbance-time traces are biexponential with a first-order first stage and a nearly zero-order second stage. By extrapolating the second stage to time zero the absorbance infinity of the first stage and the change in absorbance were determined. The stoichiometry was then calculated from the absorbance change of the first stage.

RESULTS

Reaction between $(\text{H}_2\text{O})_2\text{Co}(\text{dmgBF}_2)_2$ and H_2O_2

The reaction proceeds in two stages requiring a biexponential kinetic analysis. The first stage is first-order in $[(\text{H}_2\text{O})_2\text{Co}(\text{dmgBF}_2)_2]$ and $[\text{H}_2\text{O}_2]$. It is independent of the acid concentration in the range 0.020 - 0.10 M HClO_4 .

Cyclopentane and dimethyl ether or difficult-to-oxidize alcohols such as methanol and t-butanol (0.5 M ROH) were used as radical traps. The reaction rates, reaction profiles, or final spectra were not affected by the presence of these radical traps; thus, no radicals were detected.

The presence of more easily oxidized alcohols such as ethanol, cyclohexanol, or 2-propanol (0.5 M ROH) did affect the reaction such that only the first stage, now exhibiting a stable absorbance infinity was observed. The reaction stoichiometry remained 1:1 $((\text{H}_2\text{O})_2\text{Co}(\text{dmgBF}_2)_2:\text{H}_2\text{O}_2)$ and the addition of Cr^{2+} after the attainment of a stable absorbance infinity restored approximately 50% of the absorbance at 456 nm. This estimate is based on the initial and final spectra of the reaction mixture. The 50% yield could indicate that one reducible $(\text{H}_2\text{O})_2\text{Co}(\text{dmgBF}_2)_2^+$ ion was produced from two $(\text{H}_2\text{O})_2\text{Co}(\text{dmgBF}_2)_2$ molecules, or it could indicate that 50% of the $(\text{H}_2\text{O})_2\text{Co}(\text{dmgBF}_2)_2^+$ ion decomposed before reduction occurred.

The stoichiometry of the reaction stages was determined by the two methods described previously. Using method (A), an average value of 1.07:1.00 $((\text{H}_2\text{O})_2\text{Co}(\text{dmgBF}_2)_2:\text{H}_2\text{O}_2)$ was determined. One stoichiometric determination using method (B) supported the 1:1 stoichiometry.

The cobalt(III) complex $(\text{H}_2\text{O})_2\text{Co}(\text{dmgBF}_2)_2^+$ is much more stable under neutral conditions than under acidic conditions; therefore, the reaction of $(\text{H}_2\text{O})_2\text{Co}(\text{dmgBF}_2)_2$ with H_2O_2 was also studied in water of unadjusted pH. The stoichiometry of the reaction between $(\text{H}_2\text{O})_2\text{Co}(\text{dmgBF}_2)_2$ and H_2O_2 was unchanged. Single wavelength absorbance-time traces ($\lambda = 456 \text{ nm}$) showed reaction profiles which were the same as in acidic solution, a first stage with a poorly defined absorbance infinity followed by a slow trailing second stage which consumed all of the excess $(\text{H}_2\text{O})_2\text{Co}(\text{dmgBF}_2)_2$.

Figure A-2 illustrates the plot of k_{obs} vs. $[\text{H}_2\text{O}_2]$ suggested by equation 10. A least-squares analysis yielded a second-order rate constant of $12.8 \pm 0.5 \text{ M}^{-1}\text{s}^{-1}$ ($\mu = 0.100 \text{ M}$, $\text{HClO}_4 = 0.100 \text{ M}$).

A plausible reaction mechanism is shown in Scheme A-2. It begins with the formation of a $(\text{H}_2\text{O})_2\text{Co}(\text{dmgBF}_2)_2\text{-H}_2\text{O}_2$ adduct. The Co(II) metal center is then oxidized to Co(III)⁺ which is rapidly followed by the oxidation of the ligand to account for the second oxidizing equivalent of H_2O_2 . This represents the first reaction stage. The ligand oxidation leads to the decomposition of the macrocycle, perhaps to radical fragments. An unusual decomposition of the excess $(\text{H}_2\text{O})_2\text{Co}(\text{dmgBF}_2)_2$ occurs well after the H_2O_2 has been consumed in the first stage. The $(\text{H}_2\text{O})_2\text{Co}(\text{dmgBF}_2)_2$ remaining after the first stage decomposes at a rate in excess of the rate of simple decomposition of $(\text{H}_2\text{O})_2\text{Co}(\text{dmgBF}_2)_2$ in acid. This second stage can be attributed to the reaction of $(\text{H}_2\text{O})_2\text{Co}(\text{dmgBF}_2)_2$ with the decomposition products of the oxidized ligand. These decomposition products could lead to a radical chain decomposition of the excess $(\text{H}_2\text{O})_2\text{Co}(\text{dmgBF}_2)_2$.

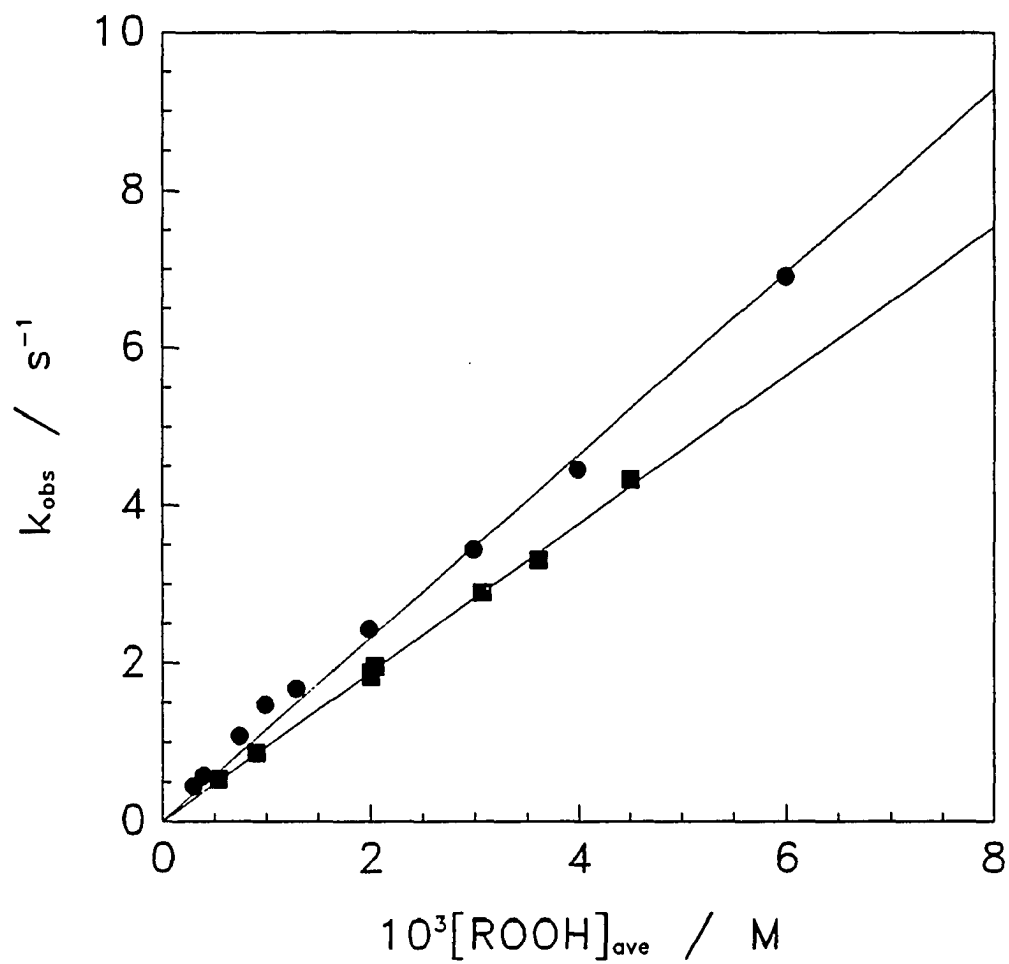
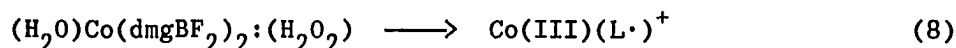
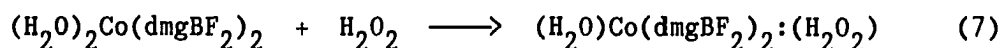


Figure A-2. Dependence of k_{obs} on $[\text{ROOH}]$, $\text{HClO}_4 = 0.100 \text{ M}$, $\mu = 0.100 \text{ M}$
 $\text{ROOH} = \text{HOOH}$ (circles), and $\text{ROOH} = \text{t-BuOOH}$ (squares)

Scheme A-2. Reaction Mechanism for $(\text{H}_2\text{O})_2\text{Co}(\text{dmgBF}_2)_2$ and H_2O_2 

$$\frac{-d[(\text{H}_2\text{O})_2\text{Co}(\text{dmgBF}_2)_2]}{dt} = k_8[(\text{H}_2\text{O})_2\text{Co}(\text{dmgBF}_2)_2][\text{H}_2\text{O}_2] \quad (9)$$

$$k_{\text{obs}} = k_8[\text{H}_2\text{O}_2] \quad (10)$$

The reaction between $(\text{H}_2\text{O})_2\text{Co}(\text{dmgBF}_2)_2$ and hydroxyl radicals generated by pulse radiolysis has also been investigated.⁴ The low solubility and large absorbance of the $(\text{H}_2\text{O})_2\text{Co}(\text{dmgBF}_2)_2$ limits the accuracy of the results; however, the rate constant for this reaction is $k = (4 \pm 2) \times 10^9 \text{ M}^{-1}\text{s}^{-1}$. A second reaction which is first-order is also observed. A transient is formed in the first reaction which decomposes with a rate constant of $(3.8 \pm 0.4) \times 10^3 \text{ s}^{-1}$. The final spectrum is consistent with a Co(III) species, but the identity of the transient and the final product is unknown.

NMR product analysis

An NMR product analysis for the reaction between $(\text{H}_2\text{O})_2\text{Co}(\text{dmgBF}_2)_2$ and H_2O_2 was attempted. The Co(III) complexes produced in the reaction are diamagnetic; thus, NMR should reveal any structural modification of the macrocyclic ring that occurred during the reaction.

$(\text{H}_2\text{O})_2\text{Co}(\text{dmgBF}_2)_2^+$ is very unstable under acidic conditions and somewhat unstable under neutral conditions. The NMR accumulation time

needed for these dilute samples is approximately 20 minutes. Therefore, a spectrum of the initial reaction products without interference from decomposition was difficult to obtain, especially under acidic conditions.

To identify the NMR spectrum of $(\text{H}_2\text{O})_2\text{Co}(\text{dmgBF}_2)_2^+$ from various decomposition products of the system several oxidants were chosen to prepare $(\text{H}_2\text{O})_2\text{Co}(\text{dmgBF}_2)_2^+$. Figure A-3 is the spectrum of the products of the reaction of $(\text{H}_2\text{O})_2\text{Co}(\text{dmgBF}_2)_2$ with a slight excess of H_2O_2 . A reaction time of 30 minutes was required to collect an NMR spectrum. This long reaction time in addition to the time required to record the spectrum may have resulted in the observation of various decomposition products. It is difficult to make peak assignments for this spectrum; however, the peaks at 2.22, 1.88, and 1.75 ppm are commonly observed in the decomposition of $(\text{H}_2\text{O})_2\text{Co}(\text{dmgBF}_2)_2^+$. The peak at 2.50 ppm and the multiplet centered around 2.5 ppm might be the initial product observed when $(\text{H}_2\text{O})_2\text{Co}(\text{dmgBF}_2)_2$ is oxidized by dilute solutions of H_2O_2 .

Figure A-4 is the spectrum of the products obtained by a rapid oxidation of $(\text{H}_2\text{O})_2\text{Co}(\text{dmgBF}_2)_2$ with a moderate excess of H_2O_2 . Figure A-4 resembles Figure A-10 and clearly shows a characteristic peaks at 2.496 and 2.547 ppm. The normal decomposition peaks at 1.86, 2.21 and 2.62 ppm are seen; however, the unusual multiplet centered around 2.5 ppm, observed in Figure A-14, is not observed.

Figure A-5 represents the spectrum of the products obtained by the bulk electrolysis of $(\text{H}_2\text{O})_2\text{Co}(\text{dmgBF}_2)_2$ in 0.10 M LiClO_4 . The electrolysis took about 30 minutes before the spectrum was recorded. The major peaks are the peaks at 2.621 and 2.555 ppm, thought to be due to the $(\text{H}_2\text{O})_2\text{Co}(\text{dmgBF}_2)_2^+$. The peaks at 1.872 and 2.676 ppm are assigned as common decomposition products.

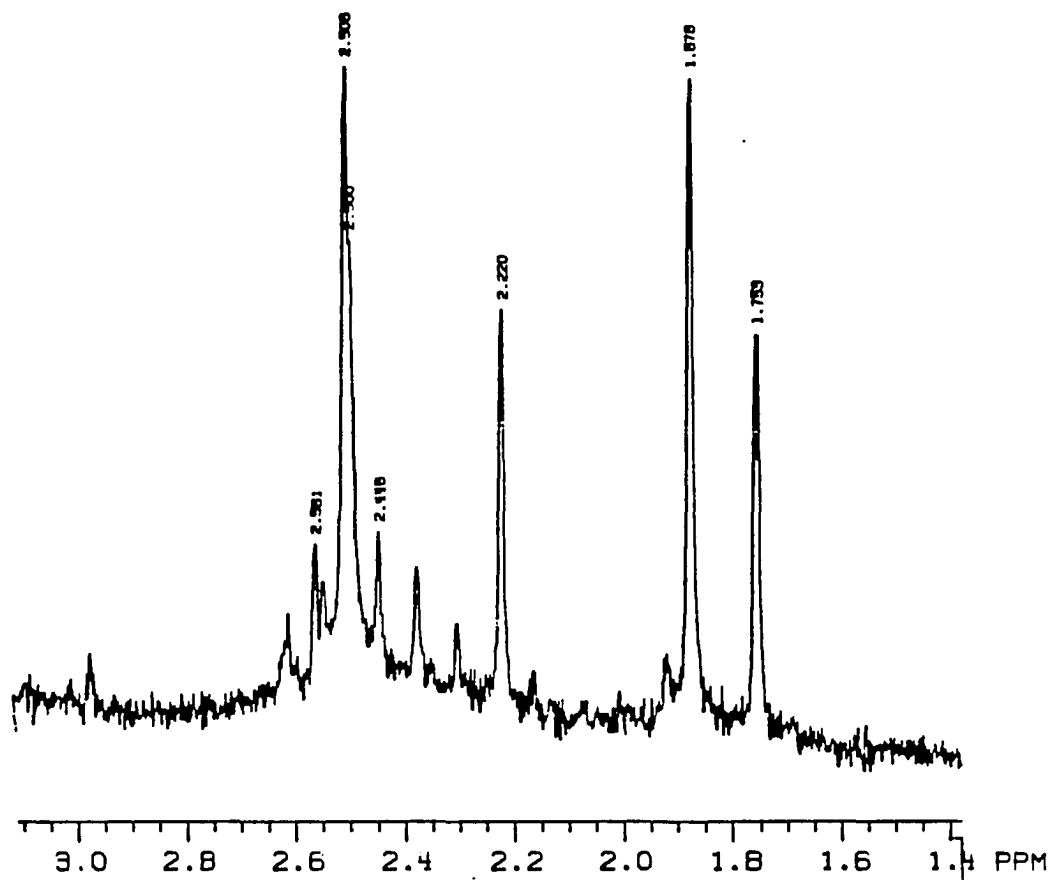


Figure A-3. NMR spectrum of the products of the reaction between $(\text{H}_2\text{O})_2\text{Co}(\text{dmgBF}_2)_2$ and a slight excess of H_2O_2 , $(\text{H}_2\text{O})_2\text{Co}(\text{dmgBF}_2)_2 \sim 5 \times 10^{-4} \text{ M}$, and $\text{H}_2\text{O}_2 \sim 6 \times 10^{-4} \text{ M}$

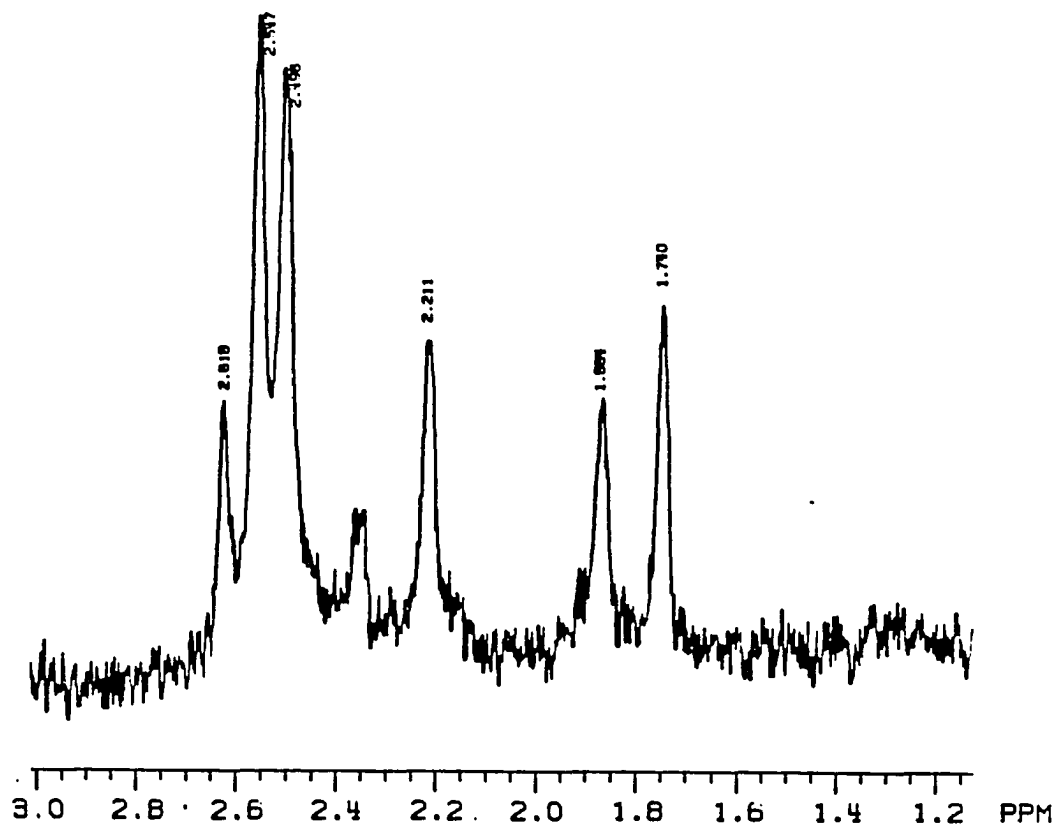


Figure A-4. NMR spectrum of the products of the reaction between $(\text{H}_2\text{O})_2\text{Co}(\text{dmgBF}_2)_2$ and a moderate excess of H_2O_2 , $(\text{H}_2\text{O})_2\text{Co}(\text{dmgBF}_2)_2 \sim 5 \times 10^{-4} \text{ M}$, and $\text{H}_2\text{O}_2 \sim 5 \times 10^{-3} \text{ M}$

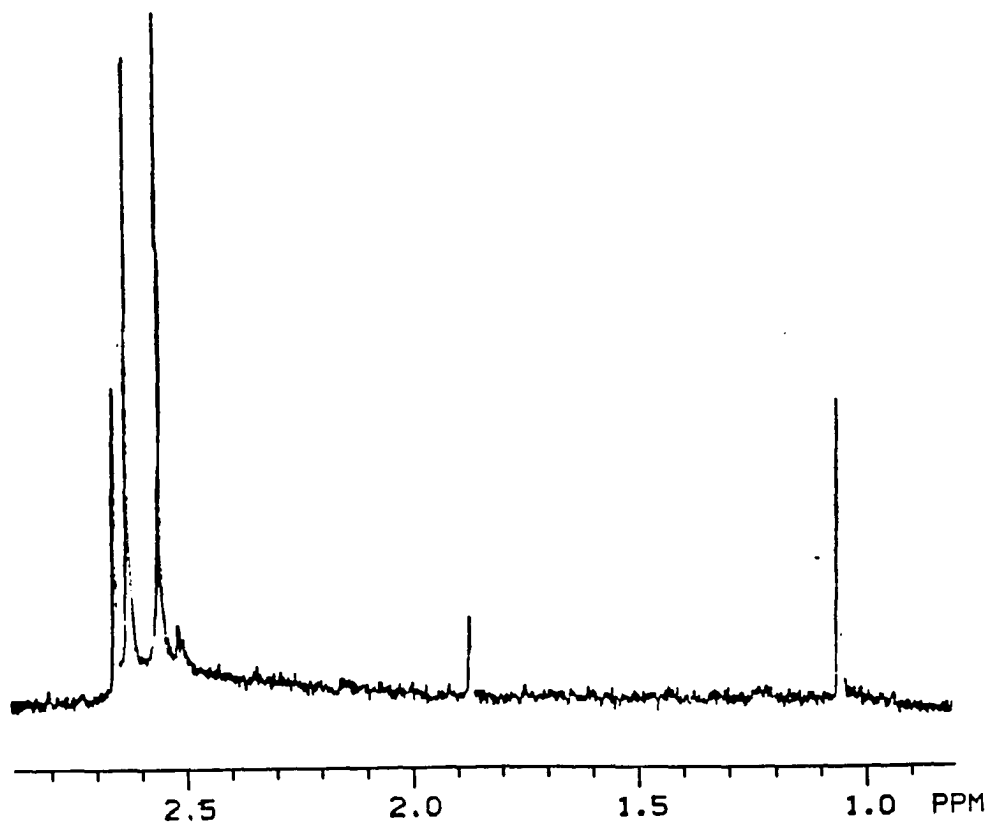


Figure A-5. NMR spectrum of the products obtained by bulk electrolysis of $(\text{H}_2\text{O})_2\text{Co}(\text{dmgBF}_2)_2$ in $\text{LiClO}_4 = 0.10 \text{ M}$

Figure A-6 represents the same sample as in Figure A-5; however, HClO_4 was added, ($0.05 \text{ M} \sim [\text{H}_3\text{O}^+]$), before the spectrum was recorded. The acid seems to enhance the intensity of the 1.857 and 2.666 ppm peaks relative to the peaks at 2.604 and 2.539 ppm. This is consistent with the observation that $(\text{H}_2\text{O})_2\text{Co}(\text{dmgBF}_2)_2^+$ is much less stable in acidic solution, and the initial decomposition products appearing as the 1.857 and 2.666 ppm peaks. These decomposition peaks are regularly occurring peaks in many of these NMR spectra.

Figure A-7 is the spectrum of the products of the reaction between $(\text{H}_2\text{O})_2\text{Co}(\text{dmgBF}_2)_2$ and $t\text{-BuOOH}$. The peaks at 2.605 and 2.538 ppm are assigned to the inequivalent equatorial methyls of $(\text{H}_2\text{O})_2\text{Co}(\text{dmgBF}_2)_2^+$. The peak at 2.214 ppm is assigned to the equatorial methyls of $\text{CH}_3\text{Co}(\text{dmgBF}_2)_2(\text{H}_2\text{O})$. The peak at 2.048 ppm is assigned to the acetone produced in the reaction and the peak at 1.063 ppm is assigned to the unreacted $t\text{-BuOOH}$. The peak at 0.986 is assigned to the axial methyl of the $\text{CH}_3\text{Co}(\text{dmgBF}_2)_2(\text{H}_2\text{O})$.

Figure A-8 is the spectrum of the products of the reaction of $(\text{H}_2\text{O})_2\text{Co}(\text{dmgBF}_2)_2$ with $\text{Na}_2\text{S}_2\text{O}_8$. The peaks at 2.65 and 1.88 ppm are assigned to decomposition products. The peaks at 2.55 and 2.61 ppm is thought to be the $(\text{H}_2\text{O})_2\text{Co}(\text{dmgBF}_2)_2^+$ and the identity of the peak at 1.08 ppm is unknown. This peak could be due to an impurity or a decomposition reaction product.

Figure A-9 represents the spectrum of the products of the reaction of $(\text{H}_2\text{O})_2\text{Co}(\text{dmgBF}_2)_2$ and $\text{Fe}(\text{ClO}_4)_3$. The spectrum was taken as quickly as possible and shows the familiar peaks at 2.533 and 2.599 ppm with very small peaks at 1.88 and 2.65 ppm.

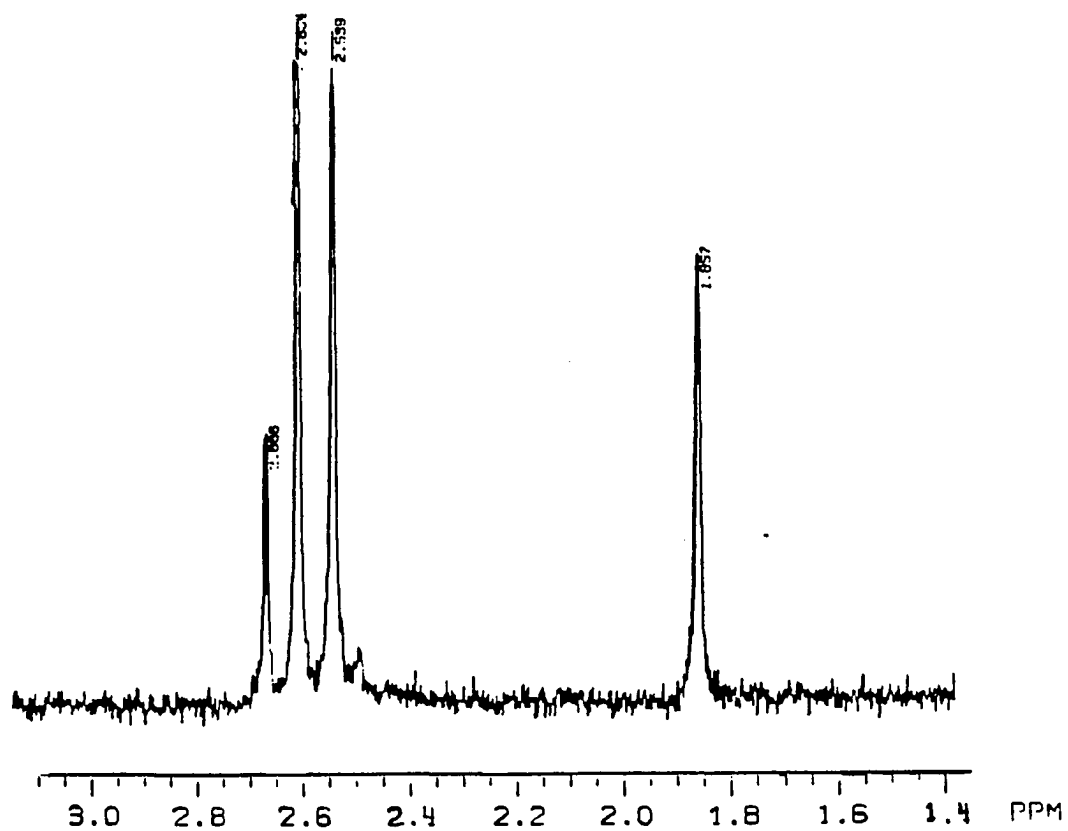


Figure A-6. NMR spectrum of the products obtained by bulk electrolysis of $(\text{H}_2\text{O})_2\text{Co}(\text{dmgBF}_2)_2$ in $\text{LiClO}_4 = 0.10 \text{ M}$. HClO_4 was added before the spectrum was recorded, $\text{HClO}_4 \sim 0.05 \text{ M}$

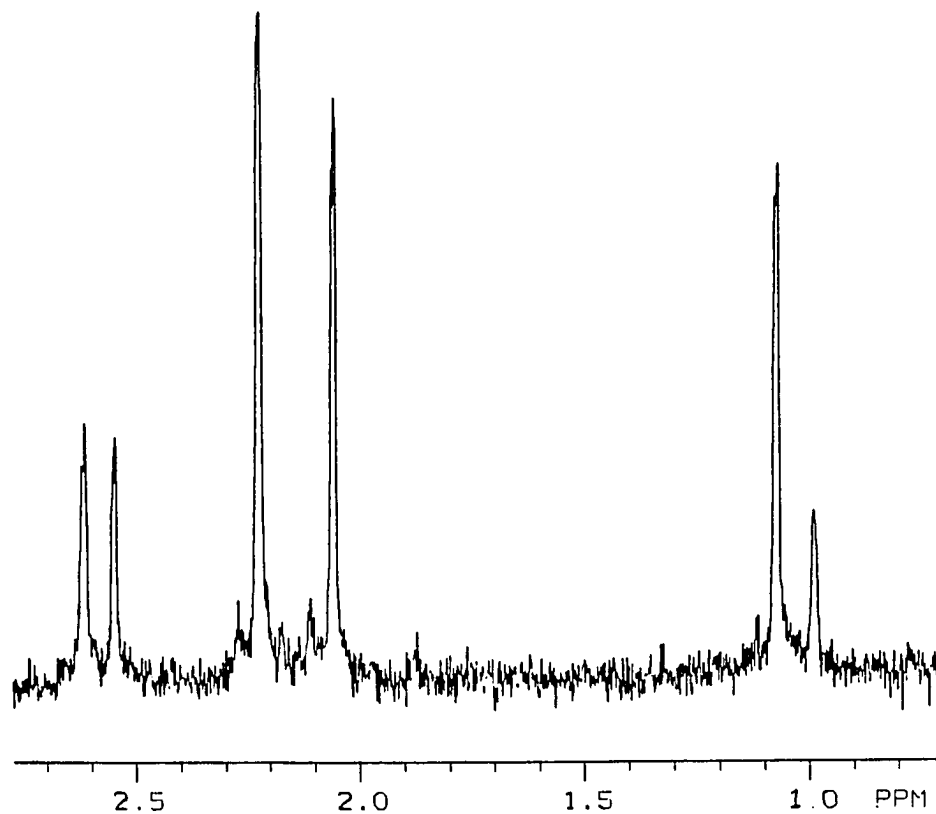


Figure A-7. NMR spectrum of the products of the reaction between $(\text{H}_2\text{O})_2\text{Co}(\text{dmgBF}_2)_2$ and $t\text{-BuOOH}$, $(\text{H}_2\text{O})_2\text{Co}(\text{dmgBF}_2)_2 \sim 5 \times 10^{-4}$ M, and $t\text{-BuOOH} \sim 1 \times 10^{-3}$ M

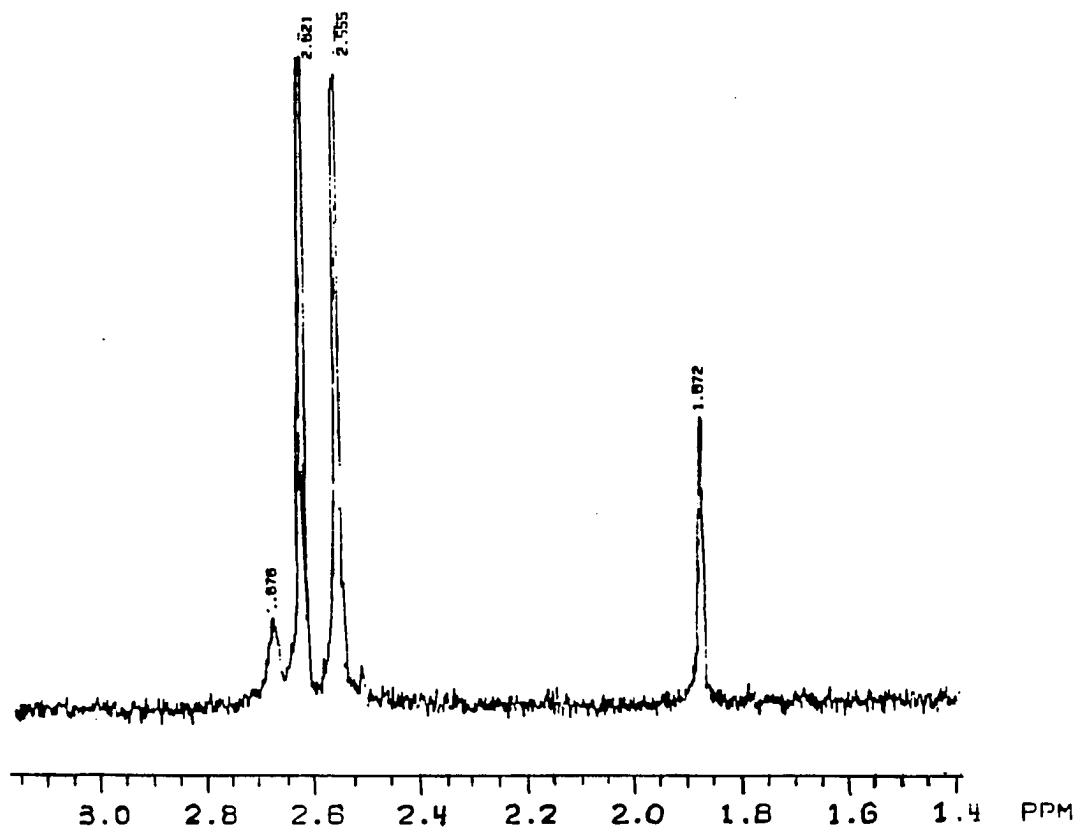


Figure A-8. NMR spectrum of the products of the reaction between $(\text{H}_2\text{O})_2\text{Co}(\text{dmgBF}_2)_2$ and $\text{Na}_2\text{S}_2\text{O}_8$, $(\text{H}_2\text{O})_2\text{Co}(\text{dmgBF}_2)_2 \sim 5 \times 10^{-4}$ M, and $\text{Na}_2\text{S}_2\text{O}_8 \sim 1 \times 10^{-3}$ M

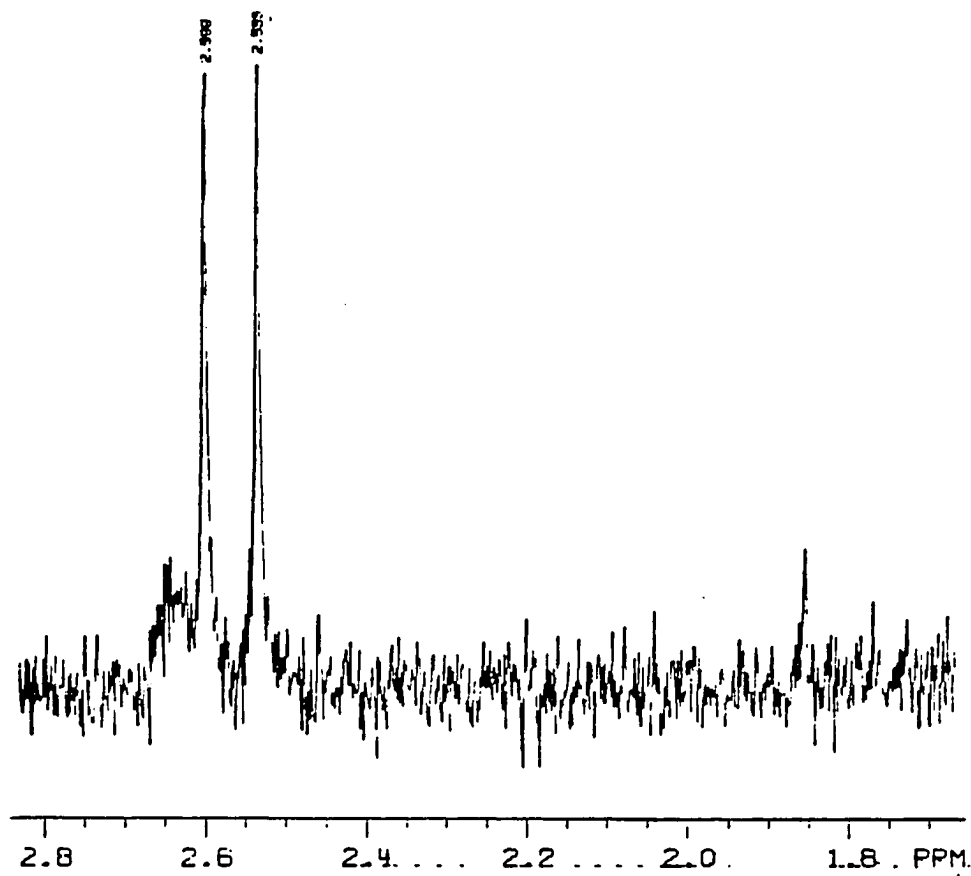


Figure A-9. NMR spectrum of the products of the reaction between $(\text{H}_2\text{O})_2\text{Co}(\text{dmgBF}_2)_2$ and $\text{Fe}(\text{ClO}_4)_3$, $(\text{H}_2\text{O})_2\text{Co}(\text{dmgBF}_2)_2 \sim 5 \times 10^{-4}$ M, and $\text{Fe}(\text{ClO}_4)_3 \sim 1 \times 10^{-3}$ M

Figure A-10 is the same sample seen in Figure A-9 except that HClO_4 was added before the spectrum was recorded, ($[\text{H}^+] \sim 0.05$). The acid and/or increased time resulted in the observation of the 1.86 and 2.65 ppm peaks. Figures A-9 and A-10 therefore suggest that the oxidation of $(\text{H}_2\text{O})_2\text{Co}(\text{dmgBF}_2)_2$ by the "clean" inner-sphere oxidant, $\text{Fe}(\text{OH})^{2+}$, results in a $\text{Co}(\text{III})^+$ complex with only two peaks, 2.533 and 2.599 ppm. This complex then decomposes to complexes which give rise to the 1.86 and 2.66 ppm peaks.

Figure A-11 represents the spectrum of the products of the reaction of $(\text{H}_2\text{O})_2\text{Co}(\text{dmgBF}_2)_2$ and FeCl_3 . Only two peaks are seen at 2.525 and 2.589 ppm. There is some evidence of a third peak at 2.63 ppm, but it appears to be a broad peak.

Figure A-12 represents the spectrum of the products of the reaction of $(\text{H}_2\text{O})_2\text{Co}(\text{dmgBF}_2)_2$ and FeCl_3 in 0.10 M HClO_4 . The peaks at 2.497 and 2.562 ppm and the decomposition product peaks at 1.819 and 2.624 ppm are clearly seen. The decomposition product peaks appear immediately in the acidic media while the immediate formation of the decomposition products is not seen under neutral conditions, Figure A-11. This is consistent with an acid-promoted decomposition pathway.

Figure A-13 represents a spectrum of the same sample used in Figure A-12; however, this spectrum was taken 1 hour after the spectrum in Figure A-12 was recorded. The peaks are seen at 2.580 and 2.498 ppm, but they are much less intense than in Figure A-12. The primary decomposition product at 2.634 ppm has a much less intense peak, but the decomposition product at 1.822 ppm has greatly increased peak intensity. Two additional peaks are seen at 1.695 and 2.170 ppm. These peaks have a much greater intensity in Figure A-14 which is a spectrum of the same sample taken 20

hours later. The experiment which includes Figures A-12, A-13, and A-14, suggests that the oxidation of $(\text{H}_2\text{O})_2\text{Co}(\text{dmgBF}_2)_2$ by FeCl_3 initially forms $(\text{H}_2\text{O})\text{Co}(\text{dmgBF}_2)_2(\text{Cl})^+$ (peaks 2.498 and 2.580 ppm), which in acid decomposes either in a consecutive or parallel path to the complex responsible for the peak at 2.634 ppm and/or then to the complex responsible for the peak at 1.822 ppm and ultimately to the complex(es) responsible for the peaks at 1.689 and 2.156 ppm.

Figure A-15 represents the spectrum of the products of the reaction between $((\text{CH}_3)_2\text{CO})_2\text{Co}(\text{dmgBF}_2)_2$ and $\text{Fe}(\text{OH})^{2+}$ in d_6 -acetone. The spectrum shows a singlet at 2.88 ppm assigned to the four equivalent macrocycle methyl groups of $((\text{CH}_3)_2\text{CO})\text{Co}(\text{dmgBF}_2)_2(\text{H}_2\text{O})$ in d_6 -acetone.

The data indicate that the NMR peaks due to the $(\text{H}_2\text{O})_2\text{Co}(\text{dmgBF}_2)_2^+$ are located about 2.55 and 2.61 ppm in D_2O . Due to the symmetry of the molecule only a singlet can be readily predicted for the four equivalent macrocycle methyl groups. The peaks are not due to a mixture of $(\text{H}_2\text{O})_2\text{Co}(\text{dmgBF}_2)_2^+$ and $(\text{H}_2\text{O})\text{Co}(\text{dmgBF}_2)_2(\text{OH})$ since this set of peaks is seen under both neutral and acidic conditions. Additionally, a mixture of these species would probably lead to an NMR time-averaged singlet, not a set of peaks. The set of peaks is also not due to a mixture of $(\text{H}_2\text{O})_2\text{Co}(\text{dmgBF}_2)_2^+$ and $(\text{H}_2\text{O})\text{Co}(\text{dmgBF}_2)_2(\text{Cl})$ since this set of peaks is seen in solutions with and without Cl^- .

The relative chemical shift of this set of peaks, (2.5 - 2.6 ppm), suggests that the macrocycle methyls are in a similar electronic environment within the molecule. Therefore, the four double bonds in the macrocycle are intact since the loss of a double bond would shift the adjacent methyl group upfield by more than one ppm. It is possible that an oxidant such as H_2O_2 would modify the macrocycle since it is a

potential source of $\cdot\text{OH}$ radicals, resulting in the inequivalency of the macrocycle methyls, but oxidants such as $\text{Fe}(\text{OH})^{2+}$ (inner-sphere oxidant) or electrical potential would probably not modify the macrocycle. It also seems unlikely that the set of peaks is due to a mixture of mono- and di- BF_2 substituted cobaloximes since several preparations of $(\text{H}_2\text{O})_2\text{Co}(\text{dmgBF}_2)_2$ give the same results.

It is, therefore, believed that the set of peaks is due to the $(\text{H}_2\text{O})_2\text{Co}(\text{dmgBF}_2)_2^+$ complex and that the two peaks arise from a distortion in the macrocycle which makes the four macrocycle methyls appear to the NMR as a pair of two equivalent methyl groups. A slight distortion of the macrocyclic ring is detected in the solid state X-ray structure lowering the symmetry to C_i from C_{2h} point group symmetry, but it is difficult to know whether this distortion is present in aqueous solution at room temperature.⁵

Reaction between $(\text{H}_2\text{O})_2\text{Co}(\text{dmgBF}_2)_2$ and t-BuOOH

The stoichiometry of the reaction was determined using the two methods described in the experimental section of this report. The stoichiometry of the reaction of $(\text{H}_2\text{O})_2\text{Co}(\text{dmgBF}_2)_2$ with t-BuOOH was 2.0:1.0 ($(\text{H}_2\text{O})_2\text{Co}(\text{dmgBF}_2)_2$:t-BuOOH) by method (A) and method (B) confirmed this result.

The stoichiometric difference between these two systems is clearly illustrated in the absorbance-time profile for the two reactions, Figure A-16. The reaction conditions are the same for the two experiments. The theoretical absorbance infinity values for 1:1 and 2:1 ($(\text{H}_2\text{O})_2\text{Co}(\text{dmgBF}_2)_2$:ROOH) are labeled on the y-axis. A mechanism consistent with this 2:1 stoichiometry is shown in Scheme A-3.

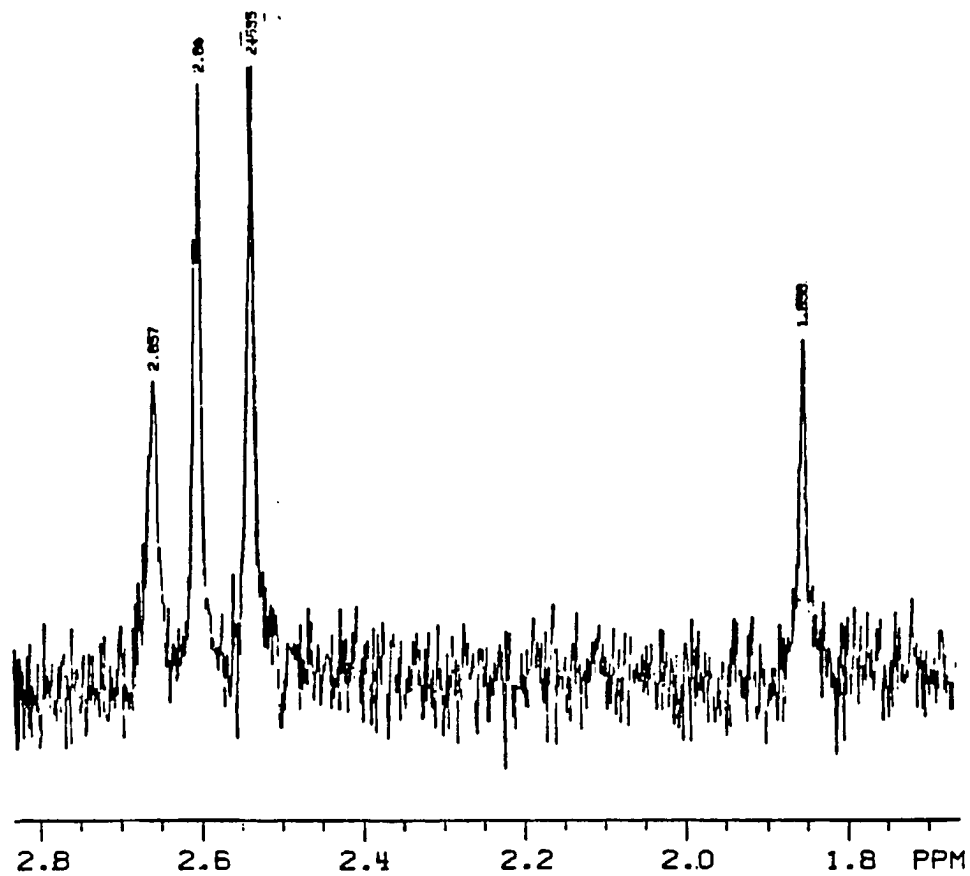


Figure A-10. NMR spectrum of the products of the reaction between $(\text{H}_2\text{O})_2\text{Co}(\text{dmgBF}_2)_2$ and $\text{Fe}(\text{ClO}_4)_3$, $(\text{H}_2\text{O})_2\text{Co}(\text{dmgBF}_2)_2 \sim 5 \times 10^{-4}$ M, $\text{Fe}(\text{ClO}_4)_3 \sim 1 \times 10^{-3}$ M, and $\text{HClO}_4 \sim 0.05$ M

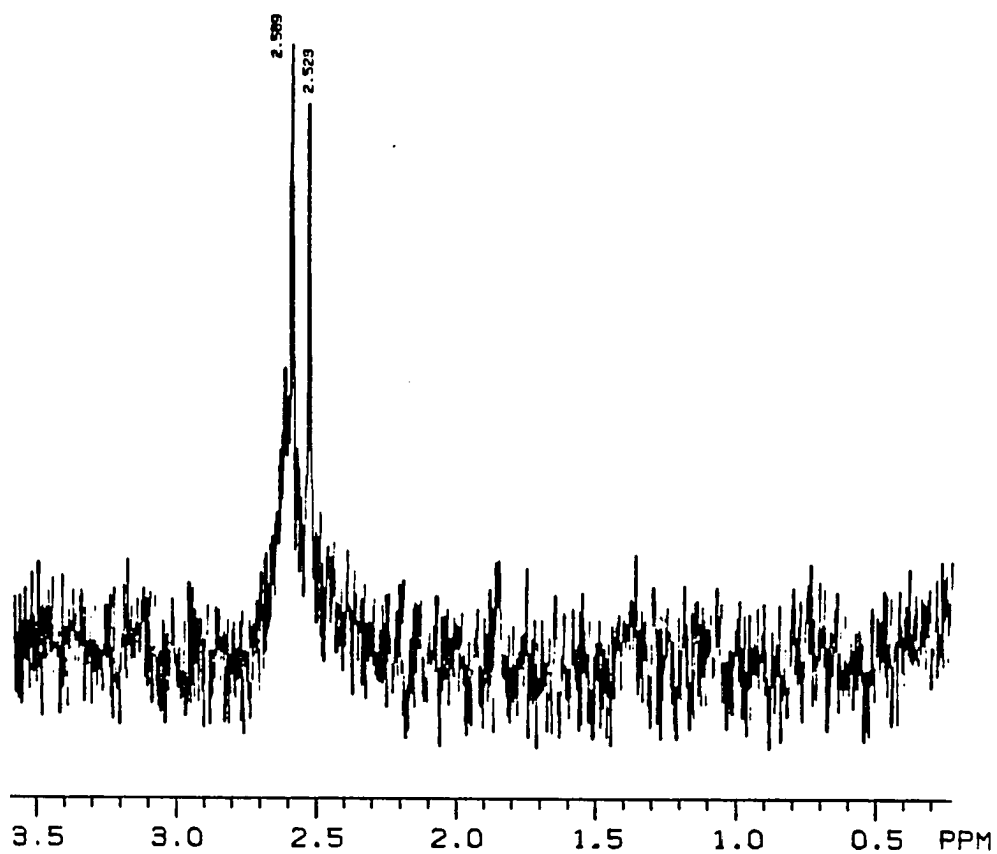


Figure A-11. NMR spectrum of the products of the reaction between $(\text{H}_2\text{O})_2\text{Co}(\text{dmgBF}_2)_2$ and FeCl_3 , $(\text{H}_2\text{O})_2\text{Co}(\text{dmgBF}_2)_2 \sim 5 \times 10^{-4}$ M, and $\text{FeCl}_3 \sim 1 \times 10^{-3}$ M

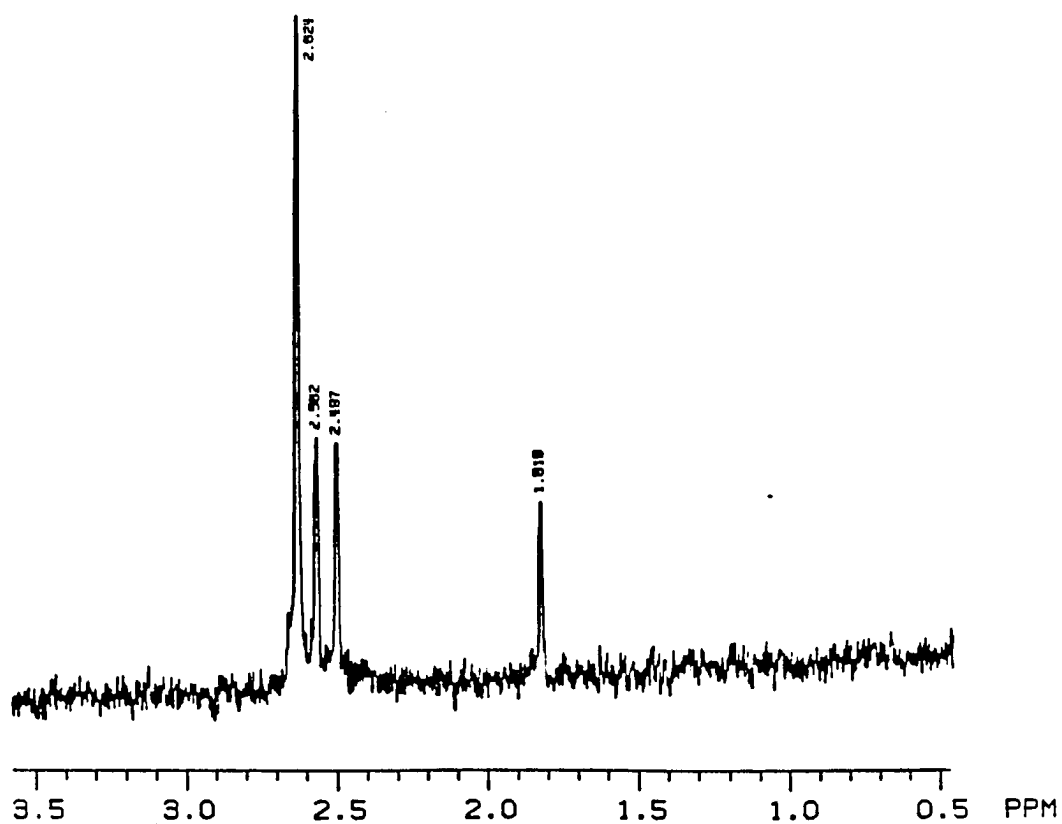


Figure A-12. NMR spectrum of the products of the reaction between $(\text{H}_2\text{O})_2\text{Co}(\text{dmgBF}_2)_2$ and FeCl_3 , $(\text{H}_2\text{O})_2\text{Co}(\text{dmgBF}_2)_2 \sim 5 \times 10^{-4} \text{ M}$, $\text{FeCl}_3 \sim 1 \times 10^{-3} \text{ M}$, and $\text{HClO}_4 = 0.10 \text{ M}$

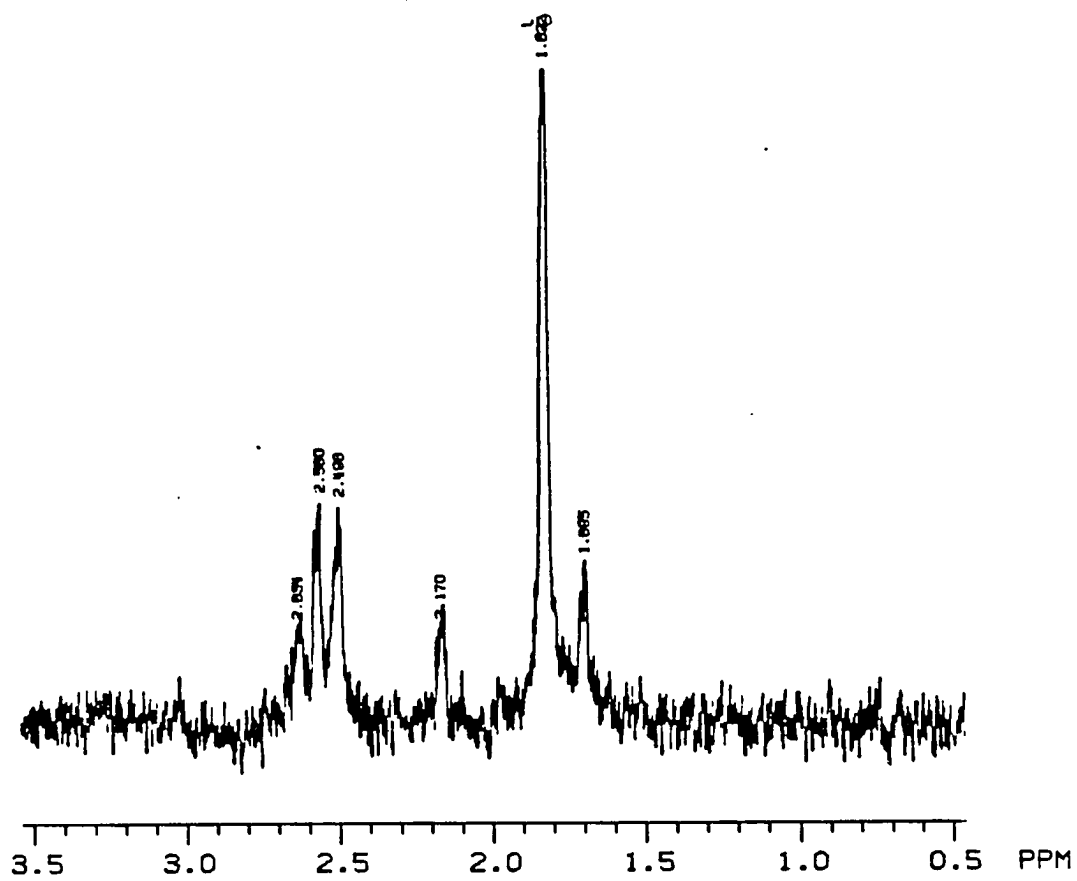


Figure A-13. NMR spectrum of the same sample used in Figure A-12; however, this spectrum was taken 1 hour after the spectrum in Figure A-12 was recorded

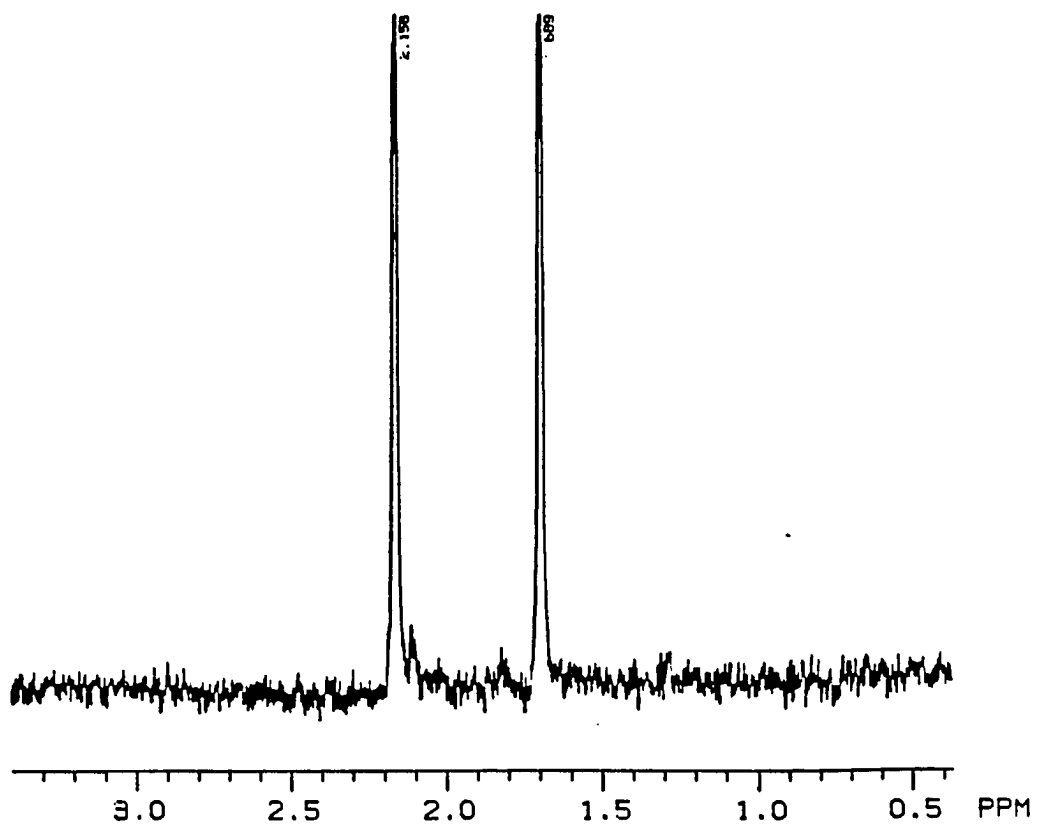


Figure A-14. NMR spectrum of the same sample used in Figure A-12; however, this spectrum was taken 20 hours after the spectrum in Figure A-12 was recorded

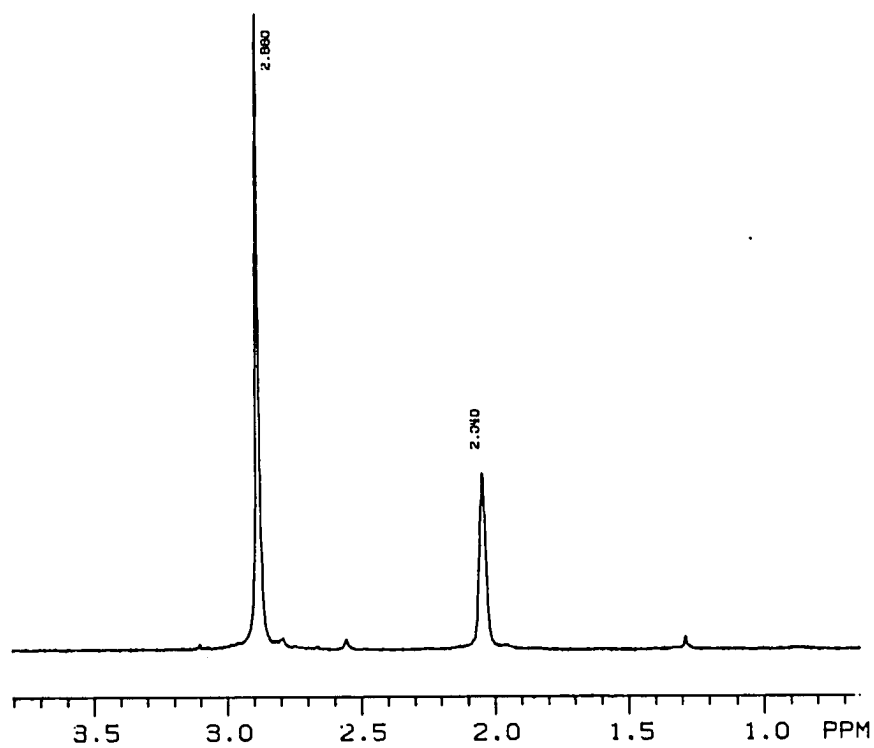


Figure A-15. NMR spectrum of the products of the reaction between $((\text{CH}_3)_2\text{CO})_2\text{Co}(\text{dmgBF}_2)_2$ and $\text{Fe}(\text{OH})^{2+}$ in d_6 -acetone, $((\text{CH}_3)_2\text{CO})_2\text{Co}(\text{dmgBF}_2)_2 \sim 5 \times 10^{-3} \text{ M}$ and $\text{Fe}(\text{OH})^{2+} \sim 5 \times 10^{-3} \text{ M}$

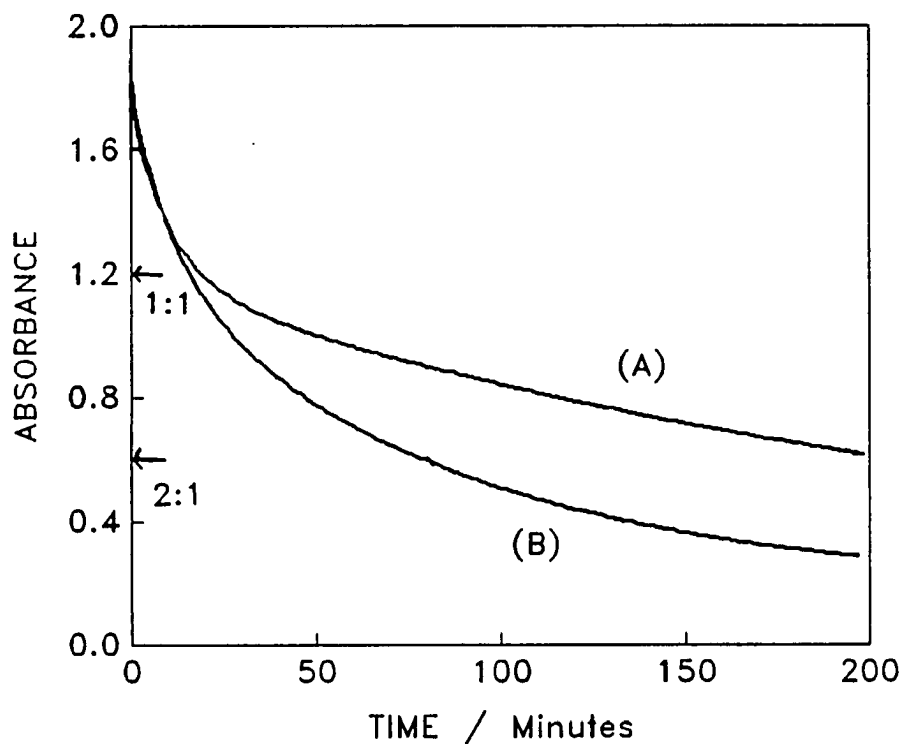
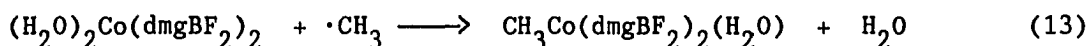
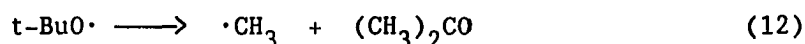
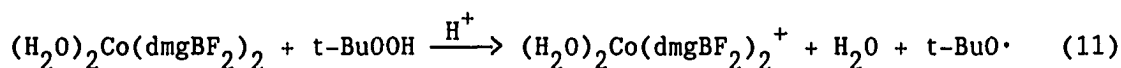


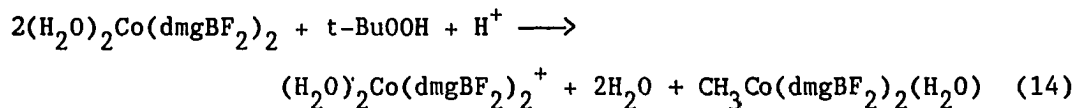
Figure A-16. The reaction between $(\text{H}_2\text{O})_2\text{Co}(\text{dmgBF}_2)_2$ and H_2O_2 (A) shows a 1:1 reaction stoichiometry ($(\text{H}_2\text{O})_2\text{Co}(\text{dmgBF}_2)_2:\text{H}_2\text{O}_2$), ($[(\text{H}_2\text{O})_2\text{Co}(\text{dmgBF}_2)_2] = 2.24 \times 10^{-4} \text{ M}$, $[\text{H}_2\text{O}_2] = 8.80 \times 10^{-5} \text{ M}$, 2 cm cell). The reaction between $(\text{H}_2\text{O})_2\text{Co}(\text{dmgBF}_2)_2$ and $t\text{-BuOOH}$ (B) shows a 2:1 reaction stoichiometry ($(\text{H}_2\text{O})_2\text{Co}(\text{dmgBF}_2)_2:t\text{-BuOOH}$), ($[(\text{H}_2\text{O})_2\text{Co}(\text{dmgBF}_2)_2] = 2.24 \times 10^{-4} \text{ M}$, $[t\text{-BuOOH}] = 8.80 \times 10^{-5} \text{ M}$, 2 cm cell)

The kinetics of the reaction of $(\text{H}_2\text{O})_2\text{Co}(\text{dmgBF}_2)_2$ with $t\text{-BuOOH}$ have also been measured. Figure A-2 illustrates the plot of k_{obs} vs. $[t\text{-BuOOH}]$ suggested by equation 16. A least-squares analysis yields a second-order rate constant, $k_{11} = 9.47 \pm 0.09 \text{ M}^{-1}\text{s}^{-1}$ ($\mu = 0.100 \text{ M}$, $\text{HClO}_4 = 0.100 \text{ M}$). A variation of the acid concentration (0.020 - 0.100 M HClO_4) showed no acid dependence.

Scheme A-3. Reaction Mechanism for $(\text{H}_2\text{O})_2\text{Co}(\text{dmgBF}_2)_2$ and $t\text{-BuOOH}$



Net reaction:



$$\frac{-d[(\text{H}_2\text{O})_2\text{Co}(\text{dmgBF}_2)_2]}{dt} = 2k_{11}[(\text{H}_2\text{O})_2\text{Co}(\text{dmgBF}_2)_2][t\text{-BuOOH}] \quad (15)$$

$$k_{\text{obs}} = 2k_{11}[t\text{-BuOOH}] \quad (16)$$

Evidence which supports the mechanism for the reaction of $(\text{H}_2\text{O})_2\text{Co}(\text{dmgBF}_2)_2$ with $t\text{-BuOOH}$ is the spectroscopic detection of $\text{CH}_3\text{Co}(\text{dmgBF}_2)_2(\text{H}_2\text{O})$ in about 67% of the theoretical yield. The spectrum of the reacted solution $(\text{H}_2\text{O})_2\text{Co}(\text{dmgBF}_2)_2$ with $t\text{-BuOOH}$ was recorded after passage through the ion-exchange column. The column retained the charged $(\text{H}_2\text{O})_2\text{Co}(\text{dmgBF}_2)_2^+$ and allowed the uncharged organocobalt to pass through the column. The NMR spectrum of the products of the reaction confirms this assignment, Figure A-7.

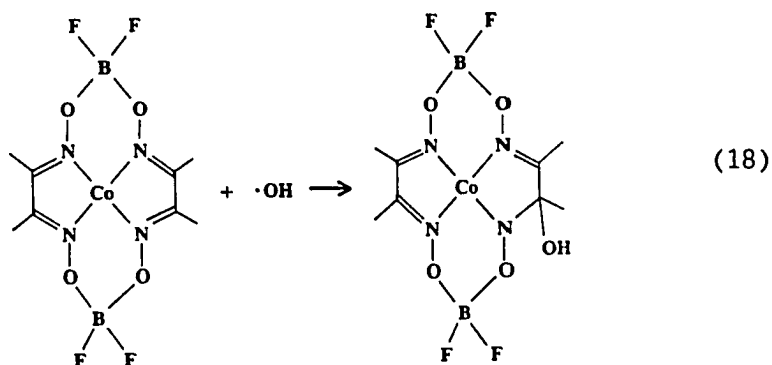
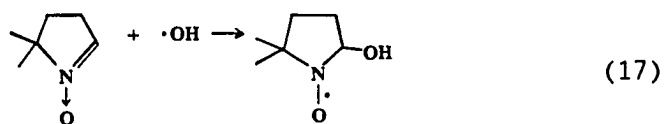
DISCUSSION

The reaction between $(\text{H}_2\text{O})_2\text{Co}(\text{dmgBF}_2)_2$ and hydrogen peroxide is analogous to the reactions of several closely related cobalt(II) macrocycles with hydrogen peroxide.² The reaction between $(\text{H}_2\text{O})_2\text{Co}([\text{14}] \text{aneN}_4)^{2+}$ and hydrogen peroxide (which is proposed to occur by a Fenton-type mechanism) appears to be an exception to this generalization.

The mechanism proposed for the reaction between $(\text{H}_2\text{O})_2\text{Co}(\text{dmgBF}_2)_2$ and hydrogen peroxide, Scheme A-2, is the simplest explanation in accord with the 1:1 ($(\text{H}_2\text{O})_2\text{Co}(\text{dmgBF}_2)_2:\text{H}_2\text{O}_2$) reaction stoichiometry. The failure to detect hydroxyl radicals indicates this free radical is not a freely released intermediate of this reaction. Since only easily-oxidized alcohols affect the course of the reaction and direct oxidation of the alcohols by $(\text{H}_2\text{O})_2\text{Co}(\text{dmgBF}_2)_2^+$ does not occur, a one-electron oxidation of the macrocyclic ring has been proposed in addition to the one-electron oxidation of the metal center. This scheme has the very reactive hydroxyl radical reacting with the macrocyclic ligand instead of a reaction with another molecule of $(\text{H}_2\text{O})_2\text{Co}(\text{dmgBF}_2)_2$ or recombination. This reaction of the hydroxyl radical would result in a ligand modification at one or more sites. A ligand modification is clearly observed for the reaction between B_{12r} and hydrogen peroxide where a detailed product analysis detects several cobalt macrocyclic species.⁶ The reaction of hydroxyl radicals with a macrocyclic ring was also seen for $\text{Co}(\text{Me}_6[\text{14}]-4,11\text{-diene})^{2+}$. The hydroxyl radical is suggested to react very readily with cobalt(II) macrocyclic complexes which contain double bonds. The attack site is suggested to be at the imine nitrogen.⁷ The hydroxyl radical could either

abstract a hydrogen from a C-H bond in the macrocyclic ring, Figure A-1 or it could add to a double bond, equation 18. Both reactions would leave a ligand modification, initially in the form of a ligand radical as a carbon-centered radical or as a nitrogen-centered radical. The macrocycle of $(\text{H}_2\text{O})_2\text{Co}(\text{dmgBF}_2)_2$ should be an efficient radical scavenger. The similarity to DMPO (5,5-dimethyl-1-pyrroline N-oxide), an efficient radical scavenger, is striking, equation 17. $(\text{H}_2\text{O})_2\text{Co}(\text{dmgBF}_2)_2$ essentially contains four radical scavenger subunits which could trap a hydroxyl radical before it could escape the vicinity of the initial reaction site, the cobalt macrocycle.

Radicals are known to react with DMPO by adding to the carbon of the carbon-nitrogen double bond, leaving a nitrogen centered radical, equation 17. This radical is stabilized by the oxygen bound to the nitrogen, creating a long-lived radical (these lifetimes are on the order of several minutes). An analogous equation for $(\text{H}_2\text{O})_2\text{Co}(\text{dmgBF}_2)_2$ with a hydroxyl radical is shown in equation 18.



The ligand modification proposed is supported by the NMR product analysis. The NMR spectrum of the product of the reaction between $(\text{H}_2\text{O})_2\text{Co}(\text{dmgBF}_2)_2$ and H_2O_2 is consistent with the ligand modification proposed in equation 18. The NMR spectrum predicted for the product of reaction 18 would have four major peaks assigned to the four inequivalent methyl groups of the macrocycle. Additional peaks could result from the decomposition products or from a mixture of products due to the attack of the hydroxyl radical at various sites on the macrocycle.

The NMR spectra of "cleanly" oxidized $(\text{H}_2\text{O})_2\text{Co}(\text{dmgBF}_2)_2$ by $\text{Fe}(\text{OH})^{2+}$, reveals a set of peaks which is attributed to the macrocycle methyl groups of $(\text{H}_2\text{O})_2\text{Co}(\text{dmgBF}_2)_2^+$. This set of peaks is thought to be due to a distortion of the macrocyclic ring due to hydrogen bonding between the two axial water molecules and the fluorine atoms of the BF_2 bridging subunits. The evidence for this assignment comes from the experiment where $((\text{CH}_3)_2\text{CO})_2\text{Co}(\text{dmgBF}_2)_2$ was oxidized to $((\text{CH}_3)_2\text{CO})\text{Co}(\text{dmgBF}_2)_2(\text{H}_2\text{O})^+$ by $\text{Fe}(\text{OH})^{2+}$ in d_6 -acetone. Since acetone is undoubtedly trapped in one of the two axial positions, the steric bulk of this molecule in this position and its inability to hydrogen bond with the fluorine atoms leaves the macrocycle without any appreciable distortion. Thus, the four methyl groups on the ring are equivalent. This is consistent with the singlet observed in the NMR spectrum of $((\text{CH}_3)_2\text{CO})\text{Co}(\text{dmgBF}_2)_2(\text{H}_2\text{O})^+$ in d_6 -acetone.

The mechanism of the reactions of $(\text{H}_2\text{O})_2\text{Co}(\text{dmgBF}_2)_2$ with various alkyl hydroperoxides, $\text{RC}(\text{CH}_3)_2\text{OOH}$, in aqueous solution (shown in Scheme A-3) is consistent with the general mechanism proposed in Scheme A-1. The cobalt products of these reactions are the corresponding organocobalt complexes, $\text{RCo}(\text{dmgH})_2\text{OH}_2$. The initial radical intermediate is $(\text{CH}_3)_3\text{CO}\cdot$, which can

undergo a rapid β -scission to form a methyl radical and an acetone molecule, an observed product. The methyl radical reacts rapidly with another molecule of $(\text{H}_2\text{O})_2\text{Co}(\text{dmgBF}_2)_2$ to form the observed product $\text{CH}_3\text{Co}(\text{dmgBF}_2)_2(\text{H}_2\text{O})$.

The reactions of $(\text{H}_2\text{O})_2\text{Co}(\text{dmgBF}_2)_2$ with hydrogen peroxide or alkyl hydroperoxides are consistent with the reactions of similar cobalt(II) macrocycles with these oxidants. The general mechanism for the reaction of the cobalt(II) macrocycles with alkyl hydroperoxides appears to be straight forward and well understood; however, the reaction with hydrogen peroxide is not well understood and includes some speculation.

SUMMARY

The characterization, kinetics, and mechanisms of the reactions of $(\text{H}_2\text{O})_2\text{Co}(\text{dmgBF}_2)_2$ with various oxidants were studied in aqueous solution. The reaction of $(\text{H}_2\text{O})_2\text{Co}(\text{dmgBF}_2)_2$ with hydrogen peroxide follows a 1:1 reaction stoichiometry ($(\text{H}_2\text{O})_2\text{Co}(\text{dmgBF}_2)_2:\text{H}_2\text{O}_2$). This reaction has a complex mechanism which includes the oxidation of the Co(II) metal center as a first stage. The reaction of $(\text{H}_2\text{O})_2\text{Co}(\text{dmgBF}_2)_2$ with t-BuOOH follows a 2:1 reaction stoichiometry ($(\text{H}_2\text{O})_2\text{Co}(\text{dmgBF}_2)_2:\text{t-BuOOH}$). The mechanism for these reactions include the formation of $(\text{H}_2\text{O})_2\text{Co}(\text{dmgBF}_2)_2^+$ and $\text{CH}_3\text{Co}(\text{dmgBF}_2)_2(\text{H}_2\text{O})$ in a 1:1 product ratio.

BIBLIOGRAPHY

1. Espenson, J. H.; Martin, A. H. J. Am. Chem. Soc., 1977, 99, 5953.
2. Heckman, R. A.; Espenson, J. H. Inorg. Chem., 1979, 18, 38.
3. Bakac, A.; Brynildson, M. E.; Espenson, J. H. Inorg. Chem., 1986, 25, 4108.
4. Meyerstein, D. Personal Communication, Ben-Gurion University of the Negev, Beer-Sheva, Israel
5. Bakac, A.; Brynildson, M. E.; Espenson, J. H. Inorg. Chem., 1986, 25, 4108.
6. Pratt, J. M. "Inorganic Chemistry of Vitamin B₁₂", Academic Press: New York, N. Y., 1972; p 288.
7. Tait, A. M.; Hoffman, M. Z.; Hayon, E. Int. J. Radiat. Phys. Chem., 1976, 8, 691.

GENERAL SUMMARY

The kinetics and mechanism of the decomposition of CrO_2^{2+} have been investigated. Two decomposition pathways have been proposed, the first consists of a bond homolysis, $\text{CrO}_2^{2+} \rightarrow \text{Cr}^{2+} + \text{O}_2$, and the second pathway a bimolecular reaction between two CrO_2^{2+} ions to form HCrO_4^- . The data do not require a description of CrO_2^{2+} as other than a superoxochromium(III) ion.

The oxidation-reduction reactions of CrO_2^{2+} with various outer- and inner-sphere reductants have been investigated. CrO_2^{2+} reacts readily with $\text{Co}(\text{sep})^{2+}$, $\text{Ru}(\text{NH}_3)^{2+}$, and V^{2+} in a manner consistent with outer-sphere mechanisms. The reactions between CrO_2^{2+} and Fe^{2+} , $(\text{H}_2\text{O})_2\text{Co}([\text{14}] \text{aneN}_4)^{2+}$, or $(\text{H}_2\text{O})_2\text{Co}([\text{15}] \text{aneN}_4)^{2+}$ proceed in a manner consistent with inner-sphere mechanisms. The chemistry of CrO_2^{2+} has been shown to be analogous to the chemistry of $(\text{H}_2\text{O})\text{Co}([\text{14}] \text{aneN}_4)\text{O}_2^{2+}$.

The characterization of $(\text{H}_2\text{O})_2\text{Co}(\text{dmgBF}_2)_2$ by various instrumental and chemical techniques has been presented. The kinetics and mechanism for the reaction of $(\text{H}_2\text{O})_2\text{Co}(\text{dmgBF}_2)_2$ with $(\text{H}_2\text{O})_5\text{Fe}(\text{OH})^{2+}$ was also discussed.

The characterization, kinetics, and mechanisms of the reactions of $(\text{H}_2\text{O})_2\text{Co}(\text{dmgBF}_2)_2$ with hydrogen peroxide and $t\text{-BuOOH}$ have been studied. The chemistry is analogous to that seen for related cobalt(II) macrocyclic complexes.

ACKNOWLEDGMENTS

I would like to thank Professor James H. Espenson and Dr. Andreja Bakac for their guidance during my graduate career.

I would also like to thank my parents, Ardell and Marie Brynildson, for their love, support, and dedication to the education of their family. Thank you for being two wonderful role models to help guide me for the rest of my life.